Università degli Studi di Torino

Scuola di Dottorato in Scienza ed Alta Tecnologia
Indirizzo di Fisica ed Astrofisica

The Alignment of the CMS Tracker and its Impact on the early Quarkonium Physics

Coordinatore
Prof. Guido Boffetta

Tutore
Prof. Ernesto Migliore

Candidato
Marco Musich

Ciclo XXIII

Date of dissertation
21^{st} February 2011

Candidate
Marco Musich

Tutor
Prof. Ernesto Migliore
Università degli Studi di Torino

Degree Board
Prof. E. Menichetti
Università degli Studi di Torino
Prof L. Ramello
Università degli Studi del Piemonte Orientale
Dr. F. Parodi
Università degli Studi di Genova

Ph.D. Coordinator
Prof. Guido Boffetta
Università degli Studi di Torino

Dedicated to my beloved one, and to ... the Schrödinger's Cat

Grow old along with me!
The best is yet to be,
The last of life, for which the first was made...

R. Browning, *Rabbi Ben Ezra* (1864)

I have measured out my life with coffee spoons;
I know the voices dying with a dying fall
Beneath the music from a farther room.
So how should I presume?

T. S. Eliot, *The Love Song of J. Alfred Prufrock* (1915)

Acknowledgements

The last three years of research towards the Ph.D. degree certainly are among the most intense and interesting periods of my life. They shaped me in both scientific as well as in personal aspects. I would like to thank everyone who made these last three years so precious and worthwhile!

In the first place I am deeply indebted with Ernesto, for the infinite care he has spent on the quality of my work and for the many things he taught me during these years. I would like to thank also all the CMS Torino group members, in particular Amedeo, Nicoló, Nadia, Lino, Marco, Nicola, Stefano, Mario, Chiara and Prof. Romero for the lively and familiar working environment.

I am particularly grateful to the "youngsters" of the crew; everyone in his/her own way was important. My sincere gratitude goes to all my Saint-Genis flatmates: Roberto, with whom I also shared the mixed blessing of *alignment*, Cristina, Daniele, Giorgia and Susy. I owe a special word of gratitude to my colleagues and *friends* Matteo and Alberto: thanks for all the help, but also for all the fun!

Among the number of people to whom I am indebted for their help and the important contribution to my work, I could not help mentioning the CMS Tracker alignment people I had the pleasure to work with: Prof. Andrei Gritsan, Alessio Bonato, Nhan Tran, Andrew Whitbeck, Frank Meier and Ernest Aguiló.

A word of thank goes to the old and new friends: Thanushan, Fabrizio, Diego, Isacco and Ivan, thanks for making my lunch times so pleasant and at the same time stimulating; Aurelio and Valentina, it has been a pleasure to share the same corridor and the enjoyable discussions during coffee breaks.

My deepest gratitude goes to my parents, to my grandmother Elsa, my uncle Ezio and to all my family for having supported me in my scientific and non-scientific endeavours. I would also like to thank Mr. and Mrs. Raicu for being so nice with me and having accepted me in their home like a relative.

And finally to Sorina, my beloved one, for being a constat presence to my side, never letting me down in the hard times, whenever I needed it, and for all that really matters and *will* matter.

Contents

Introduction 1

I Background 3

1 Physics at the Large Hadron Collider 1

1.1 Standard Model . . . 2
1.2 Experimental tests of the Standard Model . . . 4
1.3 The Large Hadron Collider . . . 7
1.3.1 LHC Operations in 2009-2010 . . . 9
1.4 Early LHC Physics . . . 10
1.4.1 Z and W boson production . . . 11
1.4.2 Top quark mass measurement . . . 12
1.4.3 B-physics and CP violation . . . 12
1.5 High energy and high luminosity Physics . . . 12
1.5.1 The Higgs boson search at LHC . . . 12
1.5.2 Supersymmetry . . . 14
1.5.3 Search for new massive vector bosons . . . 14
1.6 Heavy Quarkonia Production at LHC . . . 15
1.6.1 Color Evaporation Model (CEM) . . . 16
1.6.2 Color Singlet Model (CSM) . . . 17
1.6.3 Non Relativistic QCD (NRQCD) . . . 17

2 The Compact Muon Solenoid Experiment 21

2.1 The Inner Tracking System . . . 24
2.1.1 The pixel Tracker . . . 26
2.1.2 The strip Tracker . . . 27
2.1.3 Sensor working principle and signal readout . . . 28
2.2 The Calorimeters . . . 30

2.2.1 The electromagnetic calorimeter . . . 30
2.2.2 The hadron calorimeter . . . 31
2.3 The Magnet . . . 32
2.4 Muon system . . . 33
2.4.1 The muon Trigger . . . 34
2.5 Offline muon reconstruction in CMS . . . 35
2.5.1 Track reconstruction in the muon spectrometer alone . . . 36
2.5.2 Track reconstruction in the Inner Tracker alone . . . 36
2.5.3 Track matching: the *Global Muon* reconstruction . . . 37
2.5.4 Track parametrization in CMS . . . 38
2.6 Tracker operations and performance in 2010 . . . 40

II Research Work 43

3 The Alignment of the CMS Tracker 45
3.1 Alignment hierarchy . . . 47
3.2 Survey measurements and LAS . . . 49
3.2.1 The Tracker survey . . . 49
3.2.2 Monitoring with LAS . . . 50
3.3 Track-based alignment . . . 51
3.3.1 Coordinate systems and Track-to-hit residuals . . . 52
3.3.2 Pull definition . . . 55
3.3.3 Track based alignment formalism . . . 57
3.4 Alignment Algorithms . . . 58
3.4.1 The HIP Alignment Algorithm . . . 59
3.4.2 The Millepede Alignment Algorithm . . . 60
3.5 Alignment Workflow . . . 62

4 Tracker Alignment Validation 65
4.1 Results with Cosmic Ray Data . . . 65
4.1.1 Alignment Strategy . . . 69
4.2 Track fit quality and hit residuals . . . 71
4.2.1 Measurement of the alignment precision . . . 73
4.2.2 Monitoring of the geometry . . . 79
4.2.3 Monitoring of the tracking performance . . . 80
4.3 Results with collision data . . . 82

4.3.1 Trend of residuals vs track momentum 89
4.3.2 Tracking performance after aligment with collision tracks . . 99
4.4 Calibration of Alignment Position Errors 104
4.4.1 APE determination during comic ray data taking 106
4.4.2 Evolution of APE 121
4.4.3 APE determination after collision data taking 121
4.5 Primary Vertex Validation 124
4.5.1 Studies on simulation 128
4.5.2 Performance with collision data 131

5 Impact of alignment on early J/ψ physics 135
5.1 Data sample and event reconstruction 136
5.1.1 Event selection 136
5.1.2 Offline muon reconstruction 136
5.1.3 J/ψ event selection 137
5.2 Fraction of J/ψ from b-hadron decays 138
5.2.1 Separating prompt and non-prompt J/ψ 138
5.3 Tracker Weak Modes 140
5.3.1 Effects on the J/ψ mass 142
5.3.2 Effects on the b-fraction measurements 143

Summary 147

A Effects of the outliers in the distributions of residuals 149

B Error scaling 153

C More on systematic movements of the Pixel Tracker substructures 155

Bibliography 160

List of Tables

1.1 *Fermion properties* 4

1.2 *Gauge Bosons properties* 5

1.3 *Design LHC parameters for p-p and Pb-Pb ($^{208}Pb^{82+}$) collisions.* 8

1.4 *Expected cross sections and number of events per second and per year for one experiment at LHC at $\mathcal{L} = 2 \cdot 10^{33} cm^{-2} s^{-1}$.* 8

2.1 *Different contributions to the energy resolution of ECAL [24].* 31

3.1 *Estimated assembly precision (RMS, in μm) of Tracker components. Values are given in between the mechanical hierarchy levels they are valid for, e.g. the position accuracy of sensors in modules is 10 μm [38].* 49

3.2 *Criteria used for selection of events/tracks in different `AlCaReco` streams.* 63

4.1 *Quality cuts applied to hits and tracks used in the alignment at CRAFT.* . 69

4.2 *Table of values obtained for the different estimators of the residual misalignment for two statistically independent track samples.* 76

4.3 *Table of values obtained for different estimators of the residual misalignment. Valus for the FPIX detector are missing due to the too small fraction of cosmic tracks crossing its volume* 76

4.4 *RMS of the distribution (in μm) of the median of the residuals ($\mu_{1/2}$) (DMR) in the u' and v' coordinates for modules with more than 30 hits. The number of these modules for each subdetector compared to the total number of modules is stated in the last column. Four geometries are considered: those obtained with the three methods discussed in the text and the geometry before alignment. Results from simulations based on the combined alignment and ideal geometries are shown for comparison.* . . . 79

4.5 *Quality cuts applied to hits and tracks used in the alignment, for the Comsic and Collision data sample.* 84

4.6 *RMS of the distribution of the median of the residuals (DMR) in the u' and v' local coordinates for modules with more than 200 hits. The number of these modules compared to the total number of modules is stated in the last column. Results from simulations based on the combined alignment and ideal geometries are shown for comparison alogn with results on data.* 86

4.7 *The quality cuts applied on the data and Monte Carlo samples to perform the study of track-to-hit residuals vs track momentum.* . . . 90

4.8 *Table of the fit parameters for the track-to-hit residual trend as a function of momentum. In the table are listed also the intrinsic hit resolutions estimated from data-driven methods [48] and the estimated remaining misalignment σ_{mis} calculated as in Equation 4.14.* 97

4.9 *Table of the applied parameters applied to obtain the calibrated APE after the CRAFT aligmnent in Tracker Pixel and Tracker Endcaps.* 101

4.10 *Table of misalignment applied to track reconstruction in the simulation to reproduce the observed features of cosmic ray data after alignment in TIB and TOB, and applied parameters to calibrate the APE in the Tracker Strip Barrel.* 112

4.11 *Table of the applied parameters applied to obtain the calibrated APE after the CRAFT aligmnent in Tracker Pixel and Tracker Endcaps.* 112

4.12 *The cuts applied to select tracks for the primary vertex validation.* . . 124

5.1 *Definition, formula and size of the nine systematic distorsions (modes) used for study the impact on the geometry obtained.* 140

5.2 *Table of the systematic uncertainties Δf_b on the b-fraction due to remaining systematic misalignment for each y-p_T bin. In the table are reported also the relative uncertainty, and the mode responsible for the largest discrepancy observed with respect to the starting geometry.* 145

5.3 *Summary of relative systematic uncertainties in the b-fraction yield $\Delta f_b/f_b$ (in %). The range shows the min-max $\Delta f_b/f_b$ excursion found when changing the p_T bin for each of the three rapidity regions. In general, uncertainties are p_T-dependent and decrease with increasing p_T.* 145

List of Figures

1.1 *Left plot. $\Delta\chi^2$ of the fit of electroweak measurements from LEP, SLD and Tevatron as a function of the Higgs mass. The vertical yellow bands shows the 95% CL exclusion limit on M_H from the direct searches at LEP-II and Tevatron. Right plot. The comparison of the indirect constraints on M_W and m_t based on LEP-I/SLD data (dashed contour) and the direct measurements from the LEP-II/Tevatron experiments (solid contour). In both cases the 68% C.L. contours are plotted. Also shown is the SM prediction for the masses as a function of the Higgs mass in the region favoured by theory ($M_H < 1000$ GeV) and allowed by direct searches ($114 < M_H < 170$ GeV and $M_H < 180$ GeV) [7].* 6

1.2 *Cross section as a function of the center-of-mass energy (left) and rate of events at LHC as a function of the mass of the produced particle (right) for interesting processes [9].* 9

1.3 *Right: Integrated luminosity per day delivered to (red), and recorded by CMS (blue) during stable beams at $\sqrt{s} = 7$ TeV in 2010. .Left: Integrated luminosity versus time delivered to (red), and recorded by CMS (blue) during stable beams at $\sqrt{s} =$7 TeV centre-of-mass energy.* 10

1.4 *Left: Parton luminosity ratios between LHC and Tevatron as a function of $\sqrt{\hat{s}}$ (partonic centre of mass energy) at $\sqrt{s} = 7$ TeV. Right: Kinematic region in the (x, Q^2) plane, accessible at LHC, at $\sqrt{s} = 14$ TeV.* 11

1.5 *Higgs production mechanisms at tree level in proton-proton collisions: (a) Gluon-gluon fusion; (b) W and Z fusion; (c) $t\bar{t}$ associated production; (d) W and Z associated production.* 13

1.6 *Left: Higgs boson production cross sections at $\sqrt{s} = 7$ TeV as a function of the Higgs boson mass. Right: Branching ratios for different Higgs boson decay channels as a function of the Higgs boson mass. [14]* 13

1.7 *Spectrum and transitions of the charmonium family.* 15

1.8 *Left: leading order diagrams in QCD to produce heavy quark pairs. Right: Next-to-leading order diagrams relevant to heavy quarkonium production.* 16

2.1 *Exploded view of CMS layout [24].* 22

2.2 *Transverse view of the barrel region of the CMS detector [24].* 23

2.3 *Longitudinal view of one quarter of the CMS detector [24].* 24

2.4 *Expected momentum resolution of muons as a function of momentum p, using measurements of the muon system only (blue), the Tracker only (green) or both detectors (red). Left. Central region $0 < \eta < 0.2$. Right. Forward endcap region $1.8 < \eta < 2.0$ [24].* 27

2.5 *Schematic illustration of the pixel Tracker.* 28

2.6 *Longitudinal view of one quarter of the strip Tracker: blue modules are double sided, red ones single sided.* 28

2.7 *Schematic view of a microstrip detector (left) and of a pixel detector (right) adopted in the CMS Tracker [24].* 29

2.8 *Longitudinal view of one quarter of the CMS electromagnetic calorimeter [24].* 30

2.9 *Left: Different contributions to the energy resolution of the ECAL. The curve labelled intrinsic includes the shower containment and a constant term [24]. Right: di-phhoton invariant mass specrtum reconstructed by ECAL with about 250 nb^{-1} of data at $\sqrt{s}$ 7 TeV. The π_0 peak is visible, the mass resolution is of the order of 10%* 31

2.10 *Layout of the magnetic field of CMS [26].* 32

2.11 *Longitudinal view of one quarter of the CMS muon spectrometer [24].* . . 33

2.12 *Structure of the Level-1 Trigger system [24].* 35

2.13 *Schematic representation of the Kalman Filter based pattern recognition. The points represent hits, the curved lines track candidates and the shaded boxes the size of the search window [31].* 37

2.14 *Track parameters defined at the perigee computed with respect the origin of the global frame.* 40

2.15 *Signal to Noise ratio S/N of strip clusters for TIB (right) and TOB (left). Most Probable Values (MPV) are extracted from a gaussian convoluted with a Landau pdf.* 40

2.16 *Strip hit efficiency as a function the layer (disk) for all the Strip Tracker subdetectors. The black squares refer to all the modules, red circles to the situation when bad components are subtracted.* 41

2.17 *Left: muon tracking efficiency as a function of η for muons in data (points with errors) and simulation (hatched) measured with 2010 collision data [34]. Right: primary vertex resolution in the x direction as a function of the number of tracks used in the fitted vertex [35].* 41

2.18 *Left: measured resolution of the track transverse impact parameter as a function of the track p_T. Only central tracks with $|\eta| < 0.4$ are considered. Black and red symbols correspond to results from data and simulation [35]. Right: measured resolution of the track transverse impact parameter as a function of the track η for transverse momenta 1.0 ± 0.1 GeV (circles), in 3.0 ± 0.2 GeV (squares) and 8.0 ± 1.0 GeV/c (triangles) [35].* 42

3.1 *Left picture: the tracking device is crossed by charged particles, producing tracks. Middle picture: the geometry of the detector is assumed to be ideal, even if misaligned in the reality, and this causes wrong estimation of particle's momentum. Right picture: module positions are moved according to the corrections found after the alignment procedure, leading to a geometry close to the real one and consequently to a correct estimation of track parameters. Relative movements are greatly exaggerated* 46

3.2 *Illustration of the hierarchies implemented inside the CMS alignment software. Pixel Tracker structure is shown on the left, and strip Tracker hierarchy is shown on the right. They closely follow the hierarchies of the mechanical structures.* 48

3.3 *Schematic illustration of the local coordinates of a strip module as used for alignment. Global parameters (in parentheses) are shown for modules in the barrel detectors (TIB and TOB).* 48

3.4 *Displacement of modules in CMS global cylindrical coordinates as measured in survey with respect to design geometry. A colour code is used: black for TIB, green for TID, red for TOB, and blue for TEC [38].* 50

3.5 *Overview of the CMS Laser Alignment System. Alignment Tubes (AT), ranging from endcap to endcap, together with Alignment Ring (AR) for the Endcap monitoring, distribute the light via optical fibers through the Beam Splitter (BS).* 51

3.6 *The definition of a track-hit residual R_ξ in local x and local y direction. See text for details.* 52

3.7 *Sketch of how track-to-hit unbiased residuals are calculated.* 53

3.8 *Left: Distribution of the trend of the pull as a funcion of the number of measurments in a simple toy MC considering a straight line fit. Right, the pulls for the same toy MC using twelve measurements, a typical number for a track in CMS.* 56

3.9 *Principle of alignment. $\Delta\mathbf{R}$ and $\Delta\mathbf{x}$ signify the alignment corrections, rotations and translations, to the position of the detector unit $\mathbf{x}$. Transformation changes the local (detector) coordinates of the impact point.* . 59

3.10 *The CMS Alignment data flow.* 62

4.1 *Left: Effective fraction of the CMS experiment participating in the 2007 and 2008 global run campaigns as a function of time. The fraction of each of the seven major detector systems is represented by a bar. Only one RPC endcap was missing by September 2008 [46]. Right: The accumulated number cosmic ray triggered events with the magnet at 3.8 T as a function of days into CRAFT, beginning October 16, 2008.* 66

4.2 *Display of a cosmic muon recorded during CRAFT which enters and exits through the DT muon system, leaves measurable minimum ionizing deposits in the HCAL and ECAL, and crosses the silicon strip and pixel tracking systems. Reconstruction of the trajectory is also indicated [46]* . 67

4.3 *Collection of basic track quantities used for Tracker alignment and validation during CRAFT. First row, track momentum p and q/p, in the secondo row the polar (θ) and azimuthal (ϕ) angles, in the third row transverse d_0 and longitudinal d_z impact parameters and finally in the last row the number of hits and a map in the $\theta - \phi$ plane showing how the track direction was strongly peaked in the $\theta = 90^\circ$,$\phi = 90^\circ$ region (high-lighted in red there is the acceptance of the Tracker Barrel). The solid (red) circles represent the cosmic ray data whereas the open (blue) circles come from a MC simulation.* 68

4.4 *Left: The shaft through which the CMS detector has been lowered in the construction phase induces different acceptance in ϕ for positive and negative cosmic ray muons. Right: this effect is mitigated for high momentum muons, since the extra contribution of muons coming through the shaft is numerically less important in that kinematical regime.* 69

4.5 *Sketch of Tracker DS module: stereo module (green) is tilted of 100 mrad with respect to the rϕ component (blue).* 70

4.6 *Right: Track χ^2/ndf distributions for non-aligned (dotted line), local method (dashed-dotted line), global method (dashed line), and combined method (solid line) geometries. Right:Track χ^2/ndf distributions for Ideal alignment Monte Carlo (red solid line), combined method approach on misaligned Monte Carlo (dashed-dotted black line), combined method on data (green dashed line) geometries.* 72

4.7 *Track residuals, shown for BPIX (top left u' , top right v'), TIB (bottom left), and TOB (bottom right). The four lines correspond to positions before alignment (dotted lines) and after alignment with the global (dashed lines), local (dot-dashed lines), and combined methods (solid lines).* . . . 72

4.8 *Track residuals, shown for FPIX (top left u' , top right v'), TID (bottom left), and TEC (bottom right). The four lines correspond to positions before alignment (dotted lines) and after alignment with the global (dashed lines), local (dot-dashed lines), and combined methods (solid lines).* . . . 73

4.9 *Comparison of different estimators of residual misaligment in u' coordinate for cosmic muon data, for the six Tracker subdetector. Only modules with at least 30 hits have been considered. Black line is the mean of the residual distribution, blue the median, pink the mean value of a gaussian fit and red truncated mean (see text). Each entry of the histogram represents a Tracker module.* 75

4.10 *Median of residual in u' coordinate vs the mean of residuals for the six Tracker subdetectors. Only modules with at least 30 hits have been considered. Each entry of the histogram represents a Tracker module.* 75

4.11 *Comparison of different estimators of residual misaligment in a randomly misaligned cosmic track simulation, for the six Tracker subdetector. Only modules with at least 30 hits have been considered. Black line is the mean of the residual distribution, blue the median, pink the mean value of a gaussian fit and red truncated mean (see text)* 77

4.12 *Distribution of $\mu_{1/2}$, the median of the residuals, for modules with more than 30 hits, shown for BPIX (top left u, top right v), FPIX (second row left u , second row right v), TIB (third row left), TOB (third row right), TID (bottom left), and TEC (bottom right). Shown are distributions before alignment (black dotted), after alignment with the combined method (red solid), combined method MC (green dashed), and ideal MC (blue dash-dotted).Each entry of the histograms represents a Tracker module* 78

4.13 *Comparison of the position of the modules in the combined method geometry with respect to the design one: (y_{design} - y_{comb}) for the BPIX modules (left) and (z_{design} - z_{comb}) for the TIB modules (right) as a function of ϕ. In the plot on the left crosses (circles) represent modules of the positive (negative) x BPIX half-barrel. In the plot on the right crosses (circles) represent modules of the positive (negative) z TIB half-barrel. Each marker represents a Tracker module.* 80

4.14 *Track splitted at its point of closest approach to the nominal beamline. The two halves belonging to the same one were independently reconstructed and refit.* 81

4.15 *Differences between the track parameters measured at the point of closest approach to nominal beam-line, in the two halves of a cosmic track and scaled by $1/\sqrt{2}$. The distance of closest approach in the transverse direction d_{xy} (top) and $1/p_T$ (bottom) are shown. Four resulting geometries are reported: data non-aligned (black dotted lines), ideal Monte Carlo (blue dash-dot-dashed), and alignment result with cosmic ray data using combined method (red solid) and Monte Carlo (green dashed).* 81

4.16 *Dependence on p_T of the differences between the track parameters measured at the point of closest approach to the nominal beamline, in the two halves of a cosmic ray track and scaled by $1/\sqrt{2}$. The RMS of the distribution truncated at 95% is quoted at each momentum interval, shown for the distance of closest approach in the transverse direction d_{xy} (left) and for $1/p_T$ (right). Results are shown for the geometries derived from ideal MC (blue squares), and from the alignment result with cosmic ray data (red circles) and combined method MC (green triangles).* 81

4.17 *A typical Minimum Bias event selected for Tracker alignment.* 82

4.18 *Basic track quantities for collision tracks used for alignment validation. Top right azimuthal angle ϕ, top left track pseudorapidity (η), in the second row transverse momentum p_T (left) and curvature (right), in the third row the number of valid hits (left) and of lost hits (right) and in bottom row profile of track reduced χ^2 vs ϕ (left) and vs η (right). Shown are distributions for Design Geometry MC (black), MC with Startup alignment conditions (pink), and Data (blue).* 83

4.19 *Basic track quantities for collision tracks used for the first Tracker alignment with collision tracks: blue stands for cosmics, red for minimum bias tracks. Top left track pseudorapidity (η), top right p_T . Second row: spectra of number of BPIX hits (left) and of FPIX hits (right). Third row: spectra of number of TIB hits (left) and of TOB hits (right). Fourth row: spectra of number of TID hits (left) and of TEC hits (right).* 85

4.20 *Distribtions of χ^2/ndf. Left: the track reconstruction was performed without alignment position errors. Right: track reconstruction performed with calibrated alignment position errors. Shown are distributions for no misalignment MC (black), MC with "Startup" alignment conditions (pink), and Data (blue).* 86

4.21 *Distribution of track-to-hit residuals shown for BPIX (top left u', top right v'), FPIX (second row left u', second row right v'), TIB (third row left), TOB (third row right), TID (bottom left), and TEC (bottom right). Shown are distributions for no misalignment MC (black), MC with "Startup" alignment conditions (pink), and collision data (blue).* 87

4.22 *Distribution of $\mu_{1/2}$, the median of the residuals, for modules with more than 200 hits, shown for BPIX (top left u', top right v'), FPIX (second row left u' , second row right v'), TIB (third row left), TOB (third row right), TID (bottom left), and TEC (bottom right). Shown are distributions for no misaligment MC (black), MC with "Startup" alignment conditions (pink), and Data (blue).* 88

4.23 *Effect of Multiple Coulomb Scattering on track residuals: a) Particle trajectory deflection due to MS, b) the angular deflection is a function of the effective material thickness crossed by the particle t, which is a function of the impact angle θ_{3D}.* 90

4.24 *Collection of control distributions of basic track quantities. Top row: χ^2 distributions in linear (left) and χ^2/ndf in logarithmic scale (right). Second row: distributions of track momentum (left) and transverse momentum (p_T) right. Third row: distributions of track multiplicity and number of Tracker hits associated to a track. Bottom row: number of stereo and barrel pixel hits. Data are red dots, MC is painted in yellow.* 92

4.25 *Left: Sketch explaining the definition of local impact angle on the module surface. Right: Sketch of the selected track hit pattern for the residuals vs momentum study.* 93

4.26 *Left column: distributions of the local impact angle for the six momentum bins described in the text. Right column: distribution of cluster widths. Data are red dots, MC is painted in yellow.* 94

4.27 *Distributions of the track-to-hit residuals for the three BPIX Layers. The different momentum bins are shown with different colors.* 95

4.28 *Distributions of the track-to-hit residuals for the four TIB Layers. The different momentum bins are shown with different colors* 95

4.29 *Distributions of the track-to-hit residuals for the six TOB Layers. The different momentum bins are shown with different colors* 95

4.30 *Distributions of the trend of residuals widths as a function of track momentum. Blue corresponds to TOB, red to TIB, black to Barrel Pixel, dashed curves are MC, while solid curves data.* 96

4.31 *Distributions of the trend of residuals widths as a function of track momentum. Top row: Barrel Pixel (left) and TIB (right). Bottom row: First TOB Layers (left), Last TOB Layers (right). Dashed curves are MC, while solid curves data.* 96

4.32 *Scketch of the application of the overlap tecnique for estimating intrinsic hit resolution.* 97

4.33 *Distribution of the DMR for each layer of the Barrel of the Strip Tracker.* 98

4.34 *Comparison between the estimated alignment precision obtained with the DMR method (blue) and the residuals vs momentum trend (red).* 99

4.35 *Distribution of track-to-hit residuals widths plotted as a function of the Barrel layer for minimum bias tracks with the selection described in the text, for the six momentum bins considered in the analysis.* 99

4.36 *Left: distribution of χ^2/ndf for comsic (black) and minimum bias (red) tracks, after alignment with a mixed track sample. Right: distribution of the number of degrees of freedom.* 100

4.37 *Distributions of χ^2/ndf obtained from pseudo-experiments for cosmic and minimum bias spectra of number of degrees of freedom* 100

4.38 *Top row: distribution of $Prob(\chi^2, ndf)$ (left) and its profile vs track momentum. Middle row: profiles of $Prob(\chi^2, ndf)$ vs azimuthal angle (left) and pseudorapidity (right). Bottom row: profiles of $Prob(\chi^2, ndf)$ vs transverse impact parameter (left) and longitudinal impact parameter (right).* . 101

4.39 *Distribution of the probability of the internal Millepede-II χ^2 function vs. the transverse impact parameter of the track. Data: Cosmic ray muons, recorded in 2010 during commissioning of CMS. 200 000 tracks used [36].* 102

4.40 *Sketch explaining how track-to-hit residuals can get deteriorated by a non-planarity of the module active surface. The module surface distortion has been greatly exaggerated.* 102

4.41 *Sketch explaining the behaviour of the track angle α_{3D} as a function of the impact parameter for cosmic tracks in the Tracker Barrel.* 103

4.42 *Distributions of local impact angle of the track on the module surface α_{3D} for cosmic ray data (left) and minimum bias tracks (right).* 103

4.43 *Profiles of track-to-hit residuals in the sensitive coordinate as a function of track impact angle, in BPIX, TIB and TOB, for cosmic ray and collision tracks.* 104

4.44 *Effect of APE settings on the tracking efficiency and fake rate.* 105

4.45 *Left: Track finding efficiency vs η for simulated muons with $p_T = 100\ \mathrm{GeV}$. If the alignment uncertainty is not accounted for, the efficiency is significantly degraded [37]. Right: simulated b-jet efficiency versus non b-jet efficiency for a misalignment scenario close in performace to the "Startup" conditions, shown for the track counting high efficiency algorithm with an APE that is chosen too large or too small by a factor of two with respect to the ideal value [49].* 105

4.46 *Hit density map for CRAFT data, showing how the top and bottom part of the CMS Tracker Barrel were the most illuminated regions of the detector* 107

4.47 *Distributions of the cosine of the local impact angle* $\cos\theta_{3D}$ *(left), normalized* χ^2 *(center), track momentum (right) before and after the cut on the position of the point of closest approach.* 108

4.48 *Control region of the Strip Tracker used as a control region to determine the starting values in the APE calibration procedure.* 108

4.49 *Left: width of residuals as a function of track momentum for all cosmic tracks in TIB, TOB and Pixel Barrel. Right: Layer-wise trend of residuals as a function of momentum for tracks in the fiducial volume. The reference trend of residuals for CRAFT data is high-lighted in red, corresponding to* $p > 20$ *GeV* 108

4.50 *Left: Sketch of the random shifts applied to the modules in the simulation. Right: Layerwise residual distribution, DATA is black, MC reconstructed with misalignment only in u' direction is represented in blue, while in red is represented MC reconstructed with misalignment in u' and* γ*.* 109

4.51 *Distribution of residuals for the four layers of TIB. DATA is black, MC reconstructed with misalignment only in u' direction is represented in blue, while in red is represented MC reconstructed with misalignment in u' and* γ*.* 110

4.52 *Distribution of residuals for the six layers of TOB. DATA is black, MC reconstructed with misalignment only in u' direction is represented in blue, while in red is represented MC reconstructed with misalignment in u' and* γ*.* 110

4.53 *Left: Distribution of DMR for TIB (left) and TOB (right), DATA is black, MC reconstructed with misalignment only in u' direction is represented in blue, while in red is represented MC reconstructed with misalignment in u and* γ*.* 111

4.54 *Map of Tracker APE, after CRAFT calibration, large errors are represented with warm colors (towards red), small errors with cold colors (towards blue)* 113

4.55 *Top row: Distributions of the* χ^2 *per degree of freedom in linear (left) and logarithmic (right) scale. Bottom row: probability of* χ^2 $Prob(\chi^2, ndf)$ *(left) and profile of* χ^2 *as a function of track pseudorapidity (right). In figure are shown distributions before APE calibration (black line) and after (red line)* 114

4.56 *Left: relative track* p_T *uncertainty. Right: profile of relative track* p_T *uncertainty as a function of pseudorapidity. In figure are shown distributions before APE calibration (black line) and after (red line).* 114

4.57 *Distributions of normalized track-to-hit residuals after the APE calibration procedure: Top row Barrel Pixel (left* u' *and right* v'*), upper midder row Forward Pixel (left* u' *and right* v'*), lower middle row TIB (left) and TOB (right), bottom row TID (left) and TEC (right). Solid lines represent the results of Gaussian fits and the fit mean and sigma values are given within the plots.* 116

4.58 *Distributions of the RMS of normalized track residuals after the APE calibration procedure. Top row Barrel Pixel (left u'-coordinate and right v'-coordinate), upper-middle row Forward Pixel (left u'-coordinate and right v'-coordinate), lower middle row TIB (left) and TOB (right), bottom row TID (left) and TEC (right)* 117

4.59 *z-ϕ map of RMS of normalized track residuals after the APE calibration procedure for BPIX u' top row and v' bottom row. Each cell represents a module.* 118

4.60 *z-ϕ map of RMS of normalized track residuals after the APE calibration procedure for TIB. Each cell represents a module.* 118

4.61 *z-ϕ map of RMS of normalized track residuals after the APE calibration procedure for TOB. Each cell represents a module.* 118

4.62 *$x-y$ map of RMS of normalized track residuals after the APE calibration procedure for TEC Disk 1,2,7 and 9. Each cell represents a module* . . . 119

4.63 *Distributions of normalized split track residuals after the APE calibration procedure, for different track parameters:Top right: tranverse momentum p_T, top left: track curvature $\kappa \sim 1/p_T$ Middle row, right: polar angle θ, right: azimuthal angle ϕ. Bottom, left: transverse impact parameter d_{xy}, right: longitudinal impact parameter d_z* 120

4.64 *Trend the amplitude of the mimimum value assumed for the APE, in the different Tracker regions as a function of time.* 121

4.65 *Top row: distribution of χ^2/ndf (left) and $Prob(\chi^2, ndf)$ (right). Middle row: profiles of $Prob(\chi^2, ndf)$ vs azimuthal angle (left) and pseudorapidity (right). Bottom row: profiles of $Prob(\chi^2, ndf)$ vs longitudinal impact parameter (left) and p_T resolution (right). Data from 2010 collision events, before and after APE calibration.* 122

4.66 *Distributions of normalized track-to-hit residuals. First row: BPIX u' coordinate (left) and v' (right). Second row: TIB (left) and TOB (right). Data from 2010 collision events. Red symbols stand for uncalibrated APE, black symbols for the ϕ-uniform values, and blue symbols for tracks refitted with null values of APE.* 123

4.67 *Trend of pulls of normalized residuals for the ten layers of the Tracker Barrel. Red symbols for uncalibrated APE, black symbols for the ϕ-uniform values, and blue symbols for tracks refitted with null values of APE* . . . 123

4.68 *Left: Illustration of the primary vertex validation. Right: Definition of the transverse impact parameter.* 124

4.69 *Top row: distributions of track ϕ (left) and η (right). Bottom row: distributions of transverse impact parameter (left) and number of Pixel hits (right). Black curve refers to the minimum bias track datasample without any quality cut, while the red curve refers to the sample used for the validation, applying the cuts described in Table 4.12. Data from 2010 collisions.* 125

4.70 *Top row: vertex χ^2, distribution of vertex number of degrees of freedom (ndf), and normalized χ^2. Bottom row: d_{xy}, d_z calculated with respect to the unbiased vertex, and distribution of the number of tracks used to refit the PV. In red CMS 2010 collision data, and in black simulation in "Startup" conditions.* 126

4.71 *Unbiased vertex efficiency as a function of the number of tracks in the event. The distribution of the number of used tracks is also plotted. Open symbols stand for 2010 collision data, closed symbols for simulation.* 126

4.72 *Distributions of the unbiased transeverse d_{xy} (left) and longitudinal d_z (right) track impact parameter measured with respect the refit primary vertex. The fit function is a sum of two gaussian probability density functions, whose components are explicitluy shown (dotted lines). No selection on the tracks has been applied.* 127

4.73 *Scheme of Pixel Tracker with highlighted the sector definitions used for the primary vertex validation.* 128

4.74 *Distributions of the transverse impact parameter d_{xy} for different bins of the ϕ angle of the probe track. The red line refers to simulated tracks reconstructed applying a coherent elliptical misalignment, while the black line, referring to simulation with a "Startup" misalignment scenario, is shown for comparison in the Figure.* 129

4.75 *Left column: Distributions of the mean value of transverse impact parameter d_{xy} in bins of the ϕ of the probe track, for simulated tracks reconstructed applying a coherent elliptical misalignment (red points). Simulation with a "Startup" misalignment scenario is compared in the figure (black points). In the upper row the amplitude of the misalignment considered is $\varepsilon = 0.01$, while in the lower row it was set to $\varepsilon = 0.002$. Right column: the same distributions for the elliptical misalignments are fitted with a sinusoidal function $d_{xy}(\phi) = A\cos(\omega\phi + \varphi_0)$.* 130

4.76 *Trend of the mean value of unbiased longitudinal IP as a function of the azimuthal angle of the probe track, for simulated tracks reconstructed applying a coherent displacement of the two BPIX half-shells in the z direction (red points). Simulation with a "Startup" misalignment scenario is shown for comparison (black points). In the left figure a displacement of 10 μm has been applied, while in the right one a displacement of 50 μm has been applied.* 130

4.77 *Upper row: trends of the mean values (left) and the RMS (right) of the track d_{xy} vs ϕ. Lower row: trends of the mean values (left) and the RMS (right) of the track d_{xy} vs η. The red dots refer to values measured on July 2nd 2010, black dots refer to the startup misalignment scenario.* 131

4.78 *Upper row: trends of the mean values (left) and the RMS (right) of the track d_z vs ϕ. Lower row: trends of the mean values (left) and the RMS (right) of the track d_z as vs η. The red dots refer to values measured on July 2nd 2010, black dots refer to the startup misalignment scenario.* 132

4.79 *Left: Sketch of one half of the pixel barrel detector including the endflanges [52]. Right: Sketch of the movements observed of the BPIX halfshells.* . . 133

4.80 *Trends of the mean values of the unbiased track d_z as a function of ϕ, with superimposed step function fits to measure BPIX half-shells separation. The left plot refers to data collected on October 15th 2010, while that on the right to data from October 30th 2010. For comparison "Startup" misalignment scenario is plotted in black.* 133

4.81 *Trend of the measured separation of the BPIX half-shells as function of the day before (left) and after (right) alignment. Solid green symbols correspond to the trend of measured separations, while red symbols refer to days in which there was no sufficient data to perform the validation.* . 133

5.1 *Invariant mass spectrum of all the di-muons collected by the CMS experiment in 2010 in about 40 pb^{-1} of proton-proton collision data.* 136

5.2 *Opposite-sign dimuon invariant mass distributions in two J/ψ rapidity ranges, fitted with a Crystal Ball function plus an exponential. The poorer dimuon mass resolution at forward rapidity is caused by the smaller lever arm of the muon tracks [62].* 137

5.3 *Sketch explaining how the $\ell_{J/\psi}$ psuedo-proper decay length is calculated.* . 138

5.4 *Left: comparison of the nine geometries obtained by applying the modes described in Table 5.1 with respect to the starting aligned geometry. Right: comparison of the nine geometries obtained after the re-alignment procedure, with respect to the starting aligned geometry. Each symbol corresponds to a Tracker module.* 141

5.5 *Projection in the $m_{J/\psi}$ dimension of the two-dimensional likelihood fit in the bins $0 < p_T < 1.25$ GeV, $1.6 < |y| < 2.4$ (left) and $10.0 < p_T < 30$ GeV, $0 < |y| < 1.2$ (right).* 142

5.6 *Measured $m_{J/\psi}$ for each of the nine considered scenarios in two particular y-p_T bins. Red points refer to the situation after realignment, blue points to uncorrected mode. The error bar in the measurement of the mass comes from the fit uncertainties and are largely correlated between the different scenarios. In green is plotted the world average value of the J/ψ mass. The yellow shaded area represents the maximum Δm measured between the nominal geometry and the distorted ones (radial on the left, skew on the right), which is taken as systematic uncertainty due to alignment.* . . 142

5.7 *Projection in the $\ell_{J/\psi}$ dimension of the two-dimensional likelihood fit (in mass and $\ell_{J/\psi}$) in the bins $0 < p_T < 1.25$ GeV, $1.6 < |y| < 2.4$ (left) and $10.0 < p_T < 30$ GeV, $0 < |y| < 1.2$ (right), with their pull distributions (bottom).* 143

5.8 *Measured b-fraction for each of the nine considered scenarios in two particular y-p_T bins. Red points refer to the situation after realignment, blue points to uncorrected mode. The error bar in the measurement of the b-fraction comes from the fit uncertainties and are largely correlated between the different scenarios. The yellow shaded area represents the maximum Δf_b measured between the nominal geometry and the distorted ones (skew on the left, sagitta on the right), which is taken as systematic uncertainty due to alignment.* 144

5.9 *Fraction of the J/ψ production cross section originating from b-hadron decays, as a function of the $p_T^{J/\psi}$, as measured by CMS in three rapidity bins and by CDF, at a lower collision energy [62].* 146

A.1 *Track-to-hit residuals for two typical TIB (left) and TOB (right) modules, recorded during the 2008 cosmic ray data taking campaign.* 149

A.2 *Track-to-hit residuals for a typical TOB modules recorded during the 2008 cosmic ray data taking campaign, with superimposed a fit function based on the model in Equation A.1. The red dashed line is the pure gaussian component.* 150

A.3 *Distribution of the number of valid hits in the TIB (left) and TOB (right) subdetector. Black dots represtent the observed distribution in 2008 cosmic ray data, while in red is the randomly generated distribution of number of hits for the pseudo-experiment simulation discussed in the text.* 150

A.4 *Trend of the RMS of distributions of medians (blue points) and means (red points) for TIB (left) and TOB (right).* 151

B.1 *Left: pseudo-experiment MC distribution of a gaussian distributed random variable (residual) Right: pseudo-experiment MC distribution of the normalized residuals, using two different errors in the denominator.).* . . . 154

C.1 *Top: profiles of $\langle d_{xy} \rangle$ and $\sigma_{d_{xy}}$ as a function of the probe track ϕ. Bottom: profiles of $\langle d_{xy} \rangle$ and $\sigma_{d_{xy}}$ as a function of the probe track η. The applied movement is a shift in y of the BPIX half-shells. Red stands for the geometry obtained after the transformation, black for simulation in "Startup" conditions.* 156

C.2 *Top row: 2-D maps in the η-ϕ plane of (from left to right) $\langle d_{xy} \rangle$, $\sigma_{d_{xy}}$, $\langle d_z \rangle$ and σ_{d_z} for the BPIX half-shells shift in y. Units of measurement in the colors scales are in μm. In the bottom row the same maps are shown, in which blue stands for negative values, red for positive and the size of the marker for the magnitude of the measured value.* 156

C.3 *Top: profiles of $\langle d_z \rangle$ and σ_{d_z} as a function of the probe track ϕ. Bottom: profiles of $\langle d_z \rangle$ and σ_{d_z} as a function of the probe track η. The applied movement is a rotation of the entire BPIX around the y-axis. Red stands for the geometry obtained after the transformation, black for simulation in "Startup" conditions.* 157

C.4 *Top row: 2-D maps in the η-ϕ plane of (from left to right) $\langle d_{xy} \rangle$, $\sigma_{d_{xy}}$, $\langle d_z \rangle$ and σ_{d_z} for the rotation of the entire BPIX around the y-axis. Units of measurement in the colors scales are in μm. In the bottom row the same maps are shown, in which blue stands for negative values, red for positive and the size of the marker for the magnitude of the measured value.* . . . 157

C.5 *Top: profiles of $\langle d_{xy} \rangle$ and $\sigma_{d_{xy}}$ as a function of the probe track ϕ. Bottom: profile of $\langle d_{xy} \rangle$ and $\sigma_{d_{xy}}$ as a function of the probe track η. The applied movement is a radial expansion of the BPIX layers in the $0 < \phi < \pi/2$ quarter. Red stands for the geometry obtained after the transformation, black for simulation in "Startup" conditions.* 158

C.6 *Top row: 2-D maps in the η-ϕ plane of (from left to right) $\langle d_{xy} \rangle$, $\sigma_{d_{xy}}$, $\langle d_z \rangle$ and σ_{d_z} for a radial expansion of the BPIX layers in the $0 < \phi < \pi/2$ quarter. Units of measurement in the colors scales are in μm. In the bottom row the same maps are shown, in which blue stands for negative values, red for positive and the size of the marker for the magnitude of the measured value* 159

Introduction

The prime motivation for the Large Hadron Collider (LHC) is to investigate the hidden sectors of the Standard Model of fundamental interactions. In particular, the main goal of the physics program is the study of the electroweak symmetry breaking for which the Higgs mechanism is presumed to be responsible, by searching for the intermediate boson or supersymmetric partners explaining the mechanism.
Those sectors are accessible only at high energy scale and therefore the LHC proton beams are designed to reach an energy of 7 TeV per beam, providing collisions with a centre of mass energy of $\sqrt{s} = 14$ TeV at the design luminosity of $\mathcal{L} = 10^{34}$ cm^{-2} s^{-1}. Among the major physics signatures expected for these processes at TeV scale are the muons, and the Compact Muon Solenoid (CMS), one of the four LHC experiments, has been designed specifically for the identification and the measurement of the kinematics of high energy leptons.

The tracks of charged particles are among the most fundamental objects in the reconstruction of proton-proton collisions. Tracks are used in the reconstruction of electrons, muons, hadrons, taus, and jets as well as in the determination of the primary interaction vertices. In addition, tracks may be used to identify b-jets, in particular through evidence of a displaced vertex associated with a given jet. The high luminosity and the high energy of the colliding protons lead to challenging demands to the detector: for the particles momentum measurement, a precise inner tracking system, the Silicon Tracker has been developed, in order to provide robust, efficient, and precise reconstruction of the charged particle trajectories inside a 3.8 T axial magnetic field. For a system like the Tracker, with more than 15 000 independent modules, one of the main sources of systematic error on this measurement, and consequently on the related physics observables, is the unknown position of modules. Given the inaccessibility of the detector volume during collisions, the most accurate way to determine the silicon modules positions is to use the data from the detector itself when traversed *in situ* by charged particles.

This thesis is devoted to the alignment of the full CMS Tracker (described in Chapter 3) in 2008 and 2009 using cosmic rays particles, and then with collision data collected throughout 2010.

The alignment of the full Tracker using the cosmic rays data was first performed at the CMS Cosmic Runs at Four Tesla, CRAFT (described in Chapter 4): with the Tracker operated together with all other CMS subdetectors for the first time with the possibility to measure the momentum of the cosmic muon tracks using the magnetic field, it was possible to tune and to consolidate strategies for providing the desired alignment accuracy. My contribution is focused to the validation of the alignment

constants obtained with the CMS track-based alignment algorithms, which rely on a linearized least square combined fit of alignment parameters and track parameters. I devised and tested methods to assess the precision in the position of the modules with respect to the cosmic ray trajectories which were found of $3-4$ μm in the barrel and $3-14$ μm in the endcap detectors. Furthermore I have been responsible for the calibration of the *Alignment Position Errors* (APE) associated to the nearly hundred thousand alignment parameters. APE play a major role in track pattern recognition and affect heavily tracking efficiency and b-tagging of jets.

With the first collisions, I have developed a procedure based on unbiased primary vertices fitting, to assess alignment of the structures of the Pixel Tracker, which is now regular part of the monitoring of the alignment performances and of the standard validation procedure of Tracker alignment.

Finally I studied the impact of potential remaining systematic misalignment on the early charmonium physics obervables (Chapter 5). I studied the effects of possible non-trivial trasformations of the geometry, the so called weak modes, which leave the χ^2 of the track fits unchanged, on the measured values of the mass of the J/ψ meson and the systematic uncertainty due to misaligment in the first measurement, in the energy regime of LHC, of the fraction of J/ψ mesons produded in the decay of b-hadrons.

Part I

Background

Chapter 1

Physics at the Large Hadron Collider

Our current understanding of the subatomic world is summarized in the so called Standard Model of particle physics, a local gauge quantum field theory based on the $SU(3)_C \otimes SU(2)_L \otimes U(1)_Y$ symmetry group [1].

Extensive consistency and precision tests have been performed so far yielding extraordinary agreement of the Standard Model with experiment over a wide range of energies.

However the Standard Model has not been completely confirmed: in particular, it predicts an additional scalar field, the Higgs field, whose corresponding particle has not been observed yet. The Higgs field has been introduced, in the so called *Higgs mechanism*, [2] to break $SU(2)_L \otimes U(1)_Y$ electroweak symmetry giving masses to particles described by the Standard Model.

Direct searches for the Higgs boson, performed at LEP and Tevatron accelerators, have not given evidence yet, while setting a lower limit on its mass at about $M_H >$ 114 GeV[1] and an exclusion region around the Higgs mass region $M_H \sim$ 160 GeV.

Apart from electroweak symmetry breaking still to be confirmed, there are several reasons to believe the Standard Model only as an effective description, and to foresee a more fundamental theory. Several models proposing a wider symmetry than that of Standard Model have been proposed in order to solve the theoretical drawbacks affecting it.

The ultimate tests of the Standard Model and the possibility to search for new physics beyond it have led the scientific community to design the Large Hadron Collider (LHC), a high energy, high luminosity proton-proton collider, installed at the European Laboratory for Nuclear Research (CERN) in Geneva. The first proton-proton collisions at high energy have been recoreded in 2010. At that time LHC was the most powerful particle accelerator ever built.

[1] In the following natural units $\hbar = c =$ will be used.

In this chapter the basic concepts of Standard Model are illustrated, its different direct and indirect tests are reviewed, and finally the physics potential of the LHC is discussed.

1.1 The Standard Model

The Standard Model (SM) is a local gauge quantum field theory describing three of the four fundamental interactions: electromagnetic, weak and strong interaction.

The SM is a gauge theory based upon the $SU(3)_C \otimes SU(2)_L \otimes U(1)_Y$ symmetry group, the direct product of color symmetry group (C), weak isospin (T_L) and hypercharge (Y). This gauge group includes the symmetry group of strong interactions $SU(3)_C$ and the symmetry group of electroweak interactions, $SU(2)_L \otimes U(1)_Y$. The symmetry group associated to electromagnetic interactions, $U(1)_{EM}$ appears in the SM as a sub-group of $SU(2)_L \otimes U(1)_Y$ and it is in this sense that the weak and electromagnetic interactions are said to be unified. Associated to the gauge symmetry groups there are 12 vector (spin-1) gauge bosons: 8 bosons (g_i) for $SU(3)_C$, 3 (W_i) for $SU(2)_L$ and 1 (B) for $U(1)_Y$. The Z boson and the photon γ are seen as linear combinations of W_3 and B.

Since $SU(3)_C$ gauge invariance is not broken, the eight associated force-carriers, the gluons g_i remain massless. The strong interactions do not have an infinite range, in spite of the gluons being massless, because of confinement. The theory of quarks interacting by exchange of gluons is called Quantum Chromodynamics (QCD), to stress the parallel with Quantum Electrodynamics (QED), which also has an unbroken gauge invariance and an associated massless gauge boson: the photon.

The $SU(2)_L$ group describes the left-hand isospin, a "spin-like" algebra group associated to a weak charge carried by left-chirality fermions [2]. The subscript Y in $U(1)_Y$ refers to "weak hypercharge", related to electric charge (Q) and left isospin (t_L^3) by the relation:

$$Q = t_L^3 + \frac{Y}{2} \tag{1.1}$$

Unlike the $SU(3)_C$ one, the $SU(2)_L \otimes U(1)_Y$ gauge invariance is broken down to $U(1)_{EM}$ the unbroken gauge symmetry of QED. As a result three of the four gauge bosons of $SU(2)_L \otimes U(1)_Y$, $W^{\pm}$ and Z^0, acquire mass while the fourth, the photon, remains massless.

From the phenomenological point of view, this is not a little effect. The W and Z masses:

$$M_W = 80.423 \pm 0.039 \text{ GeV} \qquad M_Z = 91.1876 \pm 0.0021 \text{ GeV}$$

which in the SM are related at the tree level via the Weinberg or weak mixing angle

[2] In the ultra-relativistic limit ($\beta = \frac{v}{c} \sim 1$) chirality is equivalent to helicity $e = \frac{\Sigma \cdot p}{|p|}$

θ_W:

$$M_W^2 = M_Z^2 \cdot \cos^2 \theta_W \tag{1.2}$$

are responsible for the subnuclear range of the weak forces $r_{weak} \sim 1/M_W \sim 10^{-16}$ cm. In contrast the photon being massless carries the electromagnetic force which has infinite range.

Actually, the fact that the weak gauge bosons are massive indicates that $SU(2)_L \otimes U(1)_Y$ is *not* a good symmetry of the vacuum state defined as the state of lowest possible energy. In contrast, the photon being massless reflects the fact that $U(1)_{EM}$ is a good symmetry of the vacuum state. Therefore, the symmetry breaking pattern of the Standard Model must be:

$$SU(2)_L \otimes U(1)_Y \longrightarrow U(1)_{EM}$$

The dynamics of the symmetry breaking mechanism is unknown. There are good reasons to believe that a general framework is the spontaneous symmetry breaking. The term "spontaneous" here means that the symmetry is not broken explicitly by terms violating gauge symmetry in the Lagrangian (i.e. field interactions), but rather by an asymmetry of the vacuum state. In absence of an associated gauge symmetry, each spontaneously broken direction in the global (i.e. space-time independent) symmetry space gives rise to a massless, spin-zero un-physical Goldstone boson in the theory spectrum. If the direction in that abstract space corresponding to the broken symmetry corresponds also to a gauge symmetry (i.e. a space-time dependent symmetry) then the associated Goldstone boson and the massless gauge boson combine to form a massive gauge bosons. In this process, the extra degree of freedom provided by the scalar Goldstone field is absorbed in the longitudinal component of the gauge vector boson. This procedure is known as Higgs mechanism. The Higgs mechanism provides the proper masses to the W and Z gauge bosons and to the fermions and it leaves, as a consequence, the prediction of a new particle: the Higgs boson. This must be scalar and electrically neutral. This particle has not yet been observed in experiments.

The Higgs mechanism preserves the number of states. A massless gauge boson occurs in two transverse polarization [3] states. On the contrary, since a massive gauge boson can be brought to rest by a Lorentz transformation, and since there is no preferred direction in the rest frame, spatial isotropy requires three spin states. As specified by an *Equivalence Theorem* [2], at energies large compared to gauge bosons mass the longitudinal mode can be identified with the underlying Goldstone boson from symmetry-breaking sector. In this sense we can say that three particles from the otherwise unknown symmetry-breaking sector have already been discovered: the longitudinal gauge modes $W_L^{\pm}$ and Z_L.

In the Standard Model matter fields are represented by spin $s = \frac{1}{2}$ particles, fermions, divided into two categories, leptons and quarks. Both leptons and quarks have their charge conjugate partners (antiparticles) which have identical mass and spin, but additive quantum numbers opposite with respect to those of the vacuum.

[3] The terms transverse and longitudinal refer to the polarization of three-vectors: ε_T is transverse to the momentum **p** while ε_L is parallel to it

Table 1.1: *Fermion properties*

Fermions	1^{st} **gen**	2^{nd} **gen.**	3^{rd} **gen.**	**Charge**	**Interactions**
Quarks	$\begin{pmatrix} u \\ d \end{pmatrix}$	$\begin{pmatrix} c \\ s \end{pmatrix}$	$\begin{pmatrix} t \\ b \end{pmatrix}$	$+\frac{2}{3}$ $-\frac{1}{3}$	All
Leptons	$\begin{pmatrix} \nu_e \\ e \end{pmatrix}$	$\begin{pmatrix} \nu_\mu \\ \mu \end{pmatrix}$	$\begin{pmatrix} \nu_\tau \\ \tau \end{pmatrix}$	0 -1	Weak,E.M.

Three generations of fermions have been directly observed so far and up to now there is no experimental evidence of the existence of a further generation.

Fermionic matter-fields of the SM are classified in specific representations of the gauge group, and therefore have specific transformation properties with respect to the $SU(3)_C \otimes SU(2)_L \otimes U(1)_Y$ gauge group. Fermions fields are written as two components left- an right-handed Weyl spinors.

$$Q_L^i = \begin{pmatrix} u_L^i \\ d_L^i \end{pmatrix} = \left(3, 2, \tfrac{1}{6}\right), \quad u_R^i = (3, 1, \tfrac{2}{3}), \quad u_R^i = (3, 1, -\tfrac{1}{3})$$

$$L_L^i = \begin{pmatrix} \nu_L^i \\ l_L^i \end{pmatrix} = (1, 2, -\tfrac{1}{2}), \quad l_R^i = (1, 1, -1), \;\; i = 1, 2, 3$$

where the indicated numbers are the dimensions of the representation respectively for $SU(3)_C, SU(2)_L$ and the value of the hypercharge Y; the index i runs over the three generations, while the ν_R^i is not shown since it is a singlet with respect to gauge group transformation.

The quarks have an additional quantum number (a charge that comes from $SU(3)_C$ invariance of QCD lagrangian), which comes in three types. Colour is not directly observable and therefore quarks must be confined into experimentally observed colourless strongly interacting *hadrons*. These colourless composite particles are classified into baryons and mesons. The baryons are fermions made by three valence quarks, while mesons are bosons made of one quark and one antiquark.

The second type of elementary particles are the carriers of the interactions. Leaving aside gravitation, which plays a minor role at subatomic scales, all relevant interactions in elementary particle physics are known to be mediated by the exchange of a spin $s = 1$ vector boson. The photon, γ, is the exchanged particle in electromagnetic interactions, the eight gluons g_α, α=1,...,8, mediate the strong interactions among quarks, while the weak bosons $W^\pm$ and Z^0, are the corresponding intermediate bosons of the weak interactions. The main features of the two kinds of elementary constituents of matter are summarized in Tables 1.1 and 1.2.

1.2 Experimental tests of the Standard Model

The SM has been successfully tested in the last 40 years, starting from the *Gargamelle* experiment (discovery of weak neutral currents), coming to the *UA1* and *UA2* exper-

Table 1.2: *Gauge Bosons properties*

	Electromagnetic	**Weak**	**Strong**
Quantum	Photon(γ)	$W^{\pm}$ and Z	g_α gluons
Number of quanta	1	3	8
Mass (GeV)	0	$80 \div 90$	0
Coupling constant	$\alpha(\mu = m_e) \simeq \frac{1}{137}$	$G_F = 1.167 \times 10^{-5} GeV^{-2}$	$\alpha_S(M_Z) \simeq 0.1$
Range(cm)	∞	10^{-16}	10^{-13}

iments (Z and W bosons discovery), until the more recent *LEP*, *SLC* and *Tevatron* colliders (precision tests of the SM observables).

The *UA1* experiment at the S$p\overline{p}$S collider, designed for colliding protons with antiprotons at $\sqrt{s}$ = 540 GeV, led to the discovery of the W boson and to a first determination of its mass: M_W = (80.5 $\pm$ 0.5) GeV. After this important scientific achievement, the center of mass energy was increased up to 630 GeV and this allowed for the discovery of Z boson and the measurement of its mass: M_Z = (93.0 $\pm$ 2.9) GeV. A first experimental test of the parameters of the SM was therefore possible throug Equation 1.2:

$$M_W^2 = M_Z^2 \cdot \cos^2\theta_W \rightarrow \sin^2\theta_W = 0.220 \pm 0.009$$

After the Z and W bosons discovery, the real challenge became the measurements of their properties to an high precision level, as a test of the validity of the SM predictions. Particular emphasis was given to the following quantities:

- Z e W boson mass measurement to a precision level of 10^{-5} and 10^{-4}, respectively,
- the number of leptonic families,
- measurement of Z boson couplings with fermions (charged leptons and b and c quark), determining the Weinberg angle ($\sin^2\theta_W$) with an uncertainty better than per-mil,
- the non-abelian couplings among bosons in the SM (Triple and Quartic Gauge Coupling),
- quark top and Higgs boson discovery.

Two colliders were designed to measure these quantities: the Large Electron Positron collider (*LEP*) and the Stanford Linear Collider (*SLC*) [5]. *LEP* was an electron-positron collider at a centre of mass energy of 100/200 GeV during its first/second run phase. (*LEP-I*/*LEP-II*) [4, 3]. *LEP* and *SLD* collaborations achieved the first four goals of the above list with a precision which allowed to estimate, through radiative corrections to the observables, the most probable value for the Higgs boson mass, even if not directly observed, $M_H = 96^{+60}_{-38}$ GeV.

In the 1995, the $\sqrt{s}$ = 1.96 TeV proton-antiproton collisions at the Tevatron machine [6] led to the discovery of the top quark: the current measurement of its mass

(m_t =173± 1 GeV [10]) has added more precision to the global electroweak fit and allowed to set more stringent indirect bounds to the Higgs boson mass.

Observables like the top and $W^{\pm}$ masses and Z decay parameters are logarithmically sensitive to M_H through radiative corrections. These data can therefore be fitted taking the Higgs mass as a free parameter. The outcome of the procedure [7], combining results from various experiments, is summarised in the left plot of Figure 1.1. The plot shows the value of $\Delta\chi^2 = \chi^2 - \chi^2_{min}$, as a function of M_H, where the χ^2 is the one of the global fit of electroweak measurements. The solid curve is the result of the fit, while the shaded band represents the uncertainty due to not yet calculated higher order corrections. Fit privileges low values of the Higgs mass. An upper limit of 158 GeV was set at 95 % confidence level (CL): this limit increases to 186 GeV when including the *LEP-II* direct search.

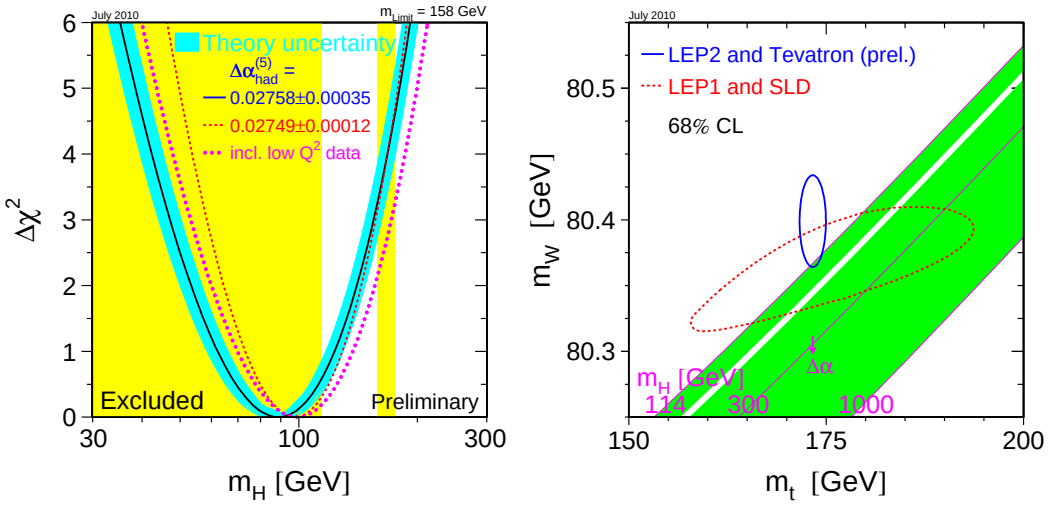

Figure 1.1: *Left plot.* $\Delta\chi^2$ *of the fit of electroweak measurements from LEP, SLD and Tevatron as a function of the Higgs mass. The vertical yellow bands shows the 95% CL exclusion limit on* M_H *from the direct searches at LEP-II and Tevatron. Right plot. The comparison of the indirect constraints on* M_W *and* m_t *based on LEP-I/SLD data (dashed contour) and the direct measurements from the LEP-II/Tevatron experiments (solid contour). In both cases the 68% C.L. contours are plotted. Also shown is the SM prediction for the masses as a function of the Higgs mass in the region favoured by theory (*$M_H <$ *1000 GeV) and allowed by direct searches (*$114 < M_H <$ *170 GeV and* $M_H <$ *180 GeV) [7].*

The electroweak results obtained up to now can be also used to determine the top quark and the W masses indirectly and the results can be compared to the direct measurements performed at *Tevatron* and *LEP-II*. This is illustrated in the right plot of Figure 1.1 which also shows the SM prediction for the Higgs mass between 114 and 1000 GeV. The indirect and direct measurements of M_W and m_t are in good agreement. To have the same statisctical weight on the Higgs mass prediction, the precision on the top mass (Δm_t) must be $\Delta m_t \simeq 7 \cdot 10^3 \Delta M_W$. Current values are $\Delta m_t = 1.3$ GeV and $\Delta M_W = 0.023$ GeV, so precision on the top mass must be improved by the LHC experiments.

LEP-II and *Tevatron* also investigated directly the production channel of the Higgs boson via W and Z associated production (or *Higgs-strahlung*) using $e^+e^- \rightarrow ZH \rightarrow X b\bar{b}$ (*LEP-II*) and $p\bar{p} \rightarrow WH \rightarrow l\nu b\bar{b}$ (*Tevatron*) decay channels.
Since it was not observed, a lower limit on the Higgs mass was set to $M_H > 114.3$ GeV by *LEP-II* and an exclusion range $158 < M_H < 175$ GeV (95% CL) was confirmed by the *Tevatron* collaborations during 2010. The exclusion bands are reported in yellow on the left plot of Figure 1.1.
Further limits are imposed from the theoretical calculations, predicting the validity of the Standard Model up to the Planck scale if the Higgs mass is in the range $130 < M_H < 180$ GeV.

1.3 The Large Hadron Collider

To explore the hidden sectors of the SM and in particular the Higgs mechanism, searching for the intermediate boson or its supersymmetric partner, the Large Hadron Collider accelerator was built [8]. The need to investigate any new physics process up to the TeV scale requires a challenging machine, able to accelerate particles at a high energy and to provide collisions with high luminosity. These requirements dictated the main features of the machine:

- a hadron collider: the fundamental constituents entering in the scattering are the partons which carry a fraction x of the four-momentum of the particles in the beam. Therefore the center-of-mass energy of the hard scattering process $\sqrt{\hat{s}}$ can span several orders of magnitude. The design center-of-mass energy of LHC for proton-proton collisions is $\sqrt{s} = 14$ TeV. In this way, partons momentum fractions x_1 , $x_2 \simeq$ 0.15-0.20 of the incoming protons momenta, give $\sqrt{\hat{s}} = \sqrt{x_1 x_2 s} \simeq$ 1-2 TeV, the energy range to be explored. With respect to an electron-positron machine, it is easier to accelerate protons to high energy since the energy lost for synchrotron radiation, proportional to γ^4 (where $\gamma = E/m$), is much lower than for the electrons.

- a proton-proton collider: with respect to a proton-antiproton machine, it is easier to accumulate high intensity beams of protons. Furthermore, the Higgs production process is dominated by gluon fusion, and therefore its cross section is nearly the same in proton-antiproton and proton-proton collisions.

- a high luminosity collider. The cross section σ determines the event rate R of a given process according to the formula $R = \mathcal{L}\sigma$. The factor $\mathcal{L}$ is called luminosity; it represents the number of collisions per unit time and cross-sectional area of the beams. It is specific to the collider parameters and does not depend on the interaction considered:

  $$\mathcal{L} = f\frac{n_1 n_2}{A}$$

  Here f is the collision frequency of bunches composed of n_1 and n_2 particles and A is the overlapping cross-sectional area of the beams. To compensate for the low cross section of the interesting processes the LHC must have a very high luminosity: the very short bunch crossing interval (25 ns, i.e. a frequency of 40

MHz) and the high number of bunches accelerated by the machine (2808 per beam) will allow to reach the peak luminosity of 10^{34} cm^{-2} s^{-1} = 10 nb^{-1}s^{-1} .

The idea behind the LHC is to reuse the existing 27 km long LEP tunnel to install the new collider. The design parameters of the machine are summarized in Table 1.3.

Parameters	**p-p**	**Pb-Pb**
Circumference (km)	26.659	
Centre of mass energy (TeV)	14	1148
Dipole magnetic field (T)	8.3	
Number of particles per bunch	2808	608
Bunch length (mm)	53	75
Bunch crossing rate (MHz)	40.08	0.0006
Design Luminosity (cm^{-2}s^{-1})	10^{34}	2×10^{27}
Beam radius at interaction point (μm)	15	

Table 1.3: *Design LHC parameters for p-p and Pb-Pb ($^{208}Pb^{82+}$) collisions.*

Figure 1.2 shows the cross sections and the production rate at LHC of interesting processes as a function of the center-of-mass energy and of the mass of the produced particle. In Table 1.4 the cross section and the number of events produced for a given process per experiment at a luminosity of $\mathcal{L} = 2 \cdot 10^{33}$ cm^{-2}s^{-1} are reported.

Process	σ	**Events/sec**	**Events/year**
$W \rightarrow e\nu$	20 nb	15	10^8
$Z \rightarrow ee$	2 nb	1.5	10^7
$t\bar{t}$	1 nb	0.8	10^7
$b\bar{b}$	0.8 mb	10^5	10^{12}
$\tilde{g}\tilde{g}$ (m= 1 TeV)	1 pb	0.0001	10^4
H (m = 0.8 TeV)	1 pb	0.001	10^4
H (m=0.2 TeV)	20 pb	0.01	10^5

Table 1.4: *Expected cross sections and number of events per second and per year for one experiment at LHC at $\mathcal{L} = 2 \cdot 10^{33} cm^{-2} s^{-1}$.*

One very remarkable aspect of LHC physics is the overwhelming background rate compared to the interesting physics processes: the Higgs production, for instance, has a cross section at least ten orders of magnitude smaller than the total inelastic cross section, as shown in Figure 1.2. In fact, the bulk of the events produced in pp collisions is either due to low p_T scattering, where the protons collide at large distance, or to QCD high p_T processes of the type $q_i\overline{q_i} \rightarrow q_k\overline{q_k}$, $gg \rightarrow gg$, or $q_ig \rightarrow q_ig$. All these events are collectively called *minimum bias* and they are in general considered not interesting since they constitute a background for other processes, where massive particles like the Higgs are created in the hard scattering. The cross section for the Higgs boson production increases steeply with the center of mass energy, while the total cross section remains almost constant. Therefore the highest center of mass energy should be used.

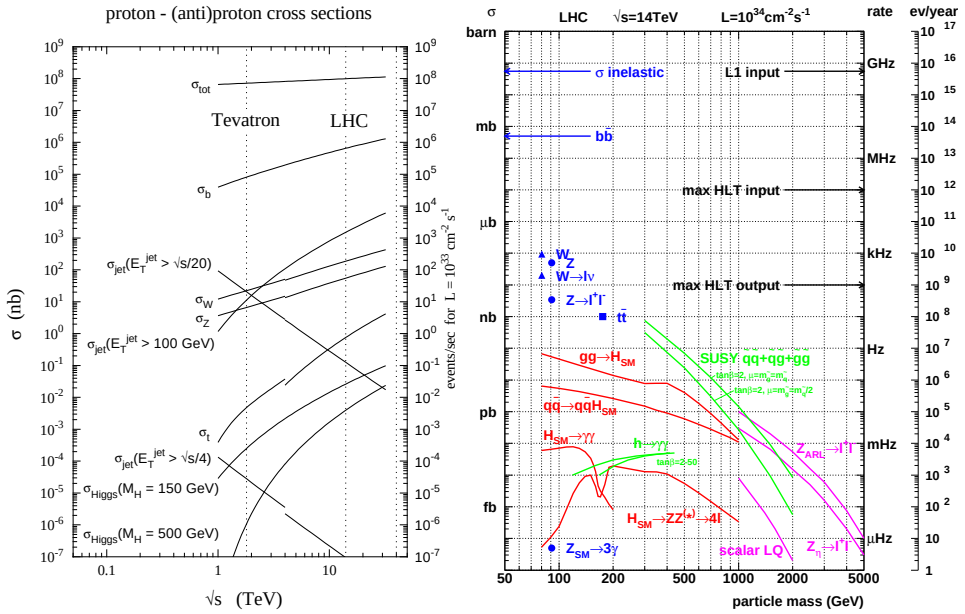

Figure 1.2: *Cross section as a function of the center-of-mass energy (left) and rate of events at LHC as a function of the mass of the produced particle (right) for interesting processes [9].*

Finally, the fact that the two partons interact with unknown energies implies that the total energy of an event is unknown. The proton remnants, that carry a sizable fraction of the proton energy, are scattered at small angles and are predominantly lost in the beam pipe, escaping undetected. Experimentally, it is therefore not possible to define the total and missing energy of the event, but only the total and missing transverse energies. Thus, all the interesting physics observable are measured in the plane transverse to the beamline.

1.3.1 LHC Operations in 2009-2010

The first beam was circulated through the LHC on the morning of 10 September 2008. CERN successfully fired the proton beam around the tunnel in stages, three kilometres at a time. The particles were fired in a clockwise direction into the accelerator and successfully steered around it at 10:28 local time. It took less than one hour to guide the stream of particles around its inaugural circuit. CERN next successfully sent a beam of protons in a counterclockwise direction, taking slightly longer than one and a half hours due to a problem with the cryogenics, with the full circuit being completed at 14:59.

On 19 September 2008, a quench occurred in about 100 bending magnets in sectors 3 and 4, causing a loss of approximately six tonnes of liquid helium, which was vented into the tunnel, and a temperature rise of about 100 K in some of the affected magnets. Vacuum conditions in the beam pipe were also lost. Most likely the cause of the problem was a faulty electrical connection between two magnets. Due to the time needed to warm up the affected sectors and then cool them back down to operating temperature meant that it would take at least several months to fix it. A total of

53 magnets were damaged in the incident and were repaired or replaced during the winter shutdown.

In the original timeline of the LHC commissioning, the first "modest" high-energy collisions at a center-of-mass energy $\sqrt{s} = 900$ GeV, twice the injection energy of the proton beams from *SPS*, were expected to take place before the end of September 2008, and the LHC was expected to be operating at $\sqrt{s} = 10$ TeV by the time of the official inauguration on 21 October 2008. However, due to the delay caused by the above-mentioned incident, the collider was not operational until November 2009.

Most of 2009 was spent on repairs and reviews from the damage caused by the quench incident. On November 20, the low-energy beams circulated in the tunnel for the first time since the incident. The early part of 2010 saw the continue ramp-up of beam in energies and early physics experiments. On 30 March 2010, LHC set a record for high-energy collisions, by colliding proton beams at a centre-of-mass energy of 7 TeV. The attempt was the third that day, after two unsuccessful attempts in which the protons had to be "dumped" from the collider and new beams had to be injected.

The LHC has been operated through the rest of 2010 at the same beam energy, increasing the instantaneous luminosity $\mathcal{L}$ either by increasing the current intensity of the beam or increasing the number of bunches per beam. The record peak luminosity of 5.62 pb^{-1}/day was recorded in late October. As can be seen in Figure 1.3 the first proton run ended officially on 4 November 2010 with a total integrated luminosity $\int \mathcal{L}dt = 47.03$ pb^{-1}. A run with lead ions started on 8 November 2010, and ended on 6 December 2010.

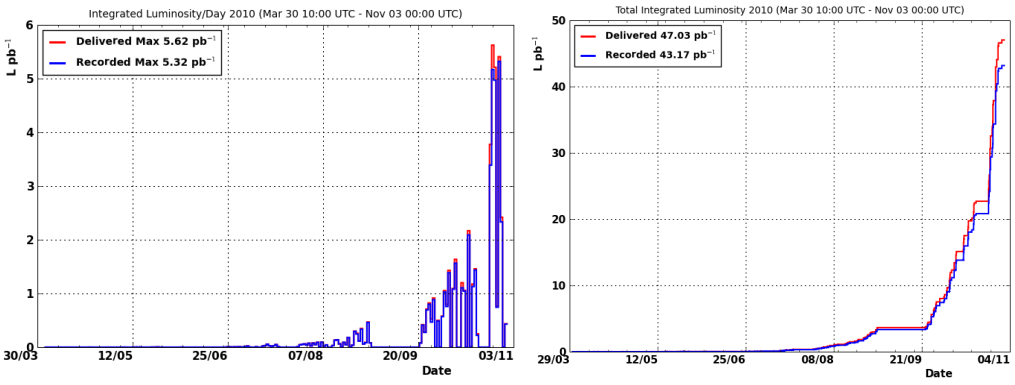

Figure 1.3: *Right: Integrated luminosity per day delivered to (red), and recorded by CMS (blue) during stable beams at $\sqrt{s} = 7$ TeV in 2010. .Left: Integrated luminosity versus time delivered to (red), and recorded by CMS (blue) during stable beams at $\sqrt{s} =$7 TeV centre-of-mass energy.*

1.4 Early LHC Physics

In the first, low luminosity phase of operations during collisions, the LHC experiments have started their physics program by measuring large cross section processes, with large number of recorded events despite the low luminosity. These processes include

"standard candle" observables such as the electroweak boson production cross sections, needed in a latter phase for more refined analysis of LHC data. Among the most significant results there are also the measurement of the top quark production cross section, the measurement of its mass, and measurements in the sector of B-hadron physics.

1.4.1 Z and W boson production

The cross sections of W and Z bosons production at LHC are huge with respect to previous experiment: at $\sqrt{s} = 14$ TeV the cross sections are $\sigma(pp \to W \to \ell\nu) \simeq$ 20 nb and $\sigma(pp \to Z \to \ell\ell) \simeq 2$ nb. Moreover the W and Z decay processes have been measured with high accuracy in previous experiments. Thus these processes play a key role during the first data taking at LHC allowing to test the detector performances (calibration of the scale of muon momentum, alignment of the muon system and of the inner tracker and understanding of the track reconstruction) and to tune the Monte Carlo programs used to describe the physics processes. The study of Z and W events will also improve the knowledge of the Parton Distribution Functions (PDF) at LHC energies and it will provide a raw luminosity monitoring. The actual knowledge of the PDF derives mainly from deep inelasting scattering experiments, like *H1* and *ZEUS*. The extrapolation of those functions to the LHC energy scale is one of the main systematic uncertainties in the measurement of the cross section of a physics process [11, 12, 13]. Using the angular distribution of the leptons produced in the reactions $pp \to WX$ and $pp \to ZX$ decays it is possible anyway to reduce this uncertainty. The kinematic region accessible at LHC is shown in Figure 1.4.

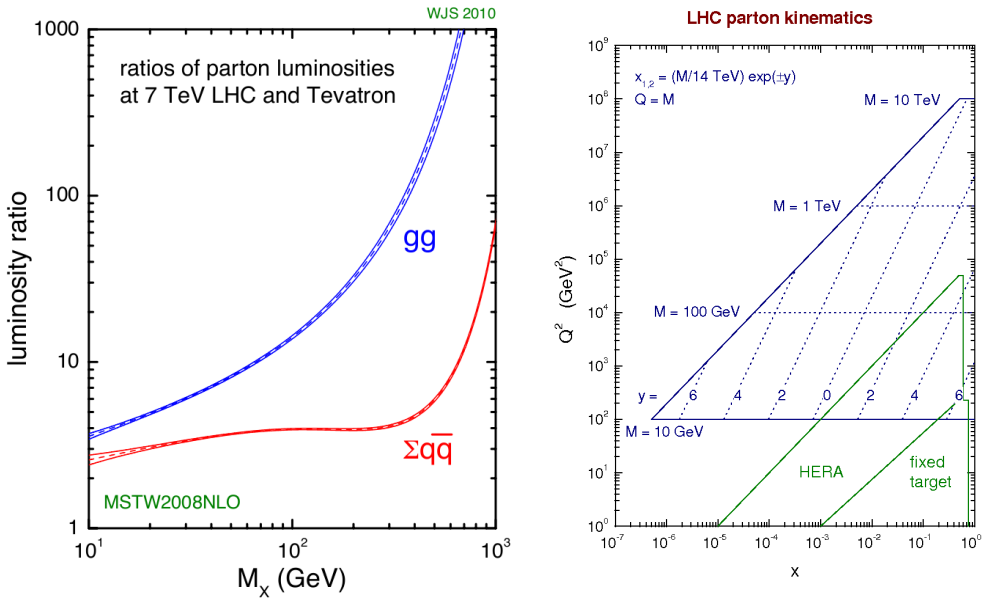

Figure 1.4: *Left: Parton luminosity ratios between LHC and Tevatron as a function of* $\sqrt{\hat{s}}$ *(partonic centre of mass energy) at* $\sqrt{s} = 7$ *TeV. Right: Kinematic region in the* (x, Q^2) *plane, accessible at LHC, at* $\sqrt{s} = 14$ *TeV.*

1.4.2 Top quark mass measurement

The most promising channel for the measurement of the top mass is $t\bar{t} \rightarrow W^+W^-b\bar{b}$ with one leptonic and one hadronic W decay, where the hadronic part is used to reconstruct the top mass and the leptonic part to select the event. The main source of uncertainty will be the jet energy scale, which is affected by the accuracy of the fragmentation model, the knowledge of the gluon radiation and the response of the detectors. The target uncertainty on m_t is smaller than 2 GeV. This will constrain the Higgs mass to better than 30% but, in order not to become the dominant source of uncertainty, the W mass will have to be measured with a precision of about 15 MeV.

1.4.3 B-physics and CP violation

Concerning the field of b-physics, LHC can benefit from a very large $b\bar{b}$ production cross section. The main interest is the study of the decays of neutral B mesons, and in particular of the CP violation in the B_d^0 - $\overline{B}_d^0$ and B_s^0 - $\overline{B}_s^0$ system. B decays can be identified in semileptonic final states, especially in the case of muons. However these leptons are usually soft and the identification is difficult due to the high backgrounds and pile-up. One LHC experiment, LHCb, is dedicated to b-physics which is currently studied also by ATLAS and CMS in the low-luminosity phase.

1.5 High energy and high luminosity Physics

When the LHC will start to deliver proton-proton collisions at high luminosity, searches of processes with small cross sections will become possible. Among these, there are the production of SM Higgs and the production of supersymmetric partners of the SM particles.

1.5.1 The Higgs boson search at LHC

The main processes which contribute to the Higgs production in a proton-proton collision at the energy scale reached by LHC are shown in Figure 1.5. The fundamental interaction takes place between the partons, i.e. quark and gluons: the gluon fusion is the dominant process on the whole M_H spectrum and only at very high masses the vector boson fusion becomes comparable (see Figure 1.6). Cross sections are typically of the order of few picobarns, which at the LHC design luminosity correspond to rates of about 10^{-2} Hz.
In the gg fusion, since the Higgs coupling with the fermion is proportional to the squared fermion mass, the main contribution comes from the diagram in which the quark exchanged in the loop is the heaviest, i.e. the top quark.

Even if other processes have small cross section, they can have a clear experimental signature, and therefore be easily detectable. The WW scattering has on average a cross section about 5 to 10 times smaller than that of gg fusion, but this channel is extremely promising thanks to its clean experimental signature as the presence of two

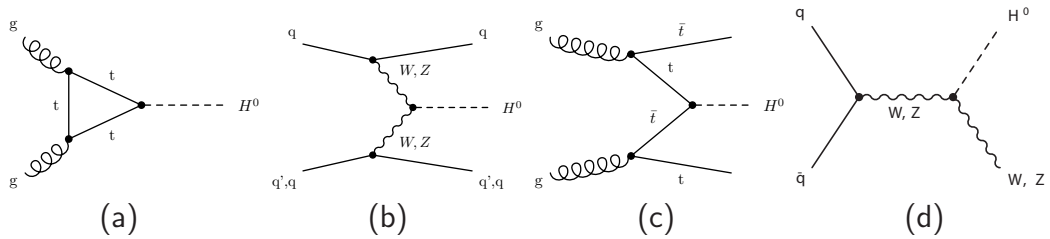

Figure 1.5: *Higgs production mechanisms at tree level in proton-proton collisions: (a) Gluon-gluon fusion; (b) W and Z fusion; (c) $t\bar{t}$ associated production; (d) W and Z associated production.*

spectator jets provides a powerful tool for tagging the signal events. The associated production channels $q_i\overline{q}_j \rightarrow WH$ or $q_i\overline{q}_i \rightarrow ZH$, where an off-shell boson is produced and radiates a Higgs, have very small cross sections, except for very low M_H. Also $gg, q_iq_j \rightarrow t\bar{t}H$ has a cross section almost 100 times smaller than that of gluon-gluon fusion. However, also in this case a powerful signature is given by the additional bosons or jets in the final state.
Once produced, the Higgs can decay in different ways, according to its mass. The branching ratios for different decay channels as a function of the Higgs mass are shown in Figure 1.6.

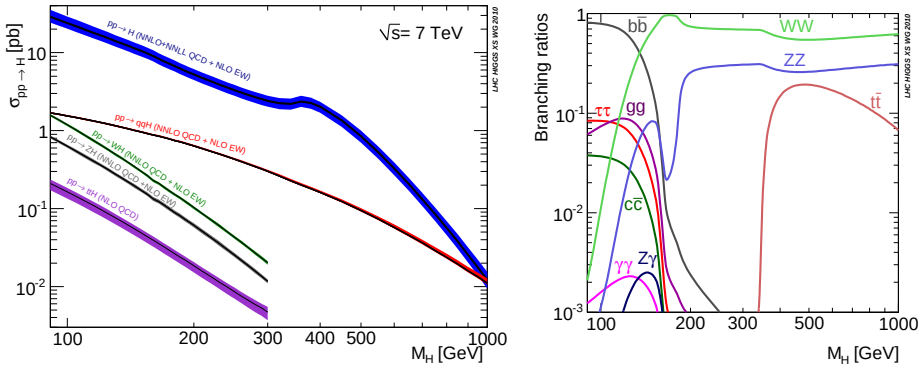

Figure 1.6: *Left: Higgs boson production cross sections at $\sqrt{s} = 7$ TeV as a function of the Higgs boson mass. Right: Branching ratios for different Higgs boson decay channels as a function of the Higgs boson mass. [14]*

They can be interpreted on the basis of the Higgs couplings, being proportional to the fermion masses and to the square of the boson masses.

Low mass Higgs ($M_H < 130$ GeV)

The heaviest available fermion is the b quark and $H \rightarrow b\bar{b}$ dominates. However, this decay channel is difficult to observe at the LHC because of the huge QCD background. In this mass region the most promising channel is $H \rightarrow \gamma\gamma$ which despite the very low branching ratio ($\simeq 10^{-3}$) has a very clean signature. The signal should appear as a narrow peak over the continuum background $q\overline{q}, gg \rightarrow \gamma\gamma$, but excellent photon energy and angular resolution are required as well as good π^0 rejection.

Intermediate mass Higgs ($130 < M_H < 500$ GeV)

The production of WW and ZZ pairs becomes allowed; the branching ratio is high, but purely hadronic final states are again not accessible. The Higgs decay in four leptons is the golden channel: even with a low branching ratio, it has a clean final state and does not suffer from irreducible background. The channel $H \rightarrow WW$ has the disadvantage that experimentally accessible final states ($\ell\nu\ell\nu$,$\ell\nu jj$) have at least one neutrino that escapes detection; however it could be a good discovery channel, especially for $M_H \simeq 2M_W$ where the WW production is at threshold and the ZZ branching ratio drops to 20%.

High mass Higgs ($M_H > 500$ GeV)

The cross section becomes low and semi-leptonic $\ell\nu jj$ and $\ell\ell jj$ final states have to be used. The Higgs width becomes also very broad so that the reconstruction of a mass peak becomes difficult.

1.5.2 Supersymmetry

Supersymmetry (SUSY) is a theory that introduces a new symmetry between bosons and fermions [15]. SUSY predicts that each particle has a supersymmetric partner whose spin differs by one half.
The simplest supersymmetric model, called the Minimal Supersymmetric Standard Model (MSSM), predicts the existence of two Higgs doublets, corresponding to five Higgs particles: two charged bosons, $H^{\pm}$, two scalar bosons, h and H and one pseudo-scalar, A. At tree level, all masses and couplings depend on two parameters, chosen to be the mass of the A boson, M_A , and the ratio of the vacuum expectation values of the two Higgs doublets, $tan\beta$.

In most of the parameter space, charged Higgs bosons decay predominantly to $\tau\nu$. For the neutral Higgs bosons, the decays to vector bosons are suppressed, so that the golden channels described for the case of a SM Higgs will not be observable. The dominant decays modes are those to $b\bar{b}$ and $\tau^+\tau^-$ but the former is hidden by the large background of b-jets. The observation of MSSM Higgs bosons will therefore rely on the identification the leptons coming from τ decays and of τ-jets.

1.5.3 Search for new massive vector bosons

The detector requirements for high momenta can be determined by considering decays of high-mass objects such as $Z' \rightarrow e^+e^-$ and $Z' \rightarrow \mu^+\mu^-$. The discovery of an object like a Z' boson will be very likely limited by the statistical significance of the signal. Ways of distinguishing between different models involve the measurement of the natural width and the forward-backward asymmetry, both of which require sufficiently good momentum resolution at high p_T to determine correctly the sign of the leptons and a pseudorapidity coverage up to $\eta = 2.4$.

1.6 Heavy Quarkonia Production at LHC

A *quarkonium* is a quark-antiquark bound state. Quarks with a mass higher than Λ_{QCD}, the scale at which perturbative expansion of QCD breaks down about 300 MeV, nominally the charm ($m_c \simeq$ 1.4 GeV), bottom ($n_b \simeq$ 4.5 GeV) and top ($m_t \simeq$ 175 GeV) quarks, are called "heavy". Heavy quarkonia are the bound states $Q\overline{Q}$, where Q is either a c or b quark since the high mass, $t\bar{t}$ pairs do not form bound states.

The lower-mass states of heavy quarkonium resonances are rather stable particles: due to their mass below the threshold for open heavy flavored meson pair production, their decay modes are either electromagnetic or OZI-suppressed (about 30% and 70% for charmonium). The ground state for $c\bar{c}$ vector mesons is the J/ψ ($m_{J/\psi} \simeq$ 3.1 GeV , $\Gamma =$ 91 keV), while the ground state for $b\bar{b}$ vector mesons is the Υ ($m_\Upsilon =$ 9.5 GeV , $\Gamma =$ 53 keV). The excited states below the open charm/beauty threshold have widths ranging from a few dozens keV to a few dozens MeV. The spectrum of the heavy charmonium states is shown in Figure 1.7.

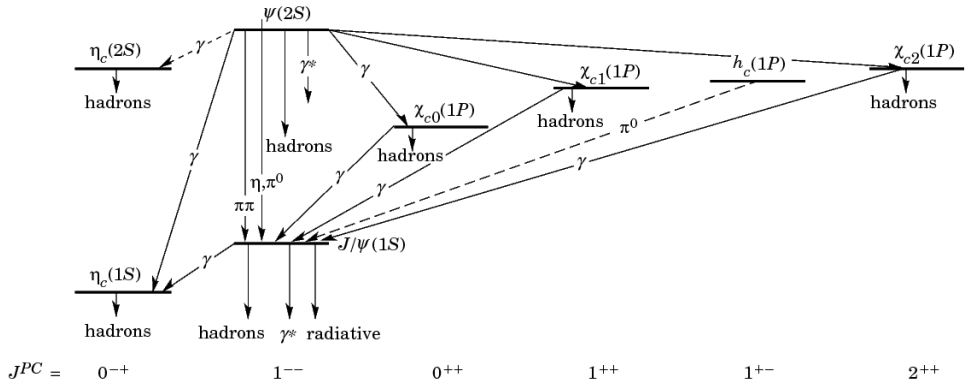

Figure 1.7: *Spectrum and transitions of the charmonium family.*

The spectroscopy of quarkonia is phenomenologically described by assuming that the $Q\overline{Q}$ pair is subjected to the Cornell potential, consisting of a Coulomb-like term accounting for gluon-exchange between the two quarks and a confining term parametrising the non-perturbative effects:

$$V(r) = -\frac{4}{3}\frac{\alpha_s(r)}{r} + k^2 r \tag{1.3}$$

The results obtained by solving the Schrödinger equation with the potential in Equation 1.3 with ad-hoc values of the parameters are in fair agreement with the observed spectra.

The mechanism of quarkonium production at hadron colliders is still an open research field. For what concerns the identification of the partons involved in the production of the $Q\overline{Q}$ pairs, earlier experiments ruled out the hypotesis of electromagnetic production via quark-quark annihilation.
Similarly, the hypotesis of $q\overline{q}$ annihilation into a gluon as the main production process was rejected after the comparison between the production rate in p-p and in $p\overline{p}$ collisions, since the difference between the $\overline{q}$ content of proton and antiproton should

lead to a suppression in pp collisions by a factor $5 \div 10$, which is not observed. Thus quarkonium production proceeds mainly via gluon fusion ($gg \to \overline{Q}Q$) or gluon fragmentation (see Figure 1.8).

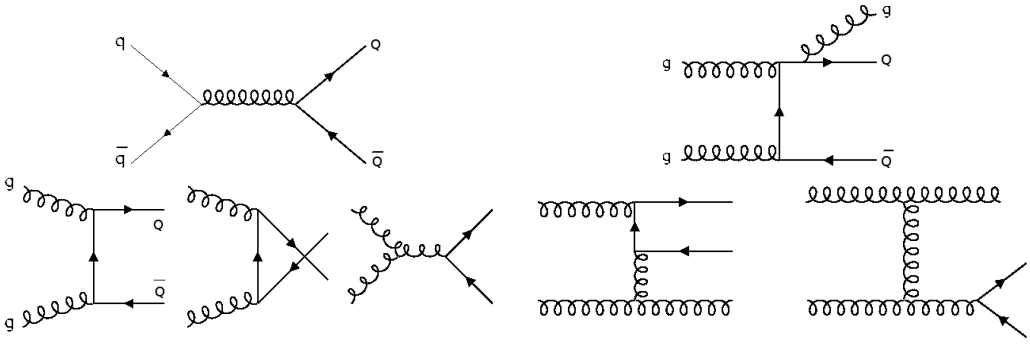

Figure 1.8: *Left: leading order diagrams in QCD to produce heavy quark pairs. Right: Next-to-leading order diagrams relevant to heavy quarkonium production.*

In both heavy-quarkonium annihilation decays and hard-scattering production, large energy-momentum scales appear. The heavy-quark mass m_Q is much larger than Λ_{QCD} and, in the case of production, the transverse momentum p_T can be much larger than Λ_{QCD} as well. This implies that the values of the QCD running coupling constant are much smaller than unity ($\alpha_S(m_c) \approx 0.25$ and $\alpha_S(m_b) \approx 0.18$). Therefore, one might hope that it would be possible to calculate the rates for heavy quarkonium decay and production accurately in perturbation theory. However, there are low-momentum, non-perturbative effects associated with the dynamics of the quarkonium bound state that invalidate the direct application of perturbation theory. In order to make use of perturbative methods, one must first separate the short-distance/high-momentum perturbative effects from the long-distance/low-momentum non perturbative effects; such a process is known with the name of *factorization* and nowadays is the basic approach to the problem of quarkonium production.

Some models were developed over the years to describe theoretically or phenomenologically the quarkonia production mechanism and such models have been tested in the nineties on data collected at Tevatron.

1.6.1 Color Evaporation Model (CEM)

The Color Evaporation Model is the most phenomenological one and was first proposed in 1977 [16, 17, 18, 19]. In the CEM, the production cross section for a quarkonium state H is a certain fraction F_H of the cross section for producing $Q\overline{Q}$ pairs with invariant mass below the $M\overline{M}$ threshold, where M is the lowest mass meson containing the heavy quark Q. This cross section has therefore an upper limit on the $Q\overline{Q}$ pair mass but no constraints on the color or spin of the final state. The $Q\overline{Q}$ pair is assumed to neutralize its color by interaction with the collision-induced color field by color evaporation. If the $Q\overline{Q}$ invariant mass is less than the heavy-meson threshold $2m_M$, then the additional energy that is needed to produce heavy-flavoured hadrons can be obtained from the nonperturbative color field. Thus, the sum of the fractions F_H over all quarkonium states H can be less than unity.

The fractions F_H are assumed to be universal so that, once they are determined by data, they can be used to predict the cross sections for other processes and for other kinematic regions. In the CEM, the production cross section for the quarkonium state H in collisions of the light hadrons h_A and h_B is, at leading order in α_S:

$$\sigma_{CEM}^{LO}[h_A h_B \to H + X] =$$
$$= F_H \sum_{i,j} \int_{4m_q^2}^{4m_M^2} d\hat{s} \int dx_1 dx_d f_i^{h_A}(x_1,\mu) f_j^{h_B}(x_2,\mu) \hat{\sigma}_{ij}(\hat{s}) \delta(\hat{s} - x_1 x_2 s) \qquad (1.4)$$

where:

- h_A and h_B are the colliding hadrons;
- ij corresponds to $q\overline{q}$ and gg pairs;
- σ_{ij} is the $ij \to Q\overline{Q}$ sub-process cross section;
- $f_i^{h_A}(x_1,\mu)$ and $f_j^{h_B}(x_2,\mu)$ are the parton densities in the colliding hadrons.

The leading-order calculation cannot describe the quarkonium p_T distribution, since the p_T of the $Q\overline{Q}$ pair is zero at LO. At NLO in α_S the subprocesses $ij \to kQ\overline{Q}$ (where k is a light quark, antiquark or gluon) produce $Q\overline{Q}$ pairs with nonzero p_T. The most recent set of F_H values have been determined from complete NLO calculations of quarkonium production in hadronic collisions.

The most basic prediction of the CEM is that the ratio of the cross sections for any two quarkonium states should be constant, independent of the process and the kinematic region. Some variations in these ratios have been observed: for example the ratio of the cross sections for χ_c and J/ψ are rather different in photoproduction and hadroproduction. Such variations present a serious challenge to the status of the CEM as a quantitative model for quarkonium production, but nevertheless the model is still widely used as simulation benchmark.

1.6.2 Color Singlet Model (CSM)

The color-singlet model (CSM) was first proposed shortly after the discovery of the J/ψ. The main concept of the CSM is that, in order to produce a quarkonium, the $Q\overline{Q}$ pair must be generated with the quarkonium quantum numbers; in particular the pair has to be produced in a color-singlet state. The model can be obtained by the NRQCD formula (see in Section 1.6.3) by dropping all the colour-octet terms and all but the colour-singlet term corresponding to the quantum numbers of the final resonance.

1.6.3 Non Relativistic QCD (NRQCD)

One convenient way to carry out the separation between perturbative and non-perturbative effects is through the use of the effective field theory Non Relativistic

QCD (NRQCD) [20, 21]. NRQCD is more than a phenomenological model since it reproduces full QCD accurately at momentum scales of order $m_Q v$ and smaller, where v is the typical heavy-quark velocity in the bound state in the CM frame ($v^2 \approx 0.3$ for charmonium, and $v^2 \approx 0.1$ for bottomonium). Virtual processes involving momentum scales of order m_Q and larger can affect the lower-momentum processes, and their effects are taken into account through the short-distance coefficients of the operators that appear in the NRQCD action. Because production occurs at momentum scales of order m_Q or larger, it manifests itself in NRQCD through contact interactions. As a result, the inclusive cross section for the direct production of the quarkonium H at large transverse momentum (p_T of order m_Q or larger) in hadron colliders can be written as a sum of products of NRQCD matrix elements and short-distance coefficients:

$$\sigma[H] = \sum_n \sigma_n(\Lambda) \langle 0|\mathcal{O}_n^H|0\rangle \tag{1.5}$$

where:

- H is the quarkonium state to be produced;
- n runs over all the quantum numbers of the $Q\overline{Q}$ pair (color, angular momentum,spin,...);
- Λ is the ultraviolet cutoff of the effective theory;
- $\sigma_n(\Lambda)$ are the short-distance coefficients;
- $\mathcal{O}_n^H$ are the four-fermion operators.

The short-distance coefficients $\sigma_n(\Lambda)$ are essentially the process-dependent partonic cross sections to make a $Q\overline{Q}$ pair, convolved with parton distributions if there are hadrons in the initial state. The $Q\overline{Q}$ pair can be produced in a color-singlet state or in a color-octet state. Its spin state can be singlet or triplet and it also can have orbital angular momentum.

The four-fermion operators create a $Q\overline{Q}$ pair in the NRQCD vacuum, project it onto a state that in the asymptotic future consists of a heavy quarkonium plus anything, and then annihilate the $Q\overline{Q}$ pair. The vacuum matrix element of such an operator is the probability for a $Q\overline{Q}$ pair to form a quarkonium plus anything. These matrix elements are somewhat analogous to parton fragmentation functions. They contain all of the nonperturbative physics associated with the evolution of the $Q\overline{Q}$ pair into a quarkonium state.
An important property of the matrix elements, which greatly increases the predictive power of NRQCD, is the fact that they are universal, i.e. process independent; they can be calculated in lattice simulations or determined from phenomenology. NRQCD power-counting rules (for more details see [22]) allow to organize the sum over operators in Equation 1.5 as an expansion in powers of v. Through a given order in v, only a finite set of matrix elements contributes. The relative importance of the terms in the factorization formula is determined not only by the size of the matrix elements but also by the sizes of the perturbative coefficients. The size of the coefficient depends

on its order in α_S, color factors and dimensionless kinematic factors such as m^2/p_T^2 .

In practical calculations of the rates of quarkonium decay and production, a number of significant uncertainties arises. In many instances, the series in α_S and v in the factorization formula in Equation 1.5 converges slowly, and the uncertainties from their truncation are large (sometimes 100% or larger). In addition, the matrix elements are often poorly determined, either from phenomenology or lattice measurements, and the important linear combinations of matrix elements vary from process to process, making tests of universality difficult. There are also large uncertainties in the heavy-quark masses (approximately 8% for m_c and approximately 2.4% for m_b) that can be very significant for quarkonium rates that are proportional to a large power of the mass. Many of the largest uncertainties in the theoretical predictions, as well as some of the experimental uncertainties, cancel in the ratios of cross sections.

Another set of observables in which many of the uncertainties cancel out consists of polarization variables, which can be defined as ratios of cross sections for the production of different spin states of the same quarkonium.

The NRQCD is in good agreement with data from CDF Run I for what concerns J/ψ and $\psi(2S)$ production cross sections but seems to fail in the case of $\Upsilon(1S)$ at low-p_T because the NRQCD curve diverges like $1/p_T$ for small values of p_T. This unphysical behaviour of the NRQCD curves is an artifact of fixed-order perturbation theory and could be removed by carrying out the appropriate resummation of soft gluons (for more details see [23]).

In conclusion NRQCD has been chosen to be in fine agreement with experimental results on quarkonium production cross sections. The measurement of polarization, represents a further important test for the model.

Chapter 2

The Compact Muon Solenoid Experiment

Among the main goals of the LHC machine there is the study of the electroweak symmetry breaking mechanism: the two major multi-purpose experiments, have been designed specifically in order to detect and discover every new physics process accessible at the LHC energies. These are the *A Toroidal LHC ApparatuS* (ATLAS) and the *Compact Muon Solenoid* (CMS) experiments. Their design differs significantly, since different solutions were chosen for the configuration of the magnetic field. ATLAS uses a toroidal field produced by three sets of air-core toroids complemented by a small solenoid in the inner region, while CMS uses a solenoidal field generated by the world's largest superconducting solenoid. Both ATLAS and CMS are conceived as general purpose experiments which at the LHC energy allow for detecting and measuring the mass of new particles produced by collisions, of mass up to the limit of 3 $\div$ 4 TeV.

The most important detector requirements for CMS to meet the goals of LHC physics program are [24]:

- good muon identification and momentum resolution over a wide range of momenta in the region $|\eta| < 2.5$ and capability to determine unambiguously the charge of muons with $p <$1 TeV;
- good di-muon mass resolution, about 1% at 100 GeV;
- good charged particle momentum resolution and reconstruction efficiency in the tracking system together with efficient triggering and offline tagging of $\tau's$ and b-jets;
- good electromagnetic energy resolution, good di-photon and di-electron mass resolution, measurement of the direction of photons and correct localization of the primary interaction vertex, π_0 rejection and efficient photon and lepton isolation at high luminosities;
- good missing energy and dijet mass resolution, using hadron calorimeters with a large hermetic geometric coverage ($|\eta| < 5$) and with fine lateral segmentation.

In order to fulfill this requirements CMS, was built according to the layout shown in Figure 2.1 [27]. The final design of the detector allows a reliable identification and precise measurement of the muon momentum by means of a redundant muon identification system, a precise measurement of photons and electrons energy with a high resolution calorimeter system and an excellent reconstruction of the charged particle tracks and measurement of their momentum resolution thanks to a high quality inner tracking system. The detector structure consists of a cylindrical barrel closed by two endcap disks.

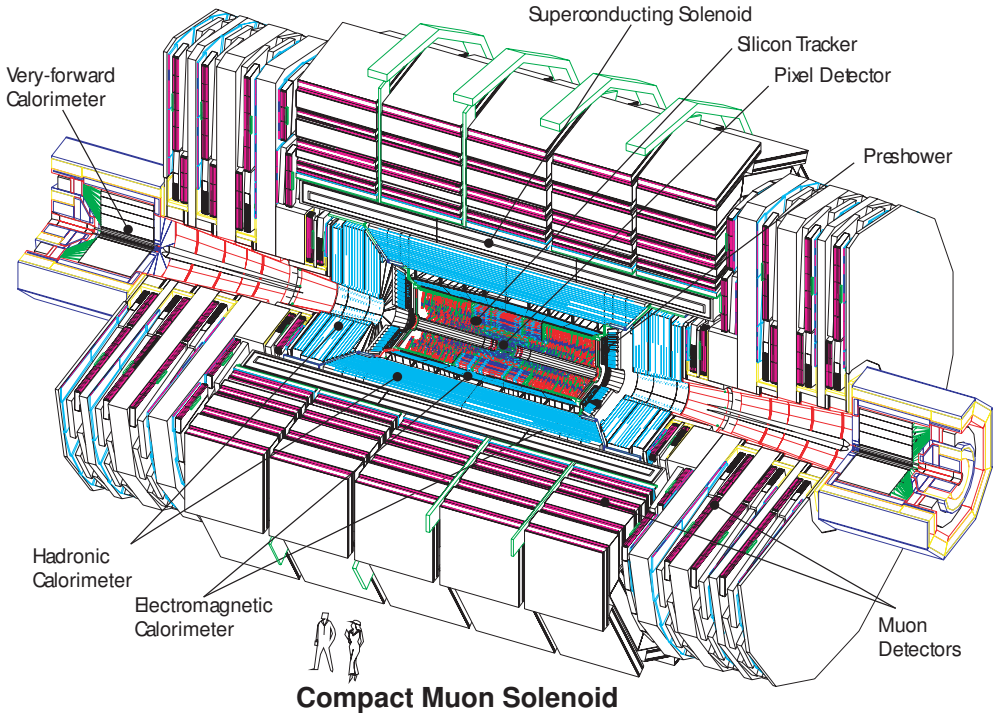

Figure 2.1: *Exploded view of CMS layout [24].*

The overall length is 21.6 m, the diameter 14.6 m and the total weight about 12 500 tons. The thickness of the detector in radiation lengths is greater than 25 X_0 for the electromagnetic calorimeter, and the thickness in interaction lengths varies from 7 to 11 λ_I for the hadronic calorimeter, depending on the η region.

For a particle carrying quadri-momentum (E, p_x, p_y, p_z), the momentum vector $\mathbf{p}$ can be divided in two components: the *longitudinal momentum* p_z and the *transverse momentum* defined as $p_T = \sqrt{p_x^2 + p_y^2}$. The *rapidity* is defined as:

$$y = \frac{1}{2}\ln\left(\frac{E + p_z}{E - p_z}\right) \tag{2.1}$$

The rapidity is used for describing angular distribution of the events, being invariant under boost of the centre-of-mass along the z direction.
For an ultra-relativistic particle ($p \gg m$) y can be approximated to the *pseudorapidity*:

$$\eta = -\ln\left(\tan\frac{\theta}{2}\right) \tag{2.2}$$

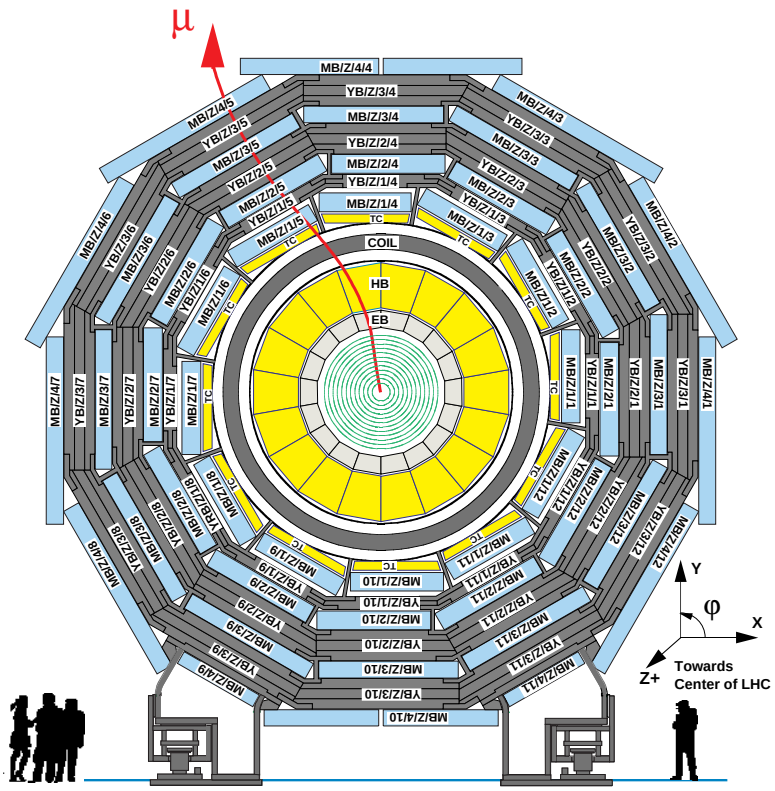

Figure 2.2: *Transverse view of the barrel region of the CMS detector [24].*

were θ is the angle between the particle momentum $\mathbf{p}$ and the z axis. The choice of a solenoidal magnetic field led to a very compact design for the CMS system, allowing calorimeters to be installed inside the magnet, with a strong improvement in the detection and energy measurement of electrons and photons. For a precise measurement of the momentum, it exploits both the constant field within the magnet and the field inside the return yoke. Moreover, tracks exiting the yoke point back to the interaction point, a property that can be used for track reconstruction. However the multiple scattering effect within the yoke degrades the resolution of the muon system. The longitudinal view of one quarter of CMS and the transverse view of the barrel region are shown in Figure 2.2.

The core of the apparatus is the magnet (CB), a 13 m long super-conductive solenoid cooled with liquid helium, which can provide a 4 T magnetic field. The magnet coil has a diameter of 5.9 m and contains the Tracker, the electromagnetic and hadronic calorimeters. The iron return yoke of the magnet (YB, YE) hosts the muon spectrometer, composed by 4 stations of drift tube detectors (DT) in the barrel region (MB) and 4 stations of cathode strip chambers (CSC) in the endcaps (ME). Both the barrel and the endcaps are equipped with resistive plate chambers (RPC) which ensure redundancy and robustness at the muon trigger system. The overall pseudorapidity coverage of the muon system goes up to $|\eta| = 2.4$.

The hadronic calorimeter (HCAL) is a brass/scintillator sampling calorimeter. The barrel and endcap parts (HB and HE) have the same pseudorapidity coverage as the electromagnetic calorimeter, and are complemented by a very forward calorimeter

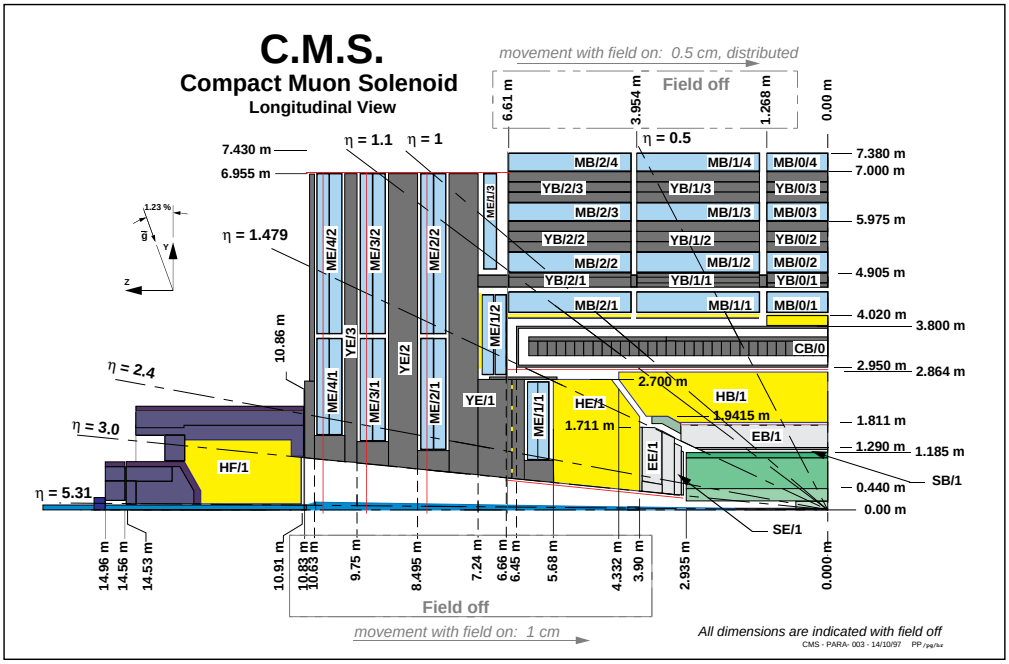

Figure 2.3: *Longitudinal view of one quarter of the CMS detector [24].*

(HF), which extends the coverage up to $|\eta| < 5.3$. Inside HCAL, the electromagnetic calorimeter (ECAL) is installed: it is an homogeneous calorimeter made of lead tungstate scintillating crystals. The pseudorapidity coverage extends up to $|\eta| < 3.0$. In the endcaps a lead/silicon pre-shower detector is installed to improve the resolution on electron and photon direction and help pion rejection.

The tracking detector is placed in the core of CMS: its design was driven by the requirement of a precise vertex reconstruction and a reliable b-tagging with very high track multiplicity. To achieve this goal very fine segmentation is crucial. The choice of CMS was to employ 10 layers of silicon microstrip detectors, which provide the required granularity and precision. In addition, 3 layers of silicon pixel detectors are placed close to the interaction region in order to improve the measurement of the impact parameter of charged particle tracks, as well as the position of primary and secondary vertices. The tracking device allows charged particle tracks reconstruction with at least 12 measurement points and a coverage of $|\eta| < 2.5$.

2.1 The Inner Tracking System

A highly performing tracking system is essential in order to fulfill the CMS physics goals. In a proton collider the longitudinal momentum of the interacting partons $p_z = p \cdot \cos\theta$ is not exactly known on a event-by-event basis, and the measurement of the physics observables is essentially performed in the transverse plane.

Therefore, it becomes essential measuring the transverse momentum $p_T = p \cdot \sin\theta$ with a very high resolution.
The trajectory of a particle with transverse momentum p_T and charge $Q = ze$ inside a magnetic field B is an helix, with radius R. The relation among these quantities is:

$$p_T = 0.3 \cdot z \cdot B \cdot R \tag{2.3}$$

where p_T is expressed in GeV, B in T e R in m. What is experimentally measured is the radius R, or better, the curvature[1] $k = Q/R$. The distribution of the measurements is gaussian, and the error can be written as the sum in quadrature of two contributions, the resolution on the measurement (δk_{res}) and the multiple Coulomb scattering (δk_{ms}):

$$\delta k = \sqrt{\delta k_{res}^2 + \delta k_{ms}^2} \tag{2.4}$$

Parametrizing the formula in terms of p_T, the particle transverse momentum resolution can be written as:

$$\frac{\delta p_T}{p_T} = C_1 p_T \oplus C_2 \tag{2.5}$$

where the term C_2 contains the multiple Coulomb scattering effects, while the angular coefficient C_1 depends on the detector geometry, in particular from the number of points used for the track reconstruction (n), its length (L), and the resolution on the single point measurement (σ_x):

$$C_1 \propto \frac{\sigma_x}{\sqrt{n} \cdot B \cdot L^2} \tag{2.6}$$

For low energetic particles C_2 dominates. C_1 is minimized having a long Tracker detector, and a consistent number of points n in the track fit. The resolution σ_x on a single measured point is given by:

$$\sigma_x = \sqrt{\sigma_{int}^2 + \sigma_{syst}^2} \tag{2.7}$$

where σ_{int} is the intrinsic resolution of the detectors and σ_{syst} the systematic error given by the unknown spatial position of hit module: this last one can be minimzed by alignment procedures.

The major requirements for the CMS Tracker can be summarized in the:

- promptness in the performance, given the high track population during the nominal LHC collisions of one (plus pile-up) event every 25 ns;
- robustness of its components to the radiation exposure, given the high density of hadronic tracks up to 10^{14} n_{eq}· cm^{-2}, where n_{eq} are "equivalent" 1 MeV neutrons;
- minimization of the crossed material, with the aim of reducing the multiple Coulomb scattering of charged particles crossing the detector, photon conversion and electron energy loss via *Bremsstrahlung*;

[1]The curvature depending on the sign of the particle can be positive or negative

- perfect alignment, internal of its components and with the muon system, in order to provide a reliable measurement of the particle momentum.

The CMS Tracker detector was designed in order to fulfill these requirements, giving at its nominal performance [28]:

- reconstruction capability in the region $|\eta| < 2.5$ with an efficiency of at least 95% for charged tracks with $p_T > 10$ GeV;
- high momentum resolution for isolated tracks:

$$\frac{\delta p_T}{p_T} = (1.5 \cdot p_T \oplus 0.5)\% \quad \text{for} \quad |\eta| < 1.6 \tag{2.8}$$

$$\frac{\delta p_T}{p_T} = (6.0 \cdot p_T \oplus 0.5)\% \quad \text{for} \quad |\eta| < 2.5 \tag{2.9}$$

  where the p_T is expressed in TeV. As shown in Figure 2.4 adding the information from the muon system, the resolution, for $p_T > 0.1$ TeV muons, becomes:

$$\frac{\delta p_T}{p_T} = (4.5\% \cdot \sqrt{p_T}) \tag{2.10}$$

- high resolution for transverse impact parameter, $\sigma(d_{xy}) = 35$ μm and longitudinal impact parameter $\sigma(d_z) = 75$ μm.

The CMS collaboration decided to build the whole detector using a silicon detector technology. This type of detector provides a high spatial resolution, from 10 to 20 μm and a fast collection of the charge deposited on the sensible elements, below 10 ns. The Tracker covers the pseudorapidity region $|\eta| < 2.5$ with a radius ranging between 4.3 cm and 120 cm in the z interval between 270 and 270 cm. The innermost region is made of pixel detectors, while the outermost one is build with strip detectors.

2.1.1 The pixel Tracker

The pixel Tracker consists of three 53.3 cm long barrel layers and two endcap disks on each side of the barrel section, as shown in Figure 2.5. The innermost barrel layer has a radius of 4.4 cm, while for the second and third layer the radii are 7.3 cm and 10.2 cm, respectively. The layers are composed of modular detector units (called modules) placed on carbon fiber supports (called ladders). Each ladder includes eight modules, consisting of thin (285 μm), segmented silicon sensors with highly integrated readout chips (ROC) connected by Indium bump-bonds. Each ROC serves a 52 $\times$ 80 array of 150 μm $\times$ 100 μm pixels.

The Barrel Pixel (BPIX) region is composed of 672 full modules and 96 half modules, each including 16 and 8 ROCs, respectively. The number of pixels per module is 66 560 (full modules) or 33 280 (half modules). The total number of pixels in the barrel section is 47 923 200.

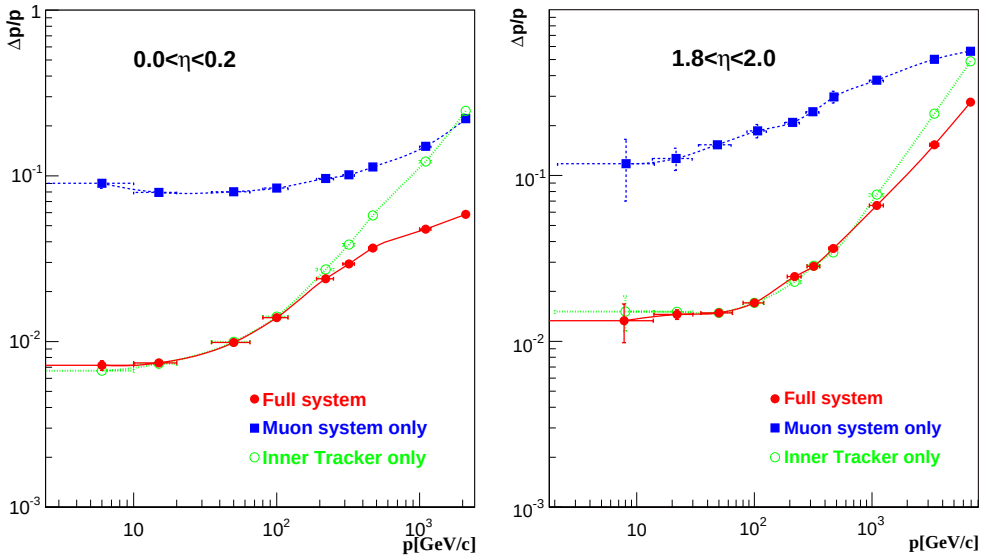

Figure 2.4: *Expected momentum resolution of muons as a function of momentum p, using measurements of the muon system only (blue), the Tracker only (green) or both detectors (red). Left. Central region $0 < \eta < 0.2$. Right. Forward endcap region $1.8 < \eta < 2.0$ [24].*

The Forward Pixel (FPIX) endcap disks, extending from 6 to 15 cm in radius, are placed at z $= \pm$ 35.5 cm and z $= \pm$ 48.5 cm. Disks are split into half-disks, each including 12 trapezoidal blades arranged in a turbine-like geometry. Each blade is a sandwich of two back-to-back panels. Rectangular sensors of five sizes are bump-bonded to arrays of ROCs, forming the so-called plaquettes. Three (four) plaquettes are arranged on the front (back) panels with overlap to provide full coverage for charged particles originating from the interaction point. The endcap disks include 672 plaquettes (270 μm thick), for a total of 17 971 200 pixels. The minimal pixel cell area is dictated by the readout circuit surface required for each pixel. In localizing secondary decay vertices both transverse (rϕ) and longitudinal (z) coordinates are important and a nearly square pixel shape is adopted. Since the deposited charge is often shared among several pixels, an analog charge readout is implemented. Charge sharing enables interpolation between pixels, which improves the spatial resolution. In the barrel section, the charge sharing in the rϕ-direction is largely due to the Lorentz effect. In the endcap pixels, the sharing is enhanced by arranging the blades in the turbine-like layout.

2.1.2 The strip Tracker

Outside the pixel detector, the Tracker (see Figure 2.6) is composed of 10 layers of silicon microstrip detectors.

The barrel region ($|\eta| < 1.6$) is divided into two parts: the Tracker Inner Barrel (TIB), covering 20 $<$ r $<$ 60 cm and the Tracker Outer Barrel (TOB), covering 60 $<$ r $<$ 120 cm. The TIB is composed by four layers of p-on-n type silicon sensors with a thickness of 320 μm and strip pitches varying from 80 to 120 μm. The first two layers are made with double sided modules, composed by two detectors mounted back to back with the strips tilted by 100 mrad. This kind of sensors provides a measurement

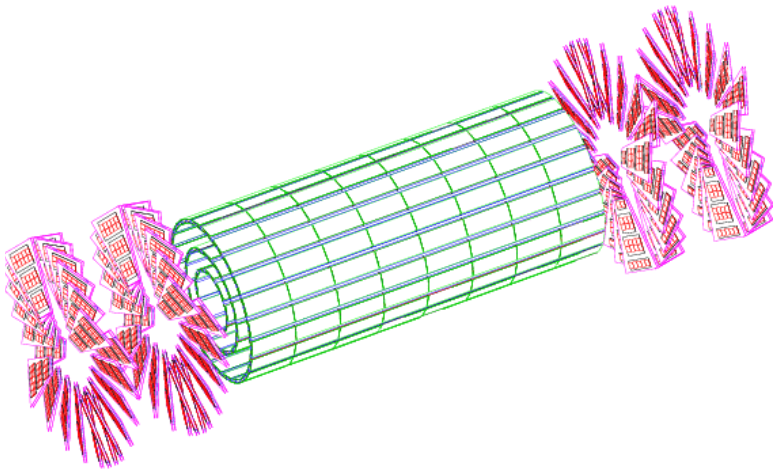

Figure 2.5: *Schematic illustration of the pixel Tracker.*

in both rϕ and r-z coordinates with a single point resolution between 23-34 μm and 230 μm respectively.
The TOB is made of six layers. In this region the radiation levels are smaller and thicker silicon sensors (500 μm) can be used to maintain a good signal- to-noise ratio for longer strip length. The strip pitch varies from 120 to 180 μm. Also the first two layers of the TOB provide a stereo measurement with a single point resolution which varies from 35 to 52 μm in the r direction and 530 μm in z.

The endcap region ($|\eta| > 1.6$) is covered by the Tracker Inner Disks (TID) and Tracker End Cap (TEC). The three disks of the TID fill the gap between the TIB and the TEC while the TEC comprises nine disks that extend into the region $120 < |z| <$ 280 cm. Both subdetectors are composed of wedge shaped modules arranged in rings, centred on the beam line, and have strips that point towards the beam line (radial topology).

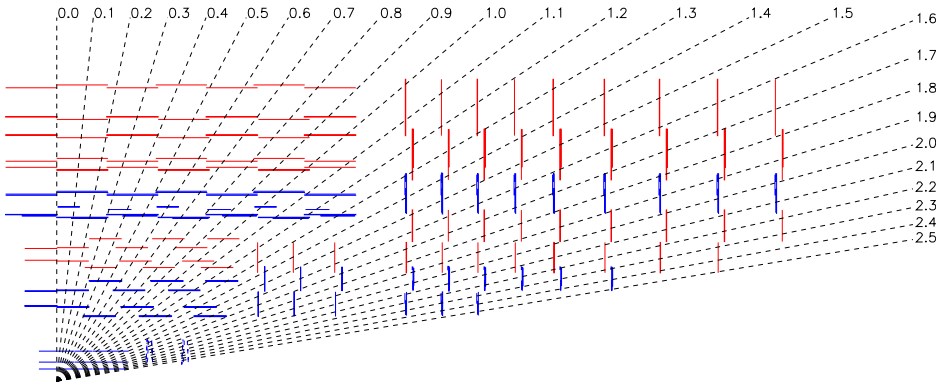

Figure 2.6: *Longitudinal view of one quarter of the strip Tracker: blue modules are double sided, red ones single sided.*

2.1.3 Sensor working principle and signal readout

The basic working principle of the silicon Tracker sensors is the pn junction. The two semiconductor regions, one doped with atoms having 3 valence electrons (p-type)

and the other doped with atoms having 5 valence electrons (n-type) are neutral if taken as single. If they become in contact, holes and electrons diffuse towards the junction, creating a depletion zone at the junction point: in this volume the electric field created offers resistance to the free charge carriers migration. The depletion region can be increased applying a reverse bias voltage to the junction: the electron and hole pairs, created in the depletion region by a ionizing particle can now drift in the electric field and be collected by the relative substrate.

The pixel sensors (Figure 2.7, right) have an active surface of 6.4 $\times$ 1.6 cm^2 segmented in cells of 150 $\times$ 100 μm^2 . The active area is a $n^+ - n$ junction, with a p^+ implant in the ground layer for polarizing the junction. The implant has an area of 78 $\times$ 78 μm^2 surrounded by a p+ guard ring: the nominal polarization voltage required to create the depletion region is 300 V, also imposed from the radiation dose, which acts inverting dopant concentration. The strip sensors (Figure 2.7, left) have an active surface of 6 $\times$ 12 cm^2 in the TIB and 6 $\times$ 18 cm^2 in the TOB with a thickness of 320 (500) μm for the innermost (outermost) sensors. They are made of silicon n-type substrate, on which are implanted, at regular distance, strips of p-type silicon. There are about 15 000 microstrip detectors, with a pitch between two neighbour strips ranging from 80 to 180 μm.

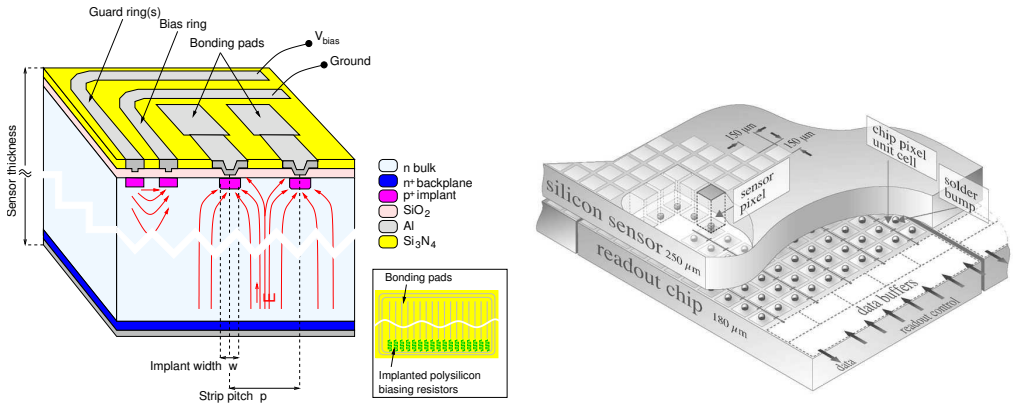

Figure 2.7: *Schematic view of a microstrip detector (left) and of a pixel detector (right) adopted in the CMS Tracker [24].*

In the pixel Tracker the readout chain starts in the pixel cell of the ROC, where the signals from individual pixels are amplified and shaped. To reduce the data rate, on-detector zero suppression is performed with adjustable thresholds for each pixel. Only pixels with charge above threshold are accepted by the ROC, marked with a time-stamp derived from the 40 MHz LHC bunch crossing clock, and stored on the chip for the time of the trigger latency (about 3.7 μs) until readout. In the strip Tracker the main components of the readout system are: 15 148 front-end detector modules that host about 76 000 APV25 readout chips [29], an analogue optical link system comprising 38 000 individual fibres, and 440 off-detector analogue receiver boards, known as Front-End Drivers (FED). The control system is driven by 46 off-detector digital transceiver boards, known as Front-End Controllers (FEC). The FECs distribute the LHC clock, triggers and control signals to the front-end detector modules via Communication and Control Units (CCU), which are hosted on 368 control rings. The APV25 readout chip samples, amplifies, buffers, and processes signals from 128 detector channels at a frequency of 40 MHz. Fast pulse

shaping is therefore required to provide bunch crossing identification and minimise event pileup. This is difficult to achieve with low noise and power levels, so the chip uses pre-amplifier and shaper stages to produce a CR-RC pulse shape with a relatively slow rise-time of 50 ns in an operating mode known as peak. An alternative mode, deconvolution, performs additional signal processing to constrain the signal to a single bunch crossing at the expense of a reduced signal-to-noise ratio. Deconvolution is expected to be the standard mode of operation during LHC collisions.

2.2 The Calorimeters

2.2.1 The electromagnetic calorimeter

The goal of the electromagnetic calorimeter is the accurate measurement of the energy and position of electrons and photons. The physics process that imposes the strictest requirements on its performance is the low mass ($m_H \simeq 120$ GeV) Higgs decay into two photons $H \rightarrow \gamma\gamma$, aiming 1% resolution on the di-photon invariant mass. The natural choice to achieve this task is a homogeneous calorimeter.

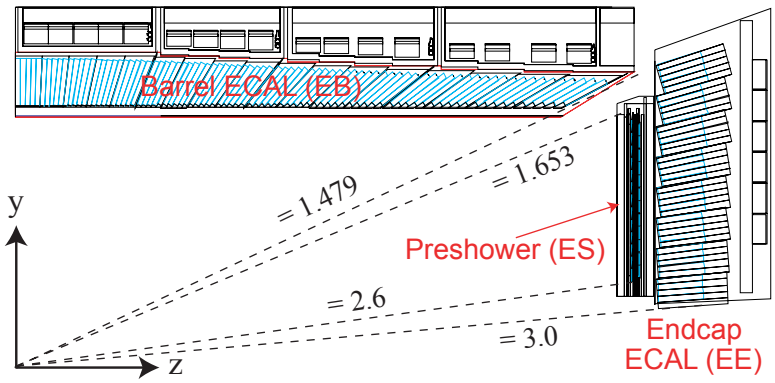

Figure 2.8: *Longitudinal view of one quarter of the CMS electromagnetic calorimeter [24].*

The ECAL is composed of 75,848 finely segmented lead tungstate ($PbWO_4$) crystals chosen because of their excellent energy resolution. Lead tungstate is a fast, radiation-hard scintillator characterised by a small Moliére radius ($R_M = 1.9$ mm) and a short radiation length ($X_0 = 8.9$ mm), that allows good shower containment in the limited space available for the detector. Moreover, these crystals are characterised by a very short scintillation decay time that allows the electronics to collect about 80% of the light within 25 ns.

A pre-shower detector is installed in front of the endcaps, consisting of two lead radiators and two planes of silicon strip detectors, with a total radiation length of $3X_0$. It allows rejection of photon pairs from π_0 decays and improve the estimation of the direction of photons, to improve the measurement of the two-photon invariant mass.

The geometric coverage of the calorimeter extends up to $|\eta| = 3.0$, as shown in Figure 2.8. The crystals are arranged in a $\eta - \phi$ grid in the barrel and a x-y grid in the endcaps and they almost pointing to the interaction point: the axes are tilted at

3° in the barrel and at 2°-5° in the endcaps with respect to the line from the nominal vertex position. The energy resolution of a calorimeter is usually parameterized as:

$$\left(\frac{\sigma_E}{E}\right)^2 = \left(\frac{a}{\sqrt{E}}\right)^2 + \left(\frac{b}{E}\right)^2 + c^2 \tag{2.11}$$

where a is the stochastic term and it includes the effects of fluctuations in the number of photo-electrons as well as in the shower containment, b is the noise from the electronics and pile-up and c is a constant term related to the calibration of the calorimeter. The values of the three constants measured on test beams are reported in Table 2.1. The different contributions as a function of the energy are shown in Figure 2.9.

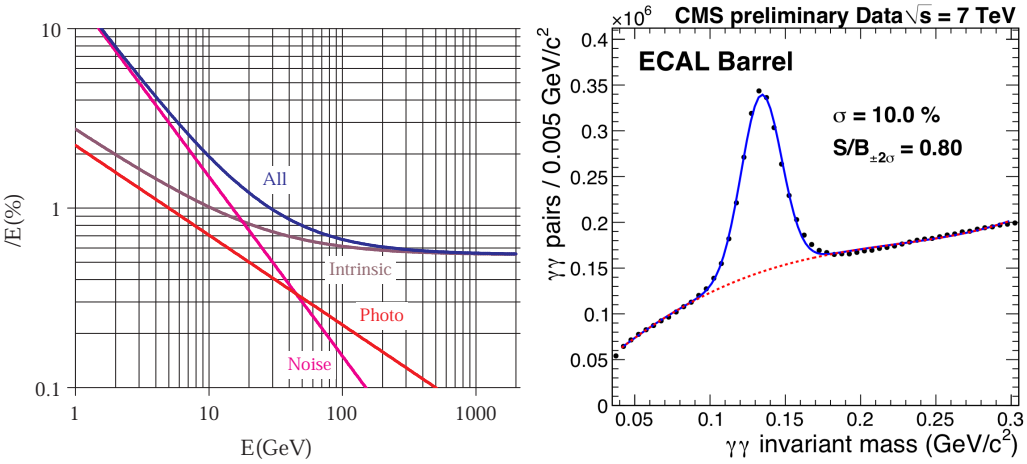

Figure 2.9: *Left: Different contributions to the energy resolution of the ECAL. The curve labelled intrinsic includes the shower containment and a constant term [24]. Right: di-phhoton invariant mass specrtum reconstructed by ECAL with about 250 nb^{-1} of data at $\sqrt{s}$ 7 TeV. The π_0 peak is visible, the mass resolution is of the order of 10%*

Table 2.1: *Different contributions to the energy resolution of ECAL [24].*

Contribution	Barrel (η=0)	Endcap (η=2)
Stochastic term a	2.7%	5.7 %
Noise (low luminosity) b	0.155 GeV	0.205 GeV
Noise (high luminosity) b	0.210 GeV	0.245 GeV
Constant term c	0.55 %	0.55%

2.2.2 The hadron calorimeter

The goal of the hadron calorimeter is to measure the direction and energy of jets, the total transverse energy and the missing transverse energy of the event. High hermeticity is required for this purpose. For this reason, the barrel and endcap parts installed inside the magnet are complemented by a very forward calorimeter which is placed outside the magnet return yokes, with a total coverage of $|\eta| < 5.3$. The barrel

and endcap HCAL cover the region $|\eta| < 3.0$. They are sampling calorimeters, whose active elements are plastic scintillators interleaved with brass absorber plates and read out by wavelength-shifting fibres. The first layer is read out separately, while all others are read out together. The absorber material has been chosen for its short interaction length, and its non-magnetic property. Both barrel and endcap are read-out in towers with a size of $\Delta\eta \times \Delta\phi = 0.087 \times 0.087$. In the barrel, full shower containment is not possible within the magnet volume, and an additional tail catcher is placed outside the magnet consisting of an additional layer of scintillators. The projective depth in terms of nuclear absorption length goes from 5.1 λ_I at $\eta = 0$ to 9.1 λ_I at $\eta = 1.3$ and is 10.5 λ_I in the endcap. The very forward calorimeter is placed outside the magnet yoke, 11 m from the interaction point. The active elements are quartz fibres parallel to the beam, inserted in steel absorber plates. The signal originated from the quartz fibres is Cerenkov light. The expected energy resolution is $\sigma/E \simeq 65\ \%\sqrt{E}\oplus 5\ \%$ in the barrel, $\sigma/E \simeq 85\ \%\sqrt{E}\oplus 5\ \%$ in the endcaps and $\sigma/E \simeq 100\ \%\sqrt{E}\oplus 5\ \%$ in the barrel (E in GeV) in the very forward calorimeter.

2.3 The Magnet

The CMS magnet [25] is a 13 m long superconducting solenoid, the largest ever built. It is able to generate a uniform magnetic field of 4 T in the inner region, storing about 2.5 GJ of energy (Figure 2.10).
It operates at a temperature of 4 K, ensured by a sophisticated helium cooling system. At such temperatures, the flat NiTb cable becomes superconducting, allowing a 20 kA current to flow without appreciable loss. The whole magnet is the contained in a enormous vacuum cylinder, which isolates it from the external environment.
Outside, an iron structure composed by five barrel layers and three disks for each endcap constitutes the iron yoke, needed to bridle the return magnetic field, which otherwise would get lost, causing disturbances.
The CMS magnet provides a large bending power, allowing a precise measurement of the transverse momentum of charged particles. A further and indipendent p_T measurement outside the solenoid is possible thanks to the iron yoke, which surrounds the muon chambers.

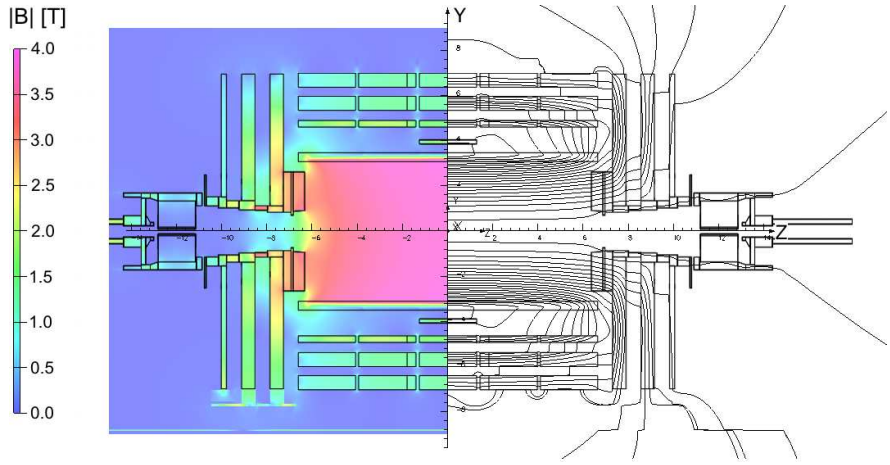

Figure 2.10: *Layout of the magnetic field of CMS [26].*

2.4 Muon system

Muons provides a clear signature for many physics processes. For this reason, the muon spectrometer must provide a robust trigger and an accurate measurement of the muon momentum and charge, also without the contribution of the Tracker. The muon system, shown in Figure 2.11, is embedded in the iron return yoke of the magnet, which shields the detectors from charged particles other than muons. The minimum value of the muon transverse momentum required to reach the system is $\simeq$ 5 GeV. The muon spectrometer consists of three independent subsystems.

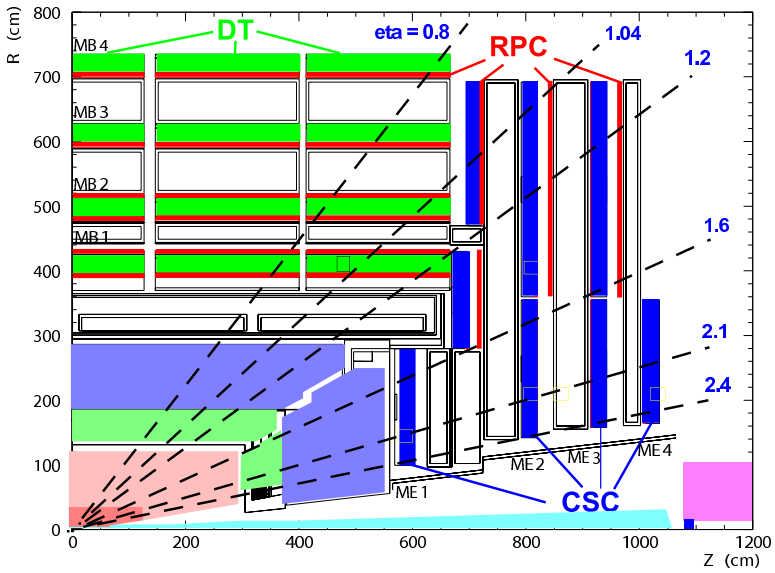

Figure 2.11: *Longitudinal view of one quarter of the CMS muon spectrometer [24].*

In the barrel ($|\eta| < 1.2$), where the track occupancy and the residual magnetic field are low, four layers (stations) of drift tube chambers (DT) are installed. The chamber segmentation follows that of the iron yoke, consisting of five wheels along the z axis, each one divided into 12 azimuthal sectors. Each chamber has a resolution of about 100 μm in rϕ and 1 mrad in ϕ.

In the endcaps ($0.8 < |\eta| < 2.4$), four disks (stations) of cathode strip chambers (CSC) are located, being this detector technology more indicated in a region suffering high particle rates and large residual magnetic field between the plates of the yoke. The innermost station consists of three concentric rings: the first one (ME1/1), being closer to the interaction point, is smaller than the other two. The other stations are composed by two rings only. The rings are formed by 18 or 36 trapezoidal chambers, which, with the exception of the outermost ring of ME1, are staggered with a small overlap in ϕ. These chambers have a spatial resolution of about 200 m (100 m for the chambers belonging to the first station) and 10 mrad in r-ϕ.

Redundancy is obtained with a system of resistive plate chambers (RPC), that are installed in both the barrel and the endcaps. RPCs have limited spatial resolution, but fast response and excellent time resolution of few ns, providing unambiguous bunch crossing identification. RPC detectors operate in avalanche mode rather than in the more common streamer mode, thus allowing the detectors to sustain higher

rates. This mode is obtained with a lower electric field, thus the gas multiplication is reduced and an improved electronic amplification is required. In the barrel the RPC chambers follow the segmentation of DT chambers. A total of six layers of RPCs are present: the first four are attached to each side of the MB1 and MB2 DT chambers. The other two are attached to the inner surface of MB3 and MB4. In the endcaps the chambers are trapezoidal distributed on four disks. They are also used to complement DTs and CSCs in the measurement of the p_T . The RPC system covers the region $|\eta|$ <2.1.

The robustness of the spectrometer is also guaranteed by the different sensitivity of DT, RPC and CSC to the background. The main sources of background particles in the LHC environment will be represented by secondary muons produced in pion and kaon decays, from punch-through hadrons and from low energy electrons originating after slow neutron capture by nuclei with subsequent photon emission. This neutron induced background will be the responsible of the major contribution to the occupancy level in the muon detectors. CSC and DT chambers, in contrast with RPC detectors, are characterised by a layer layout which helps in reducing the effect of background hits: the request of correlation between consecutive layers is particularly effective against background hits affecting only a single layer.

2.4.1 The muon Trigger

The nominal bunch crossing frequency at CMS interaction point is 40 MHz while technical difficulties in handling, storing and processing extremely large amounts of data impose a limit of about 100 Hz on the rate of events that can be written to permanent storage, as the average event size is of about 1 MB. The goal of the trigger is to perform the required huge on-line reduction of the data. The trigger must therefore be able to select events on the basis of their physics content, and online selection algorithms must have a level of sophistication comparable to that of offline reconstruction. The time available to accept or reject an event is extremely limited, being the bunch crossing time of 25 ns, a time interval too small even to read out all raw data from the detector. For this reason CMS adopts a multi-level trigger design, where each step of the selection uses only part of the available data. In this way higher trigger levels have to process fewer events and have more time available, so they can analyze the events in full details using more refined algorithms. The CMS trigger design is made of two physical steps, namely the Level-1 (L1) Trigger and the High Level Trigger (HLT).

Level-1 Trigger

The L1 Trigger is built of mostly custom-made hardware and it analyzes the detector information in a fairly coarse-grained scale. In the L1 step, the DT and CSC triggers determine the muon from the difference between segment slopes in successive layers of the muon spectrometer, whereas the RPC trigger compares the observed muon trajectory with predefined hit patterns as a function of p_T . All these triggers assume that muons are produced in a region around the LHC beam spot. The Global Muon Trigger system is responsible for matching DT and CSC candidates with RPC candidates, as well as for rejecting unconfirmed candidates of low quality. Up to four

muon candidates satisfying some minimal quality criteria and with the highest p_T are forwarded to the HLT for further processing.

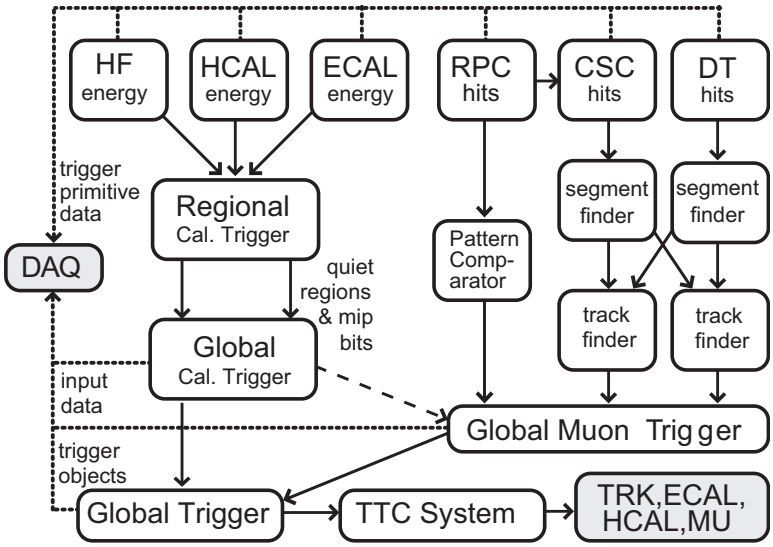

Figure 2.12: *Structure of the Level-1 Trigger system [24].*

High Level Trigger

The HLT system is software implemented in a single processor farm. In the first step of the HLT muon selection, referred to as Level-2 (L2), the L1 muon candidates are used to seed the reconstruction of tracks in the muon chambers. Unless for the seed, the L2 reconstruction follows the offline standalone reconstruction described in Section 2.5. A p_T threshold on the reconstructed L2 muon is applied and then the Level-3 (L3) reconstruction is carried out by combining L2 muons and charged-particle tracks reconstructed in the Tracker. Track parameters of the L2 muon, constrained to the interaction region, define a η ϕ region where a seed for the L3 reconstruction is found. A relaxed beam-spot constraint is applied to track candidates above a given transverse momentum threshold to obtain initial trajectory parameters. Trajectories are then reconstructed using Kalman-filter techniques. Isolation criteria, based on the sum of transverse energies in the calorimeter towers (for L2 muons) and of transverse momenta of charged-particle tracks (for L3 muons) found in a cone around the direction of the muon ($\Delta R_{cone} = 0.24$), are finally applied.

2.5 Offline muon reconstruction in CMS

In a hadron collider leptons provide a clear signature for many of the most interesting physics processes, therefore a precise and fast reconstruction of the leptons is mandatory. In this context the muons play a key role as their charge and momentum can be measured with great precision and, at least at high p_T , they can be identified unambiguously. The tracks within the muon system are built using the Kalman filter technique [31], combining the information coming from each muon sub-detector: this step is the so called stand-alone muon reconstruction. The following step is the propagation of the muon tracks to the Tracker, using some criteria to match the

reconstructed Tracker track (Tracker muon reconstruction). The information of the muon spectrometer and the Tracker system are combined in the global muon reconstruction, giving the final muon track. The reconstruction of the muons is completed by matching the muon track with the energy deposits in the calorimeters.

2.5.1 Track reconstruction in the muon spectrometer alone

The muon reconstruction chain starts with the local reconstruction in the muon spectrometer. First, hits in DTs, CSCs and RPCs are reconstructed from digitized electronics signals. Hits within each DT and CSC chamber are then matched to form a segment (track stub). The segments reconstructed in the muon chambers are used to generate seeds, consisting of position and direction vectors and an estimate of the muon transverse momentum. The seed trajectory state parameters are propagated to the innermost compatible muon detector layer, by identifying for each point the detectors that most probably contain the next hit to be included in the trajectory (navigation). After this, a pre-filter is applied in the inside-out direction. Its main purpose is to refine the seed state before the true filter. The final filter in the outside-in direction is then applied and the trajectory is built.

The pre-filter and filter are based on the same iterative algorithm: at each step the track parameters are propagated from one layer to the next. The best measurement is searched on a χ^2 basis. The χ^2 compatibility is examined at the segment level, estimating the incremental χ^2 given by the inclusion in the fit of the track segment. In case no matching hits (or segments) are found, the search continues in the next station (pattern recognition phase).

Once the hits are fitted and the fake trajectories removed, the remaining tracks are extrapolated to the point of closest approach to the beam line. In order to improve the p_T resolution a beam-spot constraint is applied.

2.5.2 Track reconstruction in the Inner Tracker alone

The track reconstruction algorithms rely on a good estimate of the proton-proton interaction region, referred to as the beamspot. The beamspot is used as a precise estimate of the primary interaction point (in the transverse direction) prior to primary vertex reconstruction and as the sole primary interaction point if no primary vertex is found. When the beamspot centre is displaced from the expected position there is a correlation between the transverse impact parameter (d_{xy}) and the angle of the track at the point of closest approach (ϕ_0). The beamspot fitter [32] uses an iterative χ^2 fitter to exploit this correlation between d_{xy} and ϕ_0 , looping over a sample of reconstructed tracks (using the old beamspot) to determine the new beamspot parameters. After the beamspot is measured, the standard track reconstruction is performed. During the 2010 data-taking, a beamspot was fitted during each LHC fill.

Starting from the location of the beamspot, an initial round of track and vertex reconstruction is performed using only pixel hits. The pixel vertices found at this stage are used in the standard tracking. The standard track reconstruction at CMS

is performed by the combinatorial track finder (CTF) [33]. Tracks are seeded from either triplets of hits in the tracker or pairs of hits with an additional constraint from the beamspot or a pixel vertex, yielding an initial estimate of the trajectory, including its uncertainty. The seed is then propagated outward in a search for compatible hits. As hits are found, they are added to the trajectory and the track parameters and uncertainties are updated. This search continues until either the boundary of the tracker is reached or no more compatible hits can be found. An additional search for hits is performed starting from the outermost hits and propagating inward. In the final step, the collection of hits is fit to obtain the best estimate of the track parameters.

The current implementation of the CTF performs six iterations. Between each iteration, hits that can be unambiguously assigned to tracks in the previous iteration are removed from the collection of tracker hits to create a smaller collection that can be used in the subsequent iteration. At the end of each iteration, the reconstructed tracks are filtered to remove tracks that are likely fakes and to provide a means of quantifying the quality of the remaining tracks. The filtering uses information on the number of hits, the normalized χ^2 of the track, and the compatibility of the track originating from a pixel vertex (see Figure 2.13). Tracks that pass the tightest selection are labelled `highPurity`. The first two iterations use pixel triplets and pixel pairs as seeds to find prompt tracks with $p_T > 0.9$ GeV. The next iteration uses pixel triplet seeds to reconstruct low-momentum prompt tracks. The following iteration uses combinations of pixel and strip layers as seeds, and is primarily intended to find displaced tracks. The final two iterations use seeds of strip pairs to reconstruct tracks lacking pixel hits.

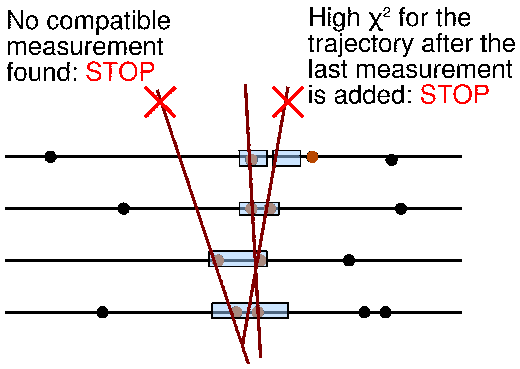

Figure 2.13: *Schematic representation of the Kalman Filter based pattern recognition. The points represent hits, the curved lines track candidates and the shaded boxes the size of the search window [31].*

2.5.3 Track matching: the Global Muon reconstruction

The track in the muon spectrometer is used to define a region of interest in the Tracker. The determination of this region is based on the stand-alone muon with the assumption that the muon originates from the interaction point.
Inside the region of interest, candidates for the muon trajectory (regional seeds) are built from pair or triplet of hits reconstructed on different Tracker layers. It is possible to use all combinations of compatible pixel and double-sided silicon strip layers in order to achieve high efficiency. In addition, a relaxed beam-spot constraint

is applied to track candidates above a given p_T threshold to obtain initial trajectory parameters. Starting from the regional seeds, the standard Tracker algorithms are used to reconstruct tracks inside the selected region of interest. The track matching is performed by propagating the muon and the Tracker tracks onto the same plane and looking for the best χ^2 value from the comparison of track parameters. If there is a suitable match between a Tracker track and stand-alone muon track, then the hits from the Tracker and the stand-alone muon track are combined in one collection and a final fit is performed over all hits, leading to the global muon. The reconstruction of the muons ends with the matching of the global muon track and the energy deposits in the calorimeters (calo muon).

2.5.4 Track parametrization in CMS

An charged particle moving in a uniform magnetic field not experiencing multiple scattering and not changing its nature throughout the measurement, say due to a decay, track follows a helical trajectory. A helix can be parametrized with respect to a reference point by five parameters.
A simple geometric parametrization is shown in Figure 2.14. Depending on the calculation in question, different parametrizations are available.

- **Curvilinear frame** $(q/p, \lambda, \phi, x_\perp, y_\perp)$ This frame can be defined at every point of the trajectory using a local cartesian coordinate system $(x_\perp|y_\perp|z_\perp)$ defned by three orthogonal unit vectors $\widehat{\mathbf{u}}$, $\widehat{\mathbf{v}}$ and $\widehat{\mathbf{t}}$. The vector $\widehat{\mathbf{t}}$ is defined as the unit vector parallel to the track, pointing in the particle directions. Using the vector $\widehat{\mathbf{z}}$ parallel to the global-z direction, the two vectors $\widehat{\mathbf{u}}$ and $\widehat{\mathbf{v}}$ are defined as:

$$\widehat{\mathbf{u}} = \frac{\widehat{\mathbf{z}} \times \widehat{\mathbf{t}}}{|\widehat{\mathbf{z}} \times \widehat{\mathbf{t}}|} \tag{2.12}$$

$$\widehat{\mathbf{v}} = \widehat{\mathbf{t}} \times \widehat{\mathbf{u}} \tag{2.13}$$

  Therefore, the $z_\perp$-axis is pointing along the particle direction, the $x_\perp$-axis is lying in the global xy-plane, and the $y_\perp$-axis is perpendicular on the two others, in order to form a right-handed cartesian coordinate system. The five parameters used in the curvilinear frame are: $x_\perp$ and $y_\perp$ as defined above, q/p being the signed curvature of the track, the dip angle of the particle 3-momentum vector λ, and the inclination angle ϕ between the tangent of the projection of the particle 3-momentum vector into the global xy -plane and the global z-direction.
  This parametrization is useful for track reconstruction, as it can be defined at every point along the track using the track length as an evolving parameter. It is the default frame used in the official software of the CMS experiment (`CMSSW`) for track reconstruction.

- **Perigee frame** $(d_{xy}, \phi_0, \kappa, d_z, tan\lambda)$. As the name suggest, the reference point is the closest approach of the trajectory to the origin of the coordinate sysyem in use. This parametrization is especially suitable for vertex fitting.
  The definition is given by the following description of a track in three dimensional space:

$$\begin{pmatrix} x(\phi) \\ y(\phi) \\ z(\phi) \end{pmatrix} = \begin{pmatrix} x_0 + d_{xy}\cos\phi_0 + \frac{\alpha}{\kappa}(\cos\phi_0 - \cos(\phi_0+\phi)) \\ y_0 + d_{xy}\sin\phi_0 + \frac{\alpha}{\kappa}(\sin\phi_0 - \sin(\phi_0+\phi)) \\ z_0 + d_z - \frac{\alpha}{\kappa}\tan(\lambda)\cdot\phi \end{pmatrix} \quad (2.14)$$

where the vector $\mathbf{x}_0 = (x_0, y_0; z_0)$ describes the reference point and the vector $\mathbf{q} = (d_{xy}, \phi_0, \kappa, d_z, tan\lambda)$ describes the helix. Assuming the z direction be parallel to the magnetic field, d_{xy} is the signed distance from the reference point in the xy-plane, ϕ_0 is the azimuthal angle to the helix center, κ is the reciprocal transverse momentum, d_z the signed distance from the reference point in z direction and $tan\lambda$ the dip angle. κ can be calculated using:

$$\kappa = \frac{Q}{p_T} \quad (2.15)$$

$$\rho = \frac{\alpha}{\kappa} \quad (2.16)$$

with Q the charge and ρ the signed radius of the helix. The constant $\alpha = 1/cB$ depends on the magnetic field.

In a more realistic description, multiple scattering has to be taken into account. Scattering processes result in an angular straggling which can be treated as an increasing error to the measurement further away form the origin of the track.
In the software framework `CMSSW`, tracks are described by the class `TrackBase` holding the following information:

- A reference point of the track: (x, y, z)
- Momentum at this given reference point (p_x, p_y, p_z)
- $5D$ curvilinear covariance matrix from the track fit:
  - $\frac{q}{|p|}$ = signed inverse of the momentum
  - $\lambda = \pi/2$ - polar angle at the given point
  - $\phi =$ azimuth at the given point
  - $d_{xy} = -x\cdot\sin\phi + y\cdot\cos\phi$ - an estimate of the impact parameter in the $xy-plane$
  - $d_{sz} = z\cdot\cos\lambda - (x\cdot\cos\phi + y\cdot\sin\phi\cdot\sin\lambda)$
- Charge Q
- Chi-square and number of degrees of freedom
- summary information of the hit pattern

Some information is redundant but available for convenience.

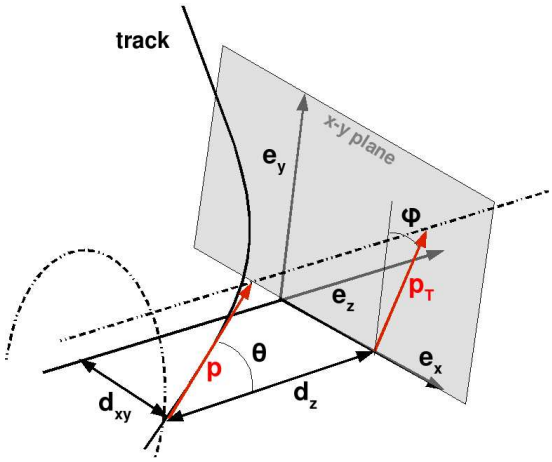

Figure 2.14: *Track parameters defined at the perigee computed with respect the origin of the global frame.*

2.6 Tracker operations and performance in 2010

During the 2010 collision data taking period the Tracker was operated with the coolant temperature kept constant at 4 °C an the bias potential applied to both the strip barrel and endcap sensors of 300 V. Small fractions of the barrel (1.0%) and endcap (3.1%) detectors were inactive resulting in a net operational fraction of 98.4 % for the entire detector. The total down-time of the Tracker during data-taking periods declared as "stable beams" was 0.81 %, corresponding to a total data loss of about 13 nb^{-1} mainly due to few isolated problems or dedicated technical runs.
In Figure 2.15 are shown the distributions of the track strip clusters Signal to Noise ratio S/N for TIB and TOB, operated in deconvolution mode (nominal conditions). The most probable value extracted, for each subdetector, form the fit of the distributions with a gaussian convoluted with a Landau model are in the range 18-24.
Figure 2.16 shows the strip hit efficiency for all the layers and disks of the Strip Tracker. After subtracting bad componenents the efficiences are all above 98%.

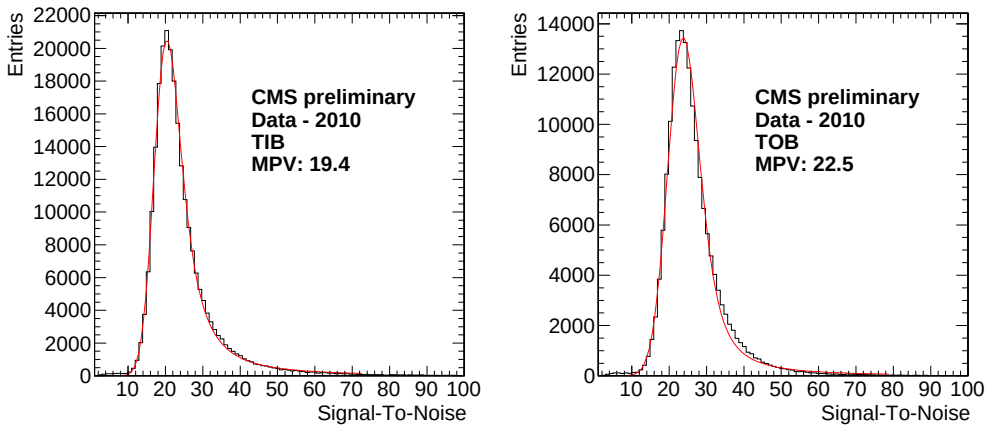

Figure 2.15: *Signal to Noise ratio S/N of strip clusters for TIB (right) and TOB (left). Most Probable Values (MPV) are extracted from a gaussian convoluted with a Landau pdf.*

The very smooth activity of the Tracker operations during 2010 and the very high

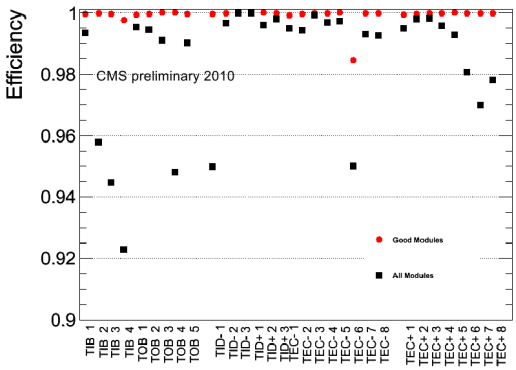

Figure 2.16: *Strip hit efficiency as a function the layer (disk) for all the Strip Tracker subdetectors. The black squares refer to all the modules, red circles to the situation when bad components are subtracted.*

hit collection efficiency allowed to make accurate measurements of the Tracker performance with the early collision data, measuring tracking efficiencies for muons and pions [34] (see Figure 2.17) , primary vertex reconstruction efficiencies and resolutions, along with the resolutions on the track impact parameter (see Figure 2.18) [35]. All results were found very close the nominal performance.

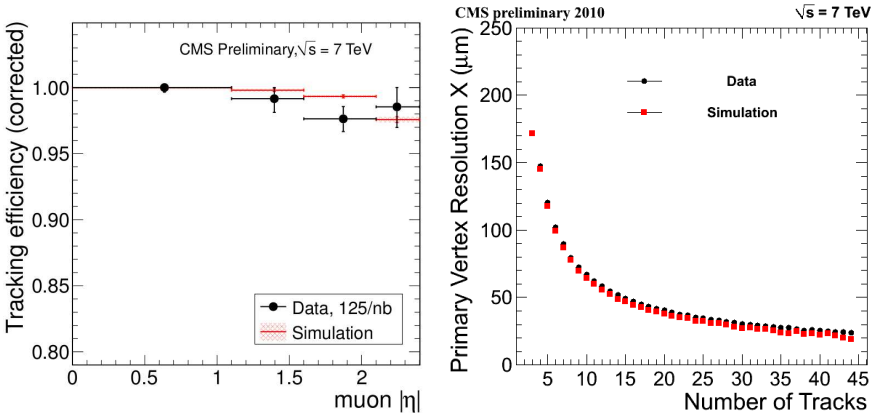

Figure 2.17: *Left: muon tracking efficiency as a function of η for muons in data (points with errors) and simulation (hatched) measured with 2010 collision data [34]. Right: primary vertex resolution in the x direction as a function of the number of tracks used in the fitted vertex [35].*

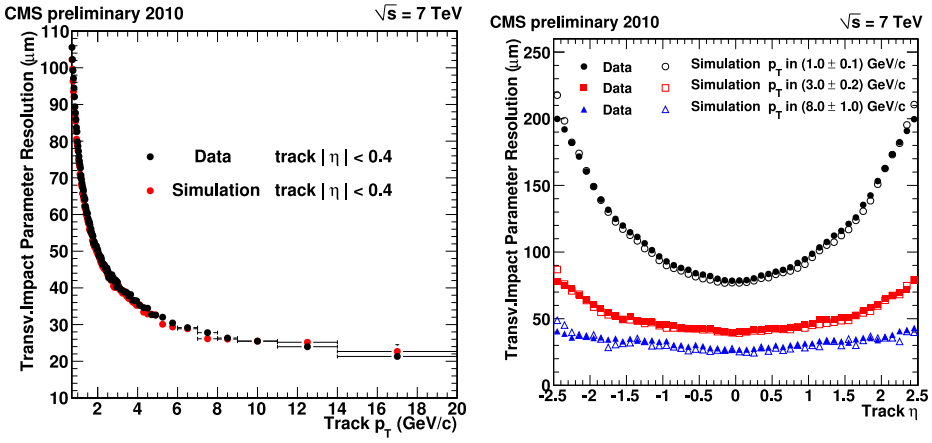

Figure 2.18: *Left: measured resolution of the track transverse impact parameter as a function of the track p_T. Only central tracks with $|\eta| < 0.4$ are considered. Black and red symbols correspond to results from data and simulation [35]. Right: measured resolution of the track transverse impact parameter as a function of the track η for transverse momenta 1.0 $\pm$ 0.1 GeV (circles), in 3.0 $\pm$ 0.2 GeV (squares) and 8.0 $\pm$ 1.0 GeV/c (triangles) [35].*

Part II

Research Work

Chapter 3

The Alignment of the CMS Tracker

Abstract

The CMS Tracker is designed to achieve excellent resolution on charged particle momenta measurement. The residual alignment uncertainties should not lead to a significant degradation of the intrinsic Tracker resolution and therefore Tracker alignment is a critical task for the CMS collaboration. In this chapter alignment procedures are reviewed and the basic formalism used in these procedures is introduced.

The *alignment* is the procedure of measuring the deviations of the position of sensitive elements in the real detector from their design value. A big challenge is to obtain alignment corrections to a precision that ensures that the track reconstruction performance is not compromised. Furthermore physics requirements like the resolution on vector boson masses (M_Z or M_W) place even more stringent constraints on the alignment precision.
For example, to achieve a desired precision on the measurement of the W boson mass of 15-20 MeV, the momentum scale has to be known to an accuracy of 0.02% to 0.025% [37], which implies the absolute detector positions to be known with a precision of better than 10 μm in the rϕ plane. Misalignment will degrade the track parameter resolution and hence affect the physics performance of the Tracker also for what concerns b-tagging and vertexing performances.
To illustrate the principle behind the alignment, let us assume to have an hypothetical neutral resonance decaying into two charged particles. Let us assume also that the daughter tracks are almost straight tracks, for example energetic muons with momentum of several tens of GeV.
Those particles in an LHC physics experiment will pass through a typical tracking device consisting of a cylindrical detector made of a large number of modules disposed on layer structures, able to provide high granularity and full angular coverage, embedded in a solenoidal magnetic field.
The resolution on the invariant mass of the decaying resonance of mass m in two charged particles can be expressed as follows:

$$\frac{\delta m}{m} \simeq \frac{1}{2}\left(\frac{\delta p_1}{p_1} \oplus \frac{\delta p_2}{p_2} \oplus \frac{\delta\theta}{cotg\theta}\right) \tag{3.1}$$

being p_1 and p_2 the momenta of the daughter tracks and θ the angular separation between the two. The resolution on the momentum measurement can be written as a function of the track sagitta s:

$$\frac{\delta p}{p} = \frac{\delta s}{s} = \frac{8}{q}\frac{1}{L^2 B} p\, \delta s \tag{3.2}$$

with B the intensity of the solenoidal magnetic field and L the lever arm of the tracking device.

Given the values chosen for the CMS experiment, $B \simeq 4$ T and $L = 1$ m, to obtain a resolution of 1% on $\delta p/p$ and hence for $\delta m/m$ we need to determine the sagitta with a precision δs of the order of 15 μm.

This means that one needs a hit reconstruction precision at least of this order of magnitude, and therefore, given Equation 2.7, a knowledge of the detector geometry not worse than the intrinsic hit reconstruction precision.

In reality, modules are displaced with respect to their design positions due to the limited mounting accuracy, with displacements ranging from a few up to several hundereds μm according to the intrinsic precision of the mounting technique, or because of external mechanical effects like changes of the temperature and humidity in the tracking device environment or variations in the magnetic field intensity. The real positions of the modules are not known a-priori and the design geometry is assumed by the track reconstruction algorithm, leading to a wrong determination of the track parameters.

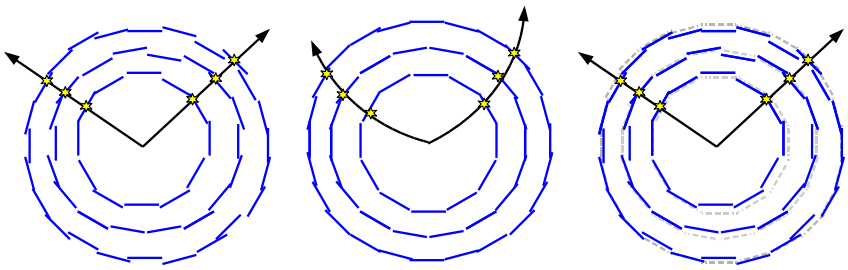

Figure 3.1: *Left picture: the tracking device is crossed by charged particles, producing tracks. Middle picture: the geometry of the detector is assumed to be ideal, even if misaligned in the reality, and this causes wrong estimation of particle's momentum. Right picture: module positions are moved according to the corrections found after the alignment procedure, leading to a geometry close to the real one and consequently to a correct estimation of track parameters. Relative movements are greatly exaggerated*

For example the track curvature and consequently the p_T estimate can be strongly biased due to an incorrect geometry assumption, as shown in Figure 3.1. The goal of the alignment procedure is to provide the corrections to be applied to the positions of the modules to allow a reconstruction of the track as close as possible to the real one. Alignment of large detectors in high energy physics often requires the determination of several thousands of alignment parameters, defining the spatial coordinates and orientation of each detector component. In the alignment process, hardware informations like optical and laser measurements, in addition with the mounting precision informations, are usually combined together with data from particle interactions, like muons from resonance decays or cosmic rays, in order to reduce the module position uncertainty down to the micrometer level. But even if the χ^2 of the track fit is minimized and pattern recognition performs well, it is still possible to end up with biased

measurements of track parameters due to remaining misalignment.

Correlated displacements of the sensors which introduce a track parameter bias can be χ^2 invariant, leading to certain coherent transformations of the geometry, the so-called "weak modes". Therefore it is mandatory to choose a varied track topology, which allows to connect different parts of the detector and effectively reduce the displacements with respect to each other, and properly balance their weights when used in input to the minimization procedure of the algorithm.
The all-silicon design of the CMS Tracker has posed new challenges in aligning a system with more than 15 000 independent modules. Given the inaccessibility of the detector volume during collisions, the most accurate way to determine the silicon detector positions is to use the data from the silicon detectors themselves when they are traversed in-situ by charged particles.

Additional information about the module positions is provided by the optical survey made during the construction phase and by the Laser Alignment System during the detector operation. Due to the complexity of the system, a hierarchical structure of the alignable objects and a coordinate system convention, has been defined.

3.1 Alignment hierarchy

Figure 3.2 shows a logical hierarchical representation of the CMS Tracker structures as implemented in the CMS software. Not all hierarchy levels shown are mechanically decoupled from their parents and therefore play a role as an independent object in the alignment procedure. For example, the *Layer* in the TOB is a logical structure that is extensively used in the tracking code, whereas it has reduced meaning as a separate alignment object since it is not a single mechanical structure. Each element of the hierarchy is free to be moved along all its six degrees of freedom [1] and the movement of the parent structure is correctly propagated down to the daughters and vice versa. The lowest object in the hierarchy which can be aligned is currently the module unit.

The global coordinate system in CMS is defined as follows. The origin is centered at the nominal collision point inside the experiment. The *y-axis* points upwards and the *x-axis* points inwards to the centre of the collider ring. Consequently the *z-axis* points along the beam axis. The azimuthal angle ϕ is measured from the *x-axis* in the $x-y$ plane, while the polar angle θ is measured from the *z-axis*. In the CMS software the coordinates are expressed in units of cm and rad.

The local coordinate system of an alignable, is defined instead with respect to the centre of its active area, as described in a detailed simulation of the detector based on `GEANT4` code. Modules in `CMS` are assumed to be rigid bodies. Three positions and three rotations, as illustrated in Figure 3.3, specify their degrees of freedom. The local positions are called u, v and w, where u is along the sensitive coordinate (i.e. across the strips), v is perpendicular to u in the sensor plane and w is perpendicular to the uv-plane, completing the right-handed coordinate system. The rotations around

[1] Assuming alignable units a rigid bodies. Recent developments may allow the description of module surface deformations in the CMS reconstruction software

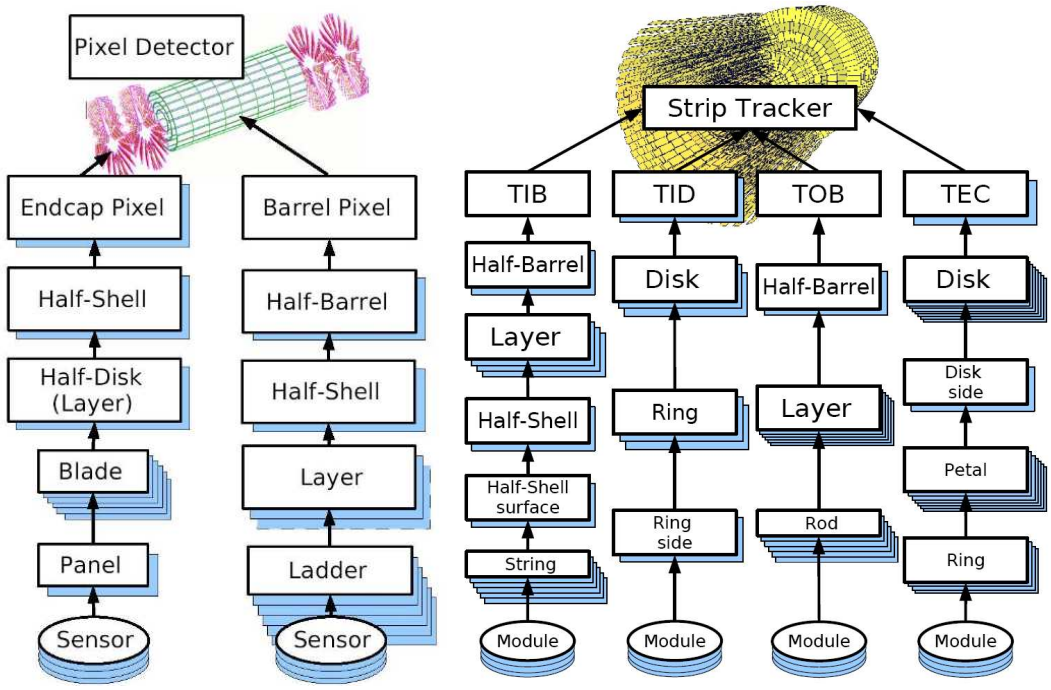

Figure 3.2: *Illustration of the hierarchies implemented inside the CMS alignment software. Pixel Tracker structure is shown on the left, and strip Tracker hierarchy is shown on the right. They closely follow the hierarchies of the mechanical structures.*

the u, v and w axes are called α, β and γ, respectively. In the case of alignment of intermediate structures like rods, strings or petals, u and v are assumed to be respectively parallel and perpendicular to the precisely measured coordinate, while for the large structures like layers and disks, the local coordinates coincide with the global ones. In addition, local u' and v' coordinates are defined such that they are parallel to u and v, but the direction is always chosen to be in positive ϕ, z, or r directions, irrespective of the orientation of the local coordinate system.

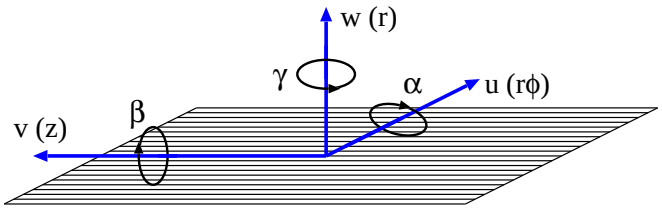

Figure 3.3: *Schematic illustration of the local coordinates of a strip module as used for alignment. Global parameters (in parentheses) are shown for modules in the barrel detectors (TIB and TOB).*

For the TID and TEC wedge-shaped sensors, where the topology of the strips is radial, the u' and v'-axes change direction across the sensor such that v' is always directed along the strips and therefore u' corresponds to the global rϕ-coordinate.

3.2 Survey measurements and LAS

3.2.1 The Tracker survey

Information about the relative position of modules within detector components and of the large-level structures within the Tracker is available from the optical survey analysis prior to or during the Tracker integration. This includes Coordinate Measuring Machine (CMM) data and photogrammetry, the former usually used for the measurement of the position of active elements and the latter for the larger object measurements. For TIB survey measurements are available for the module positions with respect to half-shells, and of Layers with respect to the Tracker Support Tube. Similarly, for TID survey measurements were done for modules with respect to the rings, rings with respect to the disks and disks with respect to the Tracker Support Tube. For TOB the cylinders were measured with respect to the Tracker Support Tube. For TEC, measurements are stored at the level of disks with respect to the endcaps and endcaps with respect to the Tracker Support Tube. Figure 3.4 illustrates the relative positions of the CMS Tracker modules with respect to the design geometry as measured in optical survey: as can be seen, differences from the design geometry as large as several millimeters are present. Since hierarchical survey measurements were performed, having TOB and TEC only large-structure information, the corresponding modules appear to be coherently displaced. An overview of the mounting precision of the strip Tracker elements is given in Table 3.1.

Table 3.1: *Estimated assembly precision (RMS, in μm) of Tracker components. Values are given in between the mechanical hierarchy levels they are valid for, e.g. the position accuracy of sensors in modules is 10 μm [38].*

TIB		TID		TID		TEC	
Sensor		Sensor		Sensor		Sensor	
	10		10		10		10
Module		Module		Module		Module	
	180		54		30		20
Shell		Ring		Rod		Petal	
	450		185		100		70
Cylinder		Disc		Wheel		Disc	
	750		350		140 (rϕ), 500(z)		150
Tube		Cylinder		Tube		TEC	
			450		1000		600
		Tube		CMS		Tube	

Concerning the pixel detectors, detailed optical surveys of both barrel and endcaps were performed as part of the construction process. In the endcap region, first module positions were measured within a panel, which contains three or four modules. Then the positions of modules were measured on a half-disk, where 12 panels are placed on each side. Finally, half-disks were placed in the half-cylinders, which were then inserted in the pixel detector volume. Half-disk and half-cylinder positions were measured with photogrammetry and were related to the active element position through photo targets which had been previously measured with coordinate measuring machines. In

the Barrel Pixel detector, only two-dimensional measurements of the module positions within a ladder were performed.

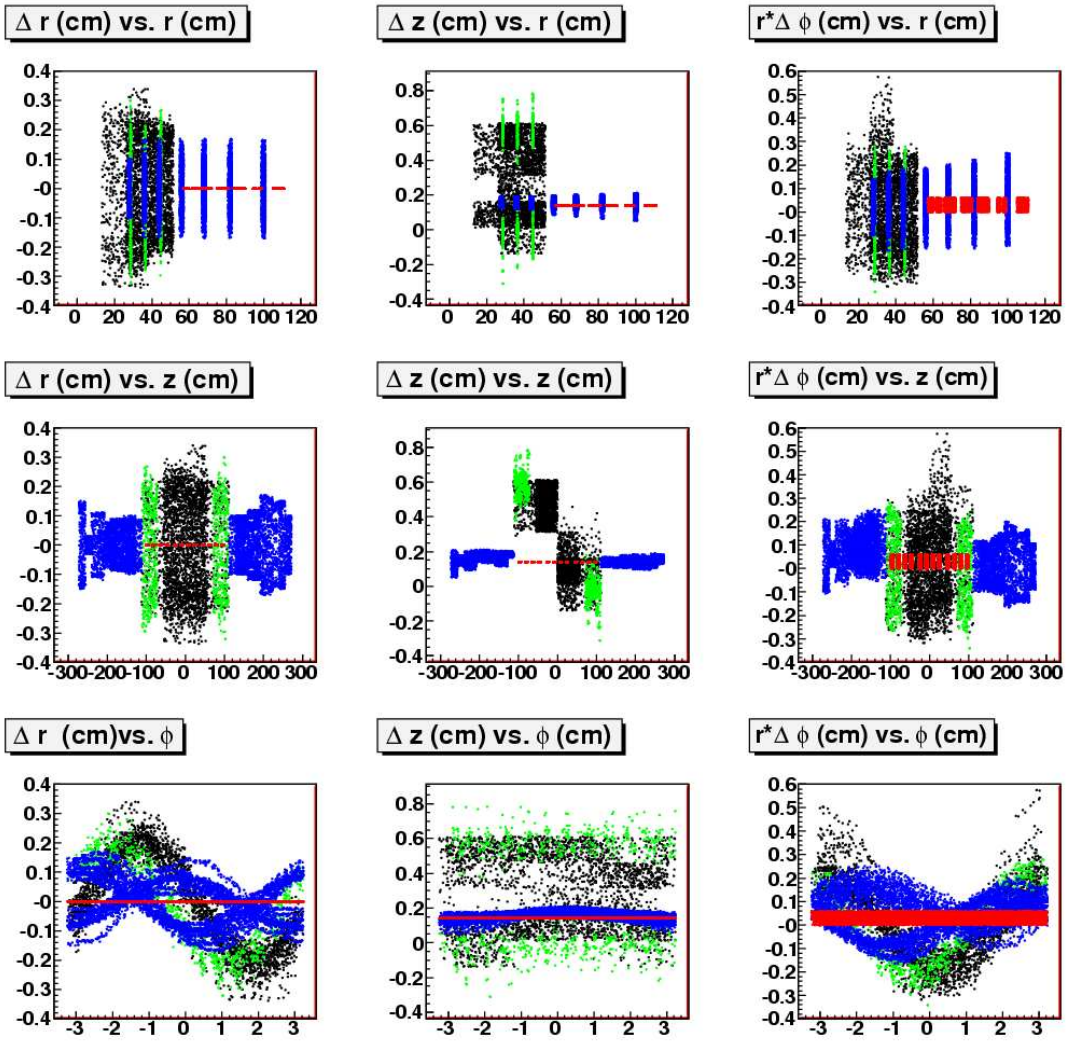

Figure 3.4: *Displacement of modules in CMS global cylindrical coordinates as measured in survey with respect to design geometry. A colour code is used: black for TIB, green for TID, red for TOB, and blue for TEC [38].*

3.2.2 Monitoring with LAS

The Laser Alignment System (LAS, see Figure 3.5) [30] uses infrared laser beams with a wavelength of $\lambda = 1075$ nm to monitor the possible movements of the Tracker structures. It operates globally on Tracker substructures (TIB, TOB and TEC disks) and cannot determine the position of individual modules. The goal of the system is to provide continuously information that can be used for alignment, giving geometrical informations on the position of the Tracker substructures at the level of 100 μm. In addition, possible movements of Tracker structure can be monitored at the level of 10 μm, providing additional input for the track based alignment. In each TEC, eight laser beams cross all nine TEC disks in ring 6 and ring 4 on the back petals, equally distributed in ϕ. Here, special silicon sensors with a 10 mm hole in the backside metallisation and covered by an anti-reflective coating are mounted. The beams are

used for the internal alignment of the TEC disks. The other eight beams, distributed in ϕ, are designed to align TIB, TOB, and both TECs with respect to each other. Finally, there is a link to the muon system, which is established by 12 laser beams (six on each side) with precise position and orientation in the Tracker coordinate system. The connection with the muon system is established by Alignment Rings, which are connected with the back part of TEC disks.

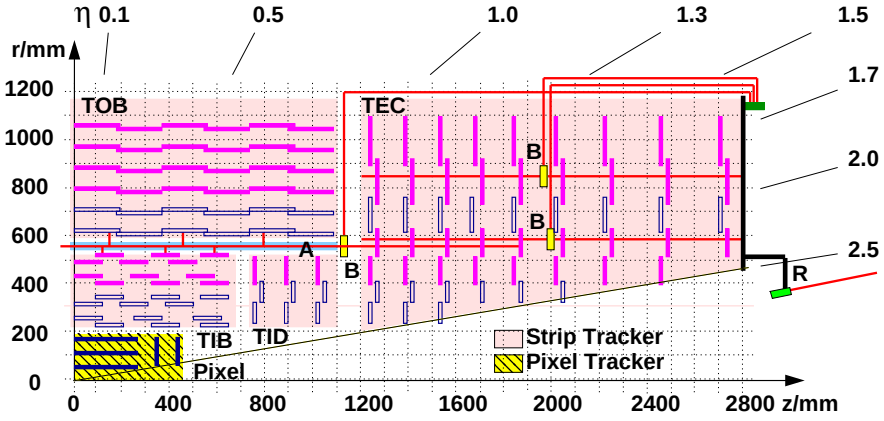

Figure 3.5: *Overview of the CMS Laser Alignment System. Alignment Tubes (AT), ranging from endcap to endcap, together with Alignment Ring (AR) for the Endcap monitoring, distribute the light via optical fibers through the Beam Splitter (BS).*

The signal induced by the laser beams on the silicon sensors decreases in intensity as the beams penetrate through subsequent silicon layers in the TEC and through beam splitters in the alignment tubes that partly deflect the beams onto TIB and TOB sensors.
To obtain optimal signals on all sensors, a sequence of laser pulses with increasing intensities, optimised for each position, is generated. Several triggers per each intensity step are taken, and the signals are averaged. In total, a few hundred triggers are needed to get a full picture of the alignment of the Tracker structure. Since the trigger rate for the LAS is around 100 Hz, this takes only a few seconds.

3.3 Track-based alignment

The use of tracks to align a tracking detector is possible under the assumption that tracks may be described using a limited and sufficient number of parameters in an appropriate way to predict their paths. Misalignment leads to a systematic distortion of the measurements per module which can be determined using sufficiently large number of tracks and their hit signals.

In CMS, the alignment software consists of two independent algorithms, tools for the study of random and systematic misalignments and an extensive collection of tools to monitor and visualize the performance and geometry of the detector. They use data from collisions or cosmic ray muons, both simulated and real data.
Most of the alignment formalism makes use of the *track-to-hit residuals* and *track* χ^2 concepts. These quanties, which will be used frequently in the following, are introduced here.

3.3.1 Coordinate systems and Track-to-hit residuals

A track-to-hit residual $\mathbf{R}(\mathbf{p},\mathbf{q})$ in the module local coordinate system is the distance between the measured position $\mathbf{m}_{hit}$ of the hit on the module and the intersection point $\mathbf{f}_{trk}$ of the track with the module plane, as sketched in Figure 3.6. A residual for measurement direction ξ is thus defined as:

$$R_\xi(\mathbf{p},\mathbf{q}) = m_{\xi,hit} - f_{\xi,tk}(\mathbf{p},\mathbf{q}) \tag{3.3}$$

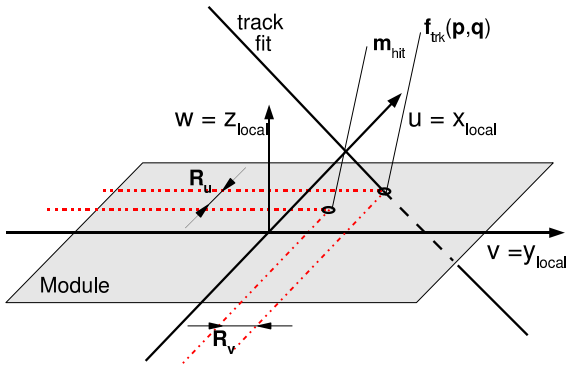

Figure 3.6: *The definition of a track-hit residual R_ξ in local x and local y direction. See text for details.*

The track-to-hit residuals $\mathbf{R}(\mathbf{p},\mathbf{q})$, are either 1- or 2-dimensional vectors according to the kind of module (e.g. for pixel modules they are bi-dimensional). Usually for tracking and alignment purposes there are two different ways of computing the residuals: "biased" and "unbiased" residuals.

- Biased residual: The track fit is performed with all the available hits which belong to the track, including the hit of the residual measurement under investigation.
- Unbiased residual: the reconstructed track does not include the data point under test (i.e. the hit on the surface where the residual is being calculated). This means that to calculate every unbiased residual on each measuring surface the track has to be refit every time removing the hit under test. Thus, computing time for unbiased residuals is larger than for biased residuals.

After considering these issues, it is worth to say that for the alignment algorithms illustrated in this thesis the biased definition of residuals is used, while for validation purposes the unbiased residual definition is preferred.

The unbiased residuals in the context of the alignment validation of the CMS Tracker are calculated by taking the distance along the sensitive coordinate between the measured hit position and the extrapolation to the sensor surface of the combined state trajectory, which is a combination of the forward predicted state (FP) and backward predicted state (BP) the parameters of the trajectory at the module surface (see Figure 3.7):

$$\mathbf{q}_{comb} = \mathbf{q}_{FP} + \frac{\mathbf{C}_{FP}}{(\mathbf{C}_{BP}+\mathbf{C}_{FP})}(\mathbf{q}_{BP}-\mathbf{q}_{FP}) \tag{3.4}$$

where the $\mathbf{q}_i$ are the track state vectors at the module surface and the $\mathbf{C}_i$ the covariance matrices.

The coordinates used to compute the residuals can either be in local form to be specifically targeted to the module geometry or in the global form, to take into account the position and orientation of the module. *Local*, here, means for individual silicon module, while *global* means related the whole Tracker. In CMS the local coordinate systems $(u'|v')$ and $(u|v)$ and the global $(r|r\phi|z)$ are used, as discussed below. The two-dimensional local coordinates are defined in a plane parallel to the module surface assumed flat.

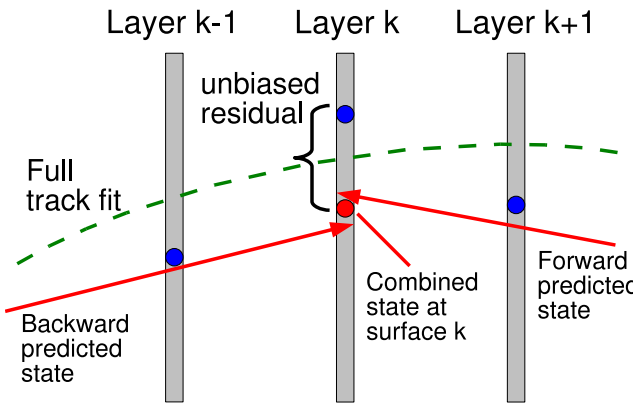

Figure 3.7: *Sketch of how track-to-hit unbiased residuals are calculated.*

The $(u|v)$ local coordinate system

In the Strip Tracker the native coordinate system $(u|v)$ is defined by the module layout and the connection of the readout electronics; the positive v-direction points from the electronics to the sensor along the strip positions, the w-direction points from the strip backplane to the strip plane and the u-direction is perpendicular to them to form a right-handed rectangular cartesian coordinate system. The global orientation of this local coordinates are mixed. The alignment constants are stored as the global module positions, which define to the local coordinate origin, and global orientations of the local coordinate axes. The values of track prediction and of the hits and their errors are given in these local coordinate system:

$$\mathbf{m}_{hit} = \begin{pmatrix} u_{hit} \\ v_{hit} \end{pmatrix}; \quad \mathbf{f}_{tk}(\mathbf{p},\mathbf{q}) = \begin{pmatrix} u_{tk}(\mathbf{p},\mathbf{q}) \\ u_{tk}(\mathbf{p},\mathbf{q}) \end{pmatrix} \tag{3.5}$$

The residuals calculated in this coordinate system are:

$$\begin{aligned} R_u &= u_{hit} - u_{tk} \\ R_v &= v_{hit} - v_{tk} \end{aligned} \tag{3.6}$$

The errors computed under the assumption of uncorrelated coordinates according to the error propagation rule are:

$$\begin{aligned} \sigma^2_{R_u} &= \sigma^2_{u_{hit}} + \sigma^2_{u_{tk}} \\ \sigma^2_{R_v} &= \sigma^2_{v_{hit}} + \sigma^2_{v_{tk}} \end{aligned} \tag{3.7}$$

The $(r|r\phi|z)$ global coordinate system

The global coordinate system $(r|r\phi|z)$ is the cylindric coordinate system of the CMS experiment. The origin is located centrally on the nominal interaction point of the LHC inside the experiment, which roughly corresponds to the center of gravity of the Tracker, the z-axis points along of the beam, the r-direction is directed radially to the outside and the rϕ-direction is the direction perpendicular to the azimuth angle. The values $\phi = 0°$ and $\phi = 180°$ are on the horizontal plane. The transformation from local to global coordinates is done via the link to the local values of the module position and orientation on the basis of the alignment constants. The uncertainties are also transformed.
In this case one has to decide which radial direction use for the rϕ residual. The value for the hit r_{hit} is used:

$$\begin{aligned} R_r &= r_{hit} - r_{tk} \\ R_{r\phi} &= r_{hit} \cdot \Delta\phi \\ R_z &= z_{hit} - z_{tk} \end{aligned} \tag{3.8}$$

The angle difference must be calculated so that the smaller angular difference is considered and it lies in the interval $(-\pi, +\pi]$.

$$\Delta\phi = \phi_{hit} - \phi_{tk} + 2\pi n \quad \text{with n} \in \mathbb{Z} \tag{3.9}$$

$$-\pi < \Delta\phi \leq +\pi \tag{3.10}$$

The errors again are calculated assuming uncorrelated coordinates using error propagation:

$$\begin{aligned} \sigma^2_{R_r} &= \sigma^2_{r_{hit}} + \sigma^2_{r_{tk}} \\ \sigma^2_{R_{r\phi}} &= \sigma^2_{r_{hit}} \cdot \Delta\phi^2 + r^2_{hit} \cdot (\sigma^2_{\phi_{hit}} + \sigma^2_{\phi_{tk}}) \\ \sigma^2_{R_z} &= \sigma^2_{z_{hit}} + \sigma^2_{z_{tk}} \end{aligned} \tag{3.11}$$

The $(u'|v')$ local coordinate system

To define the other local coordinate system $(u'|v')$ one has to take into account the orientation of local coordinates in the global system $(r|r\phi|z)$. To this end, three local points in $(u|v)$ defines the origin O $(0|0)$ and the points P_u $(1|0)$ and P_v $(0|1)$. These are means of the constant alignment in global score $(r|r\phi|z)$ converted. Now u is determined so that the positive u-direction is directed into the positive global rϕ-direction:

$$u' = \begin{cases} +u & \text{for } \phi_{P_u} - \phi_O \geq 0 \\ -u & \text{for } \phi_{P_u} - \phi_O \leq 0 \end{cases} \tag{3.12}$$

The positive v'-direction is considered separately for different subdetectors. In the central detectors TIB and TOB v' is oriented in the positive global z-direction in the forward area in TID and TEC in positive r-direction:

$$v' = \begin{cases} +v & \text{for } z_{P_v} - z_O \geq 0 \\ -v & \text{for } z_{P_v} - z_O \leq 0 \end{cases} \text{ in TIB/TOB}$$
$$\begin{cases} +v & \text{for } r_{P_v} - r_O \geq 0 \\ -v & \text{for } r_{P_v} - r_O \leq 0 \end{cases} \text{ in TID/TEC} \tag{3.13}$$

A consequence of this is that the residuals change sign when the local direction is opposite to the global direction of the mesasurement:

$$R_{u'} = \begin{cases} +R_u & \text{for } u' = +u \\ -R_u & \text{for } u' = -u \end{cases} \tag{3.14}$$

$$R_{v'} = \begin{cases} +R_v & \text{for } v' = +v \\ -R_v & \text{for } v' = -v \end{cases} \tag{3.15}$$

The errors of course are unaffected:

$$\begin{array}{ll} \sigma^2_{R_{v'}} & = \sigma^2_{R_v} \\ \sigma^2_{R_{v'}} & = \sigma^2_{R_v} \end{array} \tag{3.16}$$

Through the hierarchies in the mechanical design or location-based selection arrangement, it makes sense to study together residuals of groups of related modules. For example, the residuals distributions of all modules in the subdetectors can be summed up in layers. This allows to draw conclusions on the displacements of all positions relative to each other. Alignment accuracy of a sub-detector can be determined from the residuals of all modules of the sub-detector together.

3.3.2 Pull definition

Dividing the residual by the standard deviation of the residuals, σ_R, (not of the data point, i.e. not of the hit), it is possible get a "normalized residual": $\widehat{R} = R/\sigma_R$. However, its definition depends on which type of residuals is being considered since:

$$\begin{array}{rl} \text{Biased residual} & \sigma^2_R = \sigma^2_{fit} - \sigma^2_{hit} \\ \text{Unbiased residual} & \sigma^2_R = \sigma^2_{fit} + \sigma^2_{hit} \end{array} \tag{3.17}$$

where σ_{fit} is the standard deviation of the track fit at the coordinate of the data point, calculated by error propagation using the full fitted parameter covariance matrix. In the case of biased residuals, the σ^2_{hit} must be subtracted from σ^2_{fit} to avoid double counting as the hit has been already included in the fit. Whilst for the unbiased residuals, the errors are a straight combination of the both quantities entering in the calculation: the measurements and the extrapolations.

The normalized residuals should follow the normal distribution with null mean and unit standard deviation (referred as $N(0,1)^2$) and this should be valid for all data points.

In practice the value of the normalized residuals are influenced by the quality of the measured value itself but also by all other data points and by the position of the data point within the set of all data points. For example, in a linear model fit, the normalized residual evaluated using the "biased" definition will have a standard deviation slightly smaller than one, since the errors are overstimated, having included the errors associated to the data point under evaluation twice, one time for the fit and the other one for the point itself. This effect is worse for a low number of data points (see Figure 3.8) leading to large underestimation of the standard deviation. Instead, normalized residuals evaluated using the "unbiased" definition will have a standard deviation slightly above one, because of an error understimation, having neglected the error associated to the measured point.

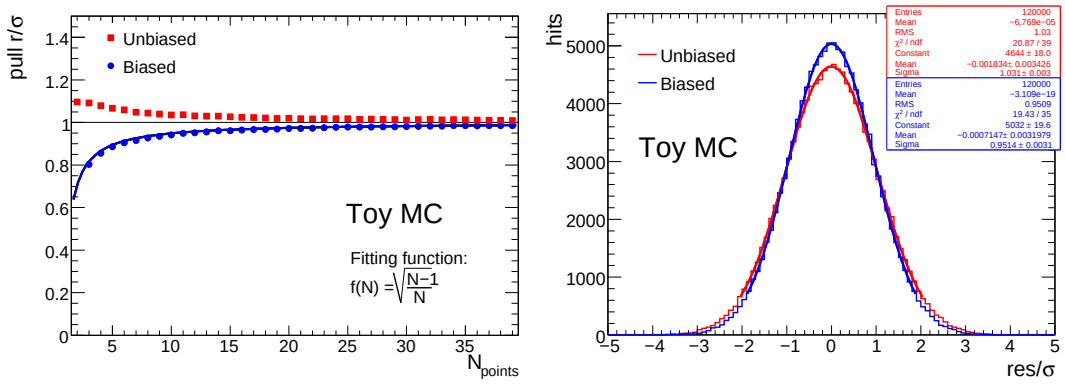

Figure 3.8: *Left: Distribution of the trend of the pull as a funcion of the number of measurments in a simple toy MC considering a straight line fit. Right, the pulls for the same toy MC using twelve measurements, a typical number for a track in CMS.*

The pull, which is the observable having the true statistical significance, is defined as the RMS of the distribution of normalized residuals:

$$pull = RMS\left(\frac{R}{\sigma_R}\right) \tag{3.18}$$

Any deviation from unity can be due to: a bias in the data (in all data points or only in a single point), a wrongly assigned standard deviation, a wrong track model, etc. i.e. the pull helps with the systematic error hunt.

[2]The normal distribution or Gaussian distribution is a bell-shaped and continuous probability distribution with a peak at its mean. It is denoted as N(μ,σ^2) where μ represents its mean or average value and σ^2 its variance.

3.3.3 Track based alignment formalism

The fundamental basis for all track-based alignment algorithms is an adapted track model[3] $\mathbf{f}(\mathbf{q},\mathbf{p})$, where the measurements $\mathbf{m}$ (hits) depend not only on the true track-parameters $\mathbf{q}$ but also on a set of alignment parameters $\mathbf{p}$ that describe the effects of sufficiently small deviations from the ideal geometry:

$$\mathbf{m} = \mathbf{f}(\mathbf{q},\mathbf{p}) + \epsilon \quad cov(\epsilon) = \mathbf{V} \tag{3.19}$$

The stochastic term ϵ, which describes the intrinsic resolution of the tracking devices and the effects of multiple scattering, is dealt with via its covariance matrix $\mathbf{V}$. Since typically high momentum particles are used, any energy-loss effects can be assumed to be deterministic and therefore directly taken care of in the track model $\mathbf{f}$ itself.

With an initial guess $\mathbf{q_0}$ for the track parameters and $\mathbf{p_0}$ for the alignment parameters, this model allows to define track-to-hit residuals, that are functions of the unknowns $\mathbf{q}$ and $\mathbf{p}$:

$$\mathbf{R}(\mathbf{q},\mathbf{p}) = \mathbf{m} - \mathbf{f}(\mathbf{q},\mathbf{p}) \simeq \mathbf{f}_0 - D_q\Delta\mathbf{q} - D_p\Delta\mathbf{p} \tag{3.20}$$

with the following definitions:

$$\mathbf{f}_0 = \mathbf{f}(\mathbf{q_0},\mathbf{p_0}), \quad \Delta\mathbf{q} = \mathbf{q} - \mathbf{q}_0, \quad \Delta\mathbf{p} = \mathbf{p} - \mathbf{p}_0 \tag{3.21}$$

$$D_q = \left.\frac{\partial\mathbf{f}}{\partial\mathbf{q}}\right|_{(\mathbf{q_0},\mathbf{p_0})}, \quad D_p = \left.\frac{\partial\mathbf{f}}{\partial\mathbf{p}}\right|_{(\mathbf{q_0},\mathbf{p_0})} \tag{3.22}$$

The goal of every track-based alignment algorithm is to determine the modules positions and orientations $\mathbf{p}$ from the minization of track-to-hit residuals $\mathbf{R}(\mathbf{q},\mathbf{p})$ on a sufficiently large set of reconstructed charged particle trajectories.
The alignment using tracks is what allows to reduce the module position uncertainty to the level of few microns.

Assuming a perfectly aligned detector, each trajectory is built from charge deposits on individual detectors, the hit, and assuming a helical track model which incorporates effects from multiple scattering and energy loss (see Section 2.5.4). Recorded measurements $\mathbf{m}_{ij}$ of the i^{th}-hit can be compared to the prediction, denoted with $\mathbf{f}_{ij}(\mathbf{p},\mathbf{q})$, of the point where the j^{th}-track crosses the module (impact point), according the track model. The predicted impact point measurement $\mathbf{f}_{ij}(\mathbf{p},\mathbf{q}_j)$ of the j^{th} - track depends on the track parameter $\mathbf{q}_j$ and module position corrections or alignment parameters $\mathbf{p}$.

Ideally all measured points of this trajectory have normal distributed residuals within a width of the nominal detector resolution. Therefore the normalized residual $\widehat{\mathbf{R}}_{ij}$ between the predicted hit position and the recorded measurement of i^{th} - hit can be written as:

[3] In the following section to avoid a too heavy notations the subscript in $\mathbf{f}_{tk}$ and $\mathbf{m}_{hit}$ used in Equation 3.3 will be dropped.

$$\widehat{\mathbf{R}}_{ij} = \frac{\mathbf{R}_{ij}}{\sigma_{ij}} = \frac{\mathbf{m}_{ij} - \mathbf{f}_{ij}(\mathbf{p}, \mathbf{q})}{\sigma_{ij}} \tag{3.23}$$

where σ_{ij} are the uncertainty of the mesurements. Since a real detector has a finite resolution defined by properties of the sensing device itself and by physical effects, like multiple scattering of particles crossing the matter, the values of σ_{ij} are non-zero and therefore calculable.

In the reality the detector is misaligned: the measured point along a trajectory differs by how much the position of the module is shifted away from its ideal position. The residual will be higher than in the ideal case, while detector resolution does not change. The basic idea is to re-adjust the positions of all the modules, by minimizing the sum of the normalized residuals of Equation 3.23. This sum is called objective function $\Omega(\mathbf{p}, \mathbf{q})$:

$$\Omega(\mathbf{p}, \mathbf{q}) = \sum_{j}^{tracks} \sum_{i}^{hits} \frac{(\mathbf{m}_{ij} - \mathbf{f}_{ij}(\mathbf{p}, \mathbf{q}))^2}{\sigma_{ij}^2} \tag{3.24}$$

and is expressed as the sum over all hits i on all tracks j and track parameters $\mathbf{q}_j$, assuming negligible correlations between hits. As this sum is weighted by the errors, it behaves as a χ^2 variable, under the assumption that residuals are gaussian distributed.

During nominal LHC operations the ideal datasets for alignment are long, almost straight muon tracks from $W^{\pm} \rightarrow \mu^{\pm}\nu$ and $Z \rightarrow \mu^{-}\mu^{+}$ events, since due to the high momentum they exprerience small multiple Coulomb scattering effects and produce several good hits for alignment, and do not interact hadronically with the material. Furthermore the Z mass constraint can be exploited not only to correlate the detector parts that are not crossed by a single collision track, e.g. the two endcaps, but also to tightly constrain the momentum scale of muon tracks. The invariant mass constraint could also be applied to any quarkonia resonance, like $J/\psi \rightarrow \mu^{-}\mu^{+}$ process, but in this case the muons have in general low momentum and this requires, due to multiple scattering effects, a special selection in order to exploit them as input for alignment. Apart from isolated muon tracks, well-measured tracks from minimum bias events, especially during the first data-taking period when the machine luminosity was very low, have been used, since they represented the only source of tracks for alignment. Finally, muons from cosmic rays represent a valuable input for alignment, especially during the commissioning phase, and the strategy and the level of precision that can be obtained from this topology of track will be widely discussed in the Chapter 4. Moreover all beam halo muons and cosmic ray tracks collected during collisions can become useful in the reduction of weak modes.

3.4 Alignment Algorithms

In the case of the CMS Tracker, with its approximately 15 000 individual modules, an amount of roughly 10^5 alignment parameters are needed for a complete description of the geometry. In this case the computation of the parameters using straightforward

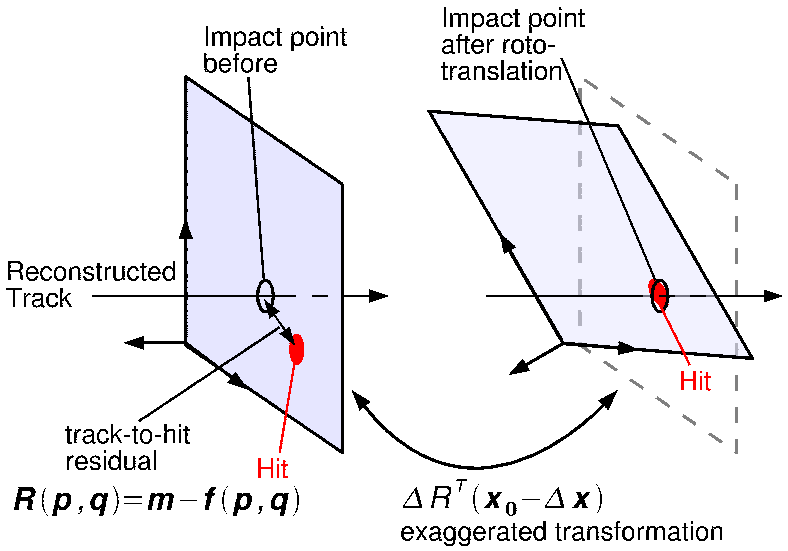

Figure 3.9: *Principle of alignment.* $\Delta\mathbf{R}$ *and* $\Delta\mathbf{x}$ *signify the alignment corrections, rotations and translations, to the position of the detector unit* $\mathbf{x}$*. Transformation changes the local (detector) coordinates of the impact point.*

recipes becomes unreasonably slow and even causes numerical instabilities. The two algorithms presented below, which are rather different examples of how to cope with such challenging circumstances, have therefore been implemented within the CMS software framework. Both of them were tested and widely employed for the Tracker alignment during the stand-alone commissioning, at CMS Global runs with cosmic data taking and during collision data-taking. Since angular corrections are small, the linearization in the alignment parameters ($\Delta\mathbf{p} = \mathbf{p} - \mathbf{p}_0$) of the Equation 3.24 is a good approximation and will be used by algorithms as a starting approach for solving large system of equations. Since the outputs from these two algorithms are independent from each other, this allows to conduct an additional validation.

3.4.1 The HIP Alignment Algorithm

The HIP algorithm [39] (for Hits and Impact Points) is a straight forward and easy to implement alignment algorithm, that computes the alignment parameters for each alignable object separately. Only when iterating over the track sample an indirect feedback between the alignable objects is established due to the track refit.

Since only individual alignable objects are involved, equation 3.20 can be factorized by evaluating the corresponding expressions for each alignable object i together with its associated parameters $\mathbf{p}_i$:

$$\mathbf{R}_i(\mathbf{p},\mathbf{q}) = \mathbf{m}_i - \mathbf{f_i}(\mathbf{q}_0,\mathbf{p}_i) \simeq \mathbf{m}_i - \mathbf{f_{i,0}} - D_{p,i}\Delta\mathbf{p}_i \tag{3.25}$$

having defined:

$$\mathbf{f}_{0,i} = \mathbf{f_i}(\mathbf{q_0},\mathbf{p}_{0,i}), \quad \Delta\mathbf{p_i} = \mathbf{p_i} - \mathbf{p}_{0,i}, \quad D_{p,i} = \left.\frac{\partial \mathbf{f_i}}{\partial \mathbf{p_i}}\right|_{(\mathbf{q_0},\mathbf{p_{0,i}})} \tag{3.26}$$

The result is then determined by minimizing the normalized squared residuals from a given set of tracks, again for each alignable object separately. The formal solution is then given by:

$$\mathbf{\Delta p_i} = \left(\sum_{tracks} D_{p,i}^T V_i D_{p,i} \right)^{-1} \left(\sum_{tracks} D_{p,i}^T V_i \mathbf{R}_i(\mathbf{p_i}) \right) \tag{3.27}$$

where the Jacobian $D_{p,i}^T$ is defined as the derivative of the residual with respect to the sensor position parameters and can be found analitically in the small angle approximation. Correlations between different modules and effects on the track parameters are accounted for by iterating the minimisation process and by refitting the tracks with new alignment constants after each iteration.

As described in [40], the HIP algorithm allows also the inclusion of the survey measurements in the formalism of Equation 3.24. This leads to an additional term in the objective function to be minimized independently for each module m in a given iteration:

$$\chi^2(\mathbf{p}_m) = \sum_{j}^{hits} \mathbf{R}_j^T(\mathbf{p}_m) \mathbf{V}_j^{-1} \mathbf{R}_j(\mathbf{p}_m) + \sum_{k}^{surveys} \mathbf{R}_{*k}^T(\mathbf{p}_m) \mathbf{V}_{*k}^{-1} \mathbf{R}_{*k}(\mathbf{p}_m) \tag{3.28}$$

This allows to include survey information in a hierarchial pattern for each sub-detector. In the HIP approach the track residuals $\mathbf{R}_j(\mathbf{p}_m)$ do not have explicit dependence on track parameters and enter the sum over hits in a given module m. The six-dimensional survey residuals $\mathbf{R}_j$ are defined as the difference between the reference and the current sensor position. The survey measurement covariance matrix $\mathbf{V}_j$ reflects both the survey precision and additional uncertainties due to changes in the detector. These errors can be configured differently for different hierarchy levels and for the degrees of freedom that should be stable, such as the longitudinal direction in a barrel ladder, and those which may change more frequently. The HIP algorithm will be denoted in the following as *local* method.

3.4.2 The Millepede Alignment Algorithm

The Millepede algorithm and its features are described in [41]. It is an unbiased algorithm that minimizes the sum of the squared residuals of all tracks at once. To achieve this goal, a system of equations, equivalent to the formal solution of an ordinary least-sqares fit, is solved. However, to achieve this in a reasonable amount of time, only the solution for the alignment parameters is computed, while the computation of the improved track parameters is dropped. This is possible because of the special structure of the equations. Firstly, the coefficient matrix is symmetric and, mostly due to the independence of the single tracks, relatively sparse. Secondly, only the alignment parameters are common parameters for all track measurements, while the specific track parameters are only relevant for each corresponding track. Given reasonable starting values $\mathbf{p}_0$ and $\mathbf{q}_{j0}$, the track model prediction $\mathbf{f}_{ij}(\mathbf{p}, \mathbf{q}_j)$

in Equation 3.24 can be written, with the linear approximation, as:

$$\Omega(\mathbf{p},\mathbf{q}) = \sum_{i}^{tracks}\sum_{i}^{hits}\frac{1}{\sigma_{ij}^2}\left(\mathbf{m}_{ij} - \mathbf{f}_{ij}(\mathbf{p}_0,\mathbf{q}_{j0}) - \frac{\partial \mathbf{f}_{ij}}{\partial \mathbf{p}}\Delta\mathbf{p} - \frac{\partial \mathbf{f}_{ij}}{\partial \mathbf{q}_j}\Delta\mathbf{q}_j\right) \tag{3.29}$$

Applying the least squares method to minimize the χ^2 results in a large linear system with one equation for each alignment parameter and all the track parameters of each track. After having defined:

$$\begin{aligned}
(\Gamma)_{kl} &= \textstyle\sum_i \left(\frac{\partial \mathbf{f}_{ij}}{\partial \mathbf{q}_{jk}}\right)\left(\frac{\partial \mathbf{f}_{ij}}{\partial \mathbf{q}_{jl}}\right)\frac{1}{\sigma_{ij}^2} \qquad (G_j)_{kl} = \textstyle\sum_i \frac{\partial \mathbf{f}_{ij}}{\partial \mathbf{q}_{il}}\frac{\partial \mathbf{f}_{ij}}{\partial \mathbf{p}_{jk}}\frac{1}{\sigma_{ij}^2} \\
(C_j)_{kl} &= \textstyle\sum_i \left(\frac{\partial \mathbf{f}_{ij}}{\partial \mathbf{p}_{jk}}\right)\left(\frac{\partial \mathbf{f}_{ij}}{\partial \mathbf{p}_{jl}}\right)\frac{1}{\sigma_{ij}^2} \qquad (\beta_j)_k = \textstyle\sum_i \left(\frac{\partial \mathbf{f}_{ij}}{\partial \mathbf{q}_{jk}}\right)\frac{\mathbf{R}_{ij}}{\sigma_{ij}^2} \\
(b_j)_k &= \textstyle\sum_i \left(\frac{\partial \mathbf{f}_{ij}}{\partial \mathbf{p}_{jk}}\right)\frac{\mathbf{R}_{ij}}{\sigma_{ij}^2}
\end{aligned} \tag{3.30}$$

the matrix structure solving the system in Equation 3.29 appears the following:

$$\begin{pmatrix} \sum \mathbf{C}_j & \dots & \mathbf{G} & \dots \\ \vdots & \ddots & 0 & 0 \\ \mathbf{G}_j^T & 0 & \mathbf{\Gamma}_j & 0 \\ \vdots & 0 & 0 & \ddots \end{pmatrix} \cdot \begin{pmatrix} \delta\mathbf{p} \\ \vdots \\ \delta q_j \\ \vdots \end{pmatrix} = \begin{pmatrix} \sum \mathbf{b}_j \\ \vdots \\ \beta_j \\ \vdots \end{pmatrix} \tag{3.31}$$

The sub-matrices $\mathbf{\Gamma}_j$ include only derivatives with respect to the track parameters. The matrices $\mathbf{G}_j$ include derivatives with respct fo both $\mathbf{p}$ and $\mathbf{q}$ parameters. Only derivatives with respect to $\mathbf{p}$ parameters are found in the matrices C_j. Matrix b includes products of global derivatives and the normalized residuals. The particular structure of the system of equations allows a reduction of its size, leading to the matrix equation:

$$\mathbf{C}'\Delta\mathbf{p} = \mathbf{b}' \tag{3.32}$$

after defining $\mathbf{C}'$ and $\mathbf{b}'$ as follows:

$$\mathbf{C}' = \sum_i \mathbf{C}'_i - \sum_i \mathbf{G}_i\mathbf{\Gamma}_i^{-1}\mathbf{G}_i^T \qquad \mathbf{b}' = \sum_i \mathbf{b}'_i - \sum_i \mathbf{G}_i(\mathbf{\Gamma_i^{-1}}\beta_i) \tag{3.33}$$

Being interested only in the n alignment parameters, the problem is reduced to the solution of a matrix equation of size n in order to extract the vector elements $\Delta\mathbf{p}$ (aligment corrections) without loss of information. Depending on the size and the sparseness of the matrix, there are several methods implemented in Millepede for solving Equation 3.32. Millepede was successfully used in the first full CMS Tracker alignment study on simulated data [42]. The algorithm will be denoted in the following

as *global method*, to characterize its mathematical approach to the alignment problem solution.

3.5 Alignment Workflow

The CMS alignment workflow has to ensure that the prompt event reconstruction can apply alignment constants that are already updated for possible rapidly changing data taking conditions. Figure 3.10 shows the alignment data flow from its origin (CMS detector) to its end (final reconstruction at Tier-0).
Part of the data recorded by CMS and selected by the High Level Trigger described in Section 2.4 are used for alignment purposes. This includes data from special calibration and alignment events as it is the case for the Laser Alignment System, and collision events that are of interest both for alignment and physics analyses. These events are reconstructed with low latency ($\simeq$ 1-2 h) at the CMS Tier-0, and this step is called express reconstruction.

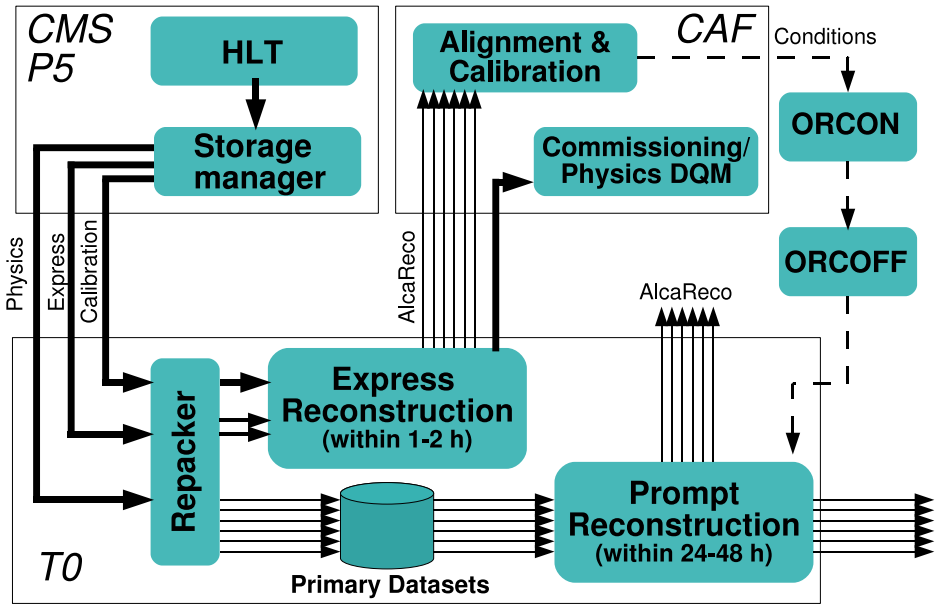

Figure 3.10: *The CMS Alignment data flow.*

A special reduced event format denoted as `AlCaReco` is stored to the CMS Analysis Facility (CAF), while all physics events are being stored in a large buffer for 24 hours. This format contains only the skimmed collections of objects needed for alignment and calibration processes. In addition some quality cuts to the track collection are included in order to select already at this level, good quality input for the alignment algorithms. Examples of these cuts for three different streams, cosmics, minimum bias and $Z \rightarrow \mu\mu$ events, is given in the Table 3.2. At the CAF, the reduced event data are input to the alignment procedure (LAS and track based alignment). Alignment parameters are then determined, validated and uploaded to the database (ORCON and ORCOFF). The CMS computing model foresees that at high luminosity calibration and alignment corrections can be produced in 24 hours and therefore used for the prompt reconstruction and production of the RECO or AOD (Analysis Object Data)[43] format of all physics events collected the day before.

A succesful test of this workflow has been performed during the CMS Software and Analysis Challenge in 2008 [44].

Table 3.2: *Criteria used for selection of events/tracks in different* `AlCaReco` *streams.*

Stream	η	p or p_T (GeV)	N_{hits}	others
`TkAlCosmics0T`	$\|\eta\| < 99.$	no cut	≥ 7	$N^{2D}_{hits} \geq 2$
`TkAlMinBias`	$\|\eta\| < 3.5$	$p >$1.5 $\wedge$ $p_T >$ 0.65	≥ 7	none
`TkAlJPsiMuMu`	$\|\eta\| < 3.5$	$p_T >$ 0.8	no cut	2.7 $< M_{\mu\mu} <$ 2.4 GeV GLB μ
`TkAlUpsilonMuMu`	$\|\eta\| < 3.5$	$p_T >$ 0.8	no cut	8.9 $< M_{\mu\mu} <$ 9.9 GeV GLB μ
`TkAlZMuMu`	$\|\eta\| < 3.5$	$p_T >$15	no cut	65 $< M_{\mu\mu} <$ 115 GeV GLB μ, μ ISO

Chapter 4

Tracker Alignment Validation

Truth is like a blanket that always leaves your feet
cold. You push it, stretch it, it'll never be enough.
Kick at it, beat it, it'll never cover any of us.
Dead Poets Society

Abstract

The validation of the alignment constants for the CMS Tracker obtained from alignment algorithms is a challenging a demanding task, because of the large number of independent alignables. A complete survey of the methods used to validate the alignment during both cosmic ray and collision data-taking will be presented.

Once a set of aligment constants is obtained a careful inspection of its performance is required. Several approaches can be used to validate the alignment results and those methods will be extensively described in this chapter. The really first quantities to be monitored are those that were used in the χ^2 minimization, such as track-to-hit residuals and the χ^2/ndf of the tracks. Then the tracking perfomance, the stability of the geometry and impact on physics observables have to be validated.

4.1 Results with Cosmic Ray Data

During Fall 2008 the CMS collaboration conducted a long-month data taking exercise known as the Cosmic Run at Four Tesla (CRAFT) with the goal of commissioning the detector before entering in the pp collision phase.

This was a unique opportunity for testing the CMS performance with all installed detector systems partecipating, with the goal of commissioning the solenoid magnet at its operating field, gaining experience operating CMS continuously for a month and finally checking the offline workflows stream and storage of the data. During this phase almost 270 million cosmic triggers were collected with all detector systems operating in the 3.8 T magnetic field with a L1 trigger rate of 600 Hz. Recorded events were processed by the offline data handling system, and then analyzed by teams dedicated to the calibration, alignment, and characterization of the detector subsystems.

As shown in Figure 4.1, most of the detector systems partecipated with more than 95% of their components switched on, and the detected inefficiency of read-out channels was mainly due to electronic failures or cabling issues which have been recovered during the subsequent shutdown period following the CRAFT operations. As CMS is located 100 m below the surface of the Earth, the cosmic muon rate relative to that at the surface is suppressed by approximately two orders of magnitude. The typical L1 trigger rate was 600 Hz, composed of about 300 Hz of cosmic triggers using all three muon systems, 200 Hz of low threshold triggers from the calorimeters, and 100 Hz of calibration triggers used to pulse the front-end electronics. This rate is well below the 100 kHz design limit for the central data acquisition system. Therefore, the cosmic muon triggers were more relaxed than those designed for collisions, with only loose requirements for the muon to point to the interaction region of the experiment.

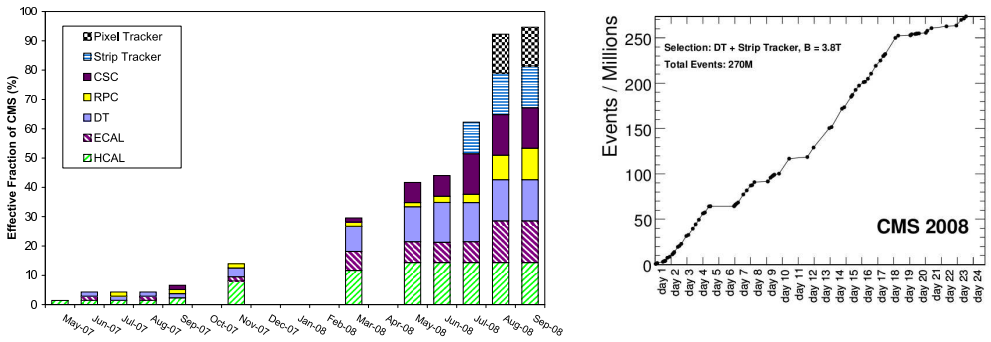

Figure 4.1: *Left: Effective fraction of the CMS experiment participating in the 2007 and 2008 global run campaigns as a function of time. The fraction of each of the seven major detector systems is represented by a bar. Only one RPC endcap was missing by September 2008 [46]. Right: The accumulated number cosmic ray triggered events with the magnet at 3.8 T as a function of days into CRAFT, beginning October 16, 2008.*

The rate of triggered cosmic muons crossing the Tracker region was about 6 Hz. The time-of-flight of cosmic muons to cross from the top to the bottom of the experiment was accounted for by introducing coarse delays of the muon trigger signals in the top half such that they are in rough coincidence with the bottom half: a two bunch crossing difference for the barrel, and one for the endcaps, where one bunch crossing corresponds to 25 ns.

A reconstructed event, a cosmic muon traversing the detector from top to bottom in the bending plane, detected by CMS is shown in Figure 4.2: muon chambers provide the trigger and particle identification while reconstruction and track parameters measurement are completed by adding the information of Tracker inner region and minimum ionizing deposits in the calorimeters.

The Tracker was active 95% of the running time during CRAFT, with 98% of the channels active. Due to the small cosmic muon rate, events with more than one track are rare. Since data of the Strip Tracker were zero suppressed during the entire exercise, only a tiny fraction of the Tracker channels are read out, leading to an average occupancy of 4×10^{-4} . The strip sensor signals were read out in peak mode, and the readout was synchronized to triggers delivered by the muon detectors. A few issues not identified during the previous commissioning of the detector, such as some

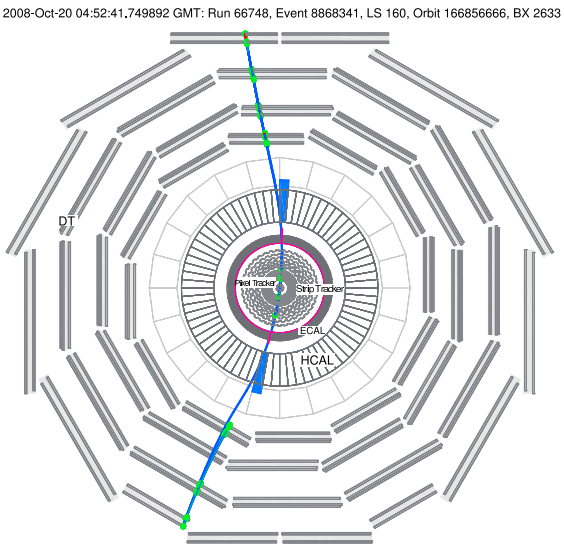

Figure 4.2: *Display of a cosmic muon recorded during CRAFT which enters and exits through the DT muon system, leaves measurable minimum ionizing deposits in the HCAL and ECAL, and crosses the silicon strip and pixel tracking systems. Reconstruction of the trajectory is also indicated [46]*

swapped cables and incorrect fibre length assumptions used in the latency calculations, were (quickly) identified by offline analysis of the cosmic data and corrected either during operation or the subsequent shutdown. The signal-to-noise ratio, which is a benchmark for the performance of the Tracker, was found to be in the range 25-30 for thin modules and 31-36 for thick ones, and within 5% from the expected values. The probability to find a cluster in a given silicon sensor that has been traversed by a charged particle (hit efficiency) has been measured as well, leading to values greater than 99% for most layers/disks.

A set of almost 4.5 million *AlCaReco* events from the `TkAlCosmicsOT` stream described in Section 3.5 have been used for the track based alignment of the Tracker [47]. On this available data set quality cuts both on hits and on tracks were applied in order to get a clean sample of tracks which can be directly used as input for the alignment algorithm minimization process (Table 4.1). The Alignment Position Errors (APE) used for the initial track reconstruction were large as they had to account for possible large displacements of the entire sub-detectors while still guaranteeing an efficient track-hit association. In the following those un-calibrated APEs will be referred to as "default", in constrast to the ones coming from the calibration procedure that will be described in Section 4.4. The CTF algorithm was used to reconstruct the cosmic muon trajectory. In total, about 3.2 million tracks were selected for alignment, out of which about 110 000 had at least one pixel hit.

According to the description of track model used in the reconstruction, the track assumes an helicoidal parametrization for its trajectory, characterized by a set of five parameters to be determined at the point of closest approach (PCA) to the nominal beamline. Two of them, the momentum and azimuthal angle spectra of cosmic muons, have been validated by a comparison with a detailed Monte Carlo simulation, requiring the same quality cuts: as shown in Figure 4.3, a very good agreement is observed.

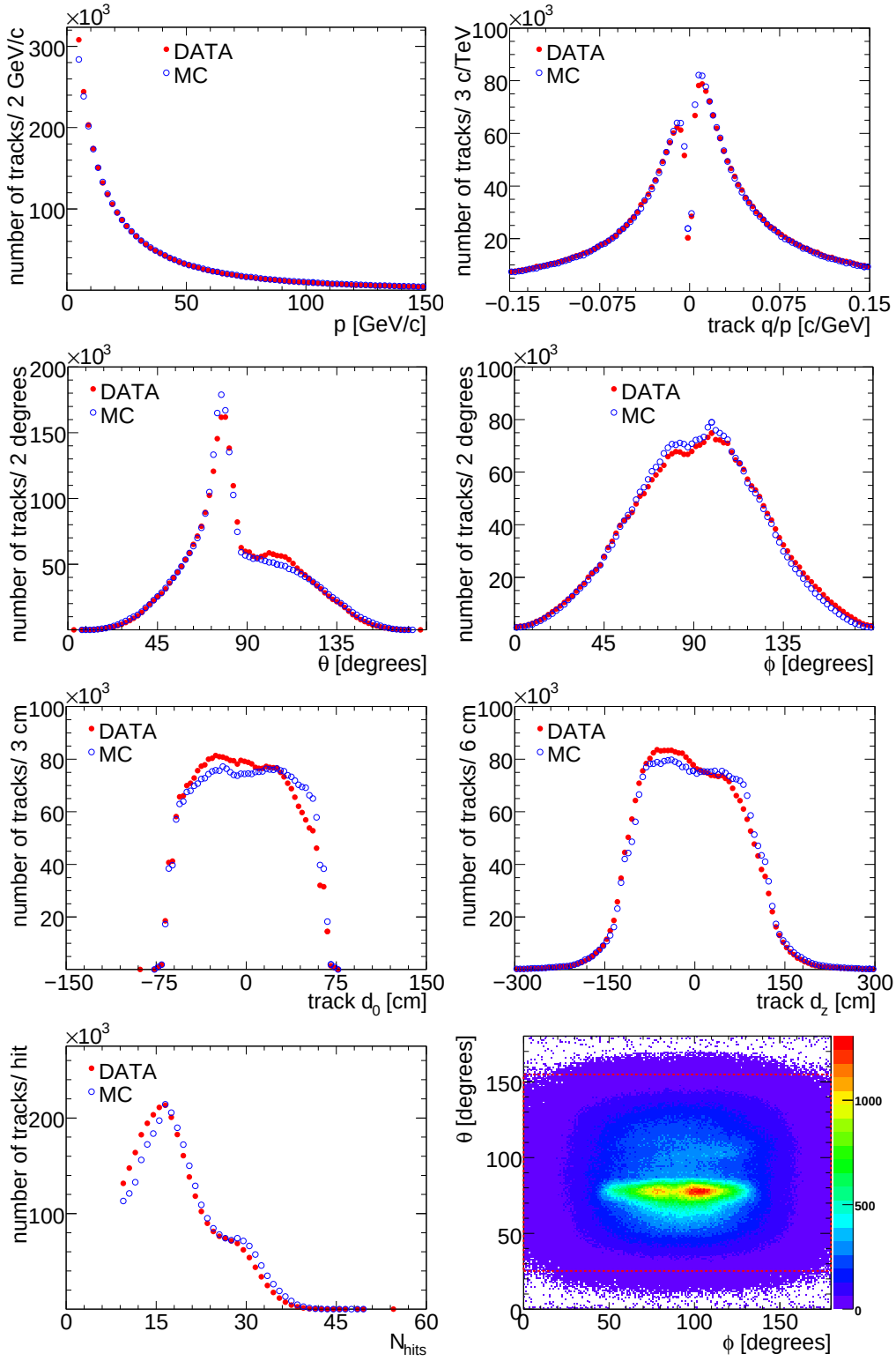

Figure 4.3: *Collection of basic track quantities used for Tracker alignment and validation during CRAFT. First row, track momentum p and q/p, in the secondo row the polar (θ) and azimuthal (ϕ) angles, in the third row transverse d_0 and longitudinal d_z impact parameters and finally in the last row the number of hits and a map in the $\theta - \phi$ plane showing how the track direction was strongly peaked in the $\theta = 90°$,$\phi = 90°$ region (high-lighted in red there is the acceptance of the Tracker Barrel). The solid (red) circles represent the cosmic ray data whereas the open (blue) circles come from a MC simulation.*

Track Quality cut	**Value**
momentum p	> 4 GeV
number of hits	≥ 8
number of 2-d hits (on Pixel or DS modules)	≥ 2
χ^2/ndf of the track fit	< 6.0
Hit Quality cut	**Value**
S/N (Strip modules)	> 12
pixel hit prob. matching template shape in u (v) dir.	> 0.001 (0.01)
track angle relative to the local uv plane	$< 20^\circ$
square pull of the hit residual	< 15

Table 4.1: *Quality cuts applied to hits and tracks used in the alignment at CRAFT.*

In this context, a different alignment strategy with respect to the one adopted during previous alignment exercises [38] was used, due to several factors present: the larger statistics available for the alignment; the presence of a magnetic field which allowed for a measurement of the transverse momentum; the presence of all the modules activated, which allowed the reconstruction of tracks crossing the entire Tracker volume.

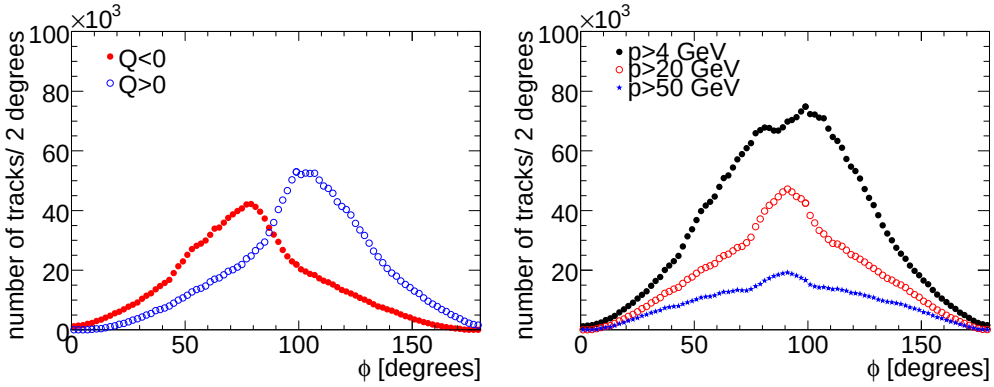

Figure 4.4: *Left: The shaft through which the CMS detector has been lowered in the construction phase induces different acceptance in ϕ for positive and negative cosmic ray muons. Right: this effect is mitigated for high momentum muons, since the extra contribution of muons coming through the shaft is numerically less important in that kinematical regime.*

4.1.1 Alignment Strategy

The statistics allowed for a separate alignment of the stereo and rϕ component of the double-sided modules, leading to a dramatic improvement in track residuals. Single-sided silicon strip modules can provide only a one-dimensional measurement in the module plane, along the local u-coordinate: the v-coordinate is only known to be within the module boundaries, with precision not sufficient for track reconstruction requirements. On the other hand, the information from the rϕ and stereo sensors in a double-sided module is combined into a two-dimensional measurement in the

combined module plane in both u and v for the pattern recognition phase. Due to the 100 mrad stereo angle between the rϕ and stereo sensors (see Figure 4.5), a small displacement in u is equivalent to a ten times larger displacement in v.

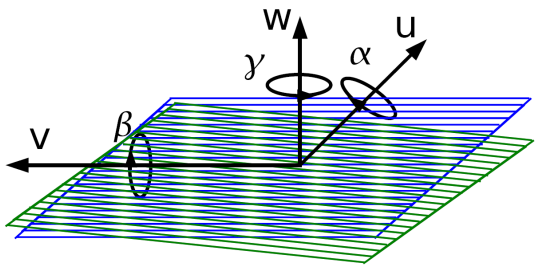

Figure 4.5: *Sketch of Tracker DS module: stereo module (green) is tilted of 100 mrad with respect to the rϕ component (blue).*

Given comparable mounting precision of modules in u and v, it was found from the data after several attempts of alignment of double-sided modules in v, that parameters obtained were much larger than the known assembly accuracy. After an alignment with the global method along both u and v of double-sided modules, the values of the alignment corrections, calculated from design geometry of the modules inside the supporting frame, were compared with the survey measurements. In the u coordinate the agreement between what recorded by survey and the shifts found by the algorithm were comparable, while along the longitudinal v they were one order of magnitude larger than known assembly accuracy. This was interpreted as un-physical corrections found by the algorithm. Following this test, the two single-sided modules of a double-sided one were aligned separately, but only in the most precise coordinates (u).
These consistency checks are extremely important for the alignment procedure: a tight control of the aligned degrees of freedom should be performed and, in case some final values are found to be not physically acceptable, is preferred to keep them as their nominal positions. An internal constraint would be the inclusion of survey measurements in the alignment procedure itself, but at the time of CRAFT alignment this feature had been implemented and used for the local algorithm only. Furthermore, the requirement of aligning the full Tracker needs a correct handling of the hierarchical structures when they are aligned together. These two requirements (separate alignment of rϕ and stereo component of double sided modules and description of highly correlated displacements of all modules in a higher level structure) led to multi-step strategies for the alignment algorithms.

Two statistical methods, *global* (Millepede) and *local* (HIP), were first run independently to solve the alignment problem, but the best results were obtained by applying the two algorithms in sequence, first global and then local, in order to take advantage of their complementary strength [1].

This combination was found to provide the best results in terms of minimization of residuals: the main effect of global method is to solve the global correlations, while local method makes use of the same track fit used in the standard CMS reconstruction and exploit the additional informations coming from survey, which can be easily

[1] Details about the strategy adopted separately by the method separately can be found in Reference [47]

incorporated, allowing for alignment with more degrees of freedom. This approach will be referred to as *combined* method in the following.

In the alignment with the global method, the detector design geometry was chosen as a starting point. In the first step the highest level structures (half-barrels, endcaps) with all six degrees of freedom together with all module units, including rϕ and stereo strip modules in a double-sided module, with the most sensitive degrees of freedom each (u, w,γ, and for pixel modules also v) were aligned. The alignment of the bigger structures is essential to easily spot possible large movements of the whole structure due to mechanical stresses or thermal effects. It was also observed that the highest level structures alignment, half barrels, together with the lowest ones, module units, introduced a strong internal correlation between structures, preventing systematic expansions and distorsions to occur which otherwise would appear in the geometry, particularly in the endcap region. In the second step all modules, all double-sided or single-sided strip modules with more than 150 hits and all pixel modules with more than 25 hits, were aligned in the TIB in u, w, α, β, γ; in the pixel system in u, v, w, γ; and in u, w, γ elsewhere. The third step was designed to recover lost correlations between the first two steps and had the same configuration as the first step, but the minimum number of hits in the strip modules was increased to 450 with respect to 425 used in the first step. The main improvement occurs between the first and the second step, while the third one is performed mainly to check the correct positioning along u of the individual components of the double-sided modules after the alignment of the whole double-sided structure along its v, performed in the second step.

The final alignment parameters were determined starting from the output of the global method analysis, then further aligning the Tracker with the local method strategy. In the first step of the local method (30 iterations), all strip modules, treating double-sided modules as rigid bodies, were aligned in six degrees of freedom using track and survey information. In the second step (20 iterations), the strip module units, treating rϕ and stereo strip modules in a double-sided module independently, were aligned in three degrees of freedom (u,w, γ). Pixel modules were not aligned in the first two steps, although pixel hits were included in the track fit. Finally in the last step (20 iterations), the pixel modules were aligned in six degrees of freedom. Modules for which the fit did not converge were left at the position found by the global algorithm.

4.2 Track fit quality and hit residuals

The resulting geometries after the alignment procedure were applied in the track reconstruction, using the selection of tracks described in Section 4.1. Due to the limited statistics the same track sample was used both for alignment and validation. All the tracks were refit with APE calibrated by tuning procedure (Section 4.4) using the parameters obtained after alignment with the combined method. The track χ^2/ndf distribution is shown in the left part of Figure 4.6.

For validation purposes a Monte Carlo simulation is performed in order to disentangle the statistical precision of track based alignment from other random effects which can occur. To model the situation of no alignment present in data at beginning of

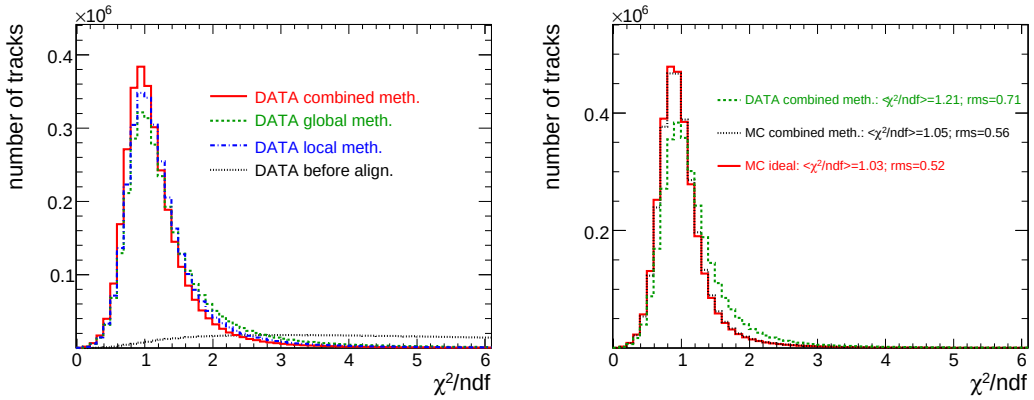

Figure 4.6: *Right: Track χ^2/ndf distributions for non-aligned (dotted line), local method (dashed-dotted line), global method (dashed line), and combined method (solid line) geometries. Right:Track χ^2/ndf distributions for Ideal alignment Monte Carlo (red solid line), combined method approach on misaligned Monte Carlo (dashed-dotted black line), combined method on data (green dashed line) geometries.*

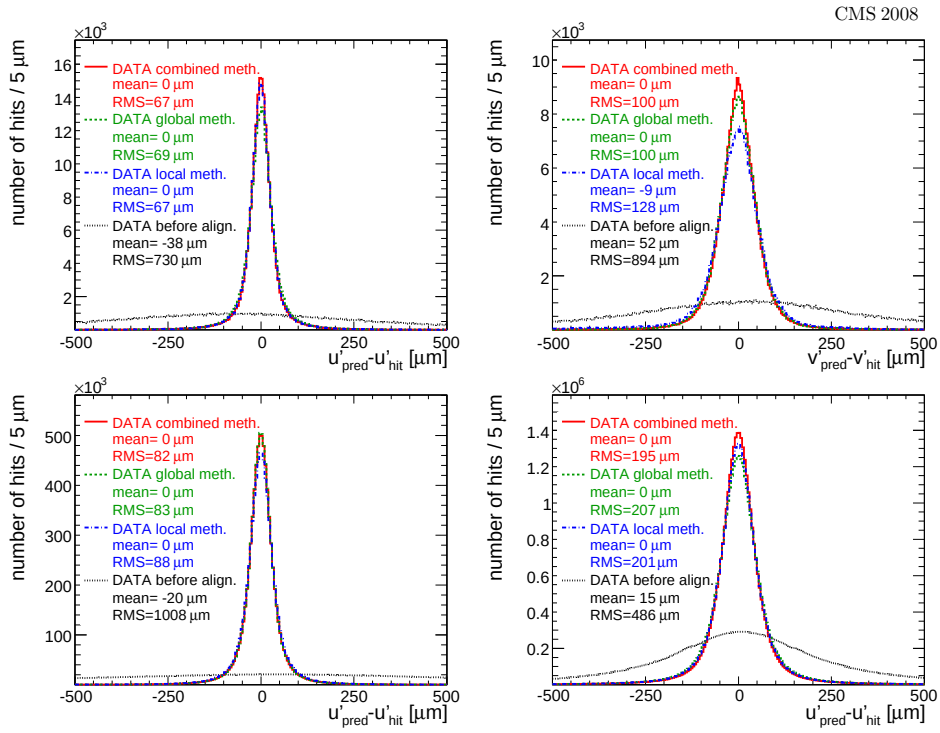

Figure 4.7: *Track residuals, shown for BPIX (top left u' , top right v'), TIB (bottom left), and TOB (bottom right). The four lines correspond to positions before alignment (dotted lines) and after alignment with the global (dashed lines), local (dot-dashed lines), and combined methods (solid lines).*

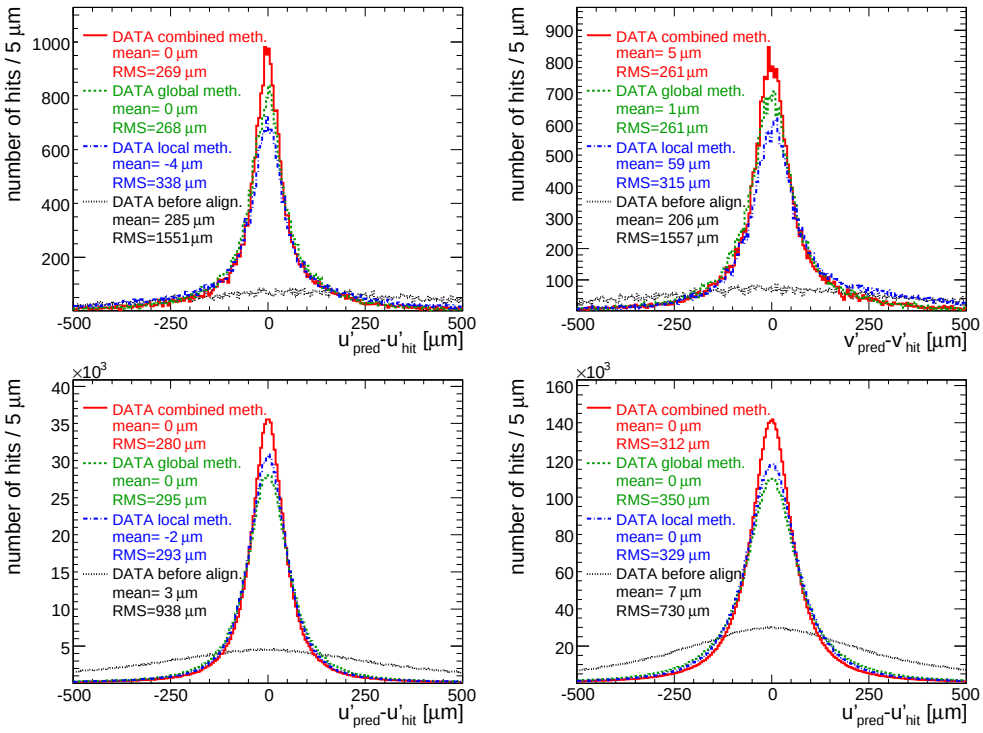

Figure 4.8: *Track residuals, shown for FPIX (top left u' , top right v'), TID (bottom left), and TEC (bottom right). The four lines correspond to positions before alignment (dotted lines) and after alignment with the global (dashed lines), local (dot-dashed lines), and combined methods (solid lines).*

CRAFT, a sample of a 3.5 million events was generated using ideal geometry and then reconstructed applying the module positions from combined method and survey values only for degrees of freedom not aligned in data. On this scenario an alignment using the same strategy (combined method) used in data is performed, providing indication of the remaining statistical uncertainties left by the alignment procedure. The geometry obtained with this procedure is called "Startup" scenario. Comparison of the track fit quality between data and MC is presented in right part of Figure 4.6.

The track-to-hit residuals in the u' and v' directions, calculated as described in Section 3.3.1 are shown in Figures 4.7 and 4.8 for the subdetectors in the barrel region. The improvement after alignment is evident if compared with non-aligned geometry. The local and global algorithms provide similar results in each subdetector, with the best performance in terms of residual minimization given by the combined method.

4.2.1 Measurement of the alignment precision

The validation using track-to-hit residuals and χ^2/ndf of tracks provides a reliable check whether the minimization process has properly worked, but cannot be used to determine accurately the remaining misalignment of the modules, since many other effects determine the spread of the distribution of residuals. The width of the residuals denoted here as σ_R is dominated by two effects other than alignment: track extrapolation uncertainties due to multiple scattering and hit position reconstruction uncertainties:

$$\sigma_R = \sigma_{tk}(p) \oplus \sigma_{hit} \oplus \sigma_{misalignment} \tag{4.1}$$

These effects are both random, while remaining misalignment produces systematic biases. If the procedure works properly, the distribution of the residuals in each module after alignment should be centered at zero.

Several estimators of the "central" value of the residual distribution could be used but it has to fulfill two severe constraints:

- to be robust since it should be resilient to outliers, representing entries of the distribution very far away from its core, mostly due to spurious effects, other than alignment, such as bad local hit reconstruction or inclusion of noise hits;
- to be of easy implementation since the algorithm calculating it has to be run for more than sixteen thousand times, one for each module of the CMS Tracker, and the full procedure has to be repeated rapidly on a regular basis to check the state of improvement of alignment conditions.

Several estimators have been evaluated both on data from cosmic muon events, and on detailed Monte Carlo simulation of the detector:

- the arithmetic mean of the distribution $\langle \mathrm{R} \rangle$
- the mean of a gaussian fit performed in two steps: first fitting the range between $\pm$ 2 RMS of the residual distribution and then re-fitting in $\pm$ 3σ around the mean of a previous fit;
- the "truncated mean" i.e. the mean value of a distribution obtained excluding 5% of the entries farthest away from zero;
- the median $\mu_{1/2}$ defined such that it separates the higher half of the residual distribution, from the lower half:

$$\int_{-\infty}^{\mu_{1/2}} f(R)dR = \int_{\mu_{1/2}}^{+\infty} f(R)dR$$

The comparison of the different estimators was done on a sample of one million of cosmic tracks recorded during the CRAFT data-taking and refit with the Tracker geometry obtained from the *combined* alignment.

Figure 4.9 shows that the distribution of the median of residuals is considerably narrower than those of the other estimators [2]. The correlation between the mean and the median of each module in Figure 4.10, a clear correlation is visible, but for several modules the calculated median is much smaller than the arithmetic mean (see Appendix A). By inspecting the distribution of the residuals of some of those modules, which all had rather few hits, it turned out that the mean value was strongly biased

[2] Since the median of the histogram is calculated by taking the center of the bin which divides the population of the histogram in two parts having the same number of entries, the precision of the estimator cannot be higher than the bin width of the original histogram, in this case 2.5 μm

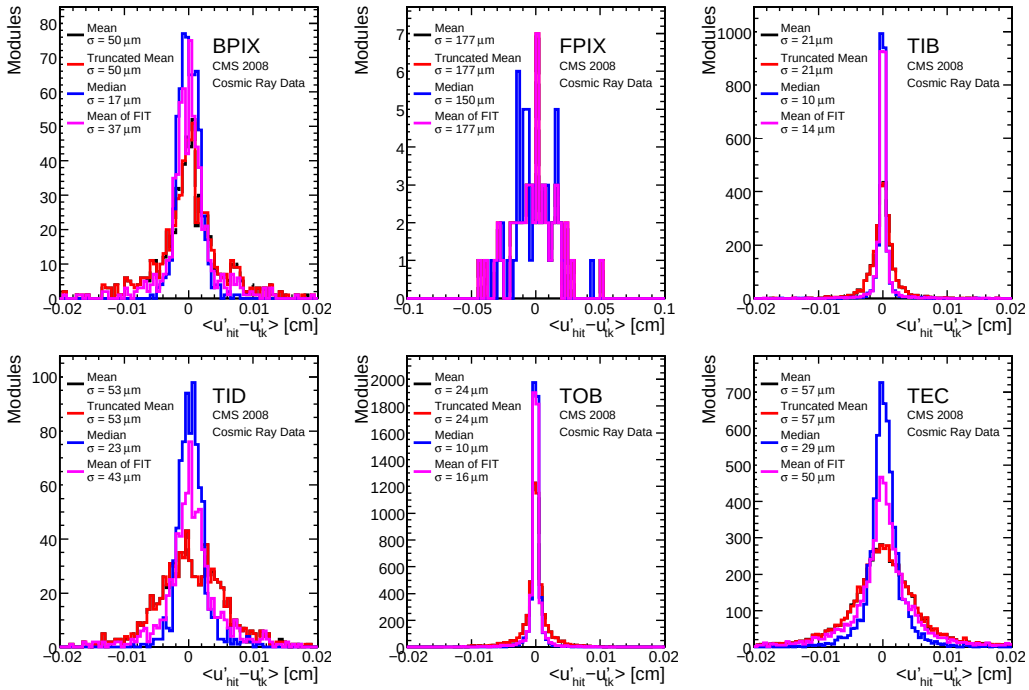

Figure 4.9: *Comparison of different estimators of residual misaligment in u' coordinate for cosmic muon data, for the six Tracker subdetector. Only modules with at least 30 hits have been considered. Black line is the mean of the residual distribution, blue the median, pink the mean value of a gaussian fit and red truncated mean (see text). Each entry of the histogram represents a Tracker module.*

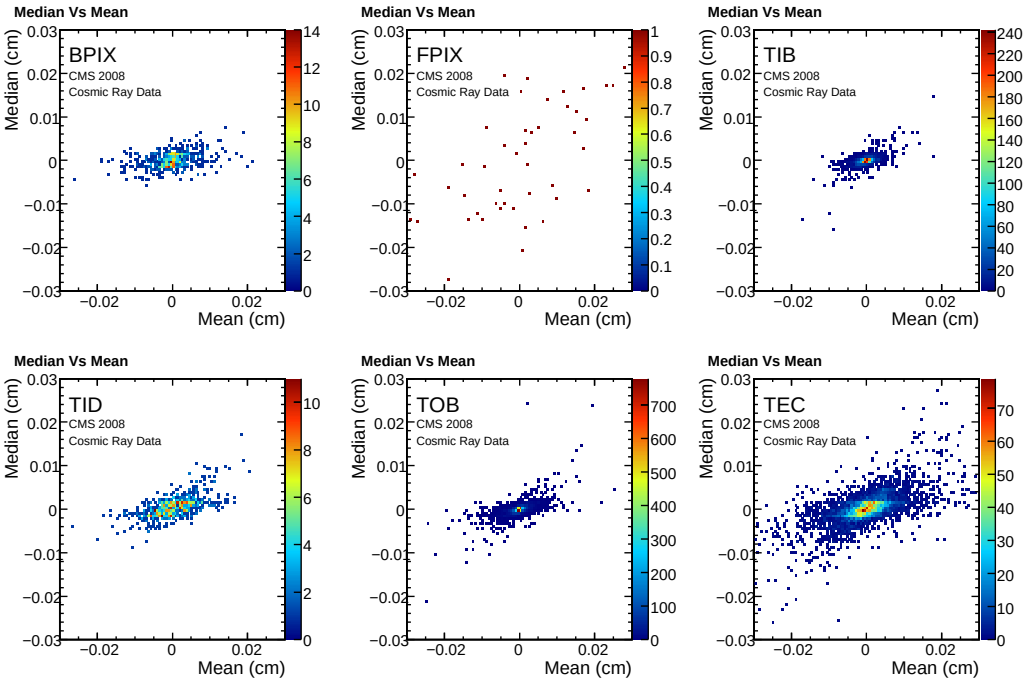

Figure 4.10: *Median of residual in u' coordinate vs the mean of residuals for the six Tracker subdetectors. Only modules with at least 30 hits have been considered. Each entry of the histogram represents a Tracker module.*

by occasional outliers most probably due to hit mis-reconstruction. Another million of cosmic tracks was analyzed to check the statistical fluctuation on the estimator and it was found that the median was the most robust, with fluctuations of about 1 μm (see Table 4.2).

Table 4.2: *Table of values obtained for the different estimators of the residual misalignment for two statistically independent track samples.*

First (second) sample				
Subdet	Mean (μm)	Tr. Mean (μm)	Median (μm)	Fit Mean (μm)
BPIX (u')	49 (49)	49 (49)	17 (18)	37 (37)
FPIX (u')	105 (100)	105 (100)	109 (100)	105 (100)
TIB (u')	21 (18)	21 (18)	10 (10)	14 (12)
TOB (u')	53 (59)	53 (53)	23 (22)	43 (37)
TID (u')	23 (22)	23 (22)	9 (10)	15 (14)
TEC (u')	56 (53)	56 (53)	29 (29)	50 (47)

The accuracy of the estimator was also tested on a Monte Carlo sample. Tracks were generated with ideal geometry and then reconstructed with a randomly misaligned geometry in the local sensitive coordinate, with the average amplitude chosen as an estimate of the realistic misaligment of the Tracker before CRAFT alignment. The first column of Table 4.3 shows the input random misalignment, the σ of the gaussian smearing in the local coordinate applied to the position of the hit. In Figure 4.11 are shown the results for the different misalignment estimators, and the RMS of the resulting distributions are summarized in Table 4.3. The RMS of the median and of the mean of a gaussian fit are the most accurate measurements of the input misalignment.

Table 4.3: *Table of values obtained for different estimators of the residual misalignment. Valus for the FPIX detector are missing due to the too small fraction of cosmic tracks crossing its volume*

Subdet	Misalignment (μm)	Mean (μm)	Tr. Mean (μm)	Median (μm)	Fit Mean (μm)
BPIX (u')	50	62	62	56	58
FPIX (u')	1000	\	\	\	\
TIB (u')	20	23	23	20	20
TOB (u')	20	24	24	22	22
TID (u')	100	84	84	86	81
TEC (u')	100	114	114	100	111

Based on these tests, the RMS value of the median distribution was taken as the most appropriate measurement of remaining misalignment in the sensitive coordinate in each subdetector. Distributions of the median of the residuals (DMR) are shown in Figure 4.12 and the corresponding RMS values of these distributions are given in Table 4.4. Overall, there is significant improvement in the track reconstruction going from the geometry without any alignment, to the alignment using tracks with

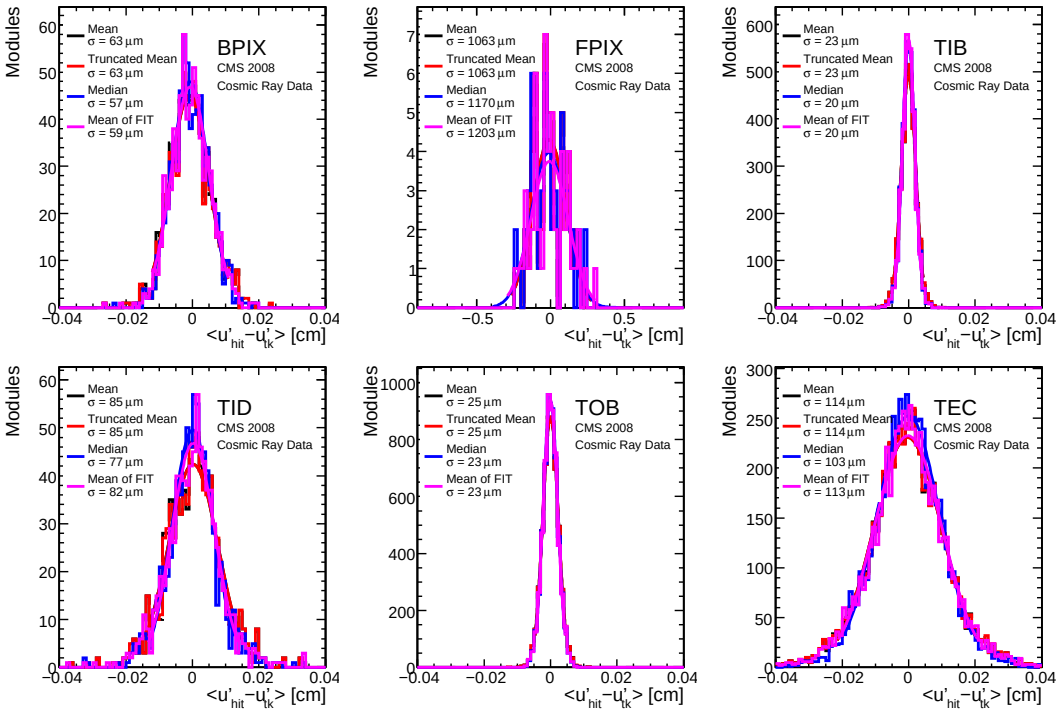

Figure 4.11: *Comparison of different estimators of residual misaligment in a randomly misaligned cosmic track simulation, for the six Tracker subdetector. Only modules with at least 30 hits have been considered. Black line is the mean of the residual distribution, blue the median, pink the mean value of a gaussian fit and red truncated mean (see text)*

the local and the global method, and finally to the combined result. With respect to cosmic ray trajectories the module positions were determined to a precision of 3-4 μm RMS in the barrel and 3-14 μm RMS in the endcaps in the most sensitive coordinate. These values are in agreement with the expected statistical precision as determined using simulated events. They are also comparable with values obtained from a simulation based on the ideal detector geometry which is an indication that alignment precision was approaching to statistical limit.

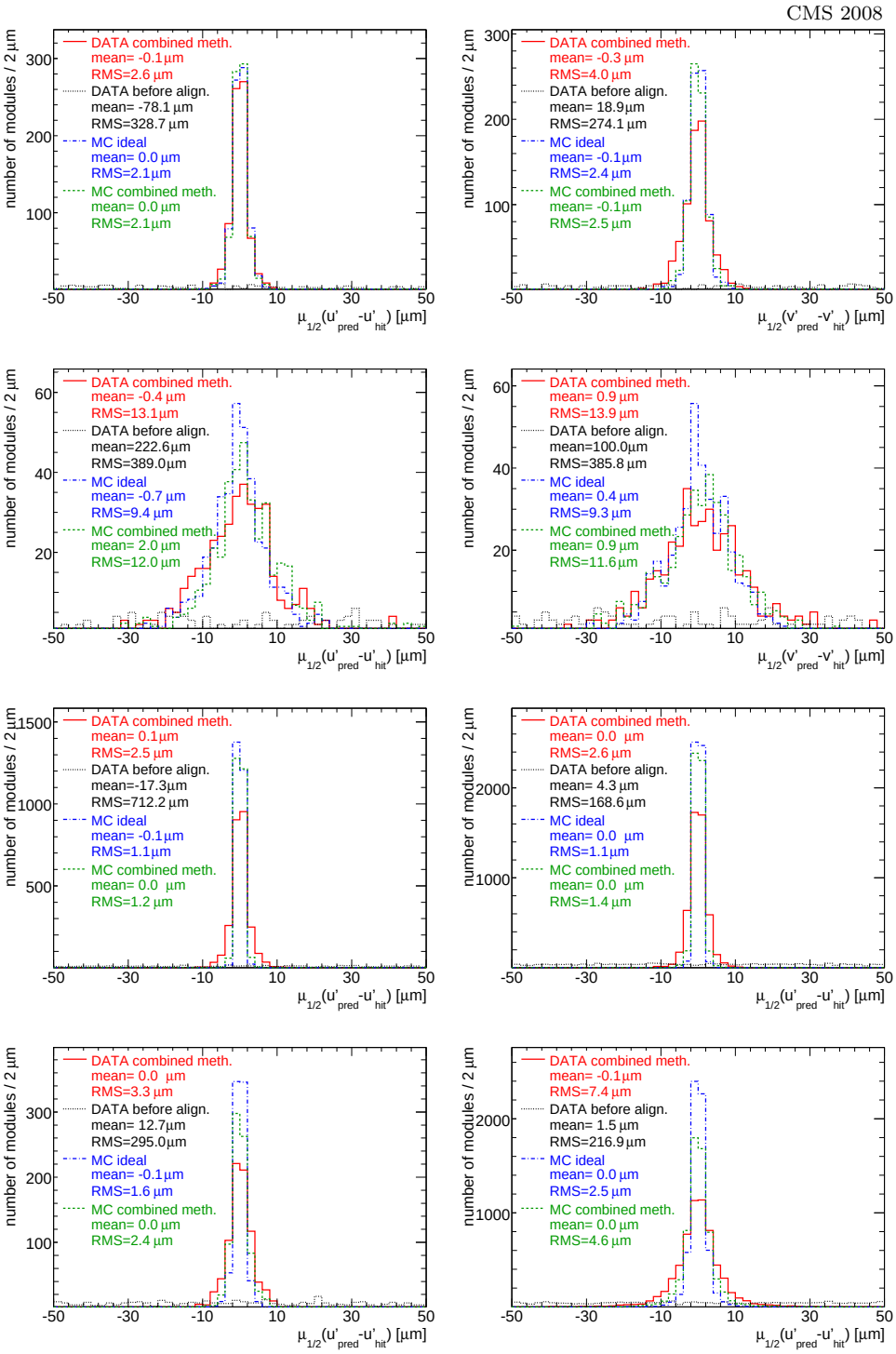

Figure 4.12: *Distribution of $\mu_{1/2}$, the median of the residuals, for modules with more than 30 hits, shown for BPIX (top left u, top right v), FPIX (second row left u , second row right v), TIB (third row left), TOB (third row right), TID (bottom left), and TEC (bottom right). Shown are distributions before alignment (black dotted), after alignment with the combined method (red solid), combined method MC (green dashed), and ideal MC (blue dash-dotted).Each entry of the histograms represents a Tracker module*

Table 4.4: *RMS of the distribution (in μm) of the median of the residuals ($\mu_{1/2}$) (DMR) in the u' and v' coordinates for modules with more than 30 hits. The number of these modules for each subdetector compared to the total number of modules is stated in the last column. Four geometries are considered: those obtained with the three methods discussed in the text and the geometry before alignment. Results from simulations based on the combined alignment and ideal geometries are shown for comparison.*

	DATA before	DATA global	DATA local	DATA combined	MC combined	MC ideal	modules
BPIX (u')	328.7	7.5	3.0	2.6	2.1	2.1	757/768
BPIX (v')	274.1	6.9	13.4	4.0	2.5	2.4	
FPIX (u')	389.0	23.5	26.5	13.1	12.0	9.4	393/672
FPIX (v')	385.8	20.0	23.9	13.9	11.6	9.3	
TIB (u')	712.2	4.9	7.1	2.5	1.2	1.1	2636/2724
TOB (u')	168.6	5.7	3.5	2.6	1.4	1.1	5129/5208
TID (u')	295.0	7.0	6.9	3.3	2.4	1.6	807/816
TEC (u')	216.9	25.0	10.4	7.4	4.6	2.5	6318/6400

4.2.2 Monitoring of the geometry

Once the results from the alignment procedure have been tested on terms of residual minimization, a detailed analysis of the position of the modules inside the Tracker geometry is needed in order to spot evidence of internal spurious shifts and rotations which can affect the reconstruction of physics observables. A comparison of two geometries obtained from track-based alignment can be done after correcting for overall residual shifts and rotations of the whole detector, or any smaller alignable element in the alignment hierarchy, with respect its center of gravity, whose position and orientation $(\mathbf{R}, \mathbf{\Omega})$ can be calculated in the rigid body formalism:

$$\mathbf{R}_k = \left(\sum_i^N w_i \cdot d\mathbf{r}_i\right)_k \Big/ \sum_i^N w_i \tag{4.2}$$

$$\sum_{k=1}^{3} \mathbf{\Omega}_k \sum_i^N w_i \left(\delta_{kl}(\mathbf{r}_i)^2 - (\mathbf{r}_i)_k(\mathbf{r}_i)_l\right) = \sum_i^N w_i \left(\mathbf{r}_i \times d\mathbf{r}_i\right)_l \tag{4.3}$$

Where $\mathbf{r}_i$ are the vector positions of the modules in the starting geometry, $d\mathbf{r}_i$ are the vectorial displacements measured in the second geometry with respect to the first, and w_i are weights to be assigned at each module (in general w_i=1). To test the consistency of the two methods, during CRAFT data analysis a comparison between the geometries from the local and the global methods module by module has been done, after correcting for an overall shift and rotations of the whole detector or sub-detector with respect to its center-of-gravity. For the BPIX modules, this test indicates an agreement between the two geometries of the order of 12 μm in the rϕ coordinate.

Furthermore a comparison between the geometry obtained with the combined method, assumed to be the best geometry describing the Tracker, with respect to the design

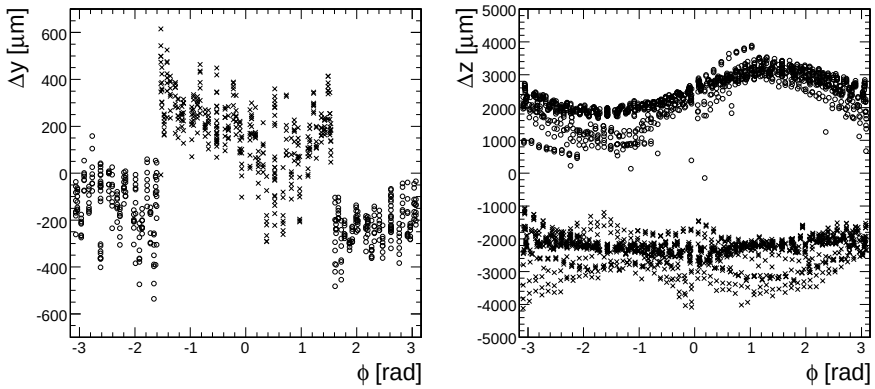

Figure 4.13: *Comparison of the position of the modules in the combined method geometry with respect to the design one: (y_{design} - y_{comb}) for the BPIX modules (left) and (z_{design} - z_{comb}) for the TIB modules (right) as a function of ϕ. In the plot on the left crosses (circles) represent modules of the positive (negative) x BPIX half-barrel. In the plot on the right crosses (circles) represent modules of the positive (negative) z TIB half-barrel. Each marker represents a Tracker module.*

one was performed. This study indicates that the two BPIX half-barrels are shifted along the vertical axis by about 0.4 mm and the two half-barrels of the TIB have an extra separation along the z axis of about 5 mm as visible in Figure 4.13. Both displacements are mechanically allowed and the large displacement of the TIB half-barrels is supported by the optical survey measurements described in [47].

4.2.3 Monitoring of the tracking performance

A check of the track parameter resolution after the alignment is done by mimicking the topology of collision tracks. A cosmic track traversing the detector close to the impact point is splitted at the point of closest approach to the nominal beamline in two halves which were independently reconstructed and refit (Figure 4.14). Both the upper and lower legs were required to have at least 3 pixel hits. Figure 4.15 shows the difference between upper and lower portions of tracks for d_{xy} (more sensitive to the alignment of the pixel detector) and $1/p_T$ (more sensitive to the strip part of the Tracker) : there is significant improvement due to Tracker alignment with good agreement between data and simulations. The results of the combined method are approaching those of a simulation with ideal detector geometry.

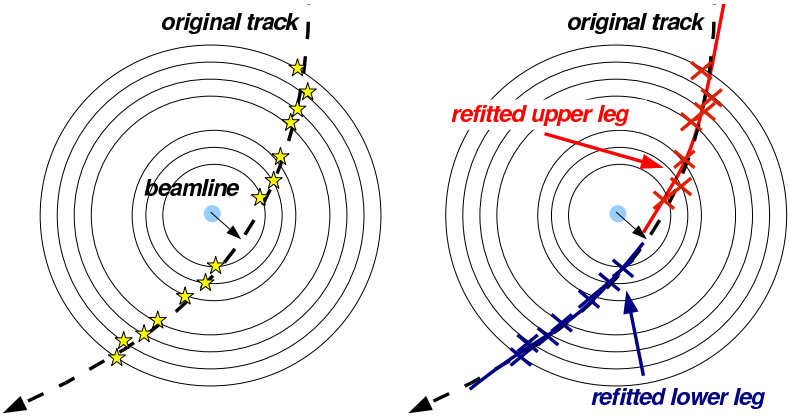

Figure 4.14: *Track splitted at its point of closest approach to the nominal beamline. The two halves belonging to the same one were independently reconstructed and refit.*

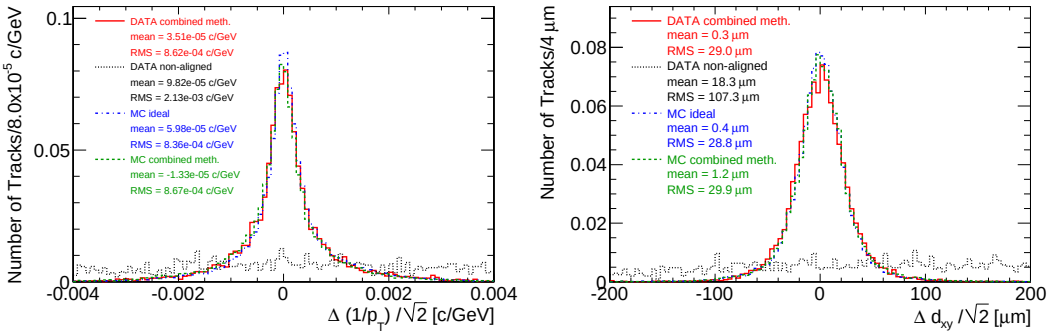

Figure 4.15: *Differences between the track parameters measured at the point of closest approach to nominal beam-line, in the two halves of a cosmic track and scaled by $1/\sqrt{2}$. The distance of closest approach in the transverse direction d_{xy} (top) and $1/p_T$ (bottom) are shown. Four resulting geometries are reported: data non-aligned (black dotted lines), ideal Monte Carlo (blue dash-dot-dashed), and alignment result with cosmic ray data using combined method (red solid) and Monte Carlo (green dashed).*

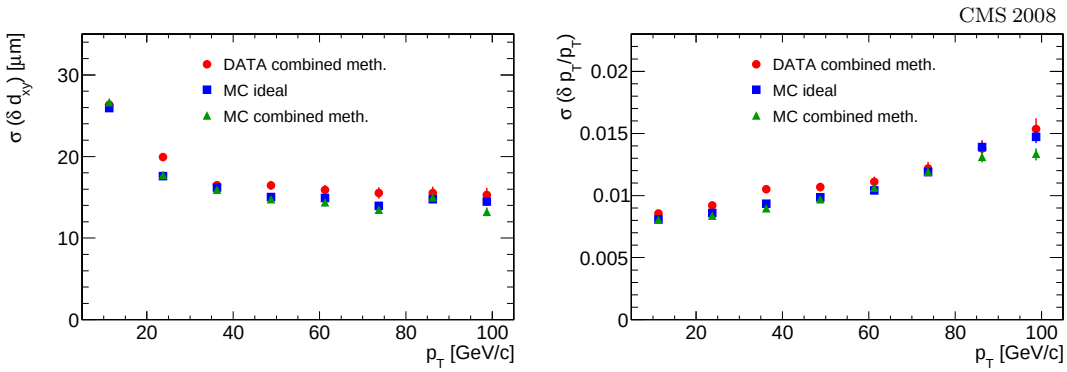

Figure 4.16: *Dependence on p_T of the differences between the track parameters measured at the point of closest approach to the nominal beamline, in the two halves of a cosmic ray track and scaled by $1/\sqrt{2}$. The RMS of the distribution truncated at 95% is quoted at each momentum interval, shown for the distance of closest approach in the transverse direction d_{xy} (left) and for $1/p_T$ (right). Results are shown for the geometries derived from ideal MC (blue squares), and from the alignment result with cosmic ray data (red circles) and combined method MC (green triangles).*

4.3 Results with collision data

On March 30^{th} 2010 at 12.58 P.M. LHC delivered to CMS for the first time $\sqrt{s}$=7 TeV collisions. CMS and the Tracker were fully operational and several hundred thousands minimum bias events were collected during the first fill. Minimum bias in the following, will denote a dataset containing a selection of CMS data based on very loose triggers, such as the coincidence of two scintillator based detectors (Beam Scintillator Counters, BSC) placed outside the CMS detector at $z = \pm 14.4$ m.

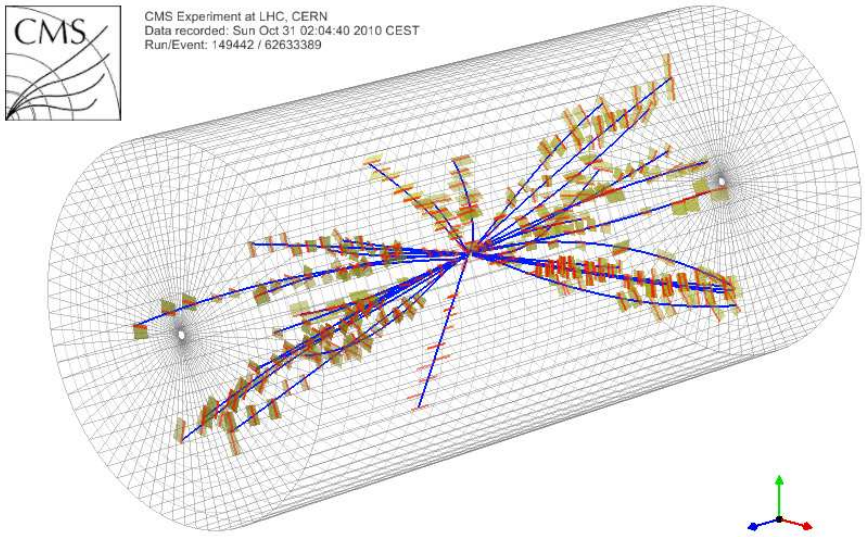

Figure 4.17: *A typical Minimum Bias event selected for Tracker alignment.*

In February 2010 a pre-collision geometry was required to check for movements of large structures after the 2009 shutdown periods mainly to monitor BPIX half-shells movements. Similarly to what was done for 2008 and 2009 cosmic data-taking [47] this geometry was obtained using 2.2 million cosmic track events with the Silicon Strip Tracker read-out with the APV chips in peak mode and running the *local method* (HIP) on top the *global method* (Millepede)

Since as of April 2010 around 1/nb of collision data had been integrated by the CMS experiment, few high momentum muons, and even fewer di-muon resonances were available at that time, so tracks coming from minimum-bias collision events have been used for alignment.

Figure 4.18 shows basic track quantities for minimum bias collision tracks used for alignment purposes, for data, simulation reconstruced with ideal alignment conditions and simulation reconstructed with a misalignment scenario for "Startup" conditions. It can be seen that the track sample is uniform in ϕ but is strongly peaked in the forward (high η) regions of the Tracker. In Figure 4.18 are shown also the transverse momentum of the tracks and the distribution of valid hits (hits attached to tracks during the track reconstruction) and lost hits (hits predicted by the track fit extrapolation but non recorded).

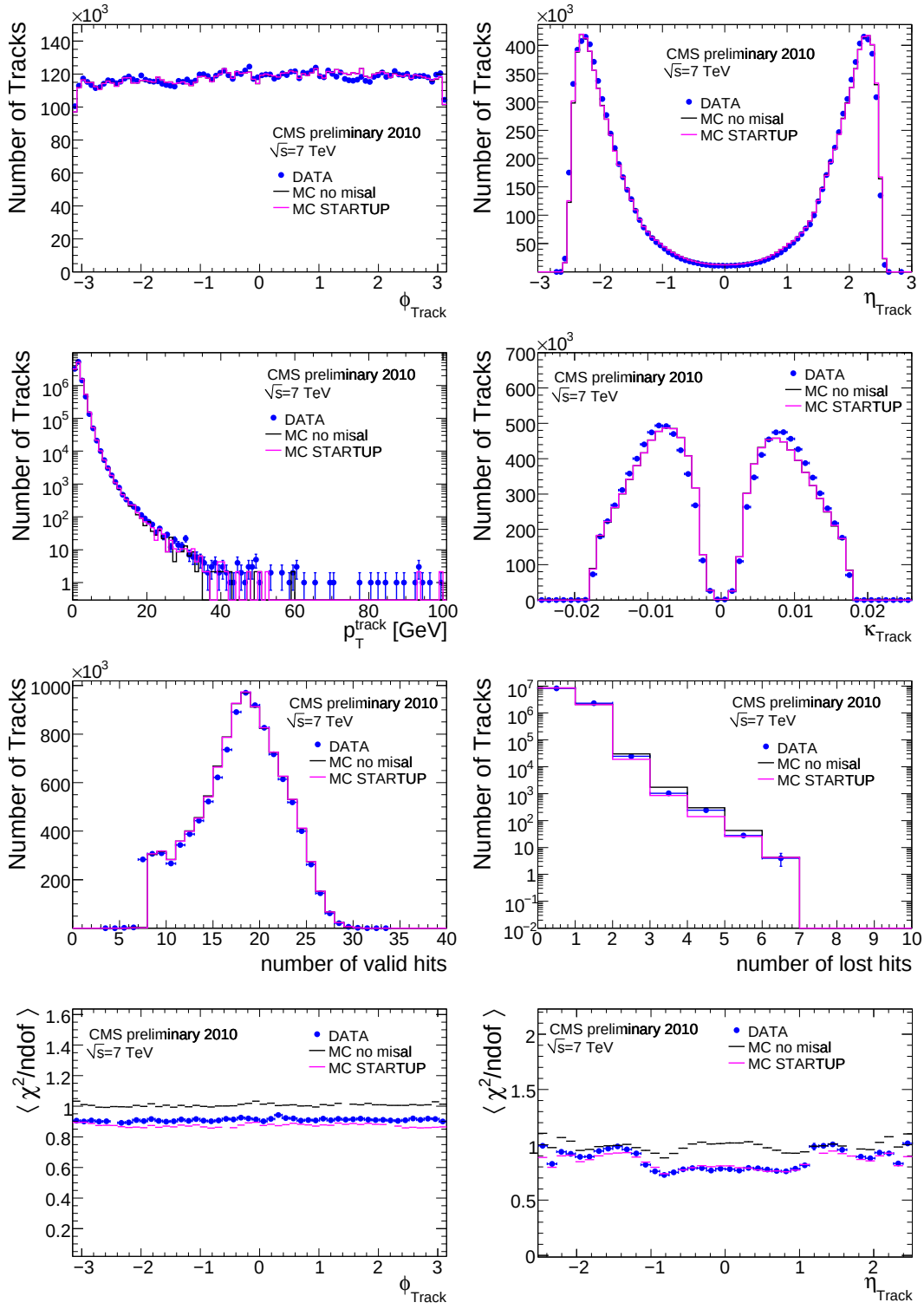

Figure 4.18: *Basic track quantities for collision tracks used for alignment validation. Top right azimuthal angle ϕ, top left track pseudorapidity (η), in the second row transverse momentum p_T (left) and curvature (right), in the third row the number of valid hits (left) and of lost hits (right) and in bottom row profile of track reduced χ^2 vs ϕ (left) and vs η (right). Shown are distributions for Design Geometry MC (black), MC with Startup alignment conditions (pink), and Data (blue).*

From past alignment experiences using simulated events [42, 44], it was known that Tracker alignment with minimum bias tracks was extremely difficult due to the lack of constraining power over potential weak modes induced by having a single topology of tracks.

The first alignment with 7 TeV collision data was then performed mixing tracks with different topologies. A selection of 1.7 million events from the `TkAlMinBias` stream corresponding to roughly to the first 1/nb, and 1.5 million events from the February 2010 cosmic data sample of the `TkAlCosmics0T` stream were used. 4.19 shows the parameters of the tracks used for alignment. The track selection criteria are listed in Table 4.5 . It is possibile to see the complementary strength of the two track samples used, since collision tracks are prevalently producing hits in the Pixel and forward detectors, while cosmic rays produce long tracks in the Tracker Barrel.

Table 4.5: *Quality cuts applied to hits and tracks used in the alignment, for the Comsic and Collision data sample.*

Cosmic Track Sample	**Value**
momentum p	$>$ 4 GeV
transverse momentum p_T	$>$ 0 GeV
number of hits	$\geq$ 8
number of 2-d hits (on Pixel or DS modules)	$\geq$ 2
S/N (Strip modules)	$>$ 14
pixel hit prob. matching template shape in u (v) dir.	$>$ 0.001 (0.01)
track angle relative to the local uv plane	$<$ 20°
Collision Track Sample	**Value**
At least one reconstructed primary vertex	
momentum p	$>$ 4 GeV
transverse momentum p_T	$>$ 2 GeV
number of hits	$\geq$ 7
number of 2-d hits (on Pixel or DS modules)	$\geq$ 2
S/N (Strip modules)	$>$ 8
pixel hit prob. matching template shape in u (v) dir.	$>$ 0.001 (0.01)
track angle relative to the local uv plane	$<$ 10°

The final strategy was to align with the local method the BPIX and FPIX modules in all six the degrees of freedom $(u, v, w, \alpha, \beta, \gamma)$ while the modules of the Silicon Strip Tracker were aligned in u, w, γ. The Tracker geometry obtained with cosmic data in February 2010 was used as a starting point.The resulting geometry was used for the physics analysis presented to the Summer 2010 conferences.

Figure 4.20 shows the performance in terms of χ^2/ndf of minimum bias tracks after refitting them with the new geometry, with respect to a misaligned simulated sample in "Startup" (see Section 4.2) conditions and one in ideal alignment conditions. The performance is very close to the ideal one. Figure 4.21 shows the performance in terms of track-to-hit residuals for the different subdetectors. Figure 4.22 and Table 4.6 show the estimated remaining misalignment in terms of the distributions of DMR. In the barrel and in the pixel subdetectors the achieved precision is at least the level of the expected precision from simulation in "Startup" conditions.

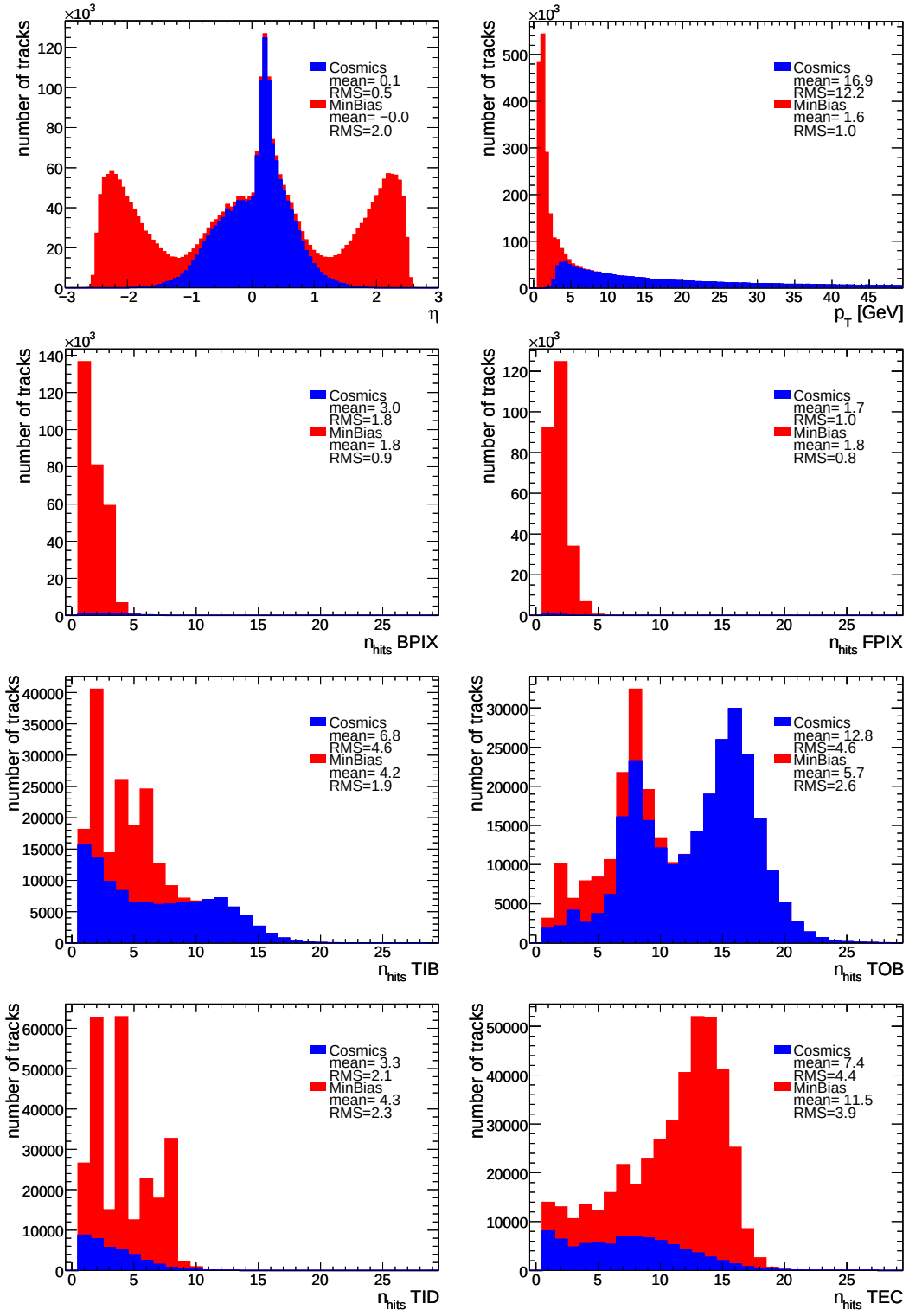

Figure 4.19: *Basic track quantities for collision tracks used for the first Tracker alignment with collision tracks: blue stands for cosmics, red for minimum bias tracks. Top left track pseudorapidity (η), top right p_T . Second row: spectra of number of BPIX hits (left) and of FPIX hits (right). Third row: spectra of number of TIB hits (left) and of TOB hits (right). Fourth row: spectra of number of TID hits (left) and of TEC hits (right).*

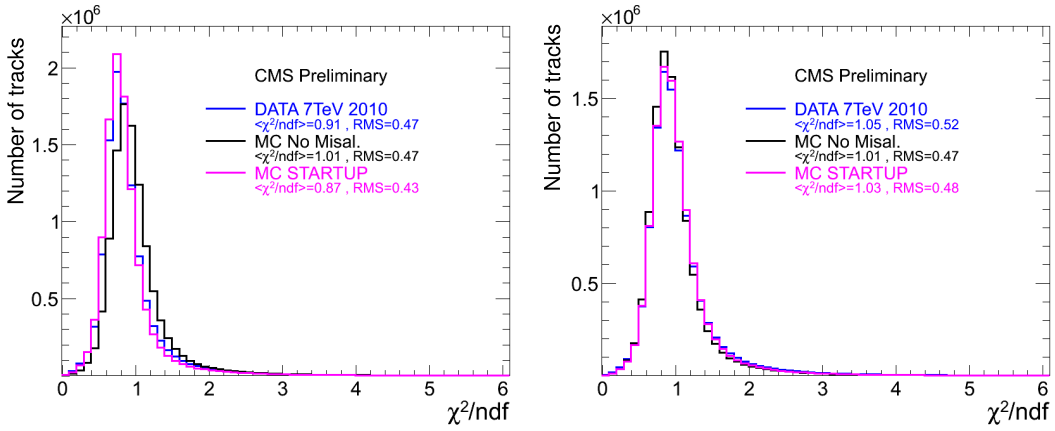

Figure 4.20: *Distribtions of χ^2/ndf. Left: the track reconstruction was performed without alignment position errors. Right: track reconstruction performed with calibrated alignment position errors. Shown are distributions for no misalignment MC (black), MC with "Startup" alignment conditions (pink), and Data (blue).*

Table 4.6: *RMS of the distribution of the median of the residuals (DMR) in the u' and v' local coordinates for modules with more than 200 hits. The number of these modules compared to the total number of modules is stated in the last column. Results from simulations based on the combined alignment and ideal geometries are shown for comparison alogn with results on data.*

	Data (μm)	MC Startup (μm)	MC No Misalign (μm)	modules
BPIX (u')	1.6	3.1	0.9	760/768
BPIX (v')	5.5	8.9	1.8	
FPIX (u')	5.7	10.7	2.5	631/672
FPIX (v')	7.3	14.4	6.1	
TIB (u')	5.1	10.1	3.2	2580/2724
TOB (u')	7.5	11.1	7.5	5125/5208
TID (u')	4.0	10.4	2.4	809/816
TEC (u')	10.1	22.1	2.9	6340/6400

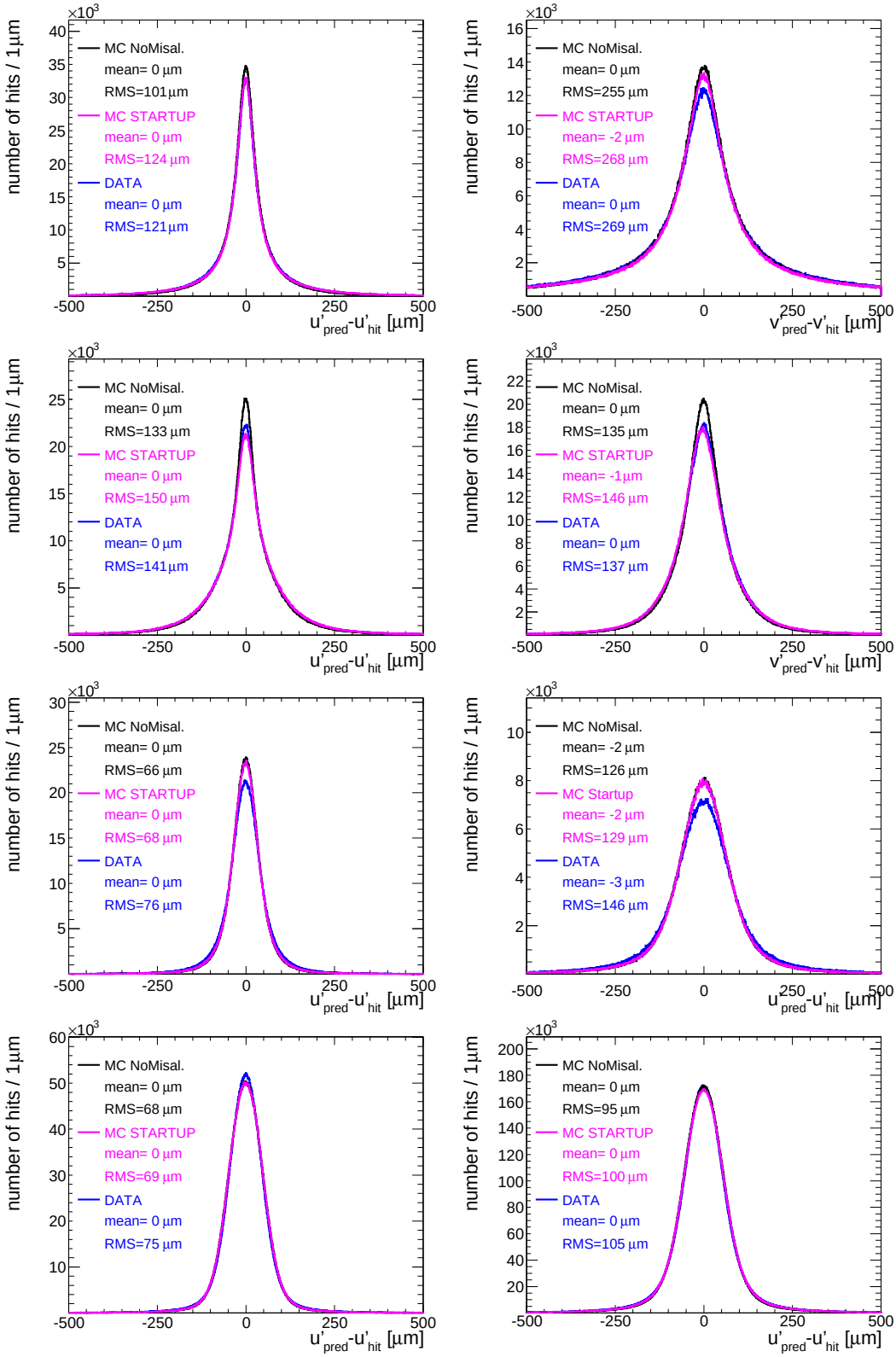

Figure 4.21: *Distribution of track-to-hit residuals shown for BPIX (top left u', top right v'), FPIX (second row left u', second row right v'), TIB (third row left), TOB (third row right), TID (bottom left), and TEC (bottom right). Shown are distributions for no misalignment MC (black), MC with "Startup" alignment conditions (pink), and collision data (blue).*

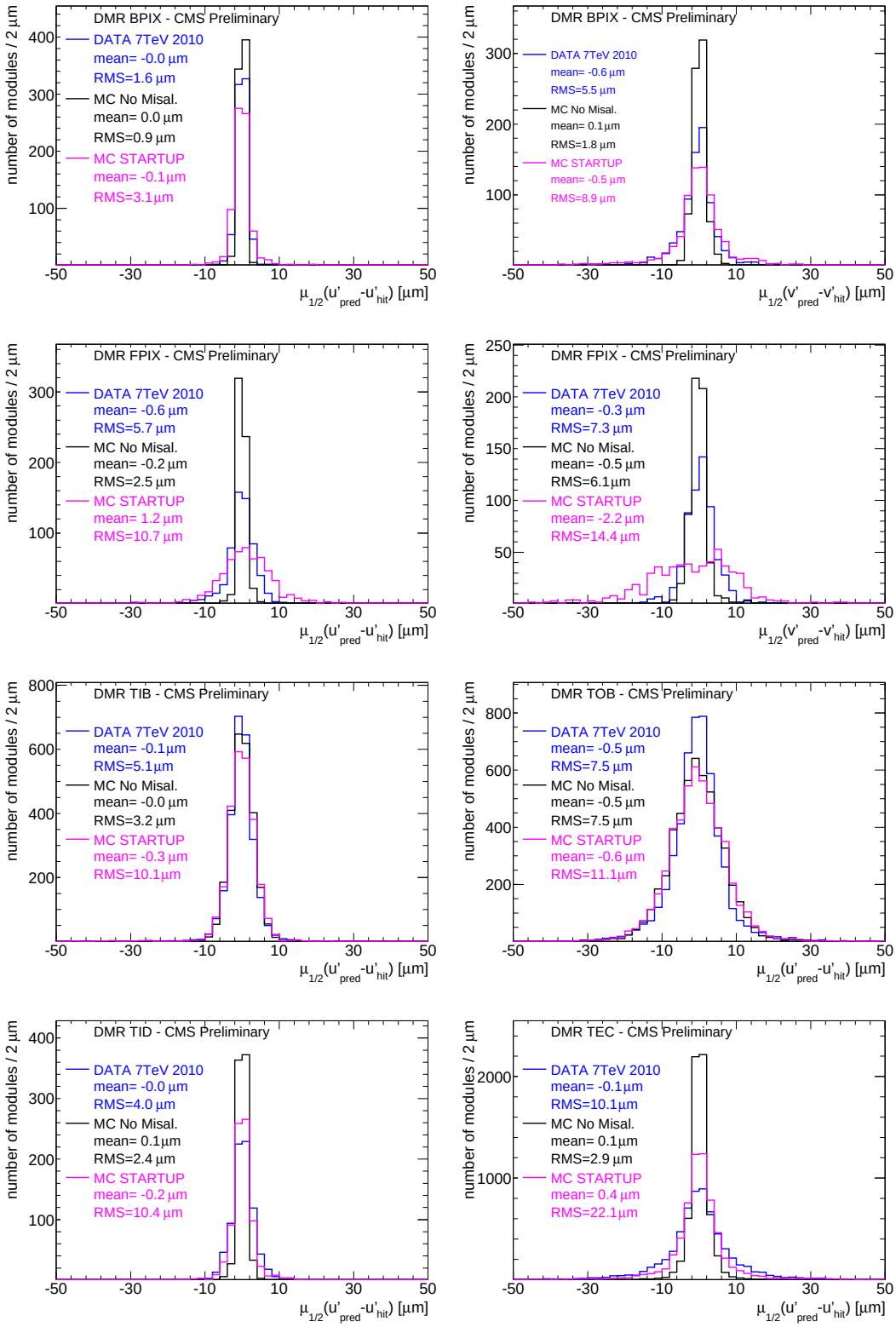

Figure 4.22: *Distribution of $\mu_{1/2}$, the median of the residuals, for modules with more than 200 hits, shown for BPIX (top left u', top right v'), FPIX (second row left u' , second row right v'), TIB (third row left), TOB (third row right), TID (bottom left), and TEC (bottom right). Shown are distributions for no misaligment MC (black), MC with "Startup" alignment conditions (pink), and Data (blue).*

4.3.1 Trend of residuals vs track momentum

The study of the trend of track-to-hit residuals as a function of track momentum can give an alternative measurement of the alignment precision, provided that the intrinsic hit precision is known.

A charged particle traversing material experiences multiple scattering, mainly due to Coulomb interaction with the nuclei in the atoms, resulting in a spatial shift and a change of the particle direction after leaving the material compared to propagation in vacuum. The mean of the deflection angle due to this effect is $\langle\theta\rangle = 0$. The distribution of the deflection angles can be approximated within certain limits as a Gaussian with standard deviation $\sigma(\theta)$ given by the following formula:

$$\sigma(\theta) = \frac{13.6MeV}{vp} z \sqrt{\frac{t}{X_0}} \left[1 + 0.038 \ \ln(t/X_0)\right] \tag{4.4}$$

where v is the velocity of the particle, p its momentum and z the charge. t/X_0 is the thickness of the traversed medium in units of radiation lenghts (see Figure 4.23)

Equation 4.4 takes into account all material traversed by the particle for the full trajectory. This angular deflection can be translated into a widening of the track-to-hit residuals (in a small angle approximation) of $\delta\sigma_R \sim l \cdot \sigma(\theta)$ where l is the lever arm, i.e. the distance between two subsequent measurement layers, typically 10 cm for the CMS Tracker. Thus Equation 4.1 reported here for convenience:

$$\sigma_R = \underbrace{\sigma_{tk}(p)}_{\propto 1/p} \oplus \underbrace{\sigma_{hit} \oplus \sigma_{mis}}_{\sim const} \tag{4.5}$$

can be rewritten in a more compact form accounting explicitely for the dependence of the track-to-hit residuals from momentum:

$$\sigma_R(p) = \frac{A(t/X_0)}{p} \oplus B \tag{4.6}$$

Track residuals should decrease as a function of track momentum, until the contribution of multiple scattering becomes negligible with respect to intrinsic resolution or misalignment effects and asymptotically:

$$\sigma_R(p) \xrightarrow{\text{p } \sim \text{ few GeV}} B = \sigma_{hit} \oplus \sigma_{misalignment} \tag{4.7}$$

Studying the trend of the residuals as a function of track momentum it is possible to extract the term which does not depend on it and ideally have an estimate of σ_{mis} if one is able to deconvolve the intrinsic hit resolution σ_{hit}.

The results presented in the following have been obtained using the data corresponding to 1.1 nb^{-1} of integrated luminosity in the runs with colliding beams at the center-of-mass energy of 7 TeV, the solenoidal magnetic field at the nominal value of 3.8 T and the silicon pixel and the silicon strip Tracker detectors enabled with the nominal high voltage bias applied to the sensors. Due to the relatively low LHC

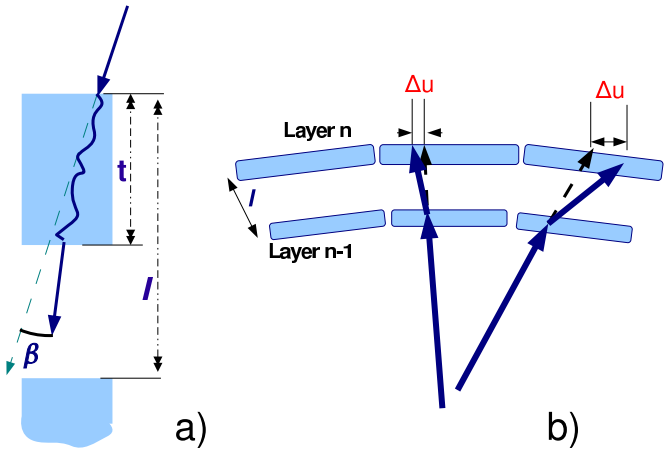

Figure 4.23: *Effect of Multiple Coulomb Scattering on track residuals: a) Particle trajectory deflection due to MS, b) the angular deflection is a function of the effective material thickness crossed by the particle t, which is a function of the impact angle* θ_{3D}.

luminosity the CMS readout was triggered by the Beam Scintillator Counter trigger to collect minimum-bias collision events and by the beam pick-up timing detector to detect the passage of the beam bunches [35].

The simulated events used are minimum-bias events (about 10 million) produced with the PYTHIA 8.1 [45] event generator, "tune 1" at a center-of-mass energy of 7 TeV.

In order to select a clean track sample to study the trends of residuals, a series of quality cuts on the event and on the tracks have been performed as listed in Table 4.7.

Event	Event Selection + Background Rejection
	At least one primary vertex (PV) $\text{ndf}_{PV} > 4$ $\lvert z\rvert_{PV} < 15$ cm $\sqrt{x_{PV}^2 + y_{PV}^2} < 2$ cm
Tracker Track	
	momentum $p > 3$ GeV/c transverse momentum $p_T > 0.65$ GeV/c number of hits ≥ 8 number of 2-d hits (on Pixel or DS modules) ≥ 2 No missing hits in the track hit pattern Barrel-only tracks (η <1.5)
Tracker Hits	
	S/N (Strip modules) > 8 pixel hit prob. matching template in u (v) dir. > 0.001 (0.01) track angle relative to the local uv plane $< 10^\circ$

Table 4.7: *The quality cuts applied on the data and Monte Carlo samples to perform the study of track-to-hit residuals vs track momentum.*

The study was restricted to the BPIX, TIB and TOB. To avoid any additional contri-

bution to the track fit uncertainty because of missing hits in the fit procedure, which lead to a larger track extrapolation error, a cut on the track hit pattern has been applied to the sample. Only tracks crossing all the 13 barrel layers (3 BPIX + 4 TIB + 6 TOB) without any non-valid hit are required; this is pictorially shown in the right part of Figure 4.25.

Comparison against detailed Monte Carlo prediction has been carried out. The comparison of basic track quantities after the applied cuts shown in Figure 4.24 indicates a very good agreement.

As the deflection due to multiple scattering goes as $\sqrt{t/X_0}$, an important quantity to be checked is the track local impact angle θ_{3D}, since if the the thickness of the crossed sensor is d, the effective silicon thickness crossed by the particle is $t = d/\cos\theta_{3D}$ and one should avoid mixing too different track topologies with very different impact angles.

The local impact angle (see left side of Figure 4.25) is defined via:

$$p_w = |\mathbf{p}|\cos\theta_{3D} \Rightarrow \theta_{3D} = \arccos\left(\frac{p_w}{|\mathbf{p}|}\right) \tag{4.8}$$

where p_z^{local} is the component along local z of the track momentum.

The track sample was divided in six bins of track momentum. The distributions of the local impact angle for data and simulation for each momentum bin are shown in Figure 4.26. The correction factor for the effective sensor thickness after the cuts is found in general close to unit, being in the range: $0.8 < \cos\theta_{3D} < 1$.

Since the shape of the distributions of residuals is somewhat far from a pure gaussian function (see Figures 4.27.4.28,4.29), the median of absolute deviations (MAD) was considered more appropriate as an estimator of the statistical dispersion than the sample variance or gaussian standard deviation. The MAD is defined as follows:

$$MAD = \mu^i_{1/2}(|R_i - \mu^j_{1/2}(R_j)|) \tag{4.9}$$

where R_i is an entry of the residuals histogram, i.e. the MAD is the median of the absolute value of the differences between the median value of the population and the values of the population itself.
In order to use the MAD as a consistent estimator of the standard gaussian deviation σ, one takes

$$\sigma = K \cdot \mathrm{MAD} \tag{4.10}$$

where K is taken to be $1/\Phi^{-1}(3/4) \approx 1.4826$, and Φ^{-1} is the inverse of the cumulative distribution function for the standard normal distribution, i.e., the quantile

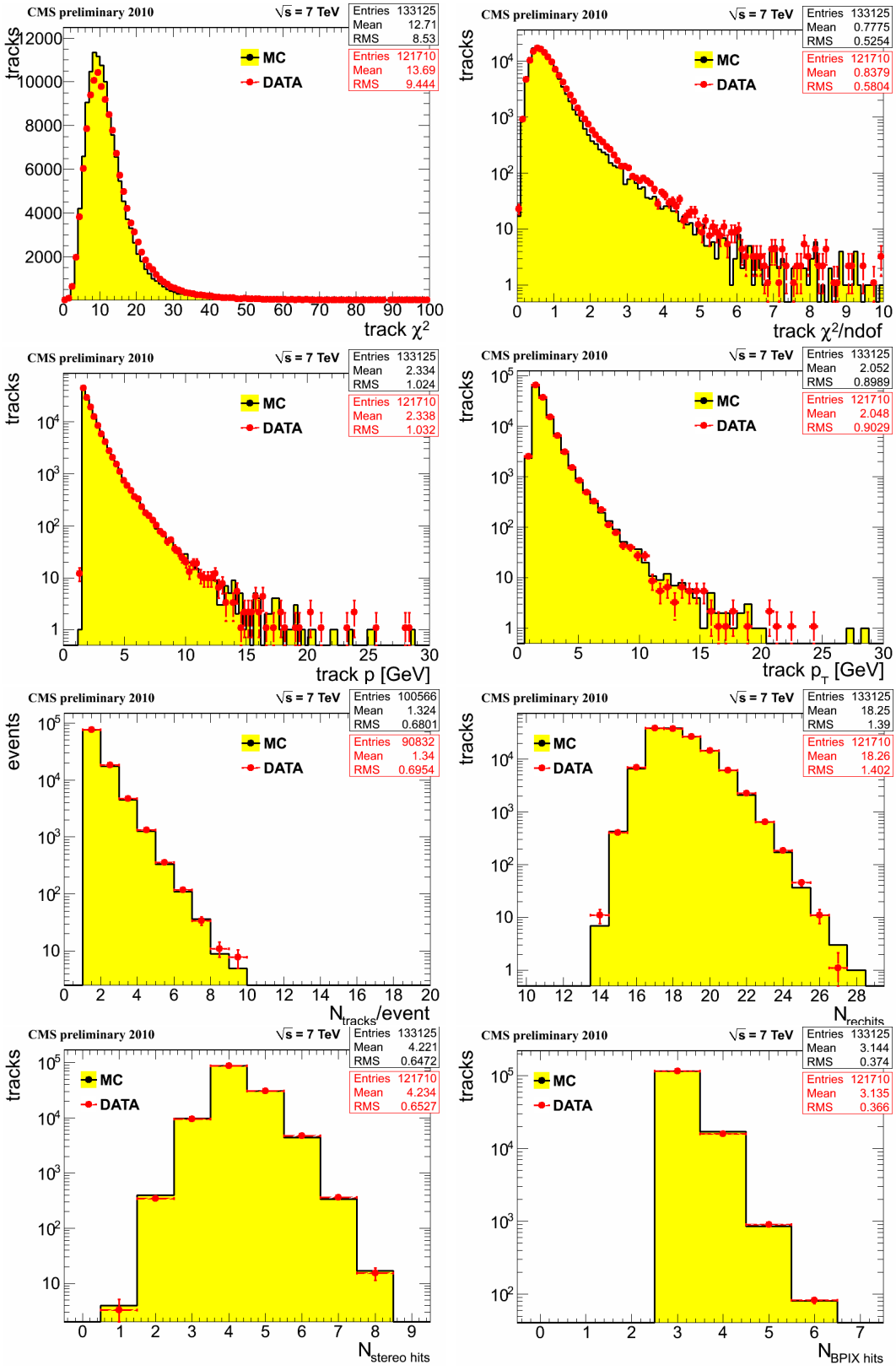

Figure 4.24: *Collection of control distributions of basic track quantities. Top row: χ^2 distributions in linear (left) and χ^2/ndf in logarithmic scale (right). Second row: distributions of track momentum (left) and transverse momentum (p_T) right. Third row: distributions of track multiplicity and number of Tracker hits associated to a track. Bottom row: number of stereo and barrel pixel hits. Data are red dots, MC is painted in yellow.*

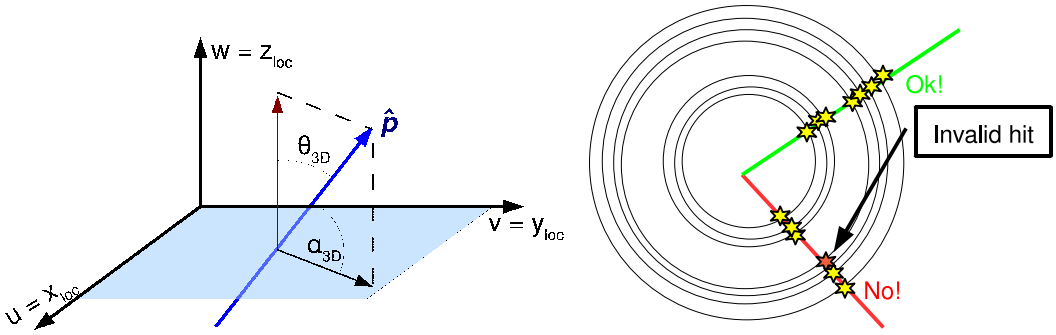

Figure 4.25: *Left: Sketch explaining the definition of local impact angle on the module surface. Right: Sketch of the selected track hit pattern for the residuals vs momentum study.*

function. [3]

After applying this factor the estimated width of the residuals was plotted as a function of track momentum. Results are shown for the BPIX, TIB, TOB in Figure 4.30 and for each Barrel Layer in Figure 4.31. The resulting trends for data and for detailed detector simulation in "Startup" conditions generally in good agreement a part from the inner layers of TOB, in which a non perfect description of the material budget in the simulation is known to be present.

The trends of residuals were fit with the function:

$$\sigma_R(p) = \sqrt{\frac{A^2}{p^2} + B^2} \tag{4.13}$$

Figures 4.30 and 4.31 show a good agreement of the experimental data with the simple model used for the fit. Then is possible to estimate the remaining misalignment using Equation 4.7

$$B = \sigma_{hit} \oplus \sigma_{mis} \rightarrow \sigma_{mis} = \sqrt{B^2 - \sigma_{hit}^2} \tag{4.14}$$

provided that one knows the intrinsic hit resolution σ_{hit}. The intrinsic hit resolution was taken from the studies described in [48], using a method based on hits in overlapping sensors of the same layer (called *overlaps*). This technique shown in Figure 4.32 minimizes effects of misalignment and reduces the potential amount of material

[3] This is because the MAD is given by:

$$\frac{1}{2} = P(|R-\mu| \leq \text{MAD}) = P\left(\left|\frac{R-\mu}{\sigma}\right| \leq \frac{\text{MAD}}{\sigma}\right) = P\left(|Z| \leq \frac{\text{MAD}}{\sigma}\right) \tag{4.11}$$

In words: for a symmetric distribution, the MAD is the distance between the 1^{st} and 2^{nd} (equivalently, 2^{nd} and 3^{rd}) quartiles, so for a symmetric distribution about the mean, the MAD is the difference between the second and third quartiles (the 50^{th} and 75^{th} percentiles). Thus the scale factor to use the MAD for the normal distribution is the 75^{th} percentile of the normal distribution with $\sigma = 1$. Hence:

$$\frac{\text{MAD}}{\sigma} = \Phi^{-1}(3/4) \approx 0.6745 \Rightarrow \sigma \approx 1.4826 \ \text{MAD} \tag{4.12}$$

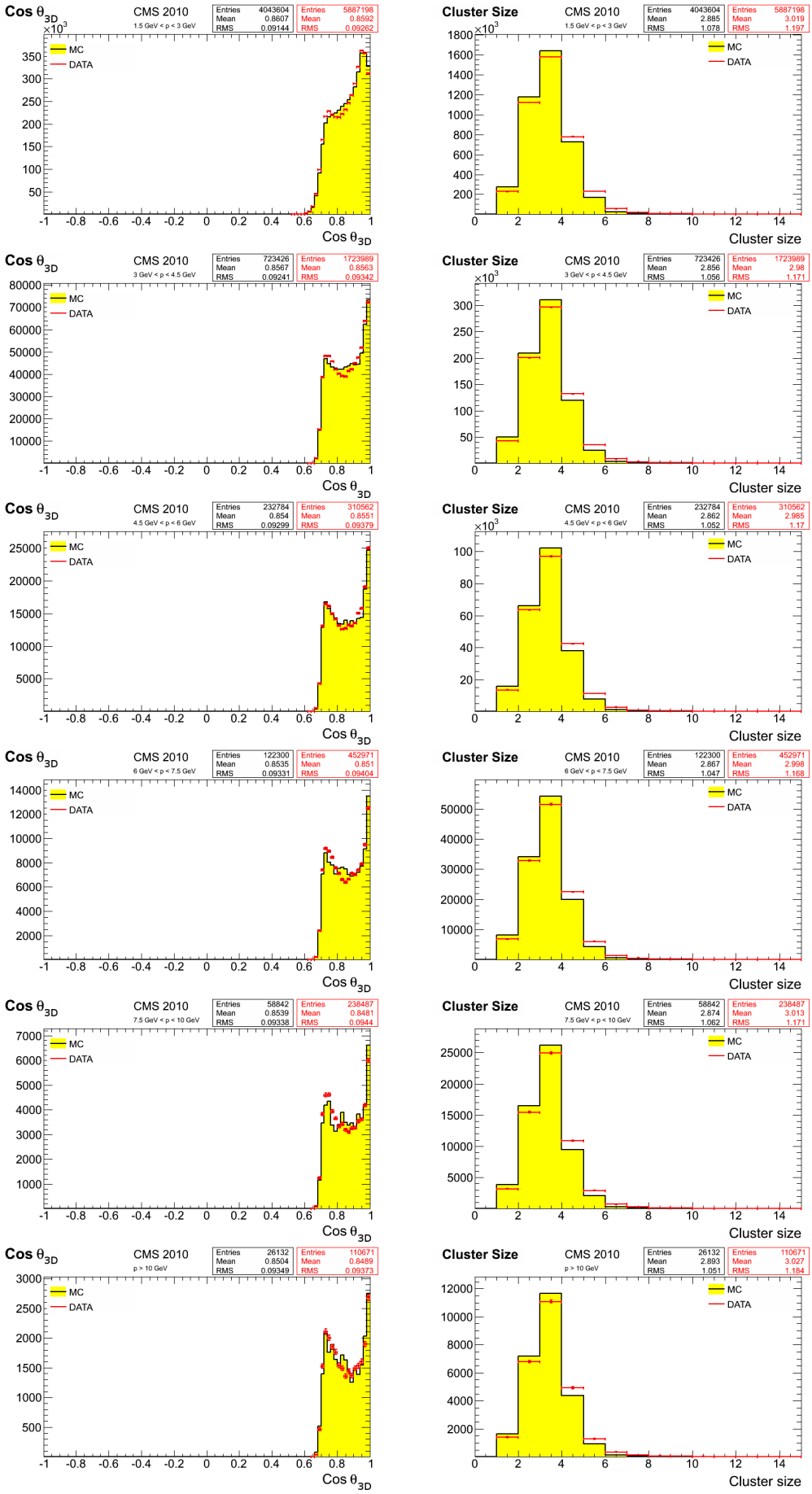

Figure 4.26: *Left column: distributions of the local impact angle for the six momentum bins described in the text. Right column: distribution of cluster widths. Data are red dots, MC is painted in yellow.*

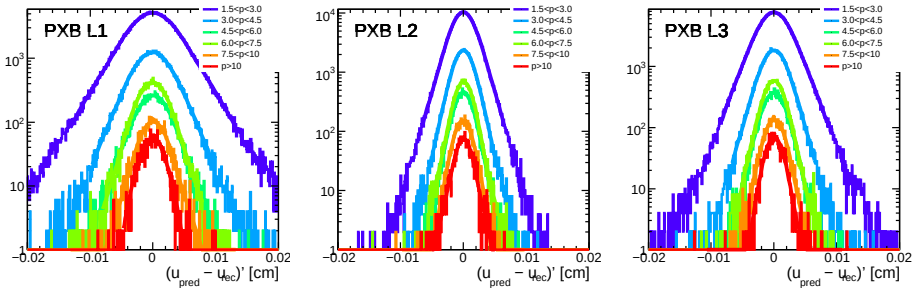

Figure 4.27: *Distributions of the track-to-hit residuals for the three BPIX Layers. The different momentum bins are shown with different colors.*

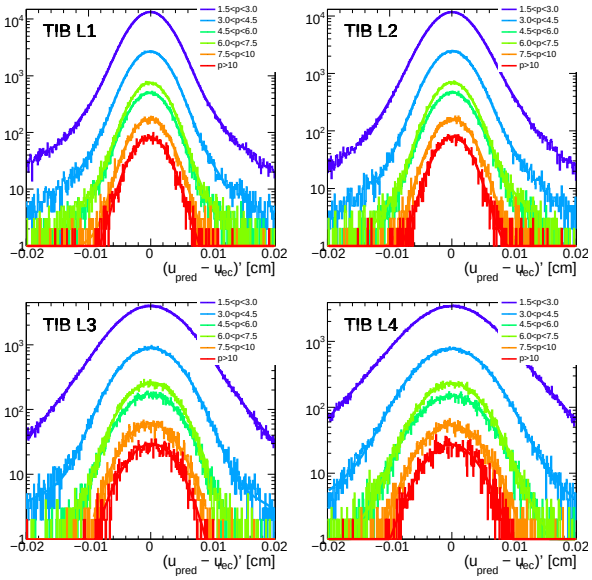

Figure 4.28: *Distributions of the track-to-hit residuals for the four TIB Layers. The different momentum bins are shown with different colors*

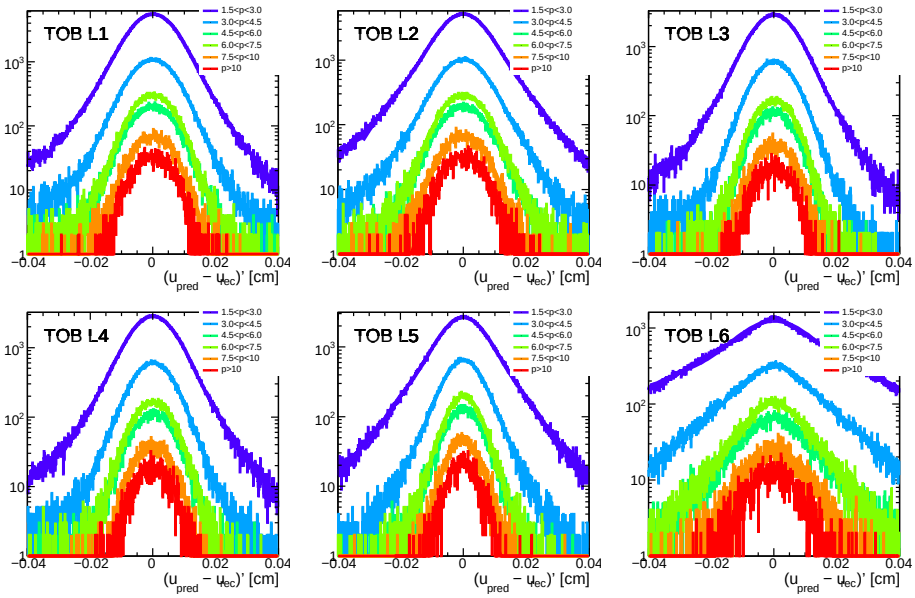

Figure 4.29: *Distributions of the track-to-hit residuals for the six TOB Layers. The different momentum bins are shown with different colors*

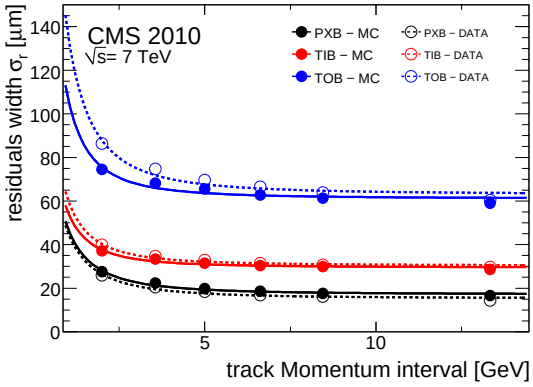

Figure 4.30: *Distributions of the trend of residuals widths as a function of track momentum. Blue corresponds to TOB, red to TIB, black to Barrel Pixel, dashed curves are MC, while solid curves data.*

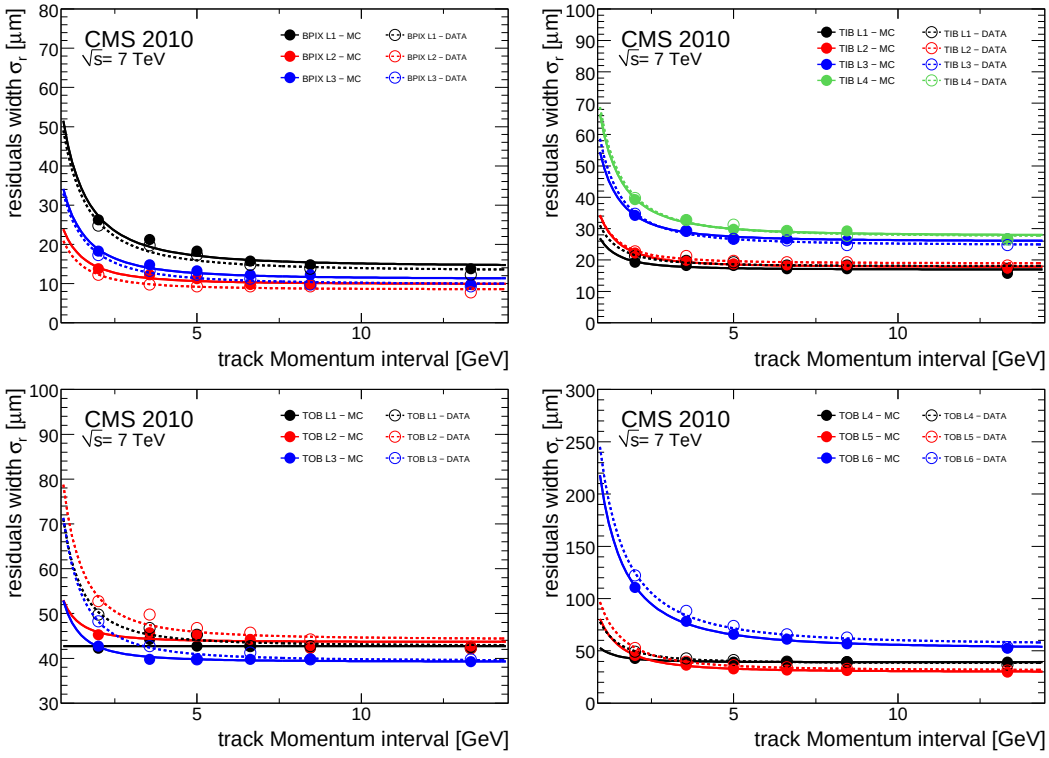

Figure 4.31: *Distributions of the trend of residuals widths as a function of track momentum. Top row: Barrel Pixel (left) and TIB (right). Bottom row: First TOB Layers (left), Last TOB Layers (right). Dashed curves are MC, while solid curves data.*

between hits.

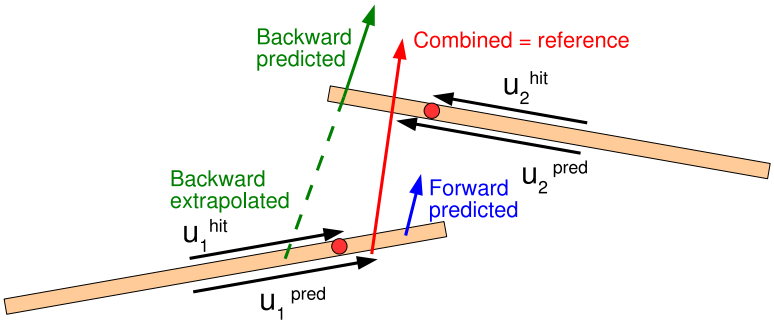

Figure 4.32: *Scketch of the application of the overlap tecnique for estimating intrinsic hit resolution.*

The instrinsic hit resolution is estimated as the width of the distribution of the so called "double differences", defined as the difference in hit and predicted positions of the two overlaps:

$$DD = \Delta u_{hit} - \Delta u_{pred} = (u_{1,hit} - u_{2,hit}) - (u_{1,pred} - u_{2,pred}) \tag{4.15}$$

This technique was applied for the strip Tracker using a clean sample of minimum bias tracks with at least 5 hits and momentum larger than 3 GeV. The results are listed in Table 4.8 along with the fit parameters of Equation 4.13.

Table 4.8: *Table of the fit parameters for the track-to-hit residual trend as a function of momentum. In the table are listed also the intrinsic hit resolutions estimated from data-driven methods [48] and the estimated remaining misalignment σ_{mis} calculated as in Equation 4.14.*

Layer	χ^2/ndf	A ($\mu m\ GeV/c$)	B (μm)	σ_{hit} (μm)	σ_{mis} (μm)	pitch (μm)
BPIX L1	7.3/4	44 ± 4	13 ± 1	\	\	100
BPIX L2	1.7/4	17 ± 1	8.5 ± 1	\	\	100
BPIX L3	4.1/4	29 ± 2	10 ± 1	\	\	100
TIB L1	3.7/4	23 ± 3	18 ± 1	17 ± 4	6 ± 4	80
TIB L2	1.5/4	26 ± 3	19 ± 1	17 ± 4	8 ± 4	80
TIB L3	1.6/4	49 ± 3	24.5 ± 1	22 ± 2	11 ± 2	120
TIB L4	4.8/4	58 ± 3	27.5 ± 1	26 ± 2	9 ± 2	120
TOB L1	5.1/4	55 ± 5	42.5 ± 1	41 ± 4	11 ± 4	183
TOB L2	12.6/4	60 ± 8	44 ± 1	41 ± 4	15 ± 4	183
TOB L3	2.5/4	55 ± 3	39.5 ± 1	36 ± 4	16 ± 4	183
TOB L4	4.8/4	63 ± 4	38 ± 1	36 ± 4	12 ± 4	183
TOB L5	1.14/4	85 ± 2	31.5 ± 1	24 ± 2	20 ± 2	122
TOB L6	51.8/4	220± 9	56 ± 20	24 ± 2	50 ± 20	122

The values of σ_{mis} obtained with this technique can be directly compared with the values obtained by the DMR (distribution of median of residuals) analysis, layer by layer, reported in Figure 4.33. The comparison is shown in Figure 4.34.

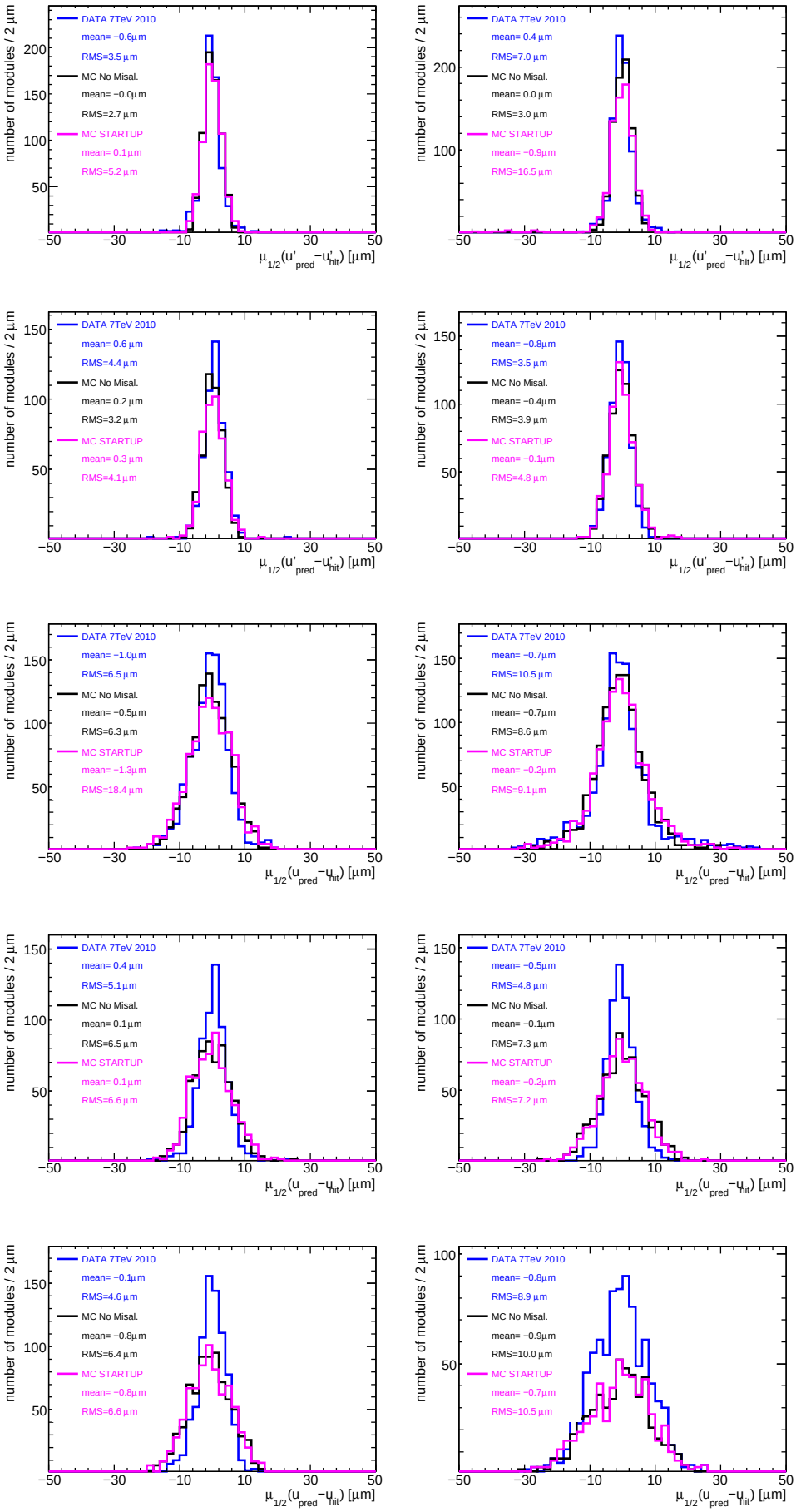

Figure 4.33: *Distribution of the DMR for each layer of the Barrel of the Strip Tracker.*

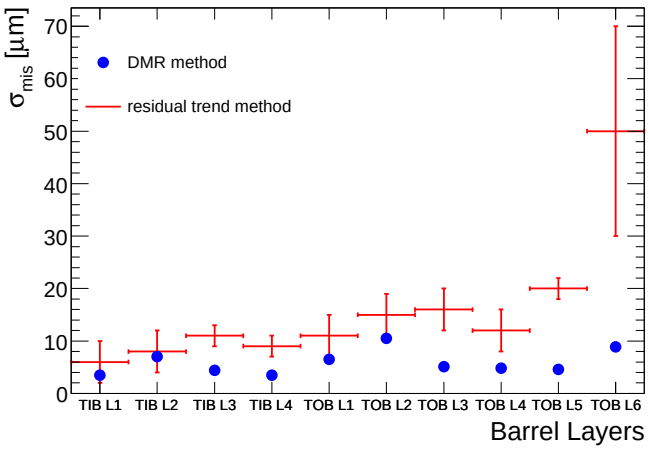

Figure 4.34: *Comparison between the estimated alignment precision obtained with the DMR method (blue) and the residuals vs momentum trend (red).*

The agreement obtained is fair given the large uncertainty of the method due for example to the mixing of different track incidence angles which accounts for a factor up to 1.4 ($= 1/\cos\theta_{3D}^{min}$). The largest discrepancy is observed in the last layer of TOB which is the least populated in terms of hit occupancy hence the one with the highest statistical uncertainty. Moreover, as explained in Section 3.3.1, TOB Layer 6 has not a forward predicted track extrapolation and the trajectory state vector at its surface completely relies on the backward prediction, giving an intrinsically worse track prediction. This is clearly seen in Figure 4.35 in which the width of the residual for TOB Layer 6 is much larger than the one for the other layers.

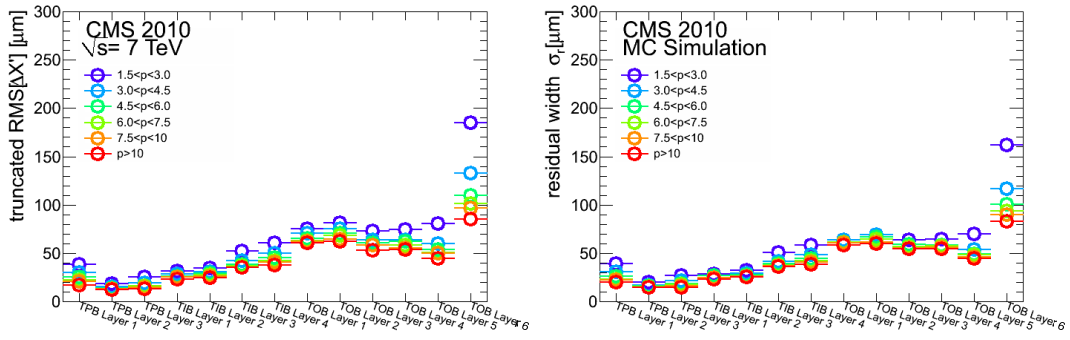

Figure 4.35: *Distribution of track-to-hit residuals widths plotted as a function of the Barrel layer for minimum bias tracks with the selection described in the text, for the six momentum bins considered in the analysis.*

4.3.2 Tracking performance after aligment with collision tracks

Collision and cosmic tracks samples were used for combined alignment after the first period of LHC operations. Using the same geometry for track fit, similar tracking performance was expected in the two samples. Figure 4.36 shows the distribution of the χ^2 per degree of freedom of tracks after alignment. Cosmic and collision tracks have distributions with a different shape and mean value.

The mean value of the χ^2/ndf of the cosmic tracks was found higher than unit, while the distribution for minimum bias tracks lower than unit. The right part of Figure 4.36

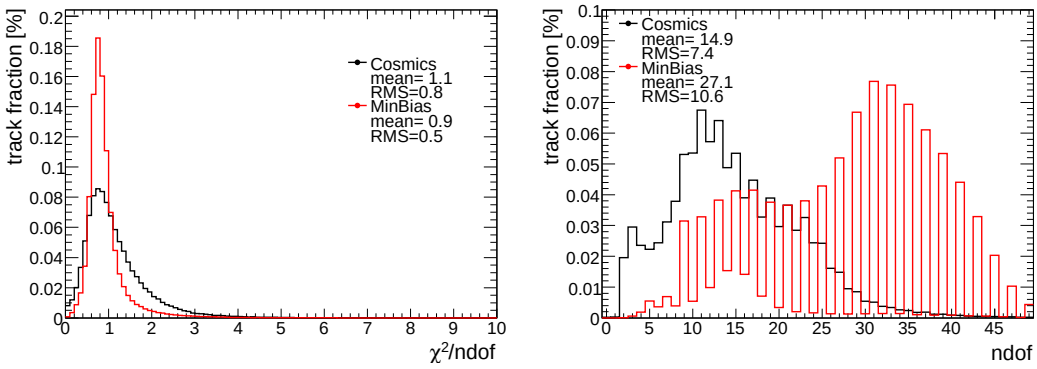

Figure 4.36: *Left: distribution of χ^2/ndf for comsic (black) and minimum bias (red) tracks, after alignment with a mixed track sample. Right: distribution of the number of degrees of freedom.*

shows that distribution of the number of degrees of freedom for the two track samples is largely different, with minimum bias tracks having far more hits, with a distinctive "comb-like" pattern due to the fact that collision tracks pass either through Pixel or double-sided layers of Tracker Endcaps, hence producing peaks at $ndf = 2k - 5$.

The effect of the different distribution of number of degrees of freedom, was tested on a simple toy Monte Carlo simulation. Figure 4.37 shows the obtained distribution of χ^2/ndf, while in Table 4.9 are listed the values of the obtained RMS[4] compared with the ones measured in data. Clearly the different distribution of ndf of the track fit produces a difference in the expected RMS but not enough to account for the large dicrepancy observed in data.

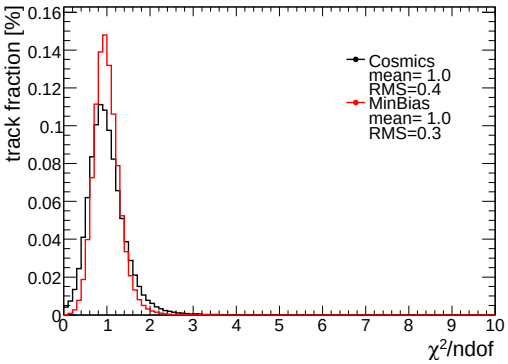

Figure 4.37: *Distributions of χ^2/ndf obtained from pseudo-experiments for cosmic and minimum bias spectra of number of degrees of freedom .*

Since the χ^2/ndf distribution depends on the number of degrees of freedom, it is

[4]Since a random variable distributed as a χ^2/ndf is expected to have RMS$= \sqrt{2/ndf}$, the expected RMS of the generated distribution is :

$$(RMS)_{exp} = \sqrt{\sum_{i}^{ndf} w_i \left(\sqrt{\frac{2}{i}}\right)^2} \tag{4.16}$$

where w_i is the fractions of tracks with i degrees of freedom.

Table 4.9: *Table of the applied parameters applied to obtain the calibrated APE after the CRAFT aligmnent in Tracker Pixel and Tracker Endcaps.*

	RMS		Mean	
Sample	DATA	Toy MC	DATA	Toy MC
Cosmics	0.75	0.44	1.1	1.0
Minimum Bias	0.49	0.30	0.9	1.0

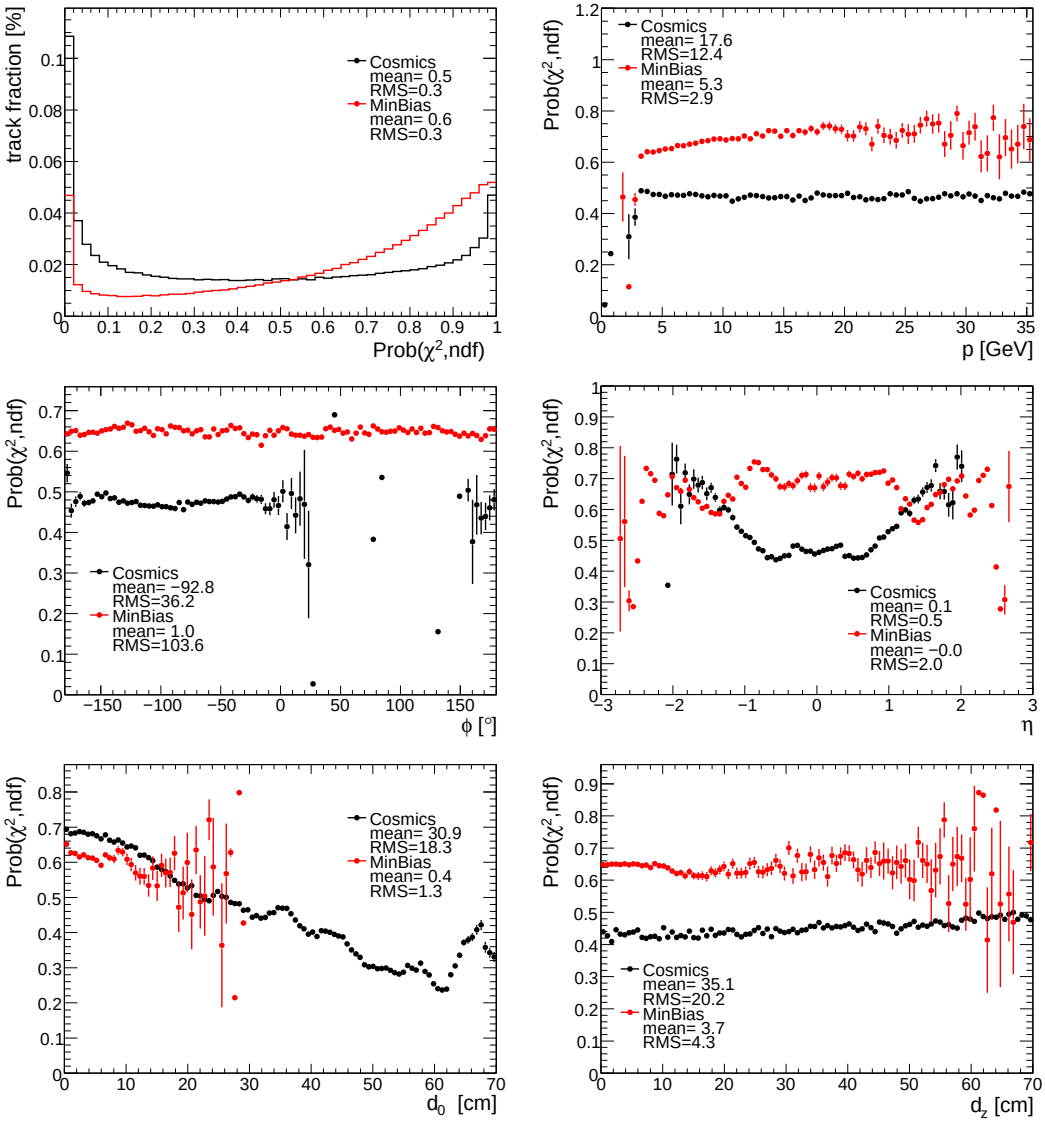

Figure 4.38: *Top row: distribution of $Prob(\chi^2, ndf)$ (left) and its profile vs track momentum. Middle row: profiles of $Prob(\chi^2, ndf)$ vs azimuthal angle (left) and pseudorapidity (right). Bottom row: profiles of $Prob(\chi^2, ndf)$ vs transverse impact parameter (left) and longitudinal impact parameter (right).*

convenient to consider the χ^2 probability which is independent from it. A uniform distribution with $\mu = 1/2$ and RMS $= 1/\sqrt{12}$ is expected when correct errors are assigned. In Figure 4.38 are shown the $Prob(\chi^2, ndf)$ distributions obtained for cosmic and minimum bias tracks, and the profiles against the track parameters. The $Prob(\chi^2, ndf)$ distribution for minimum bias tracks is unbalanced towards higher probabilities, not surprisingly because of the non-calibrated values of the APE. This effect is present in all the projections vs the track parameters. The cosmic track sample instead shows a remarkable uniformity in all the projections, a part from η (due to an improvement of the aligment performance in the endcap regions still not compensated by a correponding decrease of the errors) and in the profile in bins of the transverse track parameter. This feature observed in the alignment validation was confermed also by the *global* alignment algorithm (Figure 4.39), by inspecting the internal *MillePede* $Prob(\chi^2, ndf)$ of the track refit.

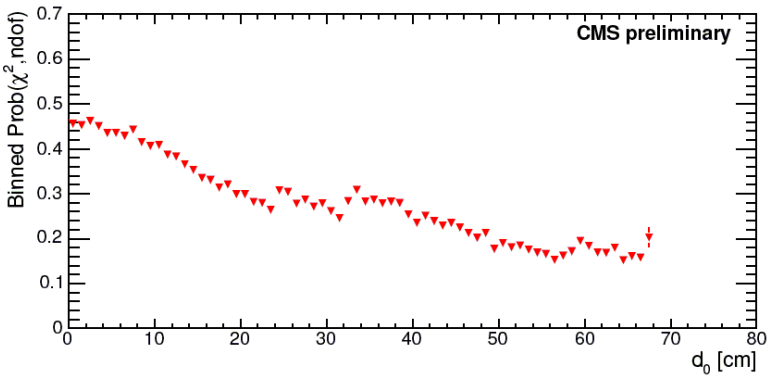

Figure 4.39: *Distribution of the probability of the internal Millepede-II χ^2 function vs. the transverse impact parameter of the track. Data: Cosmic ray muons, recorded in 2010 during commissioning of CMS. 200 000 tracks used [36].*

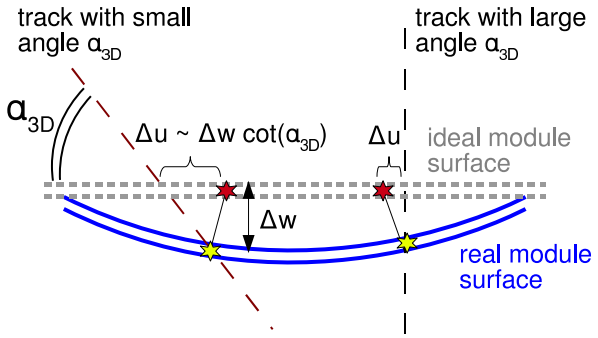

Figure 4.40: *Sketch explaining how track-to-hit residuals can get deteriorated by a non-planarity of the module active surface. The module surface distortion has been greatly exaggerated.*

This effect has been explained by certain degree of non-planarity of the module active surface. In Figure 4.40 is shown how, if the module surface has a non-planar geometry (for example a bowing in the $u - w$ plane), the track-to-hit residuals can get deteriorated. The effect is larger when the track angle from the module surface α_{3D} $= \pi/2 - \theta_{3D}$ (defined in Figure 4.25) is small. The track impact angle for collision

tracks is driven by $(q/p) \cdot r_{hit}$[5] while for cosmic traks is driven by d_0/r_{hit} where d_0 is track transverse impact parameter.

Figure 4.41 explains the behaviour of the track angle α_{3D} as a function of the transverse impact parameter for cosmic tracks in the Tracker Barrel. A cosmic track with small d_0 shows rather large track angle at every hit. For larger values of the impact parameter, the track angles at the innermost hits are smaller, and the χ^2 gets deteriorated by a wrong surface description. When the impact parameter becomes larger than the radius of a layer, the innermost hit is lost and the χ^2 jumps to a better, though still lower than ideal, value. This explains the jumps seen in the $Prob(\chi^2, ndf)$ as a function of d_0 shown in Figure 4.38.

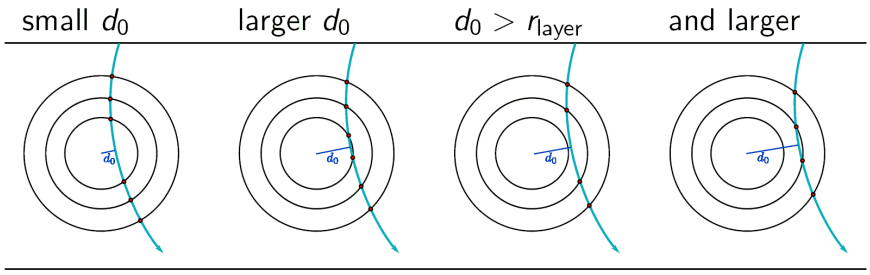

Figure 4.41: *Sketch explaining the behaviour of the track angle α_{3D} as a function of the impact parameter for cosmic tracks in the Tracker Barrel.*

Figure 4.42 shows the distributions of the impact track angle α_{3D} separately for BPIX, TIB and TOB for cosmic ray data and collision data collected during 2010. In general the impact track angle α_{3D} (a part from BPIX) is smaller in the cosmic ray sample. Explicit cuts on the angle (as detailed in Table 4.5) are visible.

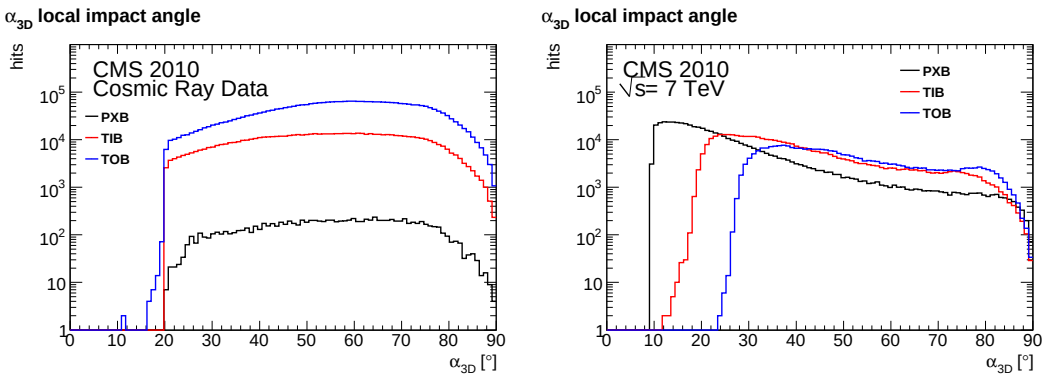

Figure 4.42: *Distributions of local impact angle of the track on the module surface α_{3D} for cosmic ray data (left) and minimum bias tracks (right).*

Figure 4.43 shows the trend of the RMS of track-to-hit residuals in BPIX, TIB and TOB as a function of the local track angle α_{3D}. As expected track-to-hit residuals are broader for grazing impact angles. The TOB residuals for collision tracks are larger than in the cosmic data sample, due to the softer track momentum spectrum and because of the enhanced multiple scattering due to the amount of material that particles have to cross before reaching the TOB. For small angles, the TIB residuals

[5] r_{hit} is radius of the hit in the global r coordinate.

are larger in cosmic data than in collision probably due to the non-planarity effect discussed above.

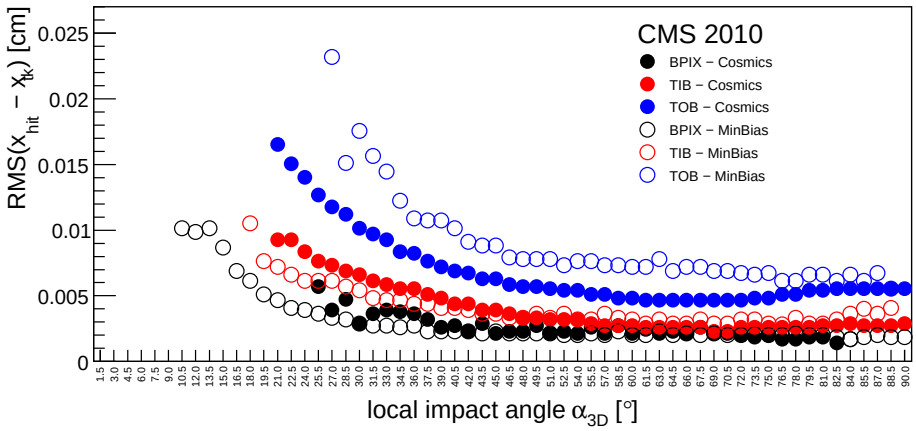

Figure 4.43: *Profiles of track-to-hit residuals in the sensitive coordinate as a function of track impact angle, in BPIX, TIB and TOB, for cosmic ray and collision tracks.*

4.4 Calibration of Alignment Position Errors

Alignment Position Errors (APE) are the estimated uncertainty on the module position in the three global coordinates. The APE are combined with the spatial resolution and the track extrapolation uncertainty of a given detector, giving the total error on the position, in global coordinates, of hits belonging to these detector modules.
The APE have a direct impact on the track reconstruction (see Figure 4.44):

- Efficiency: The bigger the APE is, the higher is the probability to associate misaligned hits to a given track seed or to match hits in two misaligned sub-detectors to one track. With the APE large enough one should almost always get the maximal track recontruction efficiency (See Figure 4.45).
- Fake rate: Setting the APE to a large value makes it more likely that a track is built out of uncorrelated hits, thus dramatically increasing the rate of fake tracks and, as a side effect, also increasing the amount of required computing time for the reconstruction.
- Momentum resolution: the p_T resolution is affected by the APE in three ways:
  - The probability of including uncorrelated hits into a track is increased with higher APE settings. This leads to an additional p_T smearing.
  - Even when a track includes only correctly associated hits, their relative weight in the fit can be distorted by the misalignment assigning larger weight than it should. The inclusion of appropriate APE reduces this bias, by a more realistic weight assignment, having as a consequence a global improvement of the resolution on all track parameters.
  - It can also alter the track fit procedure, through the artificial decrease of the χ^2, stopping the procedure before the real minimum is reached.

APE play a crucial role also in the significance of the track impact parameters used in b-tagging techniques. Figure 4.45 shows the results for the effect of choosing too large or too small APE on the "high efficiency track counting" b-tagging algorithm, on a simulated collision sample.

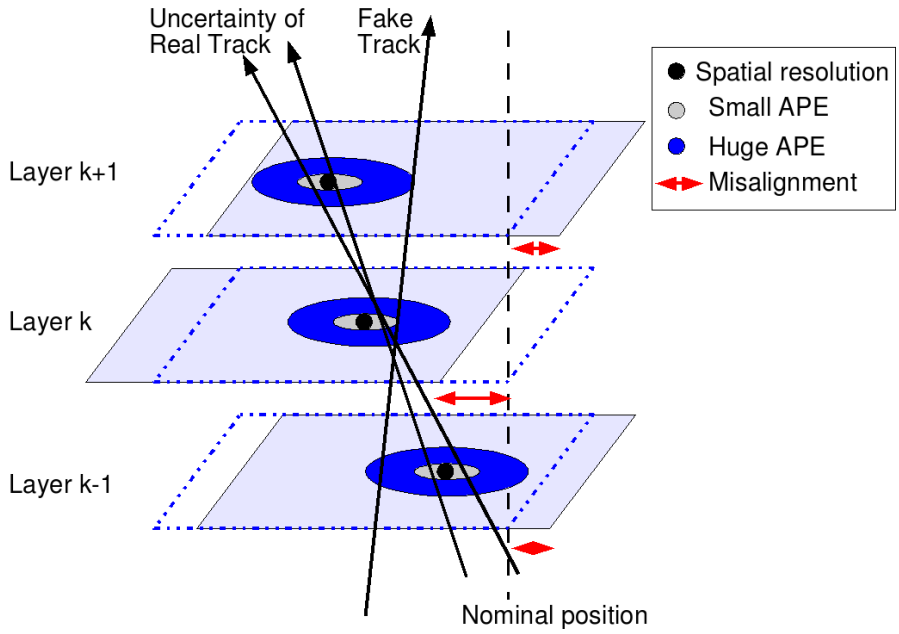

Figure 4.44: *Effect of APE settings on the tracking efficiency and fake rate.*

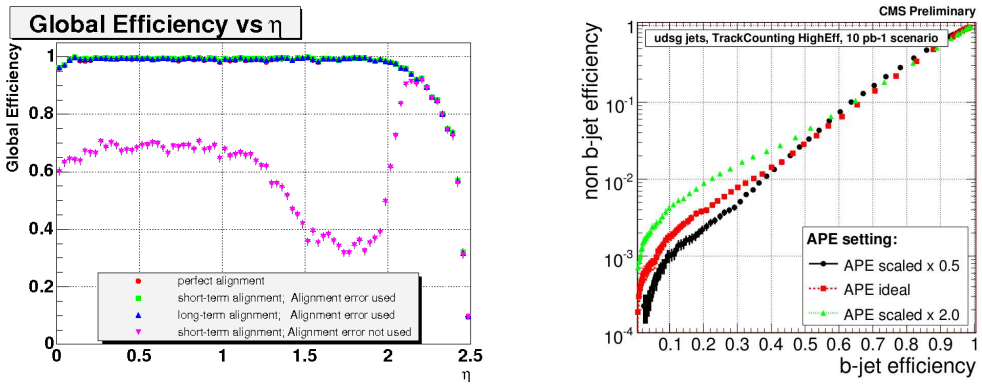

Figure 4.45: *Left: Track finding efficiency vs η for simulated muons with $p_T = 100$ GeV. If the alignment uncertainty is not accounted for, the efficiency is significantly degraded [37]. Right: simulated b-jet efficiency versus non b-jet efficiency for a misalignment scenario close in performace to the "Startup" conditions, shown for the track counting high efficiency algorithm with an APE that is chosen too large or too small by a factor of two with respect to the ideal value [49].*

Therefore for the exact determination of the track parameters, an APE as close as possible to the RMS of the residual misalignment is preferred.

The CMSSW software allows to specify APE as a 3×3 symmetric matrix, but the actual choice was to neglect correlations between coordinates and assume that only diagonal terms are present in the matrix:

$$V_{APE} = \begin{pmatrix} d_{xx} & d_{xy} & d_{zx} \\ d_{xy} & d_{yy} & d_{zy} \\ d_{zx} & d_{yz} & d_{zz} \end{pmatrix} = \begin{pmatrix} R_{xx} & 0 & 0 \\ 0 & R_{yy} & 0 \\ 0 & 0 & R_{zz} \end{pmatrix}$$

The uncertainty $\sigma^2_{\xi,align}$ of alignment parameters on the ξ coordinate ($\xi = x, y, z$), is included in track reconstruction via a sum in quadrature to the intrinsic resolution per coordinate to the give effective hit resolution:

$$\sigma^2_{\xi,eff} = \sigma^2_{\xi,hit} + \sigma^2_{\xi,align} \tag{4.17}$$

Track reconstruction depends strongly on alignment parameters $\mathbf{p}$ but also on APE, since it is based on minimization of normalized residuals.

$$\frac{R_{ij}(\mathbf{q},\mathbf{p})}{\sigma_{ij,tot}} = \sigma^{-1}_{ij,tot}\left(\xi'_{ij,track}(\mathbf{q},\mathbf{p}) - \xi'_{ij,hit}\right) \quad \sigma_{tot} = \sigma_{tot}(\sigma_{\xi,track}, \sigma_{\xi,eff}) \tag{4.18}$$

4.4.1 APE determination during comic ray data taking

The initial values of the APEs used for the prompt track reconstruction during the CRAFT, the so called "default" APE set, were large as they had to account for possible large displacements of the entire detector while still guaranteeing an efficient track-hit association. Those APEs were uniform for each sub-detector, meaning that a single value was chosen for all the modules belonging to it.

A new set of APEs was calibrated using cosmic ray data at the end or the CRAFT data taking, based on the set of alignment parameters obtained from the combined method described in Section 4.1.1 . After the alignment procedure, the resulting geometry was planned to be used for the subsequent data-taking period and it was necessary to update the position uncertainty of the Tracker modules according to the new estimated position precision, since, as it has been said before APE play a crucial role in the assignment of track momentum uncertainty, or in b-tagging techniques.

As a further simplification, in the track refit the APE for each hit was assumed to be the same in the three spatial directions (i.e. $R_{xx} = R_{yy} = R_{zz} = R_{APE}$), so the problem of assigning an APE, was reduced to producing one number for each module of the Tracker.

For an alignment performed using cosmic ray tracks, the achieved alignment precision varies within a given sub-detector because of the different illumination of modules due to their orientation relative to cosmic rays. Figure 4.46 illustrates the hit occupancy of the CMS Tracker during the cosmic data taking of CRAFT, showing that the top and bottom part of the CMS Tracker barrel were the most illuminated regions of the detector, while in the Tracker Endcaps and the Pixel Tracker a relatively small amount of hits were recorded due to the geometric acceptance of these subdetectors.
Given the large dispersion of remaining misalignment within a sub-detector or even within a layer, it was decided to calibrate the APE with the highest granularity, ideally

on a module by module basis.

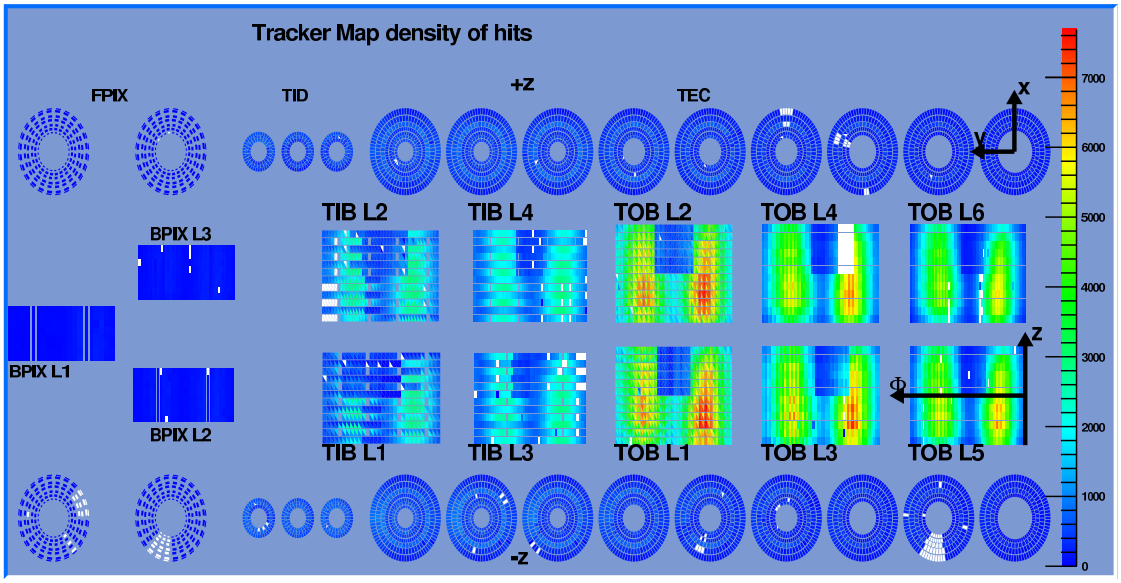

Figure 4.46: *Hit density map for CRAFT data, showing how the top and bottom part of the CMS Tracker Barrel were the most illuminated regions of the detector*

The strategy to determine the APE was the following:

- Identify a "fiducial" well illuminated and well aligned region inside the Tracker;
- Use the track-to-hit residuals and the DMR method in this fiducial region to estimate the remaining misalignment for each layer and assign this value as APE;
- Determine a law for rescaling the errors in the regions outside the fiducial volume to account for the different illumination;
- Finally, refine iteratively the estimate by correcting the value of the errors until the pull of the normalized residuals is found about unit;

As a fiducial region, the uppermost quarter of the TIB and TOB was chosen, being the best illuminated. Tracks were selected according to the hit pattern to satisfy a test-beam like pattern with all the tracks crossing all the ten Barrel Layer. To minimize the multiple scattering contribution to the track hit uncertainty, a cut on the point of closest approach (PCA) to lie within the BPIX volume was applied ($|z_{PCA}| < 30$ cm and $\sqrt{x^2_{PCA} + y^2_{PCA}} < 12$ cm) to select tracks pointing to the nominal interaction point. The effects of the cut are visible in Figure 4.47. The cosine of the impact angle on the module surface $\cos\theta_{3D}$ after the cut is peaked to 1, hence reducing the effective silicon thickness crossed by the cosmic ray. The normalized χ^2 of the track fit, for tracks passing in the selected region, improves while no bias is introduced in the track momentum spectrum.

The fiducial region illuminated after this cut is presented in Figure 4.48

Using a simulated data sample and results obtained after alignment on data, a trial and error procedure has been performed in order to provide an estimation of the remaining random misalignment of the modules in the fiducial region.

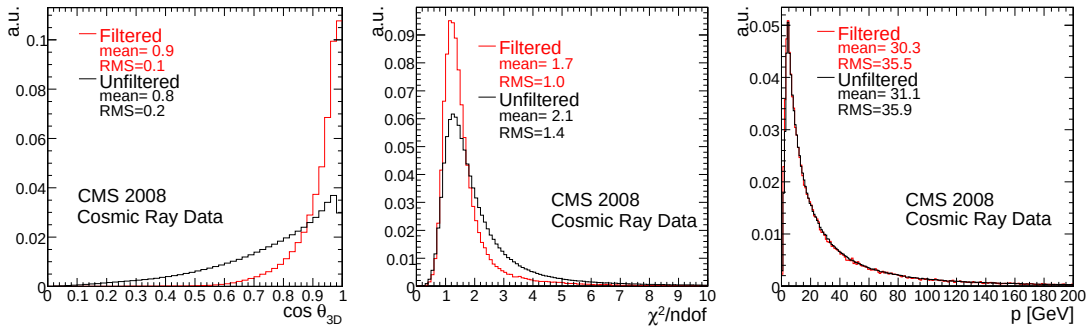

Figure 4.47: *Distributions of the cosine of the local impact angle* $\cos\theta_{3D}$ *(left), normalized* χ^2 *(center), track momentum (right) before and after the cut on the position of the point of closest approach.*

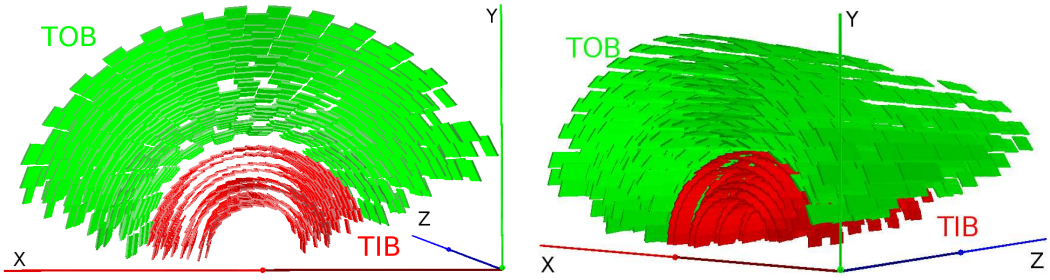

Figure 4.48: *Control region of the Strip Tracker used as a control region to determine the starting values in the APE calibration procedure.*

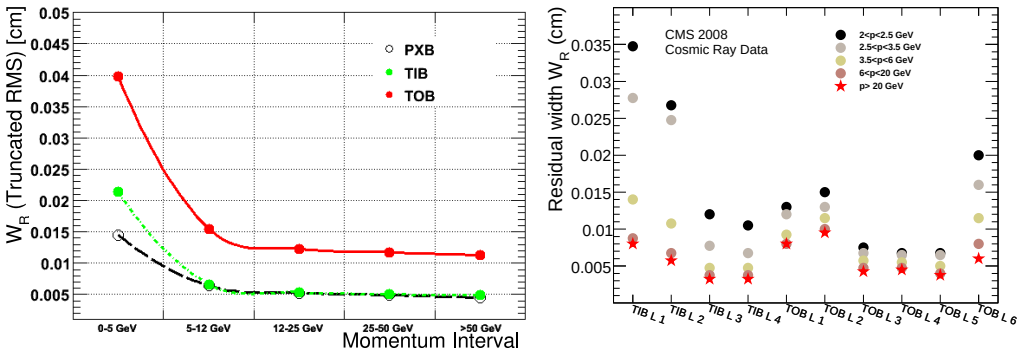

Figure 4.49: *Left: width of residuals as a function of track momentum for all cosmic tracks in TIB, TOB and Pixel Barrel. Right: Layer-wise trend of residuals as a function of momentum for tracks in the fiducial volume. The reference trend of residuals for CRAFT data is high-lighted in red, corresponding to* $p > 20$ *GeV*

The procedure consists of the following steps:

- Modules not selected in the fiducial volume are excluded from the residual distribution and from track refits;
- Truncated mean and RMS values are calculated from the central 98.76% interval of each distribution, 2.5 σ for a Gaussian-distributed variable, for each layerwise residual distribution (TIB and TOB) after alignment on data;
- Studying the trend of the width of the residuals as a function of track momentum (see left part of Figure 4.49) for the full data sample, it is possible to see how the trend starts to saturate at about 20 GeV. This is the kinematical region where the data-MC matching will be done;
- Using a simulation of the detector, the modules in TIB and TOB are randomly shifted in three dimension according to Gaussian distributions;
- Several scenarios with different misalignment were applied to the design ("true") Tracker geometry used to reconstruct the simulated data until the truncated RMS of their layerwise residual distribution, and the distribution of the median of residuals of TIB and TOB are found to be similar to those in data in all layers (right part of Figure 4.50 and Figure 4.53).

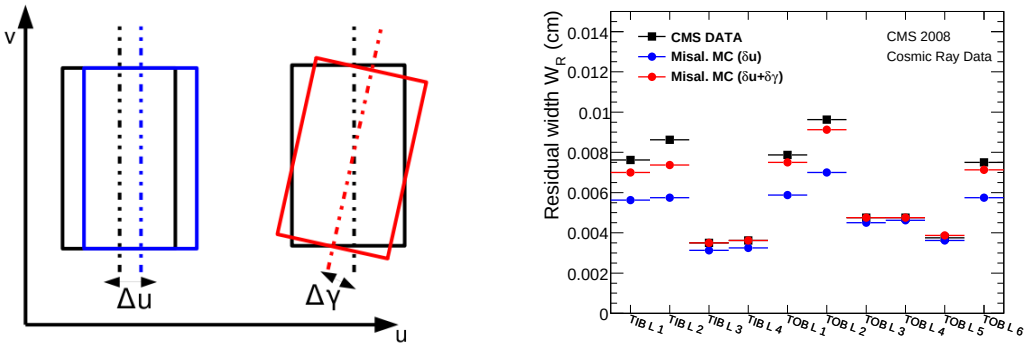

Figure 4.50: *Left: Sketch of the random shifts applied to the modules in the simulation. Right: Layerwise residual distribution, DATA is black, MC reconstructed with misalignment only in u' direction is represented in blue, while in red is represented MC reconstructed with misalignment in u' and* γ.

The most effective movements introduced in the misalignment scenario to reproduce the features of the aligned data are the shifts in u' (movement along the sensitive coordinate) and γ (rotation around the axis perpendicular to the module plane), see left part of Figure 4.50.

Misalignment was applied with different amplitudes for different layers, and separately for stereo and rϕ modules in the double-sided layers. The random translation of the module surface in the u' coordinate was sufficient to reproduce the observed witdh of the DMR distribution (see Figure 4.53) but not to reproduce the non gaussian tails seen in the track-to-hit distributions (see Figures 4.51 and 4.52). An additional misalignment in γ was necessary to catch the tail of the residual distributions, in particular in the double sided layers of TIB and TOB (Figure 4.50).

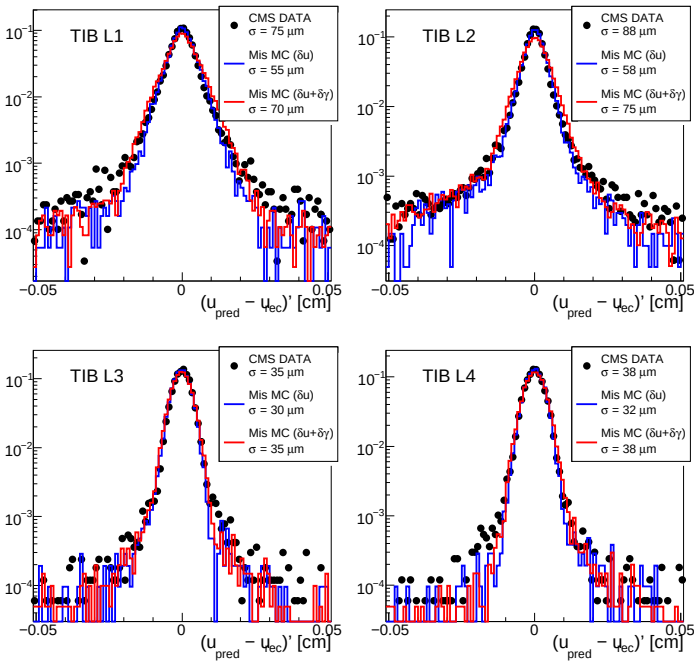

Figure 4.51: *Distribution of residuals for the four layers of TIB. DATA is black, MC reconstructed with misalignment only in u' direction is represented in blue, while in red is represented MC reconstructed with misalignment in u' and γ.*

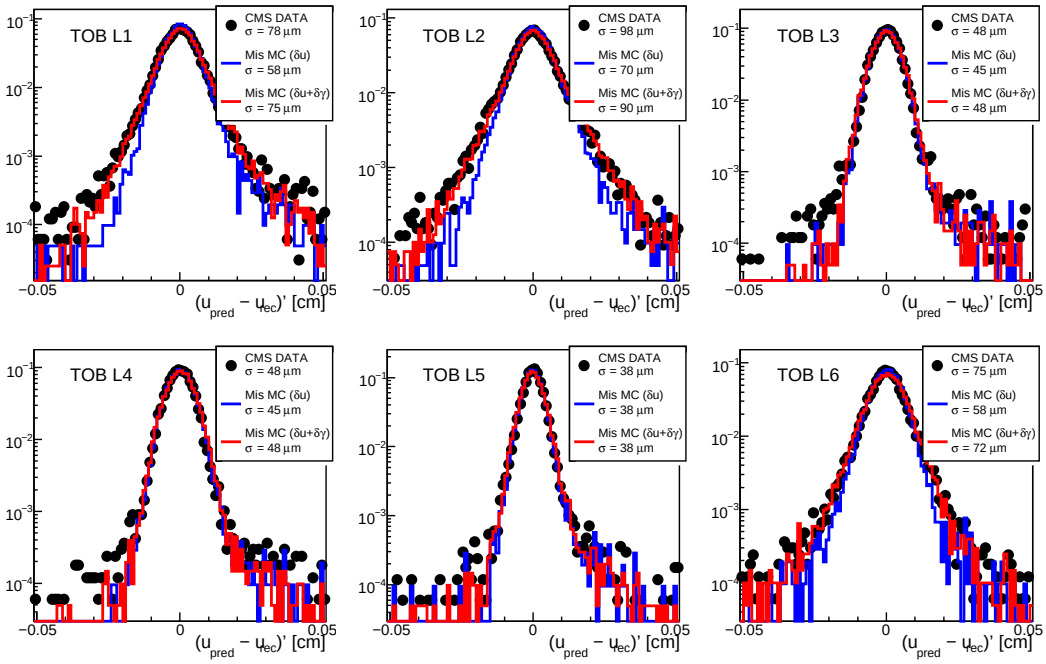

Figure 4.52: *Distribution of residuals for the six layers of TOB. DATA is black, MC reconstructed with misalignment only in u' direction is represented in blue, while in red is represented MC reconstructed with misalignment in u' and γ.*

In TIB and TOB the minimum value of the radius of the sphere representing the APE for each module, R_0, was therefore constructed taking into account the remaining misalignment measured in the fiducial volume via:

$$R_0 = \delta u' \oplus \tfrac{L}{4}\delta\gamma \quad \text{in TIB/TOB}$$

The terms $\delta u', \delta\gamma$ are the remaining misalignments in the u', γ coordinates, estimated by introducing the random misalignment (gaussian distributed) in the simulation to match the residuals and DMRs as observed in data, while $L/4$ is the average lever arm of the rotation if L is the module length ($L_{TIB} = 11.7$ cm and $L_{TOB} = 18.6$ cm). In the TIB and TOB, a common R_0 value was defined for each layer and separately for the rϕ and stereo components of the double-sided layers.

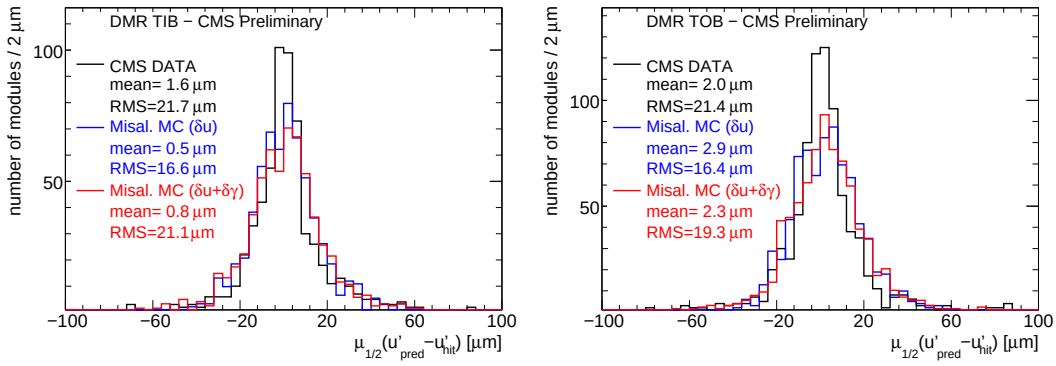

Figure 4.53: *Left: Distribution of DMR for TIB (left) and TOB (right), DATA is black, MC reconstructed with misalignment only in u' direction is represented in blue, while in red is represented MC reconstructed with misalignment in u and γ.*

Elsewhere than TIB and TOB the value of R_0 was defined at the sub-detector by the RMS of the distribution of the median of residuals $\mu_{1/2}(R_i)$, the estimator of residual misalignment described before:

$$R_0 = RMS(\mu_{1/2}(R_i)) \quad \text{in TID/TEC/BPIX/FPIX}$$

To account for the different illumination of the Tracker modules, the radius of the sphere representing the APE for each module, R_{APE}, was than scaled with the number of hits received by a module N_{hits}, using $R_{APE} = \kappa \cdot R_0\sqrt{N_{hits}/N_0}$, where N_0 is a threshold value of number of hits, above which the module is considered well aligned, dependent on the subdetector. The value of κ was chosen in order to have the Gaussian standard deviation of the distribution of the residuals normalized to their error approximately equal to unit in the symmetric interval covering 95 % of the distribution.

The values of R_{APE} were restricted to reasonable values, especially in the case of small or null N_{hits} , where a precision compatible with survey and assembly data was used.
Summarizing the master formula for obtaining calibrated APE was:

$$R_{APE} = \begin{cases} RMS(\mu_{1/2}(R_i)) & RMS(\mu_{1/2}(R_i)) > 3R_{def} \\ R_{def} & N_{hits} < N_{min} \\ \kappa R_0 \cdot \sqrt{\frac{N}{N_0}} & N_{min} < N_{hits} < N_0 \\ \kappa R_0 & N_{hits} > N_0 \end{cases}$$

Where $RMS(\mu_{1/2}(R_i))$ is the RMS of median of local residuals in the sensitive coordinate, R_{def} is the "default" value of the APE before calibration, N is the number of hits per module collected during the data-taking, and (N_0, N_{min}, κ) are parameters tuned on data in order to have pulls of residuals approaching to unit.

In Tables 4.10 and 4.11 are listed the applied parameters to obtain the calibrated APE after the CRAFT aligmnent.

Table 4.10: *Table of misalignment applied to track reconstruction in the simulation to reproduce the observed features of cosmic ray data after alignment in TIB and TOB, and applied parameters to calibrate the APE in the Tracker Strip Barrel.*

Layer	δu (μm)	$\delta\gamma$ (mrad)	R_{def} (μm)	R_0 (μm)	κ	N_0	N_{min}
TIB L12 (r-ϕ)	3	0.7	100	21	0.75	4000	100
TIB L12 (stereo)	15	0.7	100	25	0.75	4000	100
TIB L3	5	0.3	100	10	1.0	4000	100
TIB L4	5	0.4	100	13	1.0	4000	100
TOB L12 (r-ϕ)	11	0.5	100	26	1.0	8000	200
TOB L2 (stereo)	31	0.5	100	39	1.0	8000	200
TOB L3	5	0.3	100	15	1.0	8000	200
TOB L4	10	0.3	100	17	1.0	8000	200
TOB L5	8	0.3	100	16	0.9	8000	200
TOB L6	5	0.3	100	15	0.9	8000	200

Table 4.11: *Table of the applied parameters applied to obtain the calibrated APE after the CRAFT aligmnent in Tracker Pixel and Tracker Endcaps.*

Subdet	R_{def} (μm)	R_0 (μm)	κ	N_0	N_{min}
BPIX	200	14	0.75	400	25
FPIX	300	37	0.75	100	25
TID	300	23	1.0	1600	500
TEC	300	28	1.0	1400	30

A map of the values assigned for each module after the calibration procedure is shown in Figure 4.54.

The first quantity checked after the APE calibration procedure was the χ^2/ndf of the track fit.

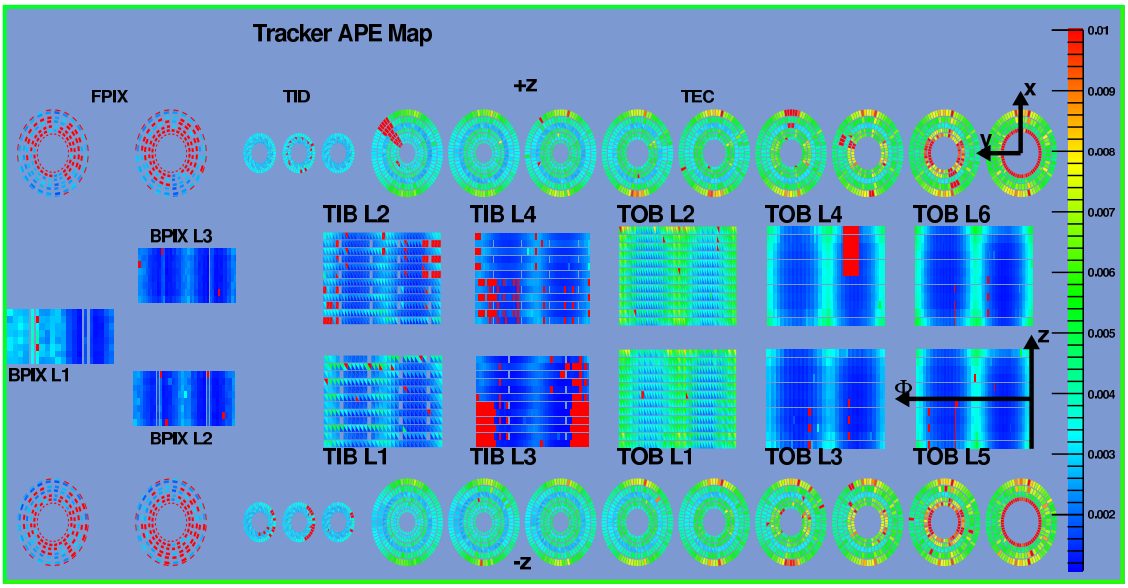

Figure 4.54: *Map of Tracker APE, after CRAFT calibration, large errors are represented with warm colors (towards red), small errors with cold colors (towards blue)*

$$\chi^2/ndf = \sum_{i}^{hits} \frac{R_i^2(\mathbf{q},\mathbf{p})}{\sigma_{i,tot}^2} = \sum_{i}^{hits} \frac{\left(\xi'_{i,track}(\mathbf{q},\mathbf{p}) - \xi'_{i,hit}\right)^2}{\sigma_{i,tot}^2} \tag{4.19}$$

And the total error $\sigma_{tot} = \sigma_{\xi,track} \oplus \sigma_{\xi,hit}$ are functions of the APE, since both the hit uncertainty $\sigma_{\xi,hit}$ and the track extrapolation uncertainty $\sigma_{\xi,track}$ depend on the APE. A proper calibration of the APE implies that the total error should be of the same magnitude of the residuals. This means that the mean value of the χ^2/ndf should be 1.

The χ^2 probability per degree of freedom, defined as:

$$Prob(\chi^2, ndf) = \int_{\chi^2_{obs}}^{\infty} d\chi^2 f(\chi^2) \tag{4.20}$$

being the probability distribution function of a cumulative function of a stochastic variable, should be uniformly distributed with mean value $1/2$ and $RMS = 1/\sqrt{12}$. This translates in the requirement that after the error calibration the following conditions hold:

$$\left\langle \frac{\chi^2(\mathbf{p},\mathbf{q})}{ndf} \right\rangle = 1 \quad \langle Prob(\chi^2, ndf) \rangle = \frac{1}{2} \tag{4.21}$$

In Figure 4.55 are shown the distributions of the χ^2 per degree of freedom and the $Prob(\chi^2, ndf)$ before and after the APE calibration. It is possible to see how the mean value of the χ^2/ndf distribution is shifted towards unit, and the distribution of $Prob(\chi^2, ndf)$ becomes more uniform.

The distribution of the normalized residuals and a simple gaussian fit of the dis-

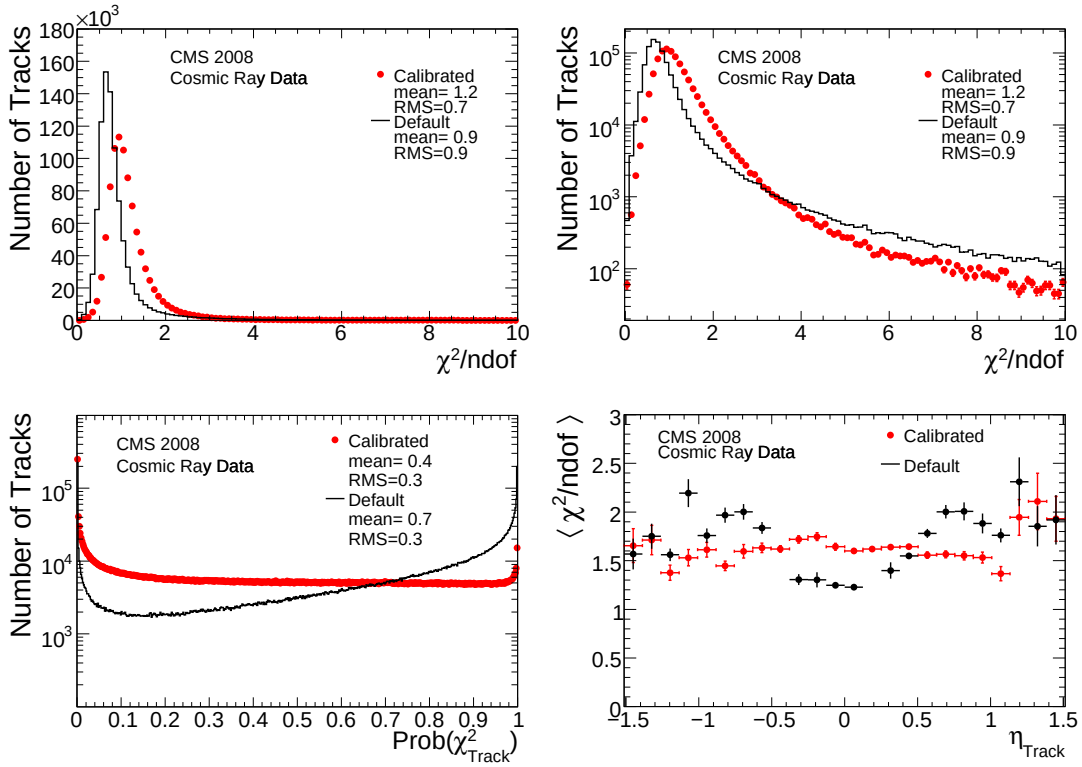

Figure 4.55: *Top row: Distributions of the χ^2 per degree of freedom in linear (left) and logarithmic (right) scale. Bottom row: probability of χ^2 $Prob(\chi^2, ndf)$ (left) and profile of χ^2 as a function of track pseudorapidity (right). In figure are shown distributions before APE calibration (black line) and after (red line)*

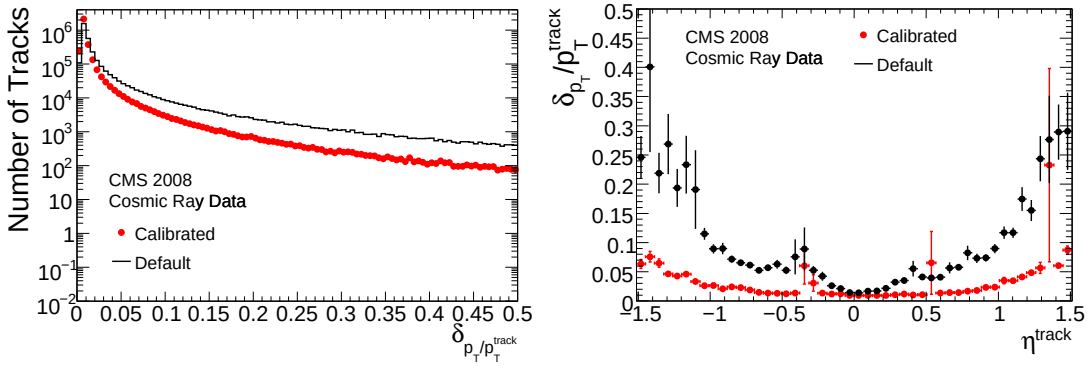

Figure 4.56: *Left: relative track p_T uncertainty. Right: profile of relative track p_T uncertainty as a function of pseudorapidity. In figure are shown distributions before APE calibration (black line) and after (red line).*

tribution, after the calibration of the APE are shown in Figure 4.57 and it can be seen that the pull of residuals for the different Tracker subdetectors is approaching to unit. In Figure 4.58 are shown the distribution of the RMS of normalized residuals: the mean value of the normalized residuals is shifted after the calibration to unit, for all the Tracker subdetectors. In Figures 4.59,4.60,4.61 the RMS of normalized residuals are shown in a $z-\phi$ map, where greenish colors represent a value close to unit, for the Barrel subdetectors and in 4.62 in a $x-y$ map for several disks of TEC. A quite remarkable uniformity of the values close to unit assumed by the pulls can be appreciated here.

Besides checking the impact of APE calibration in terms of track-to-hit residuals, the tracking performance was checked with the track-splitting method described in Section 4.2.3. Splitting long cosmic tracks pointing inside the Pixel Tracker volume at their point of closest approach (PCA), the difference of the two independently reconstructed top and bottom halves of the track were considered for the five track parameters $X = (d_{xy}, d_z, q/p_T, \theta, \phi)$. In Figure 4.63 are plotted the normalized residuals:

$$\frac{X(PCA)_{TOP} - X(PCA)_{BOT}}{\sqrt{\sigma^2_{X_{TOP}} + \sigma^2_{X_{BOT}}}} \tag{4.22}$$

The pull of split track residuals after APE calibration is around 1 for all the track parameters.

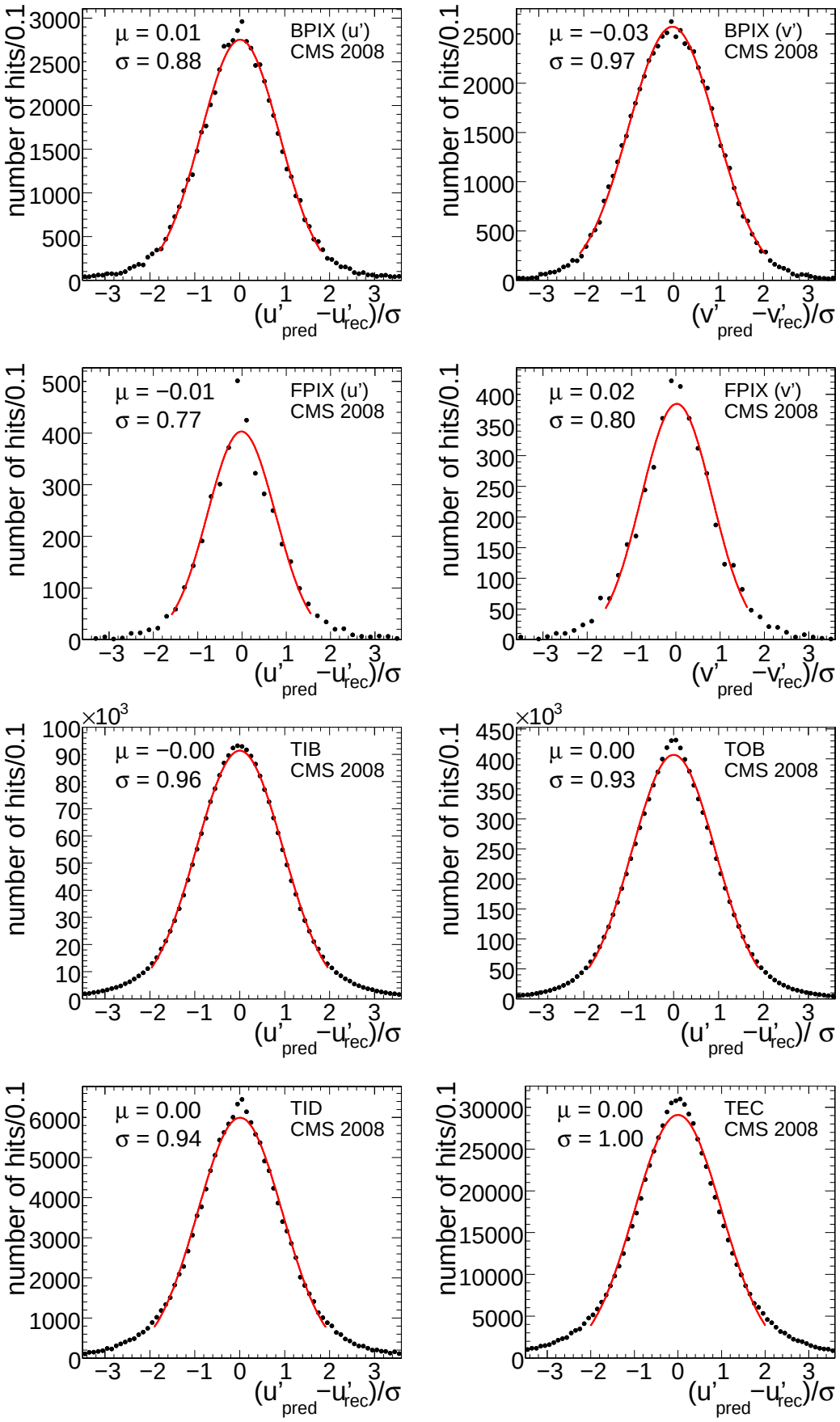

Figure 4.57: *Distributions of normalized track-to-hit residuals after the APE calibration procedure: Top row Barrel Pixel (left u' and right v'), upper midder row Forward Pixel (left u' and right v'), lower middle row TIB (left) and TOB (right), bottom row TID (left) and TEC (right). Solid lines represent the results of Gaussian fits and the fit mean and sigma values are given within the plots.*

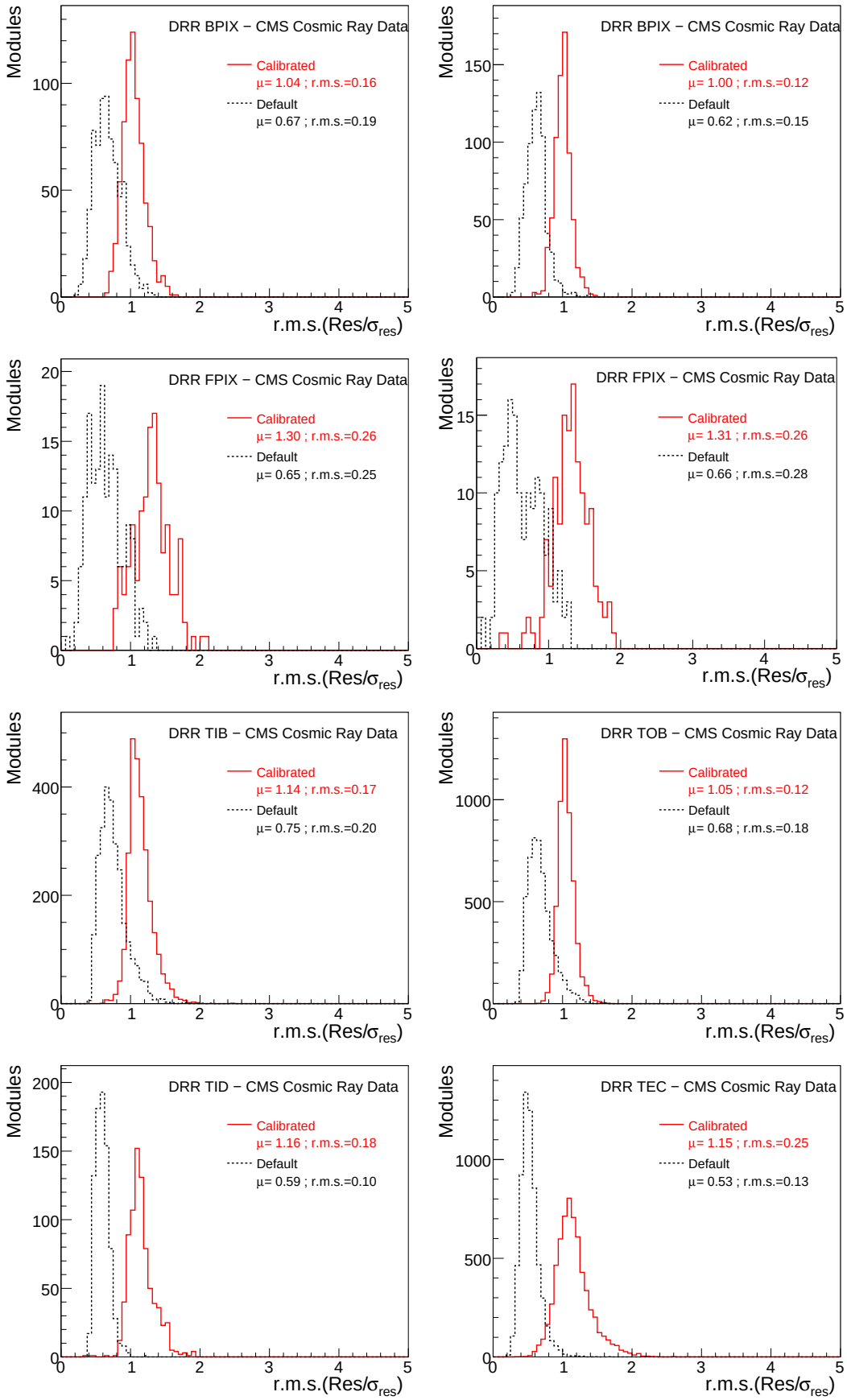

Figure 4.58: *Distributions of the RMS of normalized track residuals after the APE calibration procedure. Top row Barrel Pixel (left u'-coordinate and right v'-coordinate), upper-middle row Forward Pixel (left u'-coordinate and right v'-coordinate), lower middle row TIB (left) and TOB (right), bottom row TID (left) and TEC (right)*

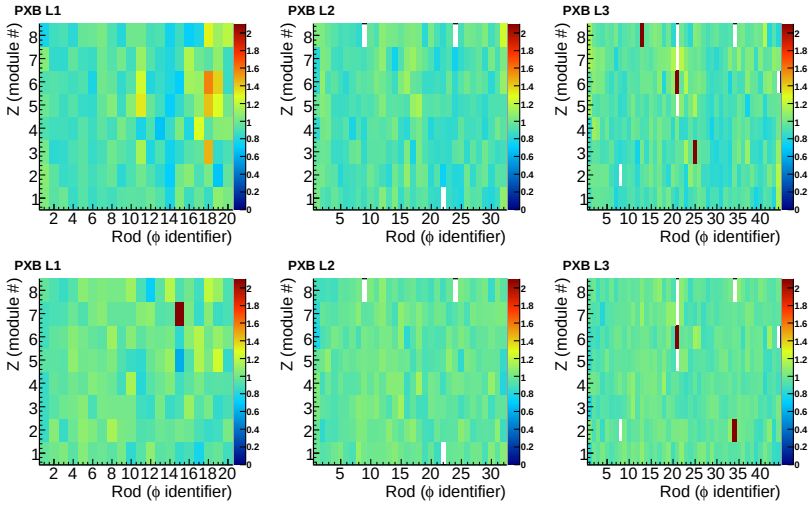

Figure 4.59: *z-ϕ map of RMS of normalized track residuals after the APE calibration procedure for BPIX u' top row and v' bottom row. Each cell represents a module.*

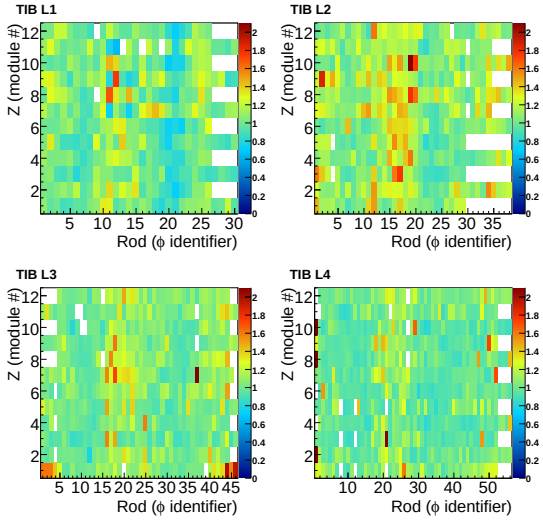

Figure 4.60: *z-ϕ map of RMS of normalized track residuals after the APE calibration procedure for TIB. Each cell represents a module.*

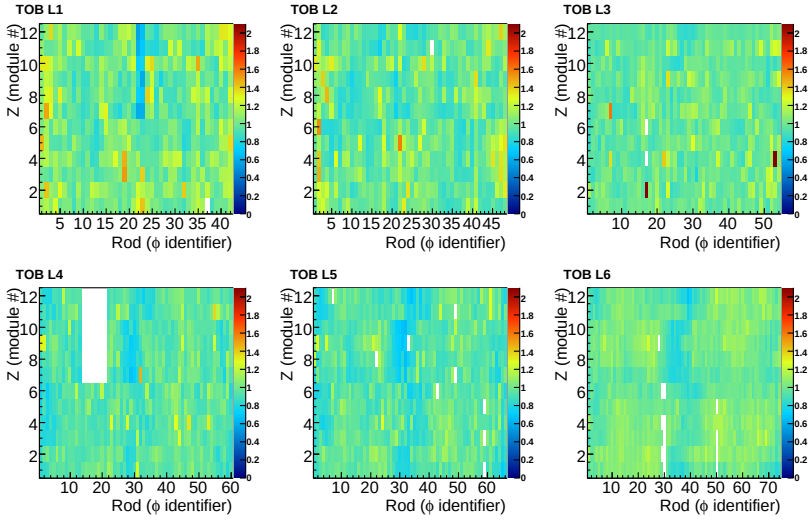

Figure 4.61: *z-ϕ map of RMS of normalized track residuals after the APE calibration procedure for TOB. Each cell represents a module.*

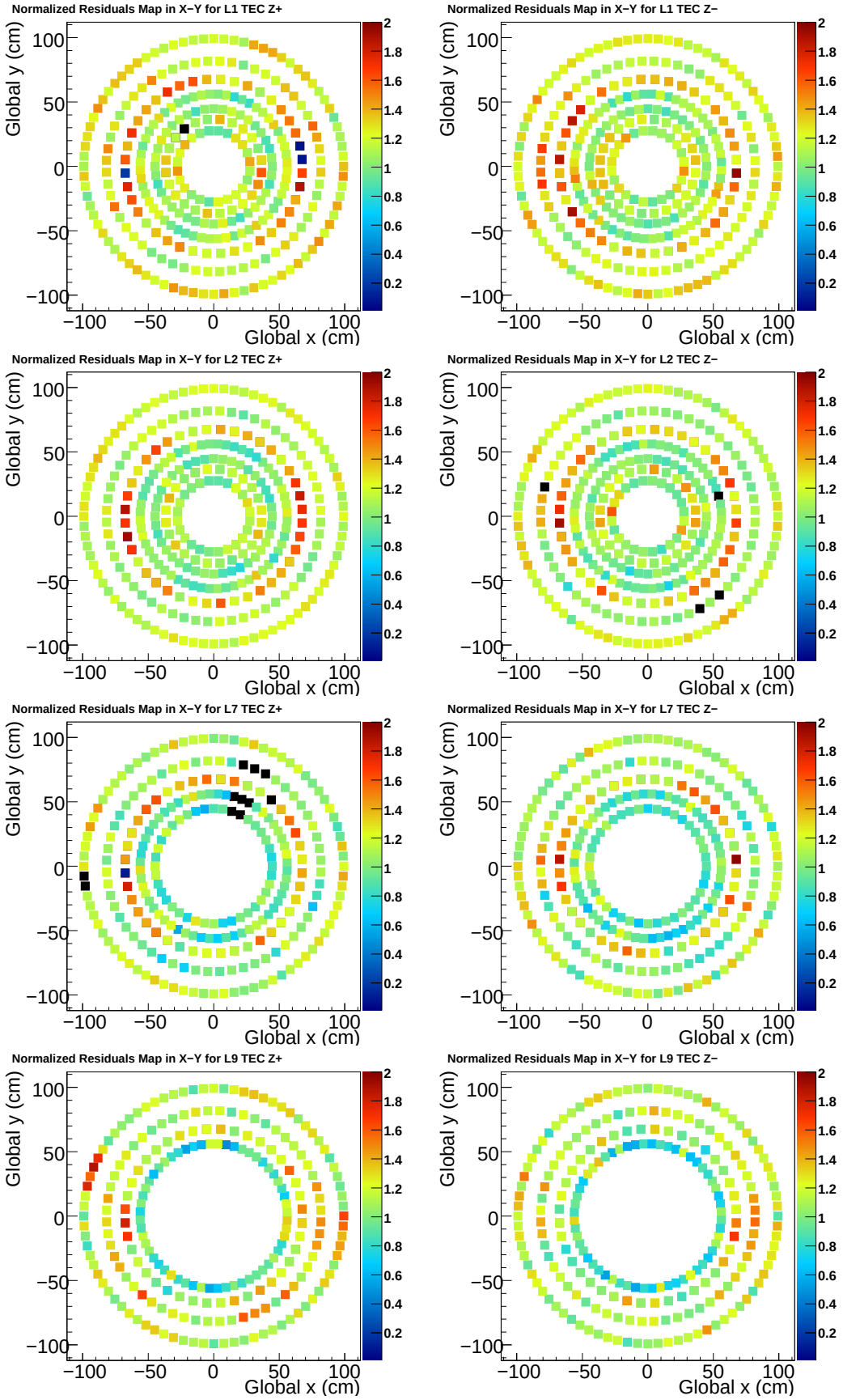

Figure 4.62: $x - y$ *map of RMS of normalized track residuals after the APE calibration procedure for TEC Disk 1,2,7 and 9. Each cell represents a module*

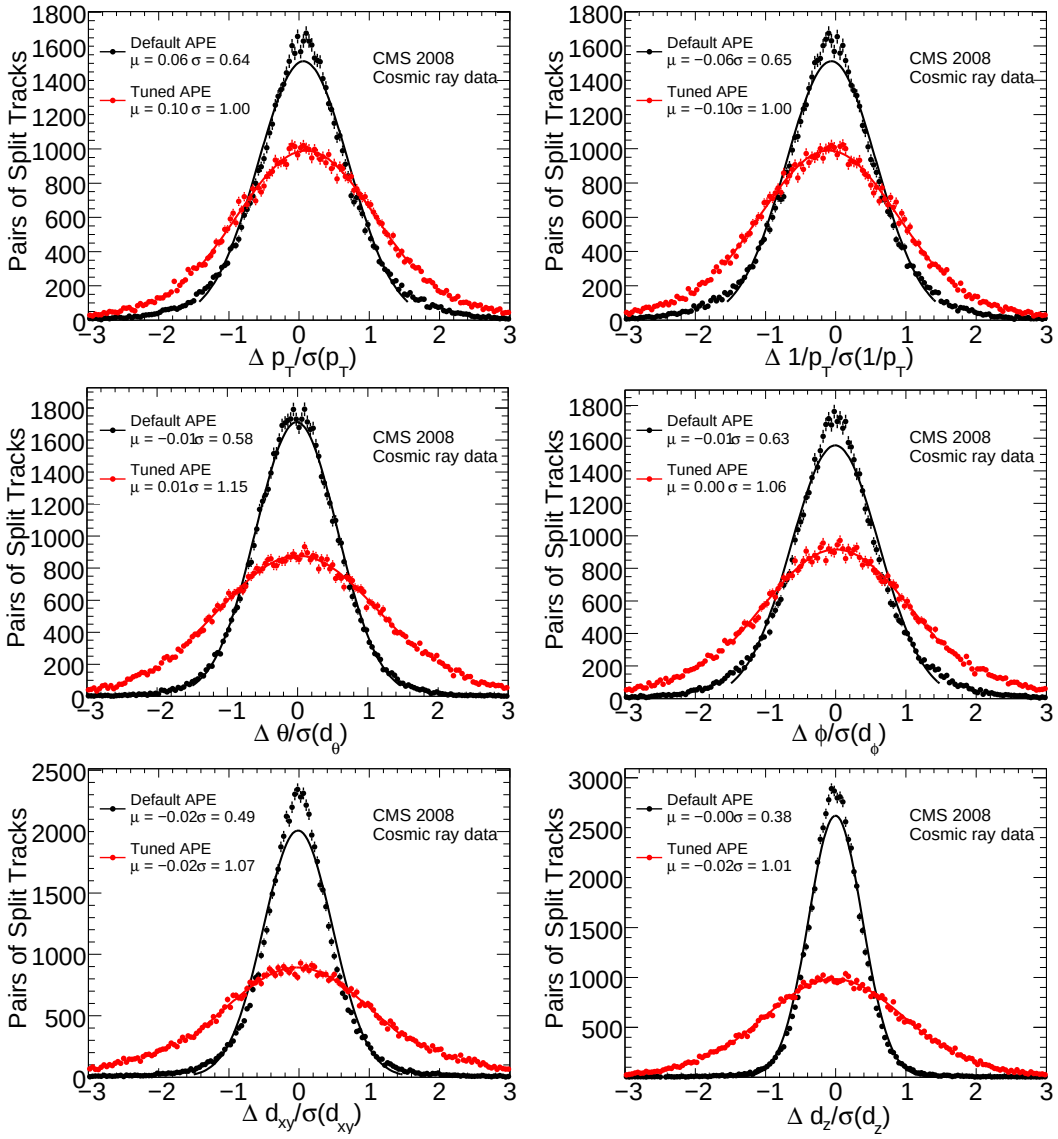

Figure 4.63: *Distributions of normalized split track residuals after the APE calibration procedure, for different track parameters:Top right: tranverse momentum p_T, top left: track curvature $\kappa \sim 1/p_T$ Middle row, right: polar angle θ, right: azimuthal angle ϕ. Bottom, left: transverse impact parameter d_{xy}, right: longitudinal impact parameter d_z*

4.4.2 Evolution of APE

After CRAFT the aligment position errors were updated after each alignment round using the same strategy described in the previous section.
The minimum value assumed by the errors ($C = \min\{R_{APE}\} = \kappa R_0$) in each layer (or subdetector) was tuned on data in order to have pulls of residuals approaching to unit according to the relation:

$$\text{pull} \propto \frac{1}{C}$$

this implies the following equation (see Appendix B):

$$\frac{\text{pull}_{obs}}{\text{pull}_{opt}} = \frac{C}{C_0} \longrightarrow C = \left(\frac{\text{pull}_{obs}}{\text{pull}_{opt}}\right) C_0 \tag{4.23}$$

In Equation 4.23 P_{obs} is the pull of normalized residuals observed before the error calibration, when the old set of errors C_0 was used for track reconstruction; $pull_{opt} = 1$ is the optimal pull and C is the mimimum value assumed by the new set of calibrated constants. This procedure was used several times after each main release of new alignment constants. Figure 4.64 shows how the minimum value of APE has evolved from CRAFT data-taking until the alignment based on 2010 collision data ("beam 10").

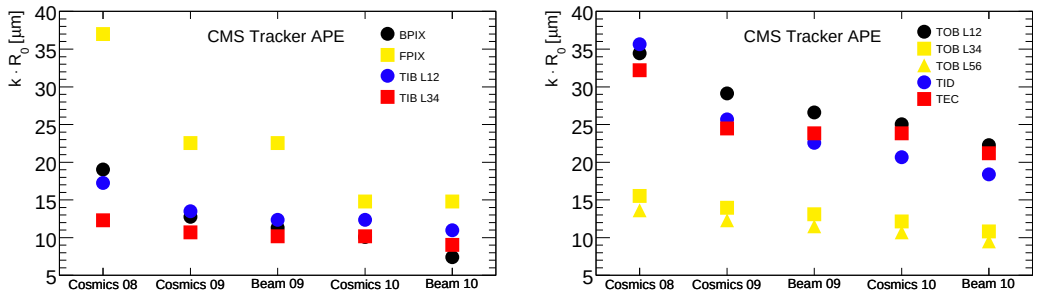

Figure 4.64: *Trend the amplitude of the mimimum value assumed for the APE, in the different Tracker regions as a function of time.*

4.4.3 APE determination after collision data taking

After the aligment performed mixing collision and comsic data described in Section 4.3 a new set of APE constant had to be released. Figure 4.38 shows a general over-estimation of the alignment errors for the collision data sample. The cosmic track sample instead, probing smaller values of track impact angles, was more sensitive to the non-planarity of the module surface, hence the larger track-to-hit residuals were compensated by the errors thus resulting in a more uniform distribution of the probability of the χ^2.

Since the constraining power of minimum bias and cosmic tracks in the endcaps is not very high, it was decided to update the APE constants only in the Tracker Barrel region. Since tracks from collisions are ϕ-symmetric, the ϕ dependence of

the errors in the Barrel, induced by the calibration with cosmic rays tracks, was no more desirable. In each Barrel layer, for all its modules, a single APE value was set to the minimum assumed by the errors in the last calibration procedure with cosmics $R_{APE} = \kappa \cdot R_0$ cfr. Section 4.4.2. In Figure 4.65 are shown the χ^2/ndf, the $Prob(\chi^2, ndf)$ and profiles of the probability as a function of different track parameters for tracks refit with the APE calibrated with cosmic rays, and the ones uniform in ϕ.

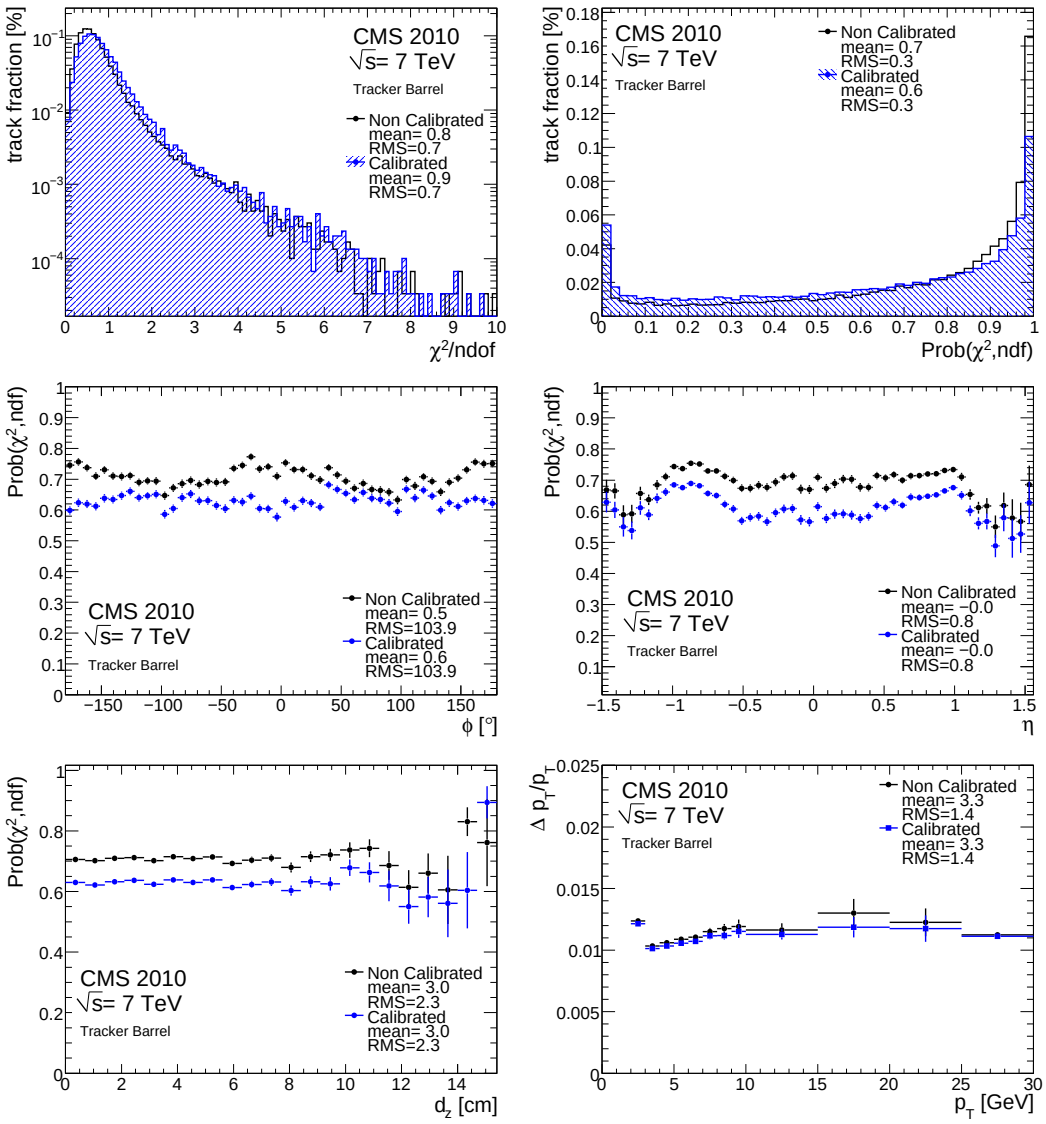

Figure 4.65: *Top row: distribution of χ^2/ndf (left) and $Prob(\chi^2, ndf)$ (right). Middle row: profiles of $Prob(\chi^2, ndf)$ vs azimuthal angle (left) and pseudorapidity (right). Bottom row: profiles of $Prob(\chi^2, ndf)$ vs longitudinal impact parameter (left) and p_T resolution (right). Data from 2010 collision events, before and after APE calibration.*

In general an improvement of the $Prob(\chi^2, ndf)$ is observed, the ϕ dependence, as expected disappears and also the p_T resolution improves. The measured average value of the probability of χ^2 is higher than $1/2$ (the expected value for ideal conditions). In Figure 4.66 are shown the distributions of normalized track-to-hit residuals for the Barrel subdetectors. The pull of these distributions for the calibrated set is higher than the one for the ϕ-dependent set, and is approaching the situation in which

no alignment position errors are used to refit the track. The fact that the pull of normalized residuals is smaller than unit even for null values of the APE, indicates an overestimation of the errors, which do not depend on aligment.

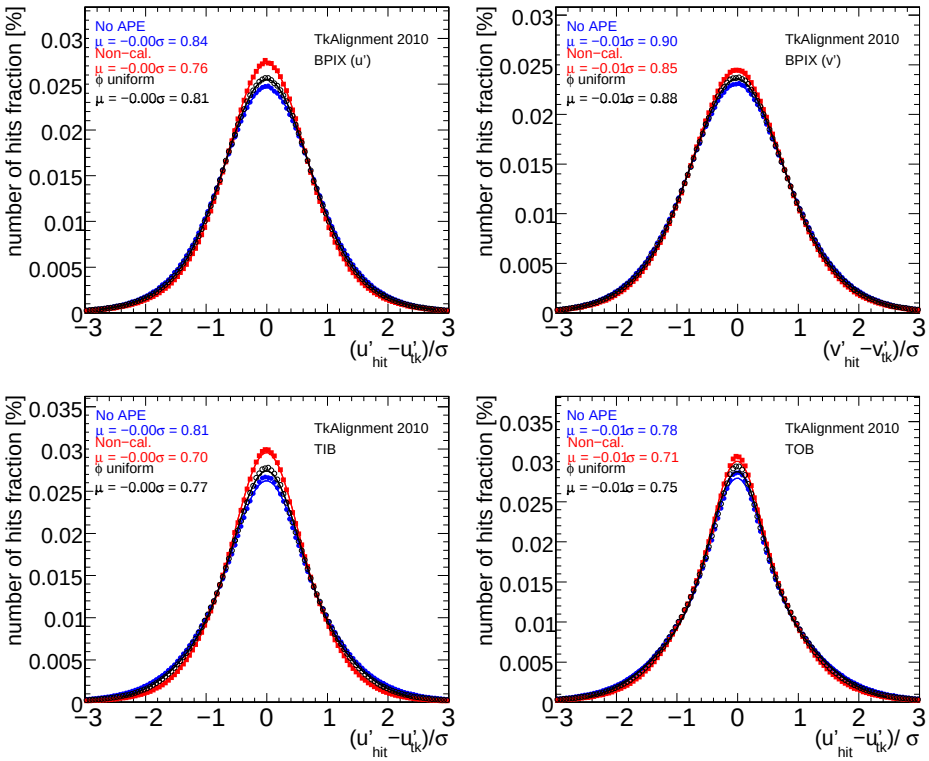

Figure 4.66: *Distributions of normalized track-to-hit residuals. First row: BPIX u' coordinate (left) and v' (right). Second row: TIB (left) and TOB (right). Data from 2010 collision events. Red symbols stand for uncalibrated APE, black symbols for the ϕ-uniform values, and blue symbols for tracks refitted with null values of APE.*

Figure 4.67 shows the trend of pulls of normalized residuals for the thirteen layers of the Tracker Barrel.

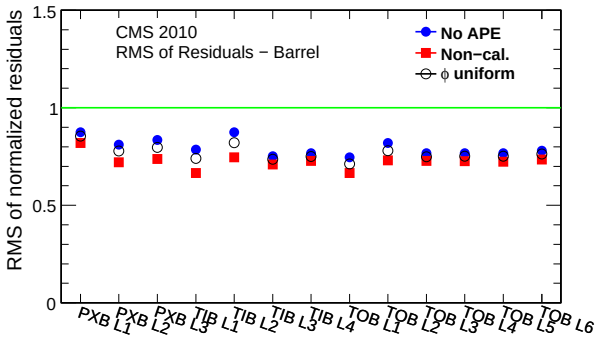

Figure 4.67: *Trend of pulls of normalized residuals for the ten layers of the Tracker Barrel. Red symbols for uncalibrated APE, black symbols for the ϕ-uniform values, and blue symbols for tracks refitted with null values of APE*

4.5 Primary Vertex Validation

During collision data-taking it was possible to monitor the alignment quality and the stability in the Pixel Tracker detector over time using a validation procedure based on the unbiased residuals of tracks originating from primary vertex (PV) with respect to the PV itsfelf. Events and tracks are selected according to Table 4.12. In Figure 4.69 can be seen some track parameters before and after the applied cuts.

Event Selection	
	Require technical trigger bit (Beam Pick Up in time) Veto beam halo events Minimal BSC activiy in either $\pm$ z
Track Selection	
	momentum $p > 0$ GeV/c transverse momentum $p_T > 1$ GeV number of Tracker hits ≥ 7 number of Pixel hits ≥ 2 At least 1 hit in BPIX Layer 1 or FPIX Disk 1

Table 4.12: *The cuts applied to select tracks for the primary vertex validation.*

For each track passing these criteria (called probes), the unbiased position of the collision point is extracted by refitting an *unbiased* primary vertex, using all and only the other tracks in the event with the vertex fitter (See Figure 4.68).

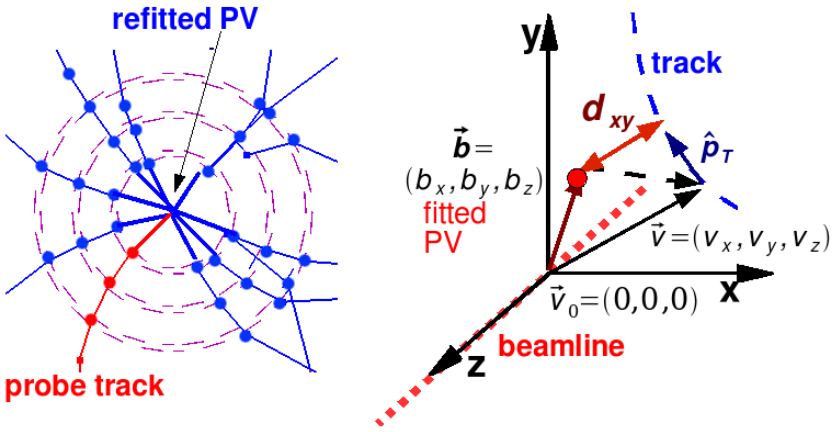

Figure 4.68: *Left: Illustration of the primary vertex validation. Right: Definition of the transverse impact parameter.*

The reconstruction of the primary interaction vertex in the event starts from the track collection. The tracks are clustered based on the z coordinate of the track at the point of closest approach to the nominal beamline. The clusters are fit with an adaptive vertex fit [50], where tracks in the vertex are assigned a weight between 0 and 1 based on their proximity to the common vertex. In Figure 4.70 are shown basic parameters of the refit vertex and in Figure 4.71 is shown the vertexing efficiency as a function of the number of tracks in the event, for 2010 collision data and simulated events, which are in fairly good agreement.

In the first very low luminosity phase the occurence of multiple PVs was very rare, so the full set of tracks was fit together. In later phases, when the the increase in instantaneous luminosity lead to a significant pile-up contamination, tracks have been clusterized, and several unbiased primary vertices per event have been refit. For each probe track then, residuals with respect to the unbiased refit PV are evaluated and plotted as a function the probe track parameters in different bins of η, ϕ and the p_T to spot degradations of the alignment (see Figure 4.68).

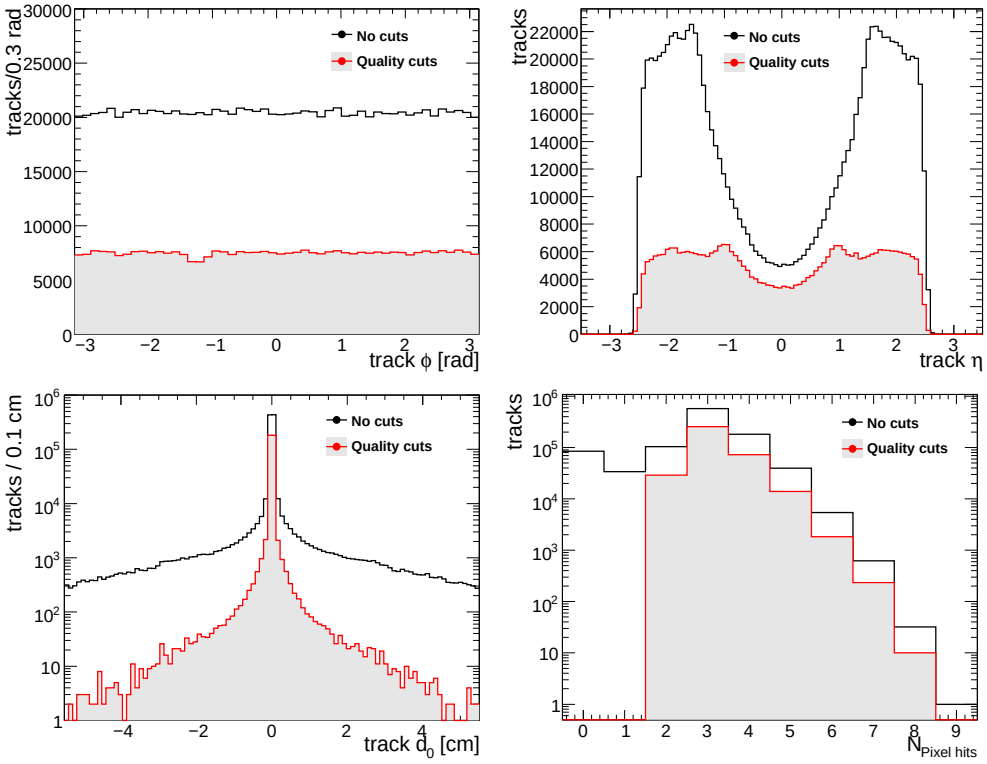

Figure 4.69: *Top row: distributions of track ϕ (left) and η (right). Bottom row: distributions of transverse impact parameter (left) and number of Pixel hits (right). Black curve refers to the minimum bias track datasample without any quality cut, while the red curve refers to the sample used for the validation, applying the cuts described in Table 4.12. Data from 2010 collisions.*

The residuals with respect the primary vertex are in effects the transverse $d_{xy}(PV)$ and longitudinal $d_z(PV)$ impact parameters (IP) of the track. If $\mathbf{b} = (b_x, b_y, b_z)$ is the position of the refitted vertex, $\mathbf{v} = (v_x, v_y, v_z)$ the position of the point of closest approach of the track with respect to the nominal interaction point, $\mathbf{p}$ the track momentum and finally $\mathbf{p}_T$ its transverse momentum, we have:

$$d_{xy}(PV) = [(\mathbf{b} - \mathbf{v}) \times \hat{\mathbf{p}}_T] \cdot \hat{z} \tag{4.24}$$

and:

$$d_z(PV) = \left[(\mathbf{b} - \mathbf{v}) \cdot \hat{\mathbf{p}}_T \left(\frac{\mathbf{p}}{p_T}\right) - (\mathbf{b} - \mathbf{v})\right] \cdot \hat{z} \tag{4.25}$$

Each calculated IP value is used to fill histograms corresponding to different bins of the track η,ϕ and p_T. For an ideal perfectly aligned Tracker, the distribution of the measured IP is centered around zero. The spread of the distributions instead depends

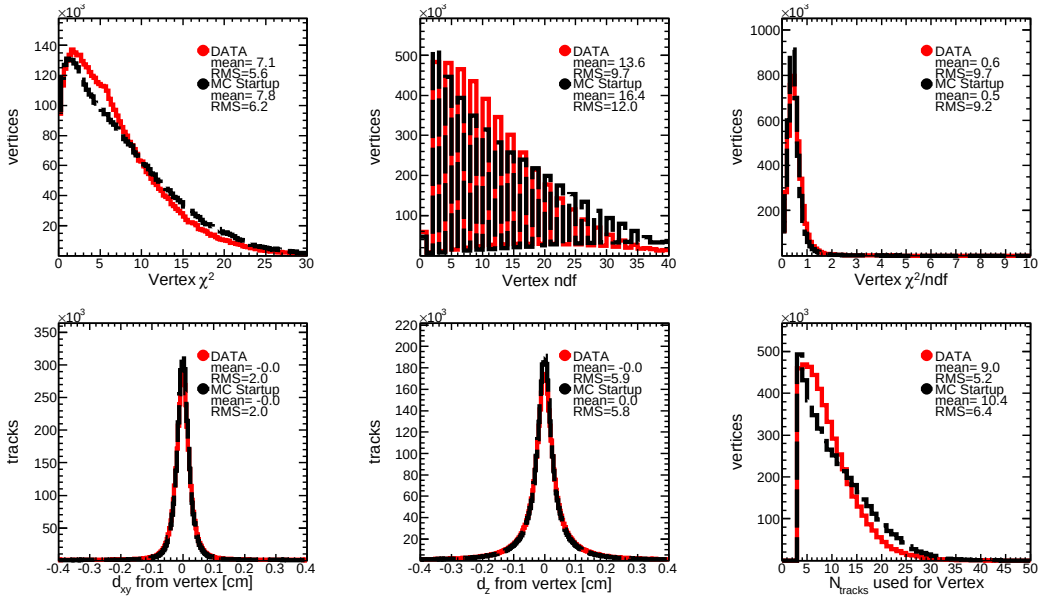

Figure 4.70: *Top row: vertex χ^2, distribution of vertex number of degrees of freedom (ndf), and normalized χ^2. Bottom row: d_{xy}, d_z calculated with respect to the unbiased vertex, and distribution of the number of tracks used to refit the PV. In red CMS 2010 collision data, and in black simulation in "Startup" conditions.*

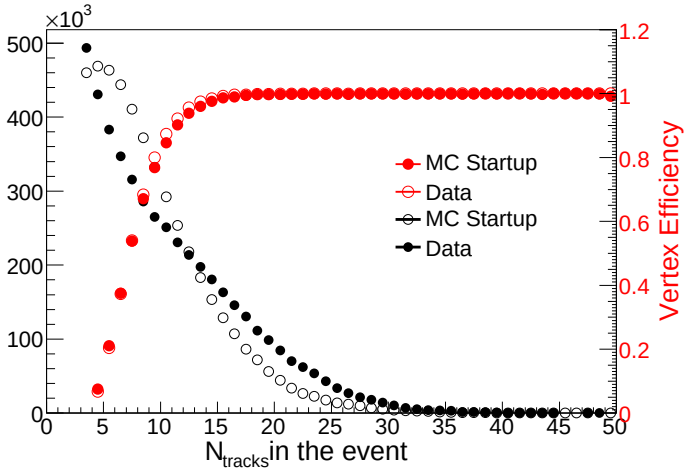

Figure 4.71: *Unbiased vertex efficiency as a function of the number of tracks in the event. The distribution of the number of used tracks is also plotted. Open symbols stand for 2010 collision data, closed symbols for simulation.*

on three terms: the uncertainty on the track impact parameter itself due to the error on the track innermost measurement and the extrapolation of the track parameters to the primary vertex through the material of the beam-pipe; the uncertainty on the primary vertex position; the fraction of selected tracks corresponding to genuinely displaced particles from decay of heavy-flavor and K^0_s or from conversions.

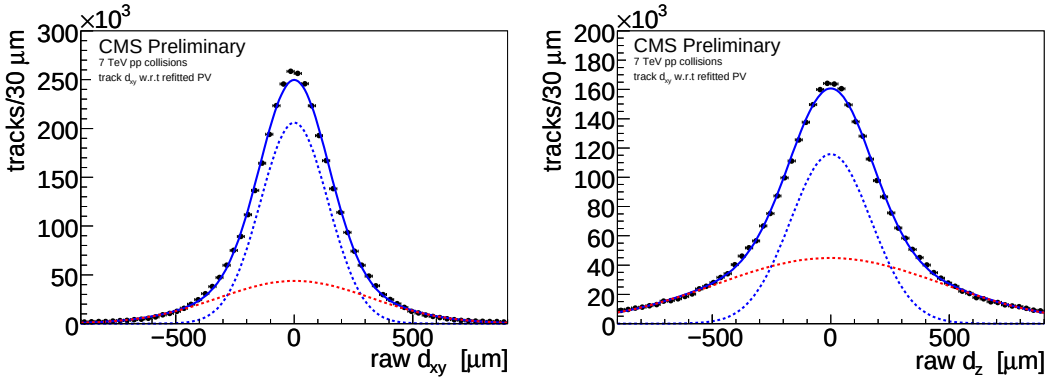

Figure 4.72: *Distributions of the unbiased transeverse d_{xy} (left) and longitudinal d_z (right) track impact parameter measured with respect the refit primary vertex. The fit function is a sum of two gaussian probability density functions, whose components are explicitluy shown (dotted lines). No selection on the tracks has been applied.*

The final IP distribution is the convolution of three probability density functions corresponding to these terms. Based on the analysis described in [35], since the fraction of selected tracks which correspond to non-prompt particles is relatively small, this contribution is ignored and the function used to fit the data is the convolution function of only two Gaussians. The chosen fit model is:

$$p(x,\mu,\sigma) = G_1(x,\mu_1,\sigma_1) + G_2(x,\mu_2,\sigma_2) \tag{4.26}$$

$$G_i(x,N_i,\mu_i,\sigma_i) = \frac{N_i}{\sqrt{2\pi}\sigma_i}\, exp\left(\frac{-(x-\mu_i)}{\sqrt{2}\sigma_i}\right)^2 \tag{4.27}$$

in which all the six free parameters are let free, and x can be either d_{xy} or d_z.
The mean value and the width of the double Gaussian distributions are calculated as:

$$\langle x\rangle = \int x p(x) dx = \frac{N_1\mu_1 + N_2\mu_2}{N_1+N_2} \tag{4.28}$$

$$\sigma^2 = \langle x^2\rangle - \langle x\rangle^2 = \frac{N_1(\mu_1^2+\sigma_1^2) + N_2(\mu_2^2+\sigma_2^2)}{N_1+N_2} - \left(\frac{N_1\mu_1 + N_2\mu_2}{N_1+N_2}\right)^2 \tag{4.29}$$

Figure 4.72 shows the distributions of the unbiased transverse d_{xy} and longitudinal d_z track impact parameters measured with respect the refit primary vertex, without any selection on the tracks; very good agreement with the fit with a sum of two gaussian probability density functions can be seen.

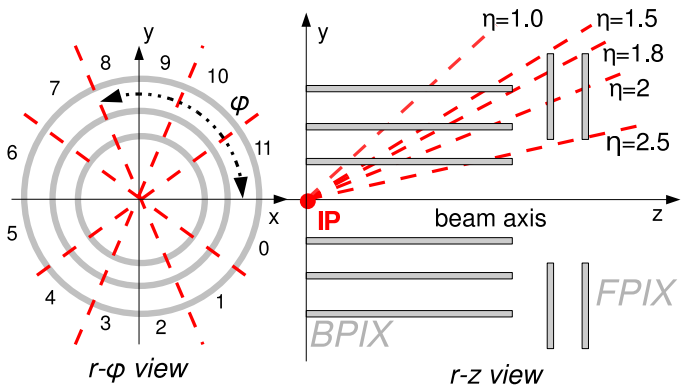

Figure 4.73: *Scheme of Pixel Tracker with highlighted the sector definitions used for the primary vertex validation.*

4.5.1 Studies on simulation

The sensitivity of the method was first tested on Monte Carlo collision events, reconstructing tracks with a geometry which simulates different movements of the entire Pixel Tracker substructures. In Figure 4.74 are shown the distributions of the transverse impact parameter d_{xy} for different bins of the ϕ angle of the probe track, according to the sector definition described in Figure 4.73, for a Monte Carlo simulation where Pixel hits have been moved according to an elliptical deformation:

$$\begin{cases} x' = & x \cdot (1 + \varepsilon \cos 2\phi) \\ y' = & y \cdot (1 + \varepsilon \cos 2\phi) \end{cases}$$

for a scenario in which the adimensional parameter ε, which corresponds to the fractional variation of the radial position of the module, has been set to 0.01.

In Figure 4.75 can be seen the trends of the mean values of unbiased transverse IP as a function of the angle ϕ of the track, for two different elliptically deformed scenarios in which the adimensional parameter ε of the deformation has been set respectively to 0.01 and 0.002. The trends are compared with that produced using the "Startup" misalignment scenario. Since the radius of the first layer of BPIX is approximately R_{L1}= 5 cm, the method can easily detect deformations down to $R_{L1} \cdot \varepsilon \approx 100$ μm.

The sensitivity of the method in z direction, was tested on a simulation in which BPIX hits have been moved applying a coherent displacement of the two BPIX half-shells in the z direction:

$$\begin{cases} z' = z & |\phi| < \pi/2 \\ z' = z + \Delta z & |\phi| > \pi/2 \end{cases}$$

Figure 4.76 shows the trends of the mean values of unbiased longitudinal IP as a function of the angle ϕ of the track, for two different scenarios in which the parameter Δz, representing the BPIX half-shells separations, has been set respectively to 10 μm and 50 μm. In this case the method is sensitive to movements down to $\Delta z = \mathcal{O}(10\mu\text{m})$.

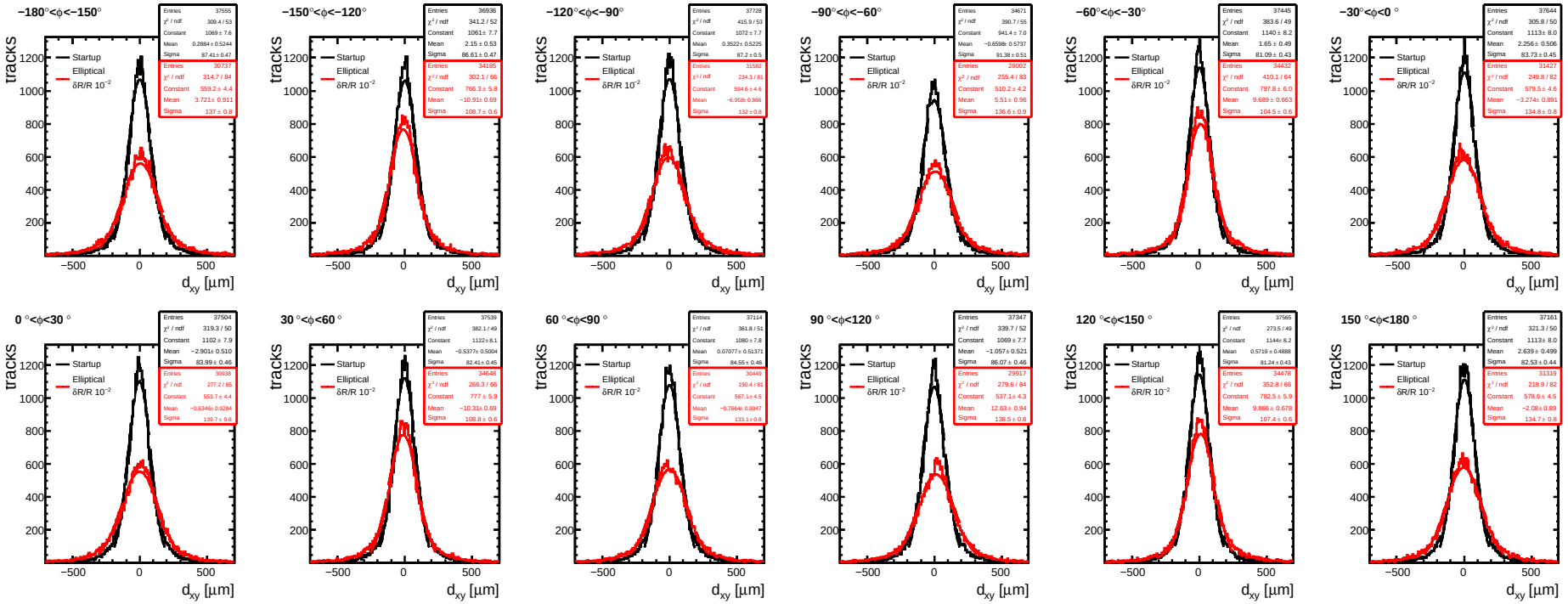

Figure 4.74: *Distributions of the transverse impact parameter d_{xy} for different bins of the ϕ angle of the probe track. The red line refers to simulated tracks reconstructed applying a coherent elliptical misalignment, while the black line, referring to simulation with a "Startup" misalignment scenario, is shown for comparison in the Figure.*

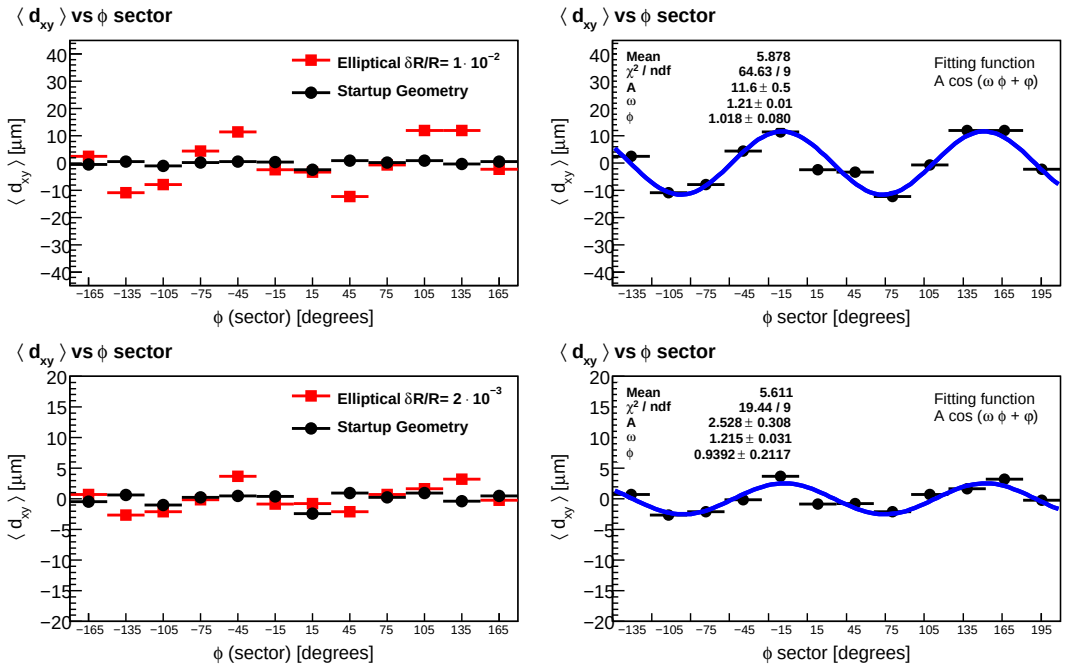

Figure 4.75: *Left column: Distributions of the mean value of transverse impact parameter d_{xy} in bins of the ϕ of the probe track, for simulated tracks reconstructed applying a coherent elliptical misalignment (red points). Simulation with a "Startup" misalignment scenario is compared in the figure (black points). In the upper row the amplitude of the misalignment considered is $\varepsilon = 0.01$, while in the lower row it was set to $\varepsilon = 0.002$. Right column: the same distributions for the elliptical misalignments are fitted with a sinusoidal function $d_{xy}(\phi) = A\cos(\omega\phi + \varphi_0)$.*

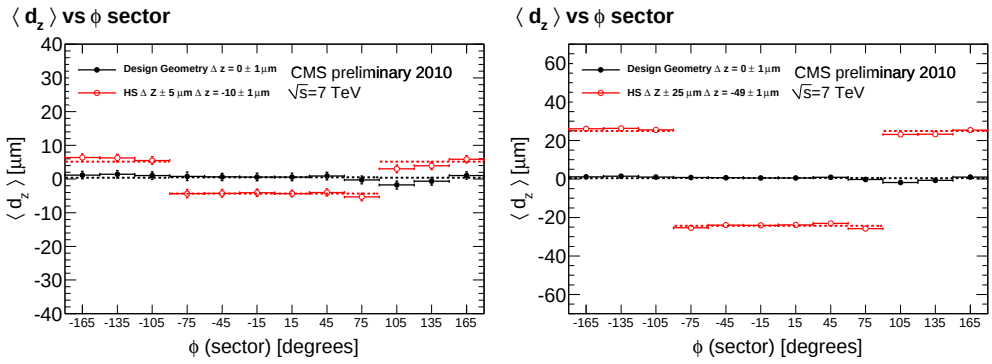

Figure 4.76: *Trend of the mean value of unbiased longitudinal IP as a function of the azimuthal angle of the probe track, for simulated tracks reconstructed applying a coherent displacement of the two BPIX half-shells in the z direction (red points). Simulation with a "Startup" misalignment scenario is shown for comparison (black points). In the left figure a displacement of 10 μm has been applied, while in the right one a displacement of 50 μm has been applied.*

4.5.2 Performance with collision data

Previous experiences in the alignment of the Tracker with cosmic rays had shown that the BPIX half-shells could move appreciably, due to changes of the environment in which the Tracker operated.

Physics analyses requiring b-tagging of jets could be very sensitive to movements of the inner layer of BPIX, so the monitoring of its geometry was mandatory. To monitor the position of the half-shells, and also other possibile deformations of the Pixel Tracker during collision data taking, an automated tool based on the method described before was deployed.

On a daily basis the `TkAlMinBias` track sample collected by the CMS Tracker the day before was analyzed and trends of the mean values and the RMS of unbiased track IP as a function of track azimuthal angle and pseudorapidity were published on a dedicated web-page [51] that could be consulted by members of the CMS collaboration.

Figures 4.77 and 4.78 are examples of the trends of the mean values and the RMS of unbiased track d_{xy} and d_z measured on July 2^{nd} 2010 as a function of the azimuthal angle ϕ and of pseudorapidity η. For comparison the distributions expected from the "Startup" misalignment scenario for simulation are also shown.

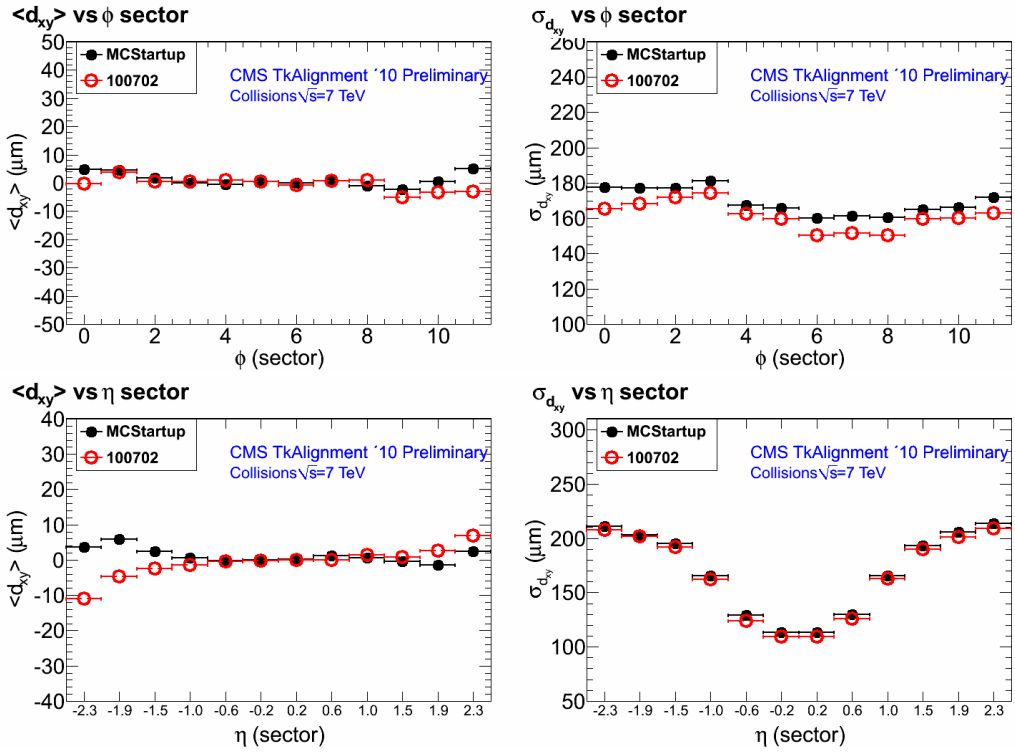

Figure 4.77: *Upper row: trends of the mean values (left) and the RMS (right) of the track d_{xy} vs ϕ. Lower row: trends of the mean values (left) and the RMS (right) of the track d_{xy} vs η. The red dots refer to values measured on July 2^{nd} 2010, black dots refer to the startup misalignment scenario.*

The most striking feature observed during the 2010 data-taking was the sporadic

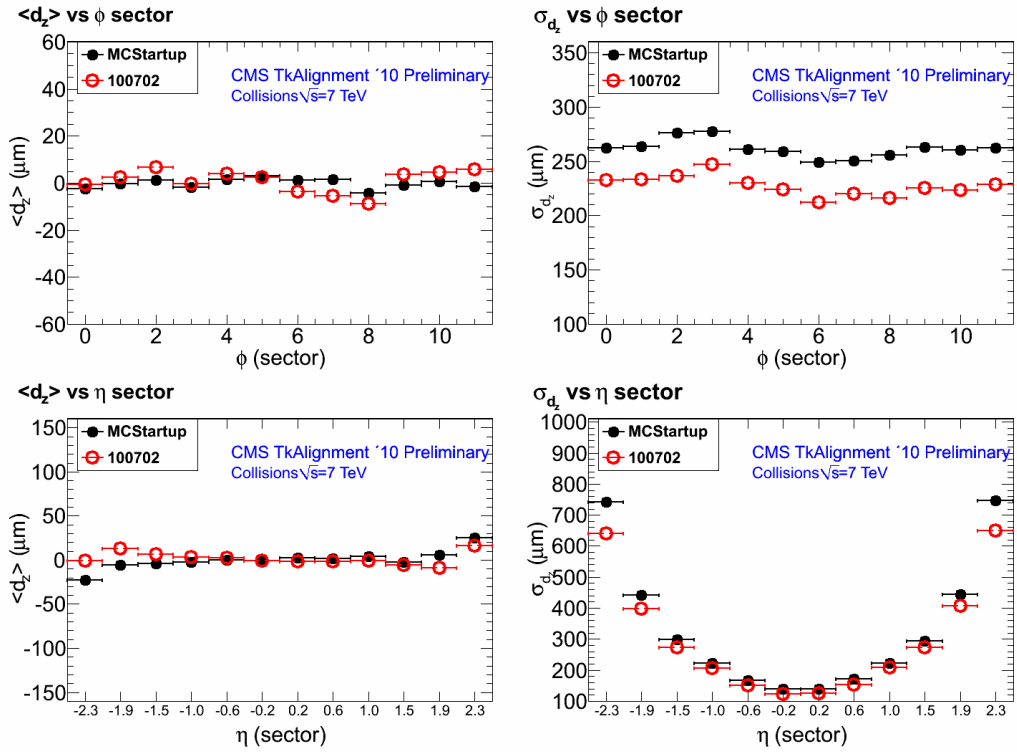

Figure 4.78: *Upper row: trends of the mean values (left) and the RMS (right) of the track d_z vs ϕ. Lower row: trends of the mean values (left) and the RMS (right) of the track d_z as vs η. The red dots refer to values measured on July 2nd 2010, black dots refer to the startup misalignment scenario.*

movement in the z direction of the BPIX half-shells (see Figure 4.79), which can be spotted by large separations between the mean values of the longitudinal impact parameter in the $|\phi| < \pi/2$ and $|\phi| > \pi/2$ regions. When writing this thesis, the cause of this movements is still not completely understood, since no clear pattern emerges when comparing the dates at which large movements occured with the agenda of Pixel Tracker operations.

The $\langle d_z \rangle$ vs ϕ profiles were fitted with a step function and the heights of the steps were quoted as the measured separation between the BPIX half-shells. As can be seen in Figure 4.80 the measured movements did not always occur in the same direction.

The movements measured with the described validation tool were taken into account for the alignment procedure with collision tracks performed at the end of year 2010, by separating the dataset in smaller samples, each one with about the same measured separation of the half-shells. Figure 4.81 shows the trend of the separation of the BPIX half-shells as a function of time, before and after the alignment procedure.

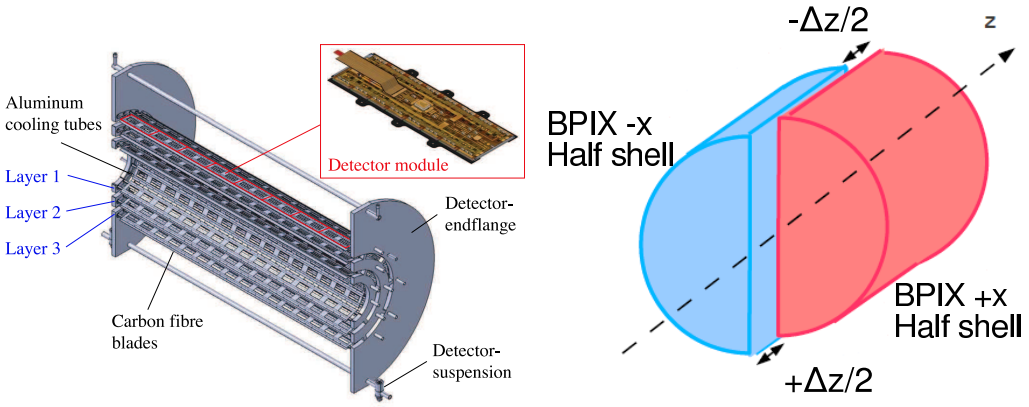

Figure 4.79: *Left: Sketch of one half of the pixel barrel detector including the endflanges [52]. Right: Sketch of the movements observed of the BPIX halfshells.*

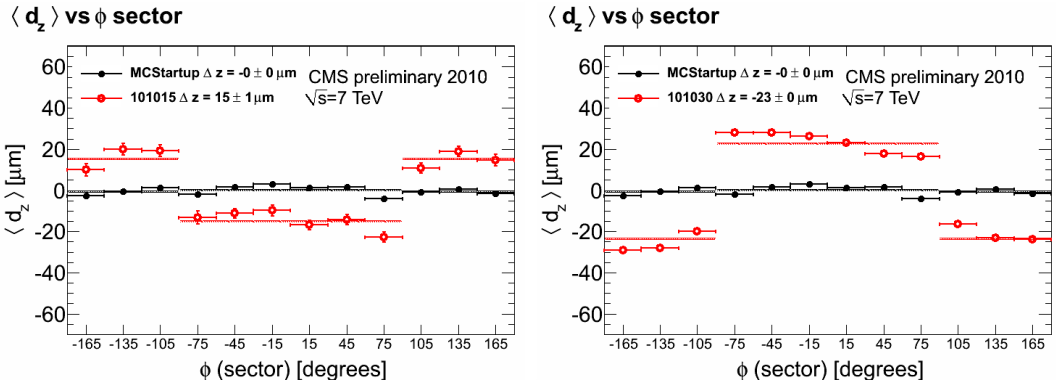

Figure 4.80: *Trends of the mean values of the unbiased track d_z as a function of ϕ, with superimposed step function fits to measure BPIX half-shells separation. The left plot refers to data collected on October 15^{th} 2010, while that on the right to data from October 30^{th} 2010. For comparison "Startup" misalignment scenario is plotted in black.*

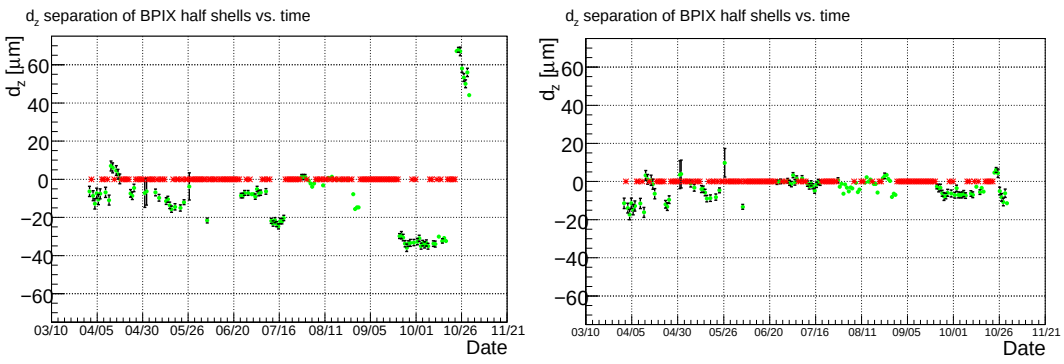

Figure 4.81: *Trend of the measured separation of the BPIX half-shells as function of the day before (left) and after (right) alignment. Solid green symbols correspond to the trend of measured separations, while red symbols refer to days in which there was no sufficient data to perform the validation.*

Chapter 5

Impact of alignment on the early charmonium physics

There are more things in heaven and earth, Horatio,
Than are dreamt of in your philosophy.
William Shakespeare

Abstract

A remaining misplacement in the position and orientation of the sensors in a detector has a remarkable impact on the track reconstruction of charged particles and finally in the measurement of the cross section of a physics process. In this chapter the effects of remaining misalignment of the CMS Tracker on the reconstruction of di-muons coming from J/ψ mesons decay are explored.

Among the most important requirements for CMS experiment to meet the goals of LHC physics program there are a good muon identification and a good di-muon mass resolution (cfr. Chapter 2). Figure 5.1 shows the invariant mass spectrum of all the di-muons collected by the CMS experiment in 2010 in roughly 40 pb^{-1} of proton-proton collision data. Narrow peaks due to resonances decaying into two oppositely charged muons are clearly visible, showing the good performance of the CMS experiment in terms of di-muon mass resolution. In the low p_T region, the first resonance decaying into di-muons to test the detector performace is the J/ψ meson.

In this chapter the effects of systematic misalignments of the Tracker on the J/ψ reconstruction will be discussed. For what concerns $m_{J/\psi}$, the high accuracy with which it is known from previous experiments (3.5 $\cdot 10^{-6}$) [10] and the narrow width of the resonance ($\Gamma_{J/\psi}$ = 91 keV) allow to use the reconstructed mass as a calibration benchmark for the muon momentum scale, and indeed the corrections found with this procedure are much larger than the effects due to misalignment. On the other hand the analysis of fraction of J/ψ mesons produced in the decay of b-hadrons (f_B) is performed for the first time in this energy regime. Therefore the effects of misalignment on f_B will be discussed in more detail.

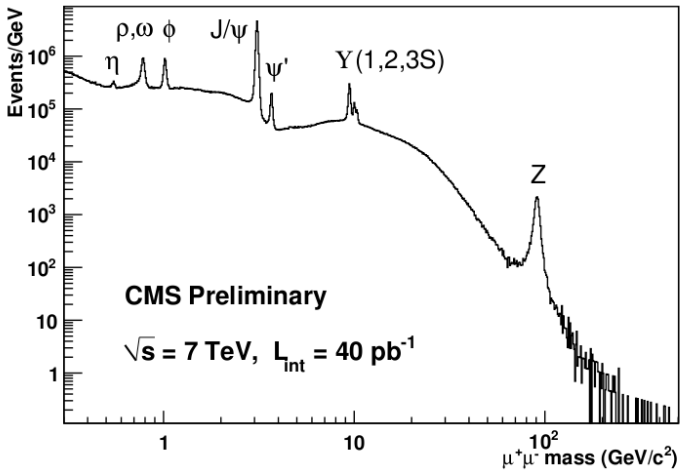

Figure 5.1: *Invariant mass spectrum of all the di-muons collected by the CMS experiment in 2010 in about 40 pb^{-1} of proton-proton collision data.*

5.1 Data sample and event reconstruction

5.1.1 Event selection

This analysis is based on a data sample recorded by the CMS detector in pp collisions at a centre-of-mass energy of 7 TeV. The sample corresponds to a total integrated luminosity of 314 ± 34 nb^{-1} [53]. During this data taking period, there were 1.6 pp collisions per bunch crossing, on average. The J/ψ mesons are reconstructed in the $\mu^+\mu^-$ decay channel. The event selection requires good quality data from the tracking, muon, and luminosity detectors, in addition to good trigger conditions.

The analysis is based on events triggered by a double-muon trigger that requires the detection of two independent muon segments at L1, without any further processing at the HLT. All three muon systems, DT, CSC and RPC, take part in the trigger decision. The coincidence of two muon signals, without any cut on p_T, is enough to keep the trigger rate reasonably low at the instantaneous luminosities of the LHC start-up.

Events not coming from pp collisions, such as those from beam-gas interactions or beam-scraping in the beam transport system near the interaction point, which produce a large activity in the pixel detector, are removed by requiring a good primary vertex to be reconstructed [54].

5.1.2 Offline muon reconstruction

In this analysis, muon candidates are defined as tracks reconstructed in the Inner Tracker which are associated with a compatible signal in the muon chambers.

Two different muon reconstruction algorithms are considered [55]. The first one provides high-quality and high-purity muon reconstruction for tracks with $p_T > 4$ GeV in the central pseudorapidity region ($|\eta| < 1.3$) and $p_T > 1$ GeV in the forward region; these muons are referred to as *Global Muons*. The second muon reconstruction algo-

rithm achieves a better reconstruction efficiency at lower momenta; these muons are referred to as *Tracker Muons*. There is an overlap between these two reconstruction methods. If a muon is reconstructed by both algorithms, it is assigned to the Global Muon category alone, making the two categories exclusive. Global Muons have a higher reconstruction purity. In both cases, the track momentum is determined by the fit in the Inner Tracker.

To reduce muon backgrounds, mostly from decays in flight of kaons and pions, and to ensure good quality reconstructed tracks, muon tracks are required to pass the following requirements: they must have at least 12 hits in the Tracker with at least two in the pixel layers, a track fit with a χ^2 per degree of freedom smaller than four, and must pass within a cylinder of radius 3 cm and length 30 cm centered at the primary vertex and parallel to the beam line. If two (or more) tracks are close to each other, it is possible that the same muon segment or set of segments is associated with more than one track. In this case the best track is selected based on the matching between the extrapolated track and the segments in the muon detectors.

5.1.3 J/ψ event selection

To select the events with J/ψ decays, muons with opposite charge are paired and their invariant mass is computed. The invariant mass of the muon pair is required to be between 2.6 and 3.5 GeV. The two muon trajectories are fitted with a common vertex constraint, and events are retained if the χ^2 probability of the fit is larger than 0.1%. This analysis uses combinations of two Global Muons, two Tracker Muons, and one Global and one Tracker Muon. On average, 1.07 J/ψ combinations were found per selected di-muon event. In case of multiple combinations in the same event, the one with the purest muon content is chosen. If there are two or more dimuon candidates of the same type (Global-Global,Global-Tracker, or Tracker-Tracker) the one of highest p_T is chosen.

The opposite-sign dimuon mass spectrum is shown in Fig. 5.2 for two different J/ψ rapidity ranges. About 27 000 J/ψ candidates have been reconstructed, of which about 19% are in the Global-Global category, 54% in the Global-Tracker category, and the remaining in the Tracker-Tracker Muon category.

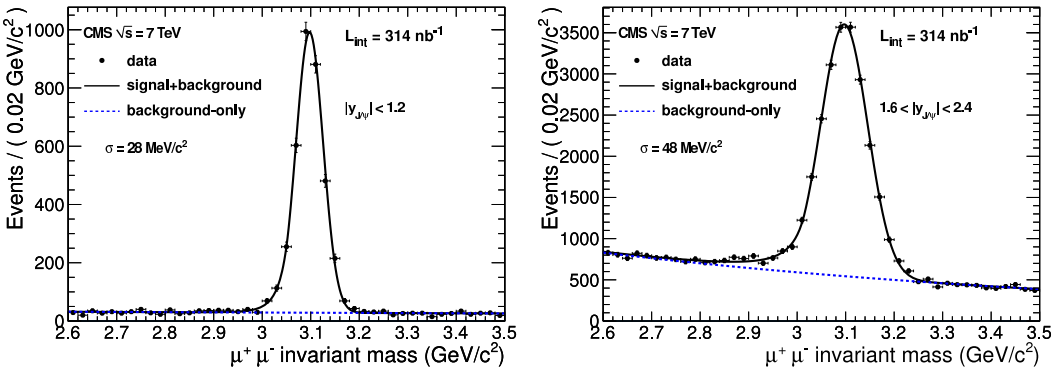

Figure 5.2: *Opposite-sign dimuon invariant mass distributions in two J/ψ rapidity ranges, fitted with a Crystal Ball function plus an exponential. The poorer dimuon mass resolution at forward rapidity is caused by the smaller lever arm of the muon tracks [62].*

5.2 Fraction of J/ψ from b-hadron decays

The production of J/ψ mesons at hadron colliders can occur in three ways: prompt J/ψ produced directly in the proton-proton collision, prompt J/ψ produced indirectly (via decay of heavier charmonium states such as χ_c), and non-prompt J/ψ from the decay of a b hadron.

The measurement of the fraction of J/ψ yield coming from b-hadron decays relies on the discrimination of the J/ψ mesons produced away from the pp collision vertex, determined by the distance between the dimuon vertex and the primary vertex in the plane orthogonal to the beam line.

The primary vertices in the event are found by performing a common fit to tracks for which the points of closest approach to the beam axis are clustered in z, excluding the two muons forming the J/ψ candidate and using adaptive weights to avoid biases from displaced secondary vertices. Given the presence of pile-up, the primary vertex in the event is not unique. According to Monte Carlo simulation studies, the best assignment of the primary vertex is achieved by selecting the one closest in the z coordinate to the dimuon vertex.

5.2.1 Separating prompt and non-prompt J/ψ

As an estimate of the b-hadron proper decay length, the quantity $\ell_{J/\psi} = L_{xy} \cdot m_{J/\psi}/p_T$ is computed for each J/ψ candidate (see Figure 5.3), where $m_{J/\psi}$ is the J/ψ mass [10] and L_{xy} is the most probable transverse decay length in the laboratory frame [59, 60]. L_{xy} is defined as

$$L_{xy} = \frac{\mathbf{u}^T \sigma^{-1} \mathbf{x}}{\mathbf{u}^T \sigma^{-1} \mathbf{u}} \quad , \tag{5.1}$$

where **x** is the vector joining the vertex of the two muons and the primary vertex of the event, in the transverse plane, $\mathbf{u}$ is the unit vector of the J/ψ p_T, and σ is the sum of the primary and secondary vertex covariance matrices.

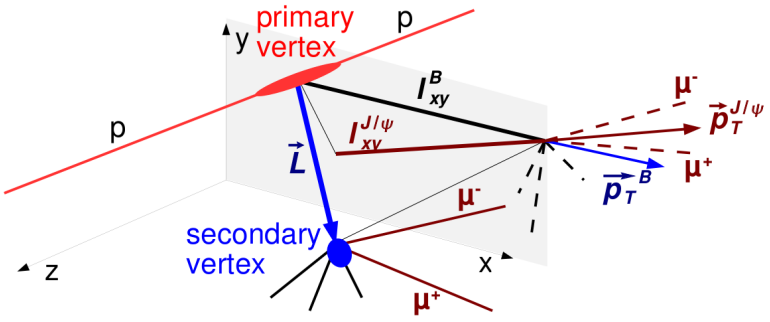

Figure 5.3: *Sketch explaining how the $\ell_{J/\psi}$ psuedo-proper decay length is calculated.*

To determine the fraction f_B of J/ψ mesons from b-hadron decays in the data an unbinned maximum-likelihood fit in each p_T and rapidity bin is performed [63]. The dimuon mass spectrum and the $\ell_{J/\psi}$ distribution are simultaneously fit by a log-likelihood function,

$$\ln L = \sum_{i=1}^{N} \ln F(\ell_{J/\psi}, m_{\mu\mu}) \tag{5.2}$$

where N is the total number of events and $m_{\mu\mu}$ is the invariant mass of the muon pair. The expression for $F(\ell_{J/\psi}, m_{\mu\mu})$ is

$$F(\ell_{J/\psi}, m_{\mu\mu}) = f_{Sig} \cdot F_{Sig}(\ell_{J/\psi}) \cdot M_{Sig}(m_{\mu\mu}) + (1 - f_{Sig}) \cdot F_{Bkg}(\ell_{J/\psi}) \cdot M_{Bkg}(m_{\mu\mu}) \tag{5.3}$$

where:

- f_{Sig} is the fraction of events attributed to J/ψ sources coming from both prompt and non-prompt components;
- $M_{Sig}(m_{\mu\mu})$ and $M_{Bkg}(m_{\mu\mu})$ are functional forms describing the invariant dimuon mass distributions for the signal and background, respectively.
- $F_{Sig}(\ell_{J/\psi})$ and $F_{Bkg}(\ell_{J/\psi})$ are functional forms describing the $\ell_{J/\psi}$ distribution for the signal and background, respectively.

  The signal part is given by a sum of prompt and non-prompt components,

  $$F_{Sig}(\ell_{J/\psi}) = f_B \cdot F_B(\ell_{J/\psi}) + (1 - f_B) \cdot F_p(\ell_{J/\psi}) \quad , \tag{5.4}$$

  where f_B is the fraction of J/ψ from b-hadron decays, and $F_p(\ell_{J/\psi})$ and $F_B(\ell_{J/\psi})$ are the $\ell_{J/\psi}$ distributions for prompt and non-prompt J/ψ, respectively.

  As $\ell_{J/\psi}$ should be zero in an ideal detector for prompt events, $F_p(\ell_{J/\psi})$ is described simply by a resolution function. The core of the resolution function is taken to be a double-Gaussian and its parameters are allowed to float in the nominal fit. Since $\ell_{J/\psi}$ depends on the position of the primary vertex, an additional Gaussian component is added, to take into account possible wrong assignments of the primary vertex; its parameters are fixed from the simulation.

  The $\ell_{J/\psi}$ shape of the non-prompt component in Eq. 5.4 is given by convolving the same resolution function with the true $\ell_{J/\psi}$ distribution of the J/ψ from long-lived b hadrons, as given by the simulation.

  For the background $\ell_{J/\psi}$ distribution $F_{Bkg}(\ell_{J/\psi})$, the functional form used by CDF [61] is used:

  $$\begin{aligned} F_{Bkg}(x) \;=\; & (1 - f_+ - f_- - f_{\rm sym}) R(x) + \\ & [\frac{f_+}{\lambda_+} e^{-\frac{x'}{\lambda_+}} \theta(x') + \frac{f_-}{\lambda_-} e^{\frac{x'}{\lambda_-}} \theta(-x') + \\ & + \frac{f_{\rm sym}}{2\lambda_{\rm sym}} e^{-\frac{|x'|}{\lambda_{\rm sym}}}] \otimes R(x' - x) \;, \end{aligned} \tag{5.5}$$

  where $R(x)$ is the resolution model mentioned above, f_i ($i = \{+, -, \mathrm{sym}\}$) are the fractions of the three long-lived components with mean decay lengths λ_i, and $\theta(x)$ is the step function. The effective parameters λ_i are previously determined with a fit to the $\ell_{J/\psi}$ distribution in the sidebands of the dimuon invariant mass distribution, defined as the regions 2.6–2.9 and 3.3–3.5 GeV.

Several sources of systematic uncertainty contribute to final sistematic uncertainty to the b-fraction measurement.

- b-hadron lifetime model;
- primary vertex estimation;
- backgrounds;
- resolution model;
- different prompt and non-prompt efficiencies;
- residual misalignments in the Tracker.

This last item will be dealt with in detail in the following section.

5.3 Tracker Weak Modes

A global translation and rotation of the whole Tracker is the simplest example of a transformation of the geometry that preserves the χ^2 of the tracks. This transformation has no effects on the internal alignment and is easily resolved by imposing the center-of-gravity of all the modules to be coincident with the design position. In the reality there are several non-trivial transformations (weak modes) of the geometry of the Tracker, which leave the χ^2 of the tracks unchanged, and can survive even after the track based alignment, if not adequately constrained. If uncorrected, they would produce systematic biases in physics observables. For instance, an uncorrected systematic rotation of the layers of the Tracker would introduce an artificial charge-dependent momentum asymmetry for the reconstructed tracks, given the use of magnetic bending to define the charge and transverse momentum of a track. Likewise, a radial expansion or compression or z-scale distortion would systematically change the measured distance scale of the detector, distorting lifetime measurements. Following the analysis described in [40] and [64], nine systematic distorsions, modeled for a cylindrical geometry, in Δr, $\Delta\phi$, and Δz as a function of r, ϕ, and z, have been considered to assess the effect of possible Tracker weak modes on the physics observables of the $pp \to J/\psi \to \mu^+\mu^-$ reaction. Table 5.1 illustrates the nine modes considered in the procedure.

Table 5.1: *Definition, formula and size of the nine systematic distorsions (modes) used for study the impact on the geometry obtained.*

	Δr	Δz	$r\Delta\phi$
vs. r	radial	telescope	curl
formula	$\Delta r{=}C \cdot r$	$\Delta z{=}C \cdot r$	$\Delta\phi{=}C_1 + C_2 \cdot r$
vs. z	bowing	z-deformation	twist
formula	$\Delta r{=}C_1 + C_2 \cdot z$	$\Delta z{=}C \cdot z$	$\Delta\phi{=}C \cdot z$
vs. ϕ	elliptical	skew	sagitta
formula	$\Delta r = r(1 - C\cos\phi)$	$\Delta z = C\cos\phi$	$r\Delta\phi = C\cos\phi$

The study consisted of the following steps:

- The geometry obtained mixing cosmics and collision tracks described in Section 4.3 was assumed as starting point;
- the position of each module of the starting geometry was changed according to the nine modes reported in Table 5.1. Figure 5.4 gives a synoptical view of each module position after applying the nine distorsions with respect to the starting aligned geometry. In order to provide a sensible comparison, the centre of both geometries is the Tracker centre of gravity, meaning that only overall translations and rotations were subtracted from both objects. The maximum amplitude of mode was taken as the largest value of the spread in positions observed by comparing the starting geometry, with another one obtained by applying the same strategy to a sub-sample of the initial dataset, which was found $\mathcal{O}(200\ \mu\text{m})$. This value lies within the construction mechanical tolerance;
- the systematically misaligned geometries were used as a starting point for nine re-alignment procedures using a *combined* strategy;
- the nine geometries obtained after the alignments were then compared, module by module, to the original aligned geometry (see Figure 5.4), in order to verify if the distortions were recovered by the alignment procedure;
- the output geometries obtained after the alignment procedure, (which may or may not contain remaining distortions) are then introduced in the standard track reconstruction procedure;
- finally the data samples reconstructed with the procedure described before were analyzed.

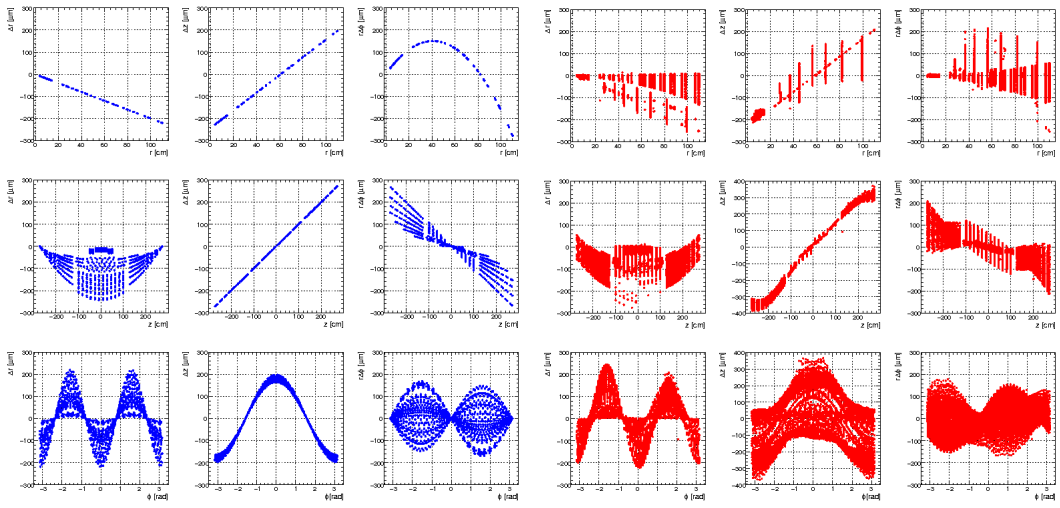

Figure 5.4: *Left: comparison of the nine geometries obtained by applying the modes described in Table 5.1 with respect to the starting aligned geometry. Right: comparison of the nine geometries obtained after the re-alignment procedure, with respect to the starting aligned geometry. Each symbol corresponds to a Tracker module.*

The remaining systematic misalignment, affecting the measured momentum of the muon tracks has an impact on the the reconstructed mass of the resonance $m_{\mu\mu}$ and on the psuedo-proper decay length $\ell_{J/\psi}$ and hence on the extraction of the b-fraction.

5.3.1 Effects on the J/ψ mass

The two-dimensional fit described in Section 5.2.1 was performed in different bins of transverse momentum $p_T^{J/\psi}$ and rapidity $y^{J/\psi}$[1] of the J/ψ meson, covering the full CMS acceptance for di-muon pairs. The binning structure was defined by a dedicated Monte Carlo study on the CMS acceptance for muon pairs coming from J/ψ decays [62]. Figure 5.5 shows the $m_{\mu\mu}$ projection of the fit for two different bins of p_T and y for the radial mode.

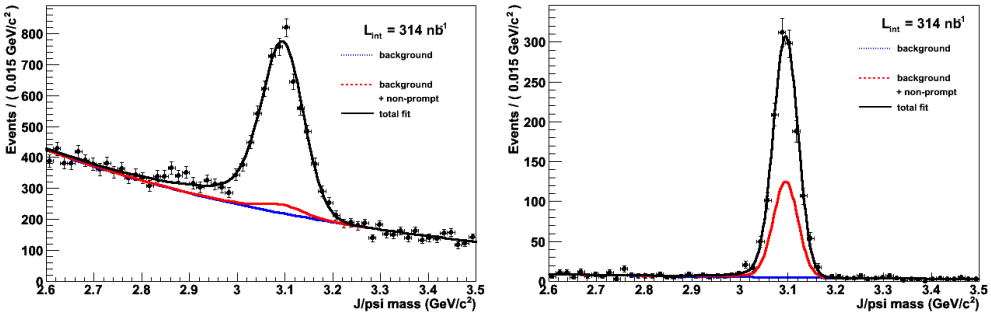

Figure 5.5: *Projection in the $m_{J/\psi}$ dimension of the two-dimensional likelihood fit in the bins $0 < p_T < 1.25$ GeV, $1.6 < |y| < 2.4$ (left) and $10.0 < p_T < 30$ GeV, $0 < |y| < 1.2$ (right).*

For each y-p_T bin the $m_{J/\psi}$ parameter was extracted for all the considered modes. The largest difference between the value obtained using the nominal geometry and the ones obtained using the deformed geometries (Δm) is taken as the systematic error due to alignment to the measurement of the mass of the J/ψ. Figure 5.6 shows for two particular y-p_T bins the measured value of the J/ψ mass, for each of the nine considered geometries.

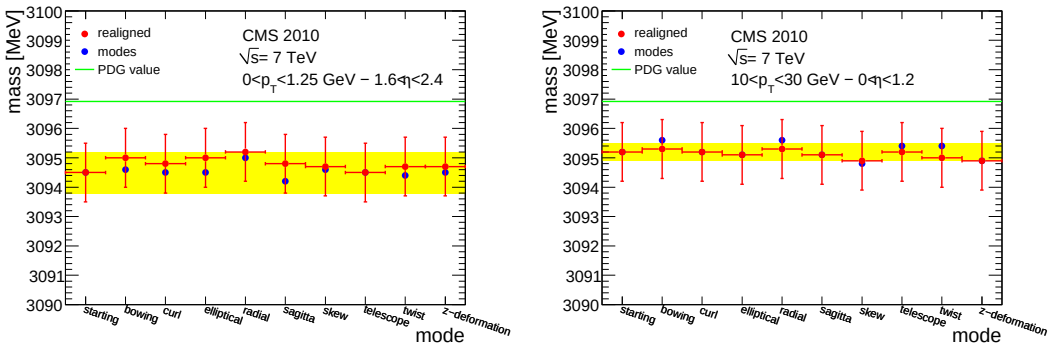

Figure 5.6: *Measured $m_{J/\psi}$ for each of the nine considered scenarios in two particular y-p_T bins. Red points refer to the situation after realignment, blue points to uncorrected mode. The error bar in the measurement of the mass comes from the fit uncertainties and are largely correlated between the different scenarios. In green is plotted the world average value of the J/ψ mass. The yellow shaded area represents the maximum Δm measured between the nominal geometry and the distorted ones (radial on the left, skew on the right), which is taken as systematic uncertainty due to alignment.*

[1] To simplify the notation in the following the superscript J/ψ will be dropped, leaving understood that kinematical quantities refer to the mesons, unless differently specified.

The measured mass of the J/ψ meson is systematically shifted to lower values with respect to the world average value, independently from the considered scenario. This behaviour is present also in a simulated sample reconstructed without misalignment. This bias can be due to systematic uncertainties due to imperfect knowledge of the magnetic field, modeling of the detector material, and eventual biases in the algorithms which fit the track trajectory [56, 57, 47]. All these effects can shift and broaden the reconstructed peaks of di-muon resonances.

Residual momentum scale effects can be determined by studying the dependence of the reconstructed di-muon peak shapes on the muon kinematics. The transverse momentum of muons was corrected for the residual scale distortion by applying correction constants (function of the muon kinematics) obtained performing a likelihood fit [58] to the invariant mass shape to minimize the difference between the reconstructed J/ψ mass and the world average value.

The systematic uncertainty on the mass shape estimated for residual systematic misalignment is by far smaller than the one introduced by this correction procedure.

5.3.2 Effects on the b-fraction measurements

The parameter f_B (b-fraction) is determined, along with the mass of the di-muon, in bins of transverse momentum p_T and rapidity y of the J/ψ meson. For each of these bins and for each considered mode, the pseudo-proper decay length $\ell_{J/\psi}$ projection of the two dimensional simultaneous likelihood fit is considered. Figure 5.7 shows the $\ell_{J/\psi}$ projection of the fit for two different bins of p_T and y for the radial mode.

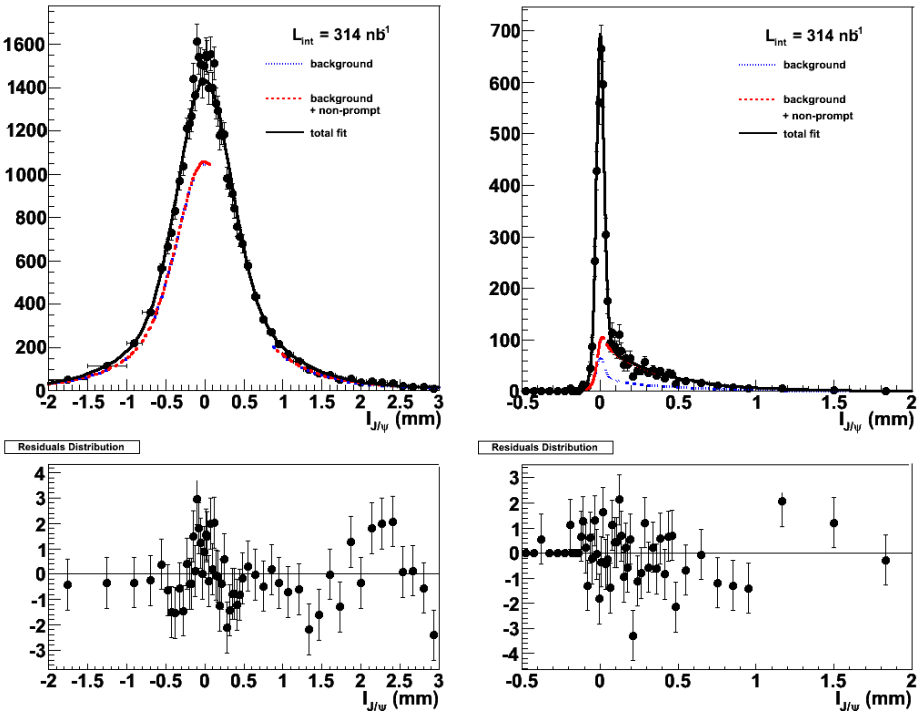

Figure 5.7: *Projection in the $\ell_{J/\psi}$ dimension of the two-dimensional likelihood fit (in mass and $\ell_{J/\psi}$) in the bins $0 < p_T < 1.25$ GeV, $1.6 < |y| < 2.4$ (left) and $10.0 < p_T < 30$ GeV, $0 < |y| < 1.2$ (right), with their pull distributions (bottom).*

For each y-p_T bin the b-fraction f_b was extracted for all the considered modes. The largest difference between the value obtained using the nominal geometry and the ones obtained using the deformed geometries (Δf_b) is taken as the systematic error due to alignment to the measurement of the b-fraction. Figure 5.8 shows for two particular y-p_T bins the measured value of the b-fraction, for each of the nine considered geometries.

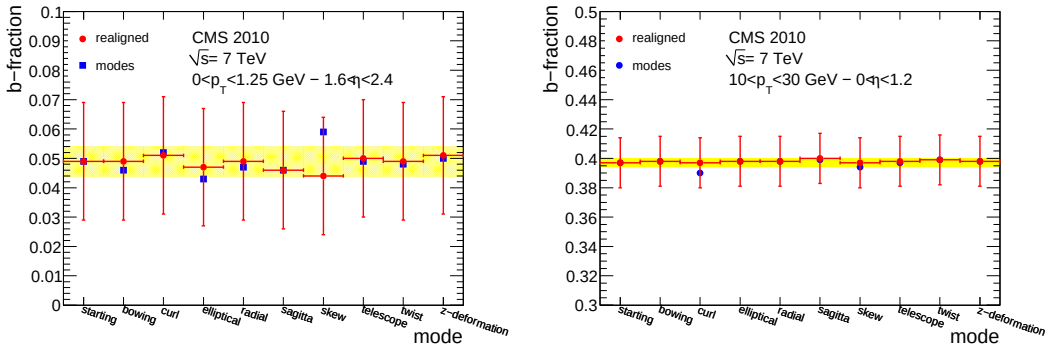

Figure 5.8: *Measured b-fraction for each of the nine considered scenarios in two particular y-p_T bins. Red points refer to the situation after realignment, blue points to uncorrected mode. The error bar in the measurement of the b-fraction comes from the fit uncertainties and are largely correlated between the different scenarios. The yellow shaded area represents the maximum Δf_b measured between the nominal geometry and the distorted ones (skew on the left, sagitta on the right), which is taken as systematic uncertainty due to alignment.*

In Table 5.2 are listed the systematic uncertainties Δf_b on the b-fraction due to alignment for each y-p_T bin, along with the modes responsible for the largest discrepancy observed with respect to the starting geometry. These errors were taken as the systematic errors due to alignment in the measurement of the b-fraction performed by the CMS experiment with the first 314 nb^{-1} of pp collision data [62]. In most bins the largest Δf_b excursion is found for distortion modes involving the z scale (z-deformation, skew, telescope). A summary of all the other systematic effects and their impact is given in Table 5.3. For comparison statistical errors on the measurement of the b-fraction range from 4% to 36 % in the differnt $y - p_T$ bins. From these Tables it is possbile to see how Tracker alignment is one of the largest sources of systematic uncertainty in the measurment, but not the largest one in any single rapidity bin.

Figure 5.9 shows the measured b-fraction. It increases strongly with $p_T$of the meson. At low p_T, essentially all J/ψmesons are promptly produced, whereas at $p_T$about 12 GeV around one third come from beauty decays. This pattern does not show a significant change with rapidity (within the current uncertainties) over the window covered by the CMS detector. The CMS results are compared to the higher-precision data of CDF [61], obtained in proton-antiproton collisions at $\sqrt{s} = 1.96$ TeV. It is interesting to note that the increase with $p_T$of the b-fraction is very similar between the two experiments, the CMS points being only slightly higher, despite the different collision energies.

Table 5.2: *Table of the systematic uncertainties Δf_b on the b-fraction due to remaining systematic misalignment for each y-p_T bin. In the table are reported also the relative uncertainty, and the mode responsible for the largest discrepancy observed with respect to the starting geometry.*

y	p_T (GeV)	Δf_b	$\Delta f_b/f_b$ (%)	mode
0-1.2	4.5 - 6.5	0.0045	2.5	skew
0-1.2	6.5 - 10.0	0.0016	0.6	sagitta
0-1.2	10.0 - 30.0	0.0021	0.5	sagitta
1.2-1.6	2.0 - 4.5	0.0066	4.7	z-deformation
1.2-1.6	4.5 - 6.5	0.0019	1.0	twist
1.2-1.6	6.5 - 10.0	0.0019	0.9	z-deformation
1.2-1.6	10.0 - 30.0	0.0057	1.6	sagitta
1.6-2.4	0.0 - 1.25	0.0051	10.5	skew
1.6-2.4	1.25 -2.0	0.0050	5.7	elliptical
1.6-2.4	2.0 - 2.75	0.0044	3.7	sagitta
1.6-2.4	2.75 - 3.5	0.0018	1.4	curl
1.6-2.4	3.5 - 4.5	0.0016	1.0	telescope
1.6-2.4	4.5 - 6.5	0.0066	3.7	z-deformation
1.6-2.4	6.5 - 10.0	0.0016	0.7	bowing
1.6-2.4	10.0 - 30.0	0.0056	1.6	radial

Table 5.3: *Summary of relative systematic uncertainties in the b-fraction yield $\Delta f_b/f_b$ (in %). The range shows the min-max $\Delta f_b/f_b$ excursion found when changing the p_T bin for each of the three rapidity regions. In general, uncertainties are p_T-dependent and decrease with increasing p_T.*

	$\lvert y\rvert < 1.2$	$1.2 < \lvert y\rvert < 1.6$	$1.6 < \lvert y\rvert < 2.4$
Tracker misalignment	$0.5 - 2.5$	$0.9 - 4.7$	$0.7 - 10.5$
b-lifetime model	$0.0 - 0.1$	$0.5 - 4.8$	$0.5 - 11.2$
Vertex estimation	0.3	$1.0 - 12.3$	$0.9 - 65.8$
Background fit	$0.1 - 4.7$	$0.5 - 9.5$	$0.2 - 14.8$
Resolution model	$0.8 - 2.8$	$1.3 - 13.0$	$0.4 - 30.2$
Efficiency	$0.1 - 1.1$	$0.3 - 1.3$	$0.2 - 2.4$

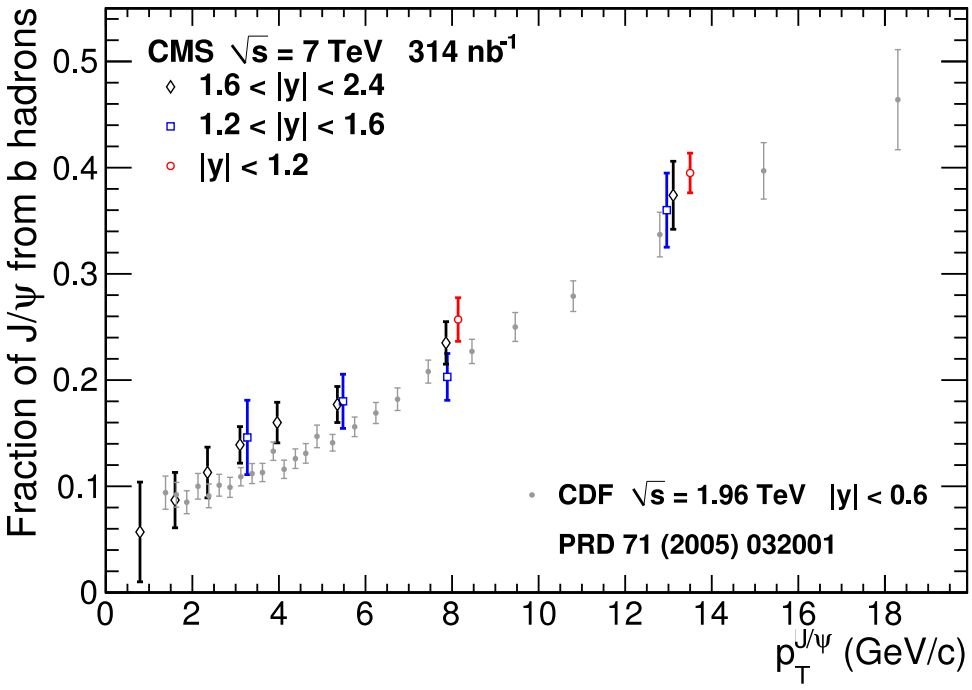

Figure 5.9: *Fraction of the J/ψ production cross section originating from b-hadron decays, as a function of the $p_T^{J/\psi}$, as measured by CMS in three rapidity bins and by CDF, at a lower collision energy [62].*

Summary

The challenging demands of the Compact Muon Solenoid detector for the measurement of the charged particles tracks have led to the design of an extremely complex inner tracking system. The unknown position of its 15 000 independent modules is one of the main sources of systematic error affecting the momentum measurement, and consequently the related physics observables. This thesis presents the achievements obtained in the study of the Inner Silicon Tracker performance, focusing on the alignment of the system using different sources of data: before with cosmic ray muons and then including tracks originated in the proton-proton collisions at $\sqrt{s} = 7$ TeV.

Track based alignment procedures, relying on a linearized least square combined fit of alignment parameters and track parameters, are expected to reduce the module position uncertainties to the level of few microns. However the correction constants provided by the alignment algorithms require thorough validation both in terms of tracking performance and impact on physics observables.

The first opportunity to operate the Tracker with the CMS solenoidal magnetic field at its design intensity was the Cosmic Run at Four Tesla in the Fall of 2008, when several millions tracks were reconstructed with a fully active Tracker. The adopted alignment strategy provided a resulting measured position for the Tracker components which significantly improved the reconstruction of the tracks. The precision of the sensors position has been derived from the distribution of the median of the cosmic muon tracks residuals to be 3 - 4 μm RMS in the barrel region and 4 - 15 μm in the endcaps in the most sensitive coordinate with respect to particle trajectories.

The remaining random displacements of the sensors were also studied using the cosmic track sample, and allowed to derive the alignment position uncertainties to be used during the track reconstruction phase. An algorithm to calibrate these uncertainties was developed and tested during the subsequent comic rays data-taking campaigns.

In 2010 the LHC delivered the first high energy collisions, enabling to use collision tracks in the alignment procedures. A substantial improvement of alignment conditions was observed in the innermost and in the forward regions of the Tracker. Collision track topology allowed to estimate remaining misalignment in the barrel region by a fit procedure to the track-to-hit residuals as a function of track momentum. Furthermore, a flexible data-driven tool, based on the unbiased adaptive refit of primary vertices was developed and tested on the 2010 data sample allowing to monitor alignment performance in the Pixel Tracker.

Finally the impact of the remaining systematic misalignment on charmonium physics observables have been evaluated on a sample of J/$\psi \to \mu\mu$ decays corresponding to an integrated luminosity of about 300 nb^{-1}. Exploiting a two dimensional likelihood fit procedure, sytematic misalignment effects on the measured J/ψ mass and on the fraction of J/ψ mesons produced in the disintegration of b-hadron have been explored.

Appendix A

Effects of the outliers in the distributions of residuals

Figure A.1 shows the track-to-hit residuals for two typical TIB modules, recorded during the 2008 cosmic ray data taking campaign.

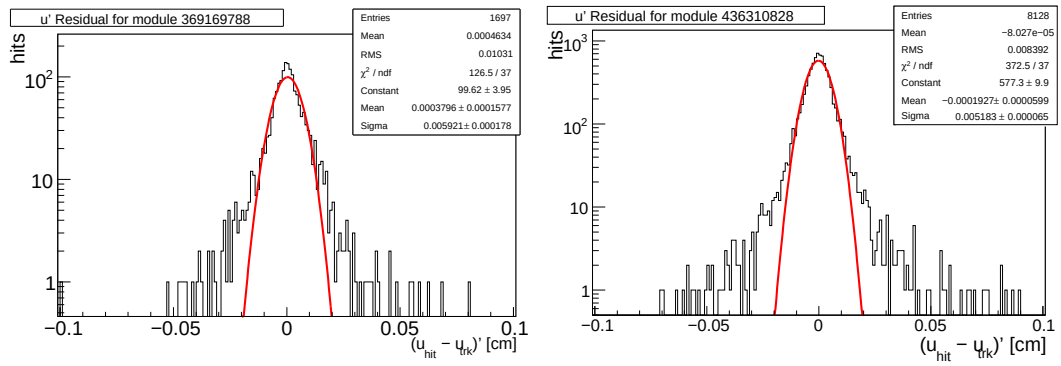

Figure A.1: *Track-to-hit residuals for two typical TIB (left) and TOB (right) modules, recorded during the 2008 cosmic ray data taking campaign.*

It can be seen that outside a gaussian core, non-gaussian tails are present. Most of the residuals lying very far away from the core of the distribution are in effect due to spurious hits (due to noise, bad clustering, etc.) and in general they are not related to alignment effects. In the estimation of the remaining misalignment, the contribution of these hits has to be excluded. In Chapter 4, it has been discussed how the RMS of the *DMR* (*D*istribution of the *M*edian of *R*esiduals) could provide a reliable estimation of the residual misalignment. In this Appendix a quantitative discussion of the effect of outliers on the mean value and the median of the distribution of residuals will be carried out. Pseudo-experiment Monte Carlo distributions of residuals have been generated for each of the 3942 TIB and 6288 TOB modules according to the following *pdf*:

$$f(R) = \underbrace{(1-f)\cdot N_{hits}\; e^{\left(-\frac{(R-\mu)^2}{2\sigma^2}\right)}}_{\text{gaussian core}} + \underbrace{f\cdot N_{hits}\; e^{-\frac{|R|}{R_0}}}_{\text{outliers}} \qquad \text{(A.1)}$$

A gaussian distribution of mean value μ and standard deviation σ has been chosen to account for the core of the residual, while an exponentially falling function, with decay

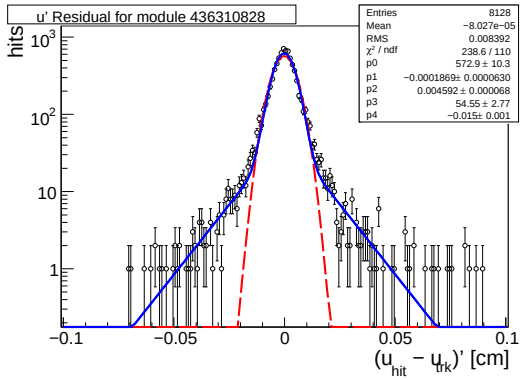

Figure A.2: *Track-to-hit residuals for a typical TOB modules recorded during the 2008 cosmic ray data taking campaign, with superimposed a fit function based on the model in Equation A.1. The red dashed line is the pure gaussian component.*

constant R_0 is used to simulate the outliers. N_{hits} is the total number of entries of the generated histogram, while f is the fraction of outlier hits. For each module the N_{hits} parameter has been randomly generated according to distribution measured in 2008 cosmic ray data, see Figure A.3.

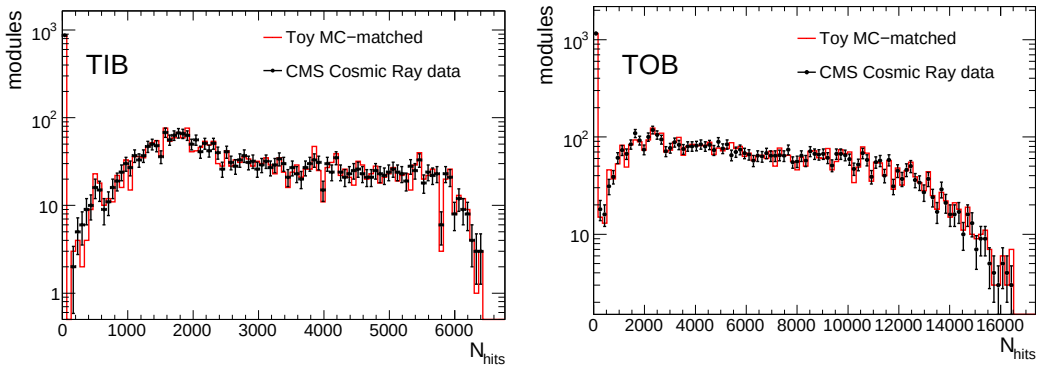

Figure A.3: *Distribution of the number of valid hits in the TIB (left) and TOB (right) subdetector. Black dots represtent the observed distribution in 2008 cosmic ray data, while in red is the randomly generated distribution of number of hits for the pseudo-experiment simulation discussed in the text.*

The width of the distribution of residuals has been set to $\sigma = 60$ μm in both TIB and TOB, while the mean value μ has been generated randomly, for each module according to a gaussian smearing of null mean value and width equal to 3 μm, to reproduce random misalignment measured in data.
The fraction of outliers has been varied in the simulation from no outliers to 5% of the total hits, in steps of 0.5%. For each of the generated residual distribution then, the arithmetic mean and the median have been extracted, and ten histograms of distribution of means and medians of residuals have been filled. The RMS of these histograms are then used to estimate the misalignment. In Figure A.4 are plotted the RMS of the DMR for the ten different fractions of outliers generated in the simulation.

The RMS of the medians distributions is clearly a robust estimator of the input misalignment even at high fractions of outliers, since the discrepancy between the estimate and the input value is always O(1 μm) which is less than the intrinsic precision of the method. The RMS of the distribution of the mean is not robust,

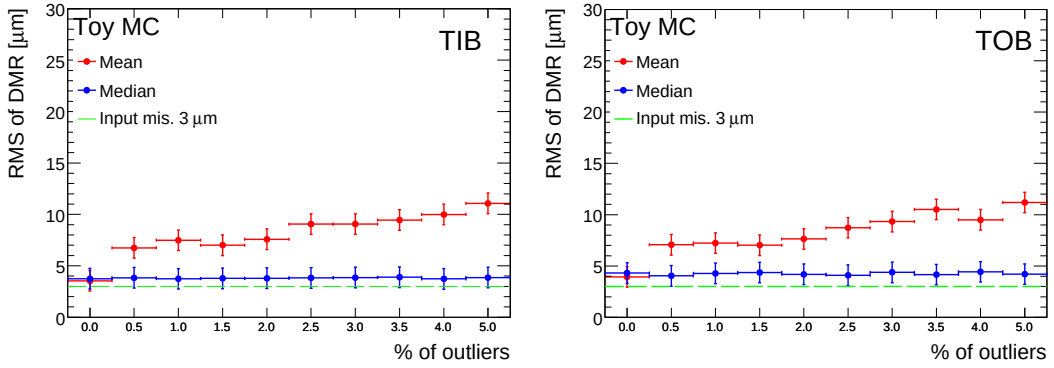

Figure A.4: *Trend of the RMS of distributions of medians (blue points) and means (red points) for TIB (left) and TOB (right).*

being affected even at low fractions of outliers. The bias introduced with the RMS of the mean of residuals is observed to be roughly linear in the number of outliers.

Appendix B

Error scaling

Track-to-hit residuals for an entire Tracker subdetector or Tracker layer can be assumed to be distributed with a gaussian probability density function:

$$f(R) = N \cdot \exp\left(-\frac{(R-\mu)^2}{2\sigma^2}\right) \tag{B.1}$$

where μ is the mean value and σ the gaussian standard deviation of the residual distribution.
To get the pull one must divide the residual R by its error σ_R.
As it was shown in Chapter 3, the uncertainty on the residual can be written as the sum of two contributions:

$$\sigma_R^2 = \sigma_{hit}^2 + \sigma_{tk}^2$$

Separating the contribution of Alignment Position Errors, C in this formula, from the other uncertainties σ_0 (namely intrinsic hit resolution and track extrapolation uncertainty):

$$\sigma_R^2 = \sigma_0^2 + C^2$$

Assuming that all the modules within the subdetector or the layer have same residual uncertainty σ_R, the normalized residual is:

$$\widehat{R} = \frac{R}{\sigma_R} = \frac{R}{\sqrt{\sigma_0^2 + C^2}}$$

As can bee seen in Figure B.1 again this variable is distributed with a gaussian p.d.f.:

$$f(\widehat{R}) = N \cdot \exp\left(-\frac{(\widehat{R}-\widehat{\mu})^2}{2P^2}\right)$$

and the width of the distribution is the pull (P): $P = \frac{\sigma}{\sqrt{\sigma_0^2+C^2}}$.

The pulls of the normalized residual distributions for a calibrated (C') and a non

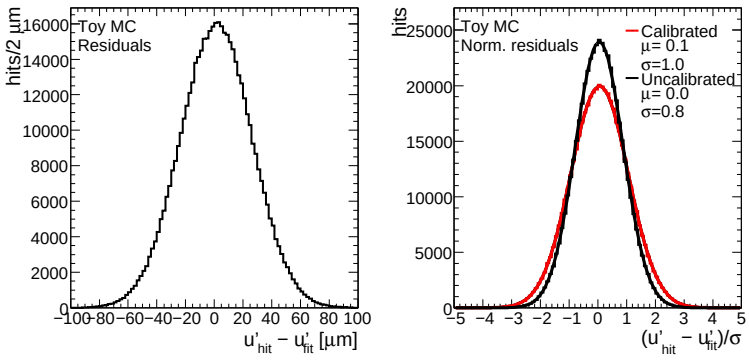

Figure B.1: *Left: pseudo-experiment MC distribution of a gaussian distributed random variable (residual) Right: pseudo-experiment MC distribution of the normalized residuals, using two different errors in the denominator.).*

calibrated (C_0) set of APE will be:

$$P' = \frac{\sigma}{\sqrt{\sigma_0^2 + C'^2}} \;\; ; \;\; P_0 = \frac{\sigma}{\sqrt{\sigma_0^2 + C_0^2}}$$

The ratio of the pulls is:

$$\frac{P'}{P_0} = \sqrt{\frac{\sigma_0^2 + C_0^2}{\sigma_0^2 + C'^2}}$$

Solving for the calibrated set:

$$P'^2(\sigma_0^2 + C'^2) = (\sigma_0^2 + C_0^2)P_0^2$$

Assuming now that the calibrated set of errors C' produces a distribution of normalized residuals with optimal pull $P' = 1$:

$$\sigma_0^2 + C'^2 = (\sigma_0^2 + C_0^2)P_0^2$$

This finally brings to the formula to obtain calibrated errors.

$$C'^2 = (P_0^2 - 1)\sigma_0^2 + C_0^2 P_0^2 \tag{B.2}$$

This relation allows to get the optimal set of alignment errors from the previous set (C_0), the estimate of the other uncertainty contributions (σ_0^2) and the observed pull of normalized residuals P_0. In the simple case where the alignment error is much larger than the intrinsic contribution ($\sigma_0^2 \ll C_0^2$) a simplification can be used:

$$C' = C_0 \cdot P_0 \tag{B.3}$$

Appendix C

More on systematic movements of the Pixel Tracker substructures

In Section 4.5 it has been shown how the Primary Vertex validation tool can spot movements of the entire Pixel Tracker substructeres. In this appendix, we explore, by using simulated collision events, the effects caused by other systematic movements.

Since the two BPIX half-shells are mechanically independent, shifts in any of the three directions are possibile. The shift along the global CMS z-axis direction has already been considered in Chapter 4. We consider here a displacement of one of the two half-shells with respect to the other in the y direction. The applied transformation on the nominal geometry is:

$$\begin{cases} y' = y & |\phi| < \pi/2 \\ y' = y + \varepsilon & |\phi| > \pi/2 \end{cases}$$

The value of the shift chosen for this exercise is ε= 25 μm. In Figure C.1 are shown the profiles of $\langle d_{xy} \rangle$ and $\sigma_{d_{xy}}$ as a function of ϕ and η of the probe track. Comparison with the "Startup" Monte Carlo curve shows a clear deviation from the expected behaviour. In Figure C.2 are shown 2-dimensional maps of the measured values in the η-ϕ space of the probe track.

Another possible movement is an overall rotation of the BPIX around the CMS global y-axis. In the small angle approximation ($\vartheta \ll 1$) the transformation to be applied on the nominal geometry is:

$$\begin{cases} x' = (1 - \vartheta^2/2) \cdot x - \vartheta \cdot z \\ z' = \vartheta \cdot z + (1 - \vartheta^2/2) \cdot x \end{cases}$$

The value of the angle chosen was ϑ= 0.5 mrad. In Figure C.3 are shown the profiles of $\langle d_z \rangle$ and σ_{d_z} as a function of ϕ and η of the probe track. Again comparison with the "Startup" Monte Carlo curve shows a clear deviation from the expected behaviour. In Figure C.4 are shown 2-dimensional maps of the measured values, in the η-ϕ space of the probe track.

Finally it is possible to consider misalignments of sub-components of the BPIX, for example the radial shift of one or more BPIX *ladders*. Applying to the nominal

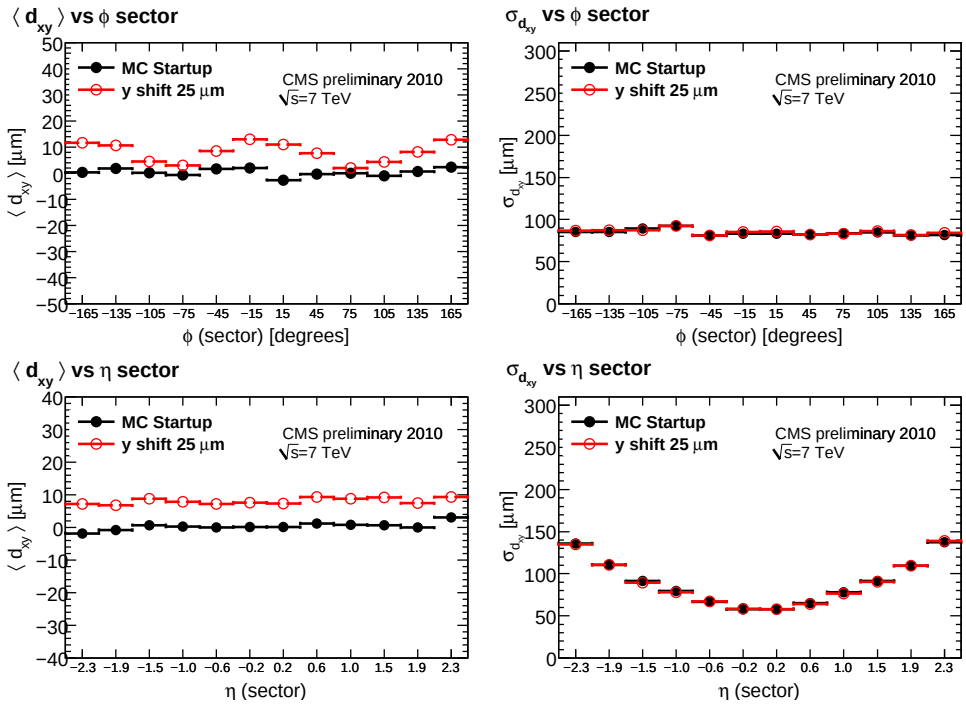

Figure C.1: *Top: profiles of $\langle d_{xy} \rangle$ and $\sigma_{d_{xy}}$ as a function of the probe track ϕ. Bottom: profiles of $\langle d_{xy} \rangle$ and $\sigma_{d_{xy}}$ as a function of the probe track η. The applied movement is a shift in y of the BPIX half-shells. Red stands for the geometry obtained after the transformation, black for simulation in "Startup" conditions.*

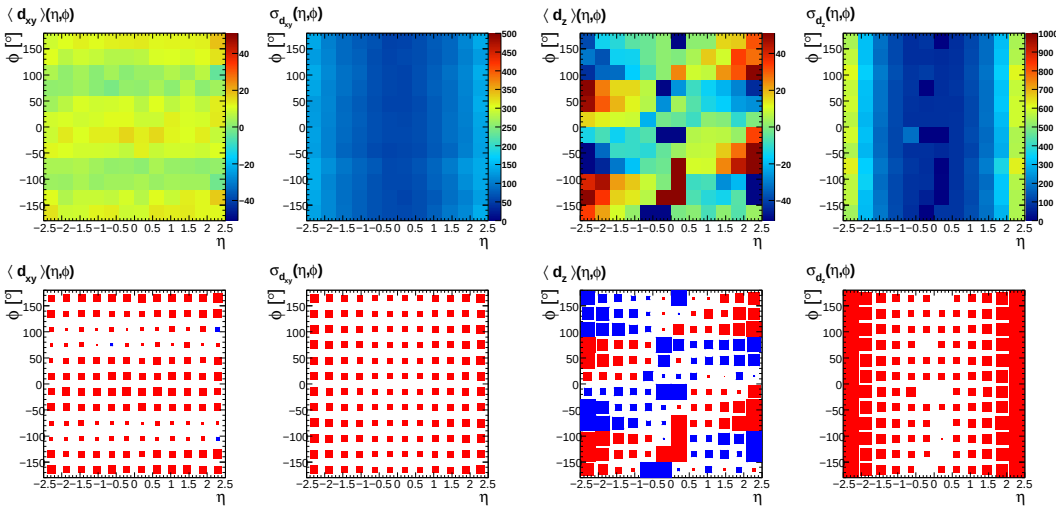

Figure C.2: *Top row: 2-D maps in the η-ϕ plane of (from left to right) $\langle d_{xy} \rangle$, $\sigma_{d_{xy}}$, $\langle d_z \rangle$ and σ_{d_z} for the BPIX half-shells shift in y. Units of measurement in the colors scales are in μm. In the bottom row the same maps are shown, in which blue stands for negative values, red for positive and the size of the marker for the magnitude of the measured value.*

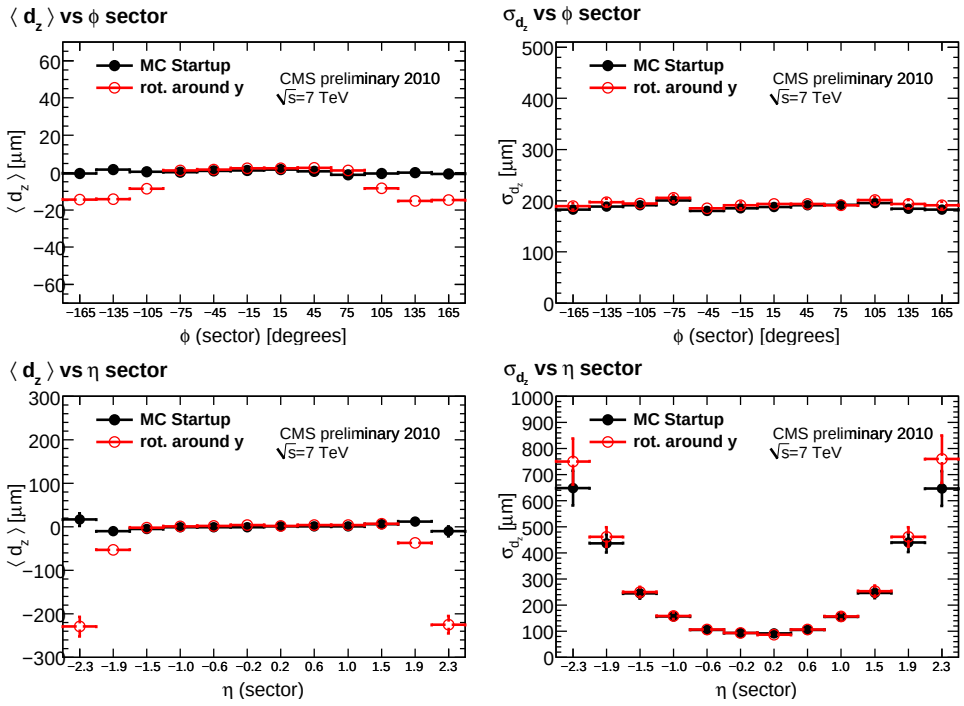

Figure C.3: *Top: profiles of $\langle d_z \rangle$ and σ_{d_z} as a function of the probe track ϕ. Bottom: profiles of $\langle d_z \rangle$ and σ_{d_z} as a function of the probe track η. The applied movement is a rotation of the entire BPIX around the y-axis. Red stands for the geometry obtained after the transformation, black for simulation in "Startup" conditions.*

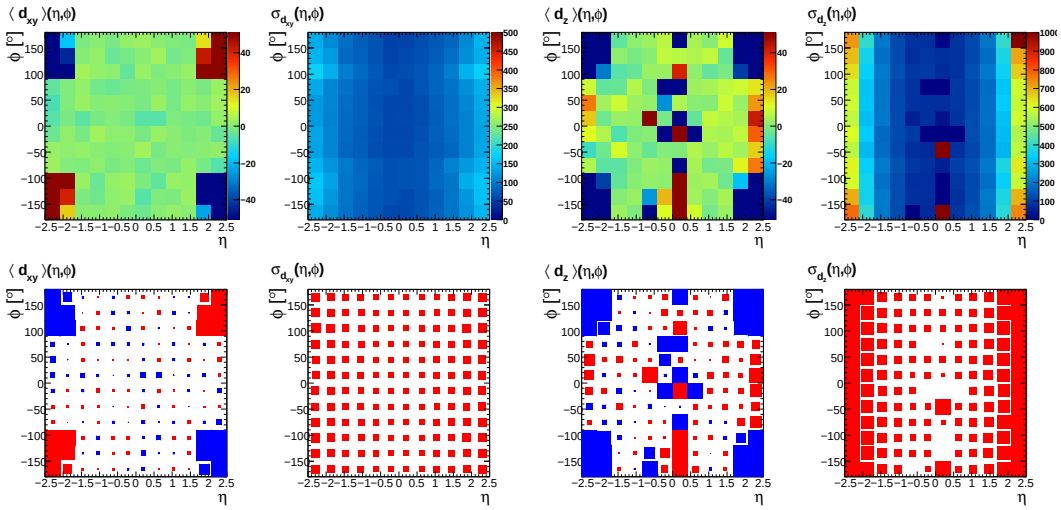

Figure C.4: *Top row: 2-D maps in the η-ϕ plane of (from left to right) $\langle d_{xy} \rangle$, $\sigma_{d_{xy}}$, $\langle d_z \rangle$ and σ_{d_z} for the rotation of the entire BPIX around the y-axis. Units of measurement in the colors scales are in μm. In the bottom row the same maps are shown, in which blue stands for negative values, red for positive and the size of the marker for the magnitude of the measured value.*

geometry the following transformation:

$$0 < \phi < \pi/2 \begin{cases} x' = x + \delta \\ y' = y + \delta \end{cases}$$

with $\delta = 70$ μm a shift in the radial direction modules of a distance Δr about 100 μm is effectively applied to the BPIX ladders in the in the $0 < \phi < \pi/2$ region. In Figure C.5 are shown the profiles of $\langle d_{xy} \rangle$ and $\sigma_{d_{xy}}$ as a function of ϕ and η of the probe track. Comparison with the "Startup" Monte Carlo curve shows a clear deviation from the expected behaviour in the $0 < \phi < \pi/2$ sector. In Figure C.6 are shown 2-dimensional maps of the measured values, in the η-ϕ space of the probe track.

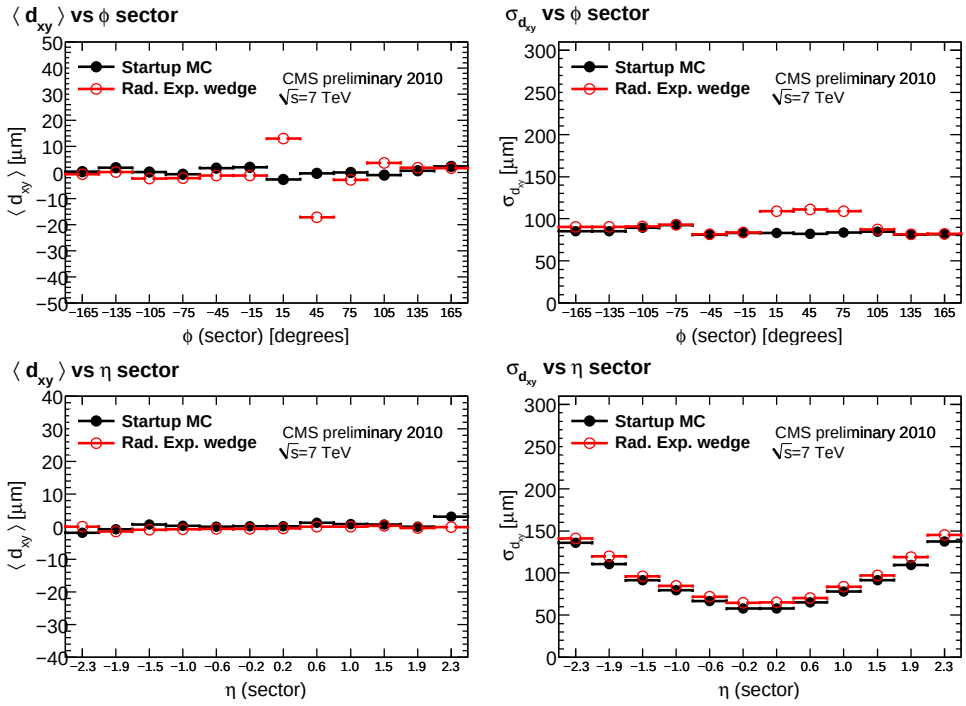

Figure C.5: *Top: profiles of $\langle d_{xy} \rangle$ and $\sigma_{d_{xy}}$ as a function of the probe track ϕ. Bottom: profile of $\langle d_{xy} \rangle$ and $\sigma_{d_{xy}}$ as a function of the probe track η. The applied movement is a radial expansion of the BPIX layers in the $0 < \phi < \pi/2$ quarter. Red stands for the geometry obtained after the transformation, black for simulation in "Startup" conditions.*

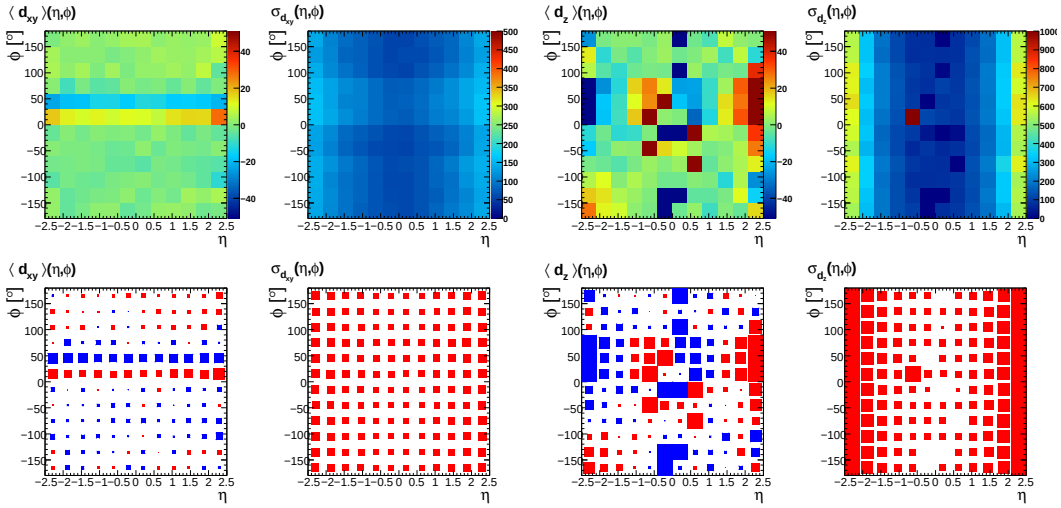

Figure C.6: *Top row: 2-D maps in the η-ϕ plane of (from left to right) $\langle d_{xy} \rangle$, $\sigma_{d_{xy}}$, $\langle d_z \rangle$ and σ_{d_z} for a radial expansion of the BPIX layers in the $0 < \phi < \pi/2$ quarter. Units of measurement in the colors scales are in μm. In the bottom row the same maps are shown, in which blue stands for negative values, red for positive and the size of the marker for the magnitude of the measured value*

References

[1] S.L. Glashow, Nucl. Phys. **22** (1961) 579;
S. Weinberg, Phys. Rev. Lett. **19** (1967) 1246;
A. Salam, *Elementary Particle Theory*, Almquist & Wisksells, Stockholm (1968) p. 367.

[2] S. Dawson, *Introduction to Electroweak Symmetry Breaking*, hep-ph/9901280;

[3] *LEP Design Report*, CERN 1984;

[4] P. Proudlock *LEP200 Design Report* Tech. Rep. SL-PC-Tech-Note-91-87, CERN, Geneva,1991;

[5] *SLC Design Hadbook: Stanford Linear Collider. Design Report*, Stanford, CA:SLAC, 1984;

[6] Tevatron I Gropup *Design Report Tevatron I Project*, FERMILAB-DESIGN-1984-01, 1984;

[7] The LEP collaboration, the LEP electroweak working group and the SLD Heavy Flavour Group, *A Combination of Preliminary Electroweak Measurements and Constraints on the Standard Model*, LEPEWWG/2003-01 (2003); `http://lepewwg.web.cern.ch/LEPEWWG/`;

[8] The LHC study group, *LHC the Large Hadron Collider: conceptual design*, CERN/AC/95-05 vol.II (1995);

[9] J. M. Campbell et al., *Hard interactions of quarks and gluons: a primer for LHC physics*, Rep. Prog. Phys. 70, pg.89-193 (2007);

[10] C. Amsler et al. (Particle Data Group), Physics Letters B667, 1 (2008) and 2009 partial update for the 2010 edition;

[11] A. D. Martin et al. *Uncertainties of predictions from parton distributions I: Experimental errors*, Eur. Phys. J. C 28 pg.455 (2003);

[12] J. Pumplin et al. *New Generation of Parton Distributions with Uncertainties from Global QCD Analysis*, JHEP 2002-07:012, `arXiv:hep-ph/0201195v3` (2002);

[13] *HERA and LHC: a Workshop on the Implication of HERA for LHC Physics*, `e-print: hep-ph/0601012` (2004-2005);

[14] LHC Higgs Cross Section Working Group *Handbook of LHC Higgs Cross Sections: 1. Inclusive Observables* `arXiv:1101.0593`;

[15] H. T. Haber et al. *The search for Supersimmetry: probing physics beyond the Standard Model*, Physics Report 117, pg.75 (1985);

[16] H. Fritzsch, Phys.Lett. B, 67:217, 1977;

[17] F. Halzen, Phys.Lett. B, 69:105, 1977;

[18] J.F. Owens M. Glück and E. Reya, Phys.Lett. D, 17:2324, 1978;

[19] Y. Keung V.D. Barger and R.J. Phillips. Phys.Lett. B, 91:253, 1980;

[20] W. E. Caswell and G. P. Lepage. *Effective lagrangians for bound state problems in qed, qcd, and other field theories.* Phys.Lett. B, 167:437, 1986;

[21] B. A. Thacker and G. Peter Lepage. *Heavy-quark bound states in lattice QCD*. Phys.Lett. D, 43(1):196-208, 1991;

[22] Geoffrey T. Bodwin, Eric Braaten, and G. Peter Lepage. *Rigorous qcd analysis of inclusive annihilation and production of heavy quarkonium*. ERRATUM-IBID.D, 55:5853, 1997;

[23] K. Anikeev et al. *B physics at the Tevatron: Run II and beyond*, 2002;

[24] The CMS collaboration, *Detector performance and software*, Physics Technical Design Report, Vol. I, CERN/LHC 2006-001, CMS TDR 8.1 (2006);

[25] The CMS collaboration, *The Magnet Project Technical Design Report* Tech.Rep. CERN/LHCC 97-10 and CMS TDR1, CERN 1997;

[26] S. Chatrchyan *et al.*, *Precise Mapping of the Magnetic Field in the CMS Barrel Yoke using Cosmic Rays*, JINST, vol. 5, T03021, 2010;

[27] R. Adolphi et al., *The CMS experiment at the CERN LHC*, JINST 0803 (2008) S08004 [JINST 3 (2008) S08004];

[28] The CMS collaboration, *The Tracker Project*, Technical Design Report, CERN/LHC 1998-006, CMS TDR 5 (1998);

[29] M. Raymond et al., *The CMS Tracker APV25 0.25 mm CMOS Readout Chip*, Proceedings of the 6th workshop on electronics for LHC experiments, Krakow, Poland (2000);

[30] The CMS collaboration, *The Tracker Project*, Technical Design Report, CERN/LHC 1998-006, CMS TDR 5 (1998);

[31] R. Frühwirth, *Application Of Kalman Filtering to Track and Vertex Fitting*, Nucl. Instrum. Meth. A 262, pg.444 (1987);

[32] T. Miao, H. Wenzel, and F. Yumiceva, *Beam Position Determination Using Tracks*, CMS Note 2007/021 (2007);

[33] W. Adam et al., *Track Reconstruction in the CMS Tracker*, CMS Note 2006/041 (2006).

[34] The CMS Collaboration, *Measurement of Tracking Efficiency* CMS-PAS-TRK-10-002;

[35] The CMS Collaboration, *Tracking and Vertexing Results from First Collisions* CMS-PAS-TRK-10-001;

[36] C. Kleinwort, F. Meier, *Alignment of the CMS Silicon Tracker and how to improve detectors in the future*, arXiv:1010.2039 (2010);

[37] F. P. Schilling *Track Reconstruction and Alignment with the CMS Silicon Tracker*, arXiv:physics/0610005v1;

[38] W. Adam et al., *Alignment of the CMS Silicon Strip Tracker during stand-alone Commissioning*, JINST 4:T07001 (2009);

[39] V. Karimäki, T. Lampén, F.P. Schilling, *The HIP Algorithm for Track Based Alignment and its Application to the CMS Pixel Detector*, CMS NOTE-2006/018, (2006);

[40] D. N. Brown, A. V. Gritsan, Z. J. Guo, D. A. Roberts, *Local Alignment of the BABAR Silicon Vertex Tracker*, Nucl. Instr. Methods Phys. Res. A 603, 467, 2009;

[41] V. Blobel, C. Kleinwort *A New Method for the High-Precision Alignment of Track Detectors*, Proceedings of the Conference on Advanced Statistical Techniques in ParticlePhysics, Durham (UK), e-print: hep-ex/0208021, March 2002;

[42] M. Stoye *Calibration and Alignment of the CMS Silicon Tracking Detector*, CERN-THESIS-2007-049;

[43] The CMS Collaboration, *The CMS Computing Project Technical Design Report*, CERN-LHCC-2005-023;

[44] R. Adolphi et al., *The 2008 CMS Computing, Software and Analysis Challenge*, CMS IN-2008/044;

[45] T. Sjöstrand, S. Mrenna, and P. Skands, *A Brief Introduction to PYTHIA 8.1*, Comput.Phys.Commun. 178 (2008) 852867;

[46] The CMS collaboration, *Commissioning of the CMS Experiment and the Cosmic Run at Four Tesla*, JINST 5:T03001 (2010), arXiv:0911.4845;

[47] The CMS collaboration, *Alignment of the CMS Silicon Tracker during Commissioning with Cosmic Rays*, JINST 5:T03009 (2010), arXiv:0910.2505;

[48] The CMS collaboration, *Commissioning and Performance of the CMS Silicon Strip Tracker with Cosmic Ray Muons.*, JINST 5 (2010) T03008 , arXiv:0911.4996;

[49] The CMS collaboration *Impact of Tracker Misalignment on the CMS b-Tagging Performance*, CMS-PAS-BTV-07-003 (2009);

[50] W. Waltenberger, R. Früwirth, and P. Vanlaer, *Adaptive Vertex Fitting*, CMS Note 2007/008 (2007);

[51] http://musich.web.cern.ch/musich/CronPVValidation/

[52] C. Amsler et al., *Mechanical design and material budget of the CMS barrel pixel detector*, JINST 4 P05003 (2009);

[53] The CMS Collaboration, *Measurement of CMS Luminosity*, CMS Physics Analysis Summary, CMS-PAS-TRK-10-00 (2010);

[54] The CMS Collaboration, *Tracking and Primary Vertex Results in First 7 TeV Collisions*, CMS Physics Analysis Summary, CMS-PAS-TRK-10-005 (2010);

[55] The CMS Collaboration, *Performance of muon identification in pp collisions at* $\sqrt{s}$*= 7 TeV*, CMS Physics Analysis Summary, CMS-PAS-MUO-10-002 (2010);

[56] The CMS Collaboration, *Precise mapping of the magnetic field in the CMS barrel yoke using cosmic rays*, JINST, 5-T03021 (2010);

[57] The CMS Collaboration, *Studies of Tracker Material in the CMS Detector*, CMS Physics Analysis Summary, CMS-PAS-TRK-10-003 (2010);

[58] The CMS Collaboration, *Measurement of Momentum Scale and Resolution using Low-mass Resonances and Cosmic Ray Muons*, CMS Physics Analysis Summary, CMS-PAS-TRK-10-004, (2010);

[59] The ALEPH collaboration, *Measurement of the* $\bar{B}^0$ *and* B^- *meson lifetimes*, Phys. Lett.,B307-194 (1993);

[60] The ALEPH collaboration, Erratum-ibid., B325-537, (1994);

[61] The CDF Collaboration, *Measurement of the* J/ψ *meson and* b*-hadron production cross section in* $p\overline{p}$ *collisions at* $\sqrt{s} = 1960\ \mathrm{GeV}$, Phys. Rev., D71-032001, (2005);

[62] The CMS Collaboration, *Prompt and non-prompt* J/ψ *production in pp collisions at* $\sqrt{s}$ *= 7 TeV*, CERN-PH-EP-2010-046, arXiv:1011.4193 (2010);

[63] N. Adam [...] M. Musich, et al. *Inclusive total and differential production cross section of* J/ψ *and b-hadron production in pp collisions at* $\sqrt{s} = 7$ *TeV with the CMS experiment*, CMS AN 2010/138 (2010);

[64] R. Castello, *Alignment of CMS Tracker detector using cosmic ray particles and its impact on early physics performance*, CMS-TS-2010-027, CERN-THESIS-2010-150 (2010);